The Department of Mechanical Engineering at
The University of Texas at El Paso
Proudly Presents

5th Southwest Energy Science & Engineering Symposium

Saturday, April 4th, 2015

The University of Texas at El Paso
500 W. University Ave.
El Paso, Texas 79968

5th Southwest Energy Science and Engineering Symposium

April 4th, 2015
Wyndham Airport Hotel and Water Park
2027 Airway Blvd
El Paso, TX 79925

Department of Mechanical Engineering
College of Engineering
University of Texas El Paso
500 W. University Ave.
El Paso, Texas 79968
Phone: (915)-747-5450 Fax: (915)-747-5019
seses@utep.edu

Web Link: http://engineering.utep.edu/seses/

FOREWARD

Welcome to the Southwest Energy Science and Engineering Symposium sponsored by Shell. The purpose of the symposium is to encourage communication among the engineers and scientists in and around the El Paso area's universities and industries.

The following individuals and organizations are acknowledged for their assistance with the symposium.

Conference Chair:	Dr. Ahsan Choudhuri, University of Texas El Paso
Technical Chair:	Dr. Pavana Prabhakar, University of Texas El Paso
Logistics Committee:	Carmen Medellin, University of Texas El Paso
Hosted By:	College of Engineering Department of Mechanical Engineering & Center for Space Exploration and Technology Research (cSETR) University of Texas El Paso
Welcome and Introduction:	Dr. Richard Schoephoerster Dean, College of Engineering University of Texas El Paso
Session Chairs:	Dr. Deidra Hodges, University of Texas El Paso Dr. Binata Joddar, University of Texas El Paso Dr. Yirong Lin, University of Texas El Paso Dr. Norman Love, University of Texas El Paso Dr. Paras Mandal, University of Texas El Paso Dr. Pavana Prabhakar, University of Texas El Paso Dr. C.V. Ramana, University of Texas El Paso Dr. Evgeny Shafirovich, University of Texas El Paso Dr. Eric Smith, University of Texas El Paso Dr. Vinod Kumar, University of Texas at El Paso Dr. Calvin Stewart, University of Texas El Paso Dr. Miguel Velez, University of Texas El Paso
Keynote Address:	**Jeane L. Hull** Executive Vice President, Technical Services Peabody Energy **Robert Romanosky, Jr., Ph.D** Deputy Director DOE/NETL Office of Coal and Power R&D U.S. Department of Energy

Southwest Energy Science and Engineering Symposium

UNIVERSITY OF TEXAS EL PASO
APRIL 4th, 2015

7:30 am	**REGISTRATION**	Wyndham Airport Hotel	Room: Rosewood
8:00 am	**BREAKFAST**	Wyndham Airport Hotel	Room: Rosewood
8:00 am	**OPENING NOTES**	Dr. Pavana Prabhakar Assistant Professor Department of Mechanical Engineering University of Texas El Paso	
8:00 am	**INTRODUCTION**	Dr. Ahsan Choudhuri Professor & Chair Department of Mechanical Engineering	
8:10 am	**WELCOME**	Dr. Richard Schoephoerster Dean, College of Engineering University of Texas El Paso	Room: Rosewood
8:15 am	**KEYNOTE PRESENTATION - I**	**Jeane L. Hull** Executive Vice President Technical Services Peabody Energy	Room: Rosewood
9:30 am	**PARALLEL TECHNICAL SESSIONS I**		
	Session 1-A	SCO2 Power Cycle	Room: Walnut
	Session 1-B	Smart Sensing	Room: Sandalwood
	Session 1-C	SMARTGRIDS-I	Room: Satinwood
	Session 1-D	Thin Films & Coatings	Room: Orchid
10:30 am	**BREAK**		
10:50 am	**PARALLEL TECHNICAL SESSIONS II**		
	Session 2-A	Additive Manufacturing	Room: Walnut
	Session 2-B	MHD Power Generation	Room: Sandalwood
	Session 2-C	SMARTGRIDS-II	Room: Satinwood
	Session 2-D	Energy Storage	Room: Orchid
11:50 am	**LUNCH**		Room: Rosewood
11:50 am	**KEYNOTE PRESENTATION - II**		Room: Rosewood

Robert Romanosky, Jr.,Ph.D
Deputy Director
DOE/NETL Office of Coal and Power R&D
U.S. Department of Energy

1:10 pm	**PARALLEL TECHNICAL SESSIONS III**		
	Session 3-A	Composites	Room: Walnut
	Session 3-B	Coatings, Explosives & Composite Synthesis	Room: Sandalwood
	Session 3-C	High-temperature Synthesis	Room: Satinwood
	Session 3-D	Creep, Fatigue & Corrosion	Room: Orchid
2:30 pm	**BREAK**		
2:50 pm	**PARALLEL TECHNICAL SESSIONS IV**		
	Session 4-A	Turbulent Combustion and Propulsion	Room: Walnut
	Session 4-B	Optimization Studies	Room: Sandalwood
	Session 4-C	Pavements	Room: Satinwood
	Session 4-D	Computational Modeling & Analysis	Room: Orchid
3:50 pm	**ADJOURN**		

ABOUT THE SPEAKERS

Jeane L. Hull

Jeane L. Hull is the Executive Vice President and Chief Technical Officer for Peabody Energy. In her role she leads supply chain management activities as well as technical, project, and operations support functions across Peabody's global platform.

Prior to her current role, Jeane was Group Vice President for Peabody's Powder River Basin and Southwest operations. In that role she was responsible for all operational aspects for Peabody's four Wyoming mines—North Antelope Rochelle, Caballo, Rawhide and School Creek; two New Mexico mines—El Segundo and Lee Ranch; and the Kayenta Mine in Arizona. Jeane joined Peabody Energy in May 2007 as Senior Vice President of Engineering and Technical Services. In that role she was responsible for global delivery of engineering, environmental, geology and design and construction services.

Prior to joining Peabody, Jeane was the Chief Operating Officer for Kennecott Utah Copper, a subsidiary of mining and metals giant Rio Tinto. In this role, she had operational responsibility for the mine, concentrator, smelter and refinery. Jeane held numerous management positions with Rio Tinto and affiliates, including 13 years with Kennecott Energy, where she served as Vice President of Operations for Kennecott Utah Copper, Vice President of Technical Services and Business Improvement for Kennecott Energy and General Manager of Spring Creek Coal, as well as other engineering and operations positions.

Prior to joining Rio Tinto, Jeane spent 12 years with Mobil Mining and Minerals and Mobil Chemical Company. She has additional engineering, environmental and regulatory affairs experience in the public and private sector.

A registered professional engineer, Jeane graduated from the South Dakota School of Mines and Technology with a Bachelor of Science degree in Civil Engineering. She holds a MBA from Nova University in Florida. She is a Six Sigma Green Belt. Jeane serves as a council member for the University of Wyoming School of Energy Resources, the industry advisory board for the mining department at Missouri Science and Technology University and the advisory board for the South Dakota School of Mines and Technology. Jeane also was recently elected to the Board of Directors for Interfor a leading global lumber supplier. Interfor has operations across Canada and the US and is headquartered in Vancouver, Canada.

ABOUT THE SPEAKERS

Dr. Romanosky

Dr. Romanosky is currently the Deputy Director, Office of Coal and Power R&D at the National Energy Technology Laboratory. The Office of Coal and Power R&D has responsibility for the Carbon Capture, Gasification, Turbine, Fuel Cell, Carbon Storage, Crosscutting, and Advanced Combustion Programs. Dr. Robert Romanosky received both his M.S. and Ph.D. from West Virginia University in analytical chemistry/instrumentation. He has been with the U.S. Department of Energy, National Energy Technology Laboratory, since 1978, spending 18 years working in areas involved in all aspects of both laboratory and process research dealing with advanced instrumentation and process analysis on power systems. For the next 17 years, Dr. Romanosky was the Technology Manager for Power Systems Advanced Crosscutting Research. This technology area encompasses research activities in Advanced Materials, Plant Optimization Technologies, Advanced Systems Modeling, Coal Utilization Sciences, and University Training and Research.

The Advanced Materials Program fosters exploratory research whose aim is to generate new materials, ideas and concepts which have the potential to significantly improve the performance or cost of existing fossil systems or enable the development of new systems and capabilities. Plant Optimization Technologies supports the development of novel sensors and control systems critical to the implementation and optimization of advanced fossil fuel-based power generation systems, including new classes of sensors capable of monitoring key parameters (temperature, pressure, and gases) while operating in harsh environments. The Advanced Systems Modeling work entails a broad spectrum of computational work including development of science based models of fossil fuel conversion phenomenon, simulation capabilities that couple unit processes in advanced power generation technologies, and virtual power plant simulations. The University Training and Research Programs support fossil research applicable to all NETL Office of Coal and Power Technologies.

PARALLEL TECHNICAL SESSIONS I

Session 1-A: SCO2 Power Cycle Session Chair: Norman Love, UTEP	Room: Walnut Wyndham El Paso Airport
9:30 am	**Entropy and Property Analysis of a Supercritical Combustion Process** L. Bugarin, A.S.M. Chowdhury, A. Badhan, N. Afrose, N. D. Love, and A. Choudhuri, *UTEP*
9:50 am	**Thermodynamic Cycle Analysis of Directly Heated Supercritical Oxy-Fuel Gas Turbine** A. S. M. Chowdhury, A. Badhan, L. Bugarin, N. J. Afrose, N. D. Love, A. R. Choudhuri, *UTEP*
10:10 am	**Conceptual Design of a Supercritical Oxyfuel Combustor Based on Lox/Methane Rocket Engine Technologies** A. S. M. Chowdhury, J. F. Chessa, N. D. Love, A. R. Choudhuri, *UTEP*
Session 1-B: Smart Sensing Session Chair: Yirong Lin, UTEP	Room: Sandalwood Wyndham El Paso Airport
9:30 am	**Concept and Preliminary Testing of a Metamaterial Based Passive Wireless Temperature Sensor** H. Karim, D. Delfin, L. A. Chavez, M. A. I. Shuvo, R. B. Wicker, Y. Lin, A. Choudhuri, *UTEP*
9:50 am	**A Passive, Wireless Temperature Sensor for Harsh Environment Applications Based on Frequency Selective Surface Structures** D. Delfin, H. Karim, L. A. Chavez, J. A. Romero, R. E. Enriquez, R. Martinez, R. Sarker, M. A. I. Shuvo, R. Rumpf, Y. Lin, *UTEP*
10:10 am	**Temperature Measurements using a Lithium Niobate Pyroelectric Ceramic** Md. R. H. Sarker, H. Karim, R. Martinez, D. Delfin, R. Enriquez, M. A. I. Shuvo, N. D. Love, Y. Lin, *UTEP*
Session 1-C: SMARTGRIDS-I Session Chair: Miguel Velez, UTEP	Room: Satinwood Wyndham El Paso Airport
9:30 am	**Invited Talk: Interdisciplinary Center of Research Excellence in Design of Intelligent Technologies for Smartgrids (Icredits): Research Agenda** S. Brahma, H. Cao, R. Galves, S. Misra, E. Pontelli, S. Ramade, T. Son, W. Yeoh, *NMSU*
10:00 am	**Cyber Security Model for Power System based on Game Theory** G. K. Chalamasetty, P. Mandal, B. Tseng, *UTEP*
10:20 am	**Impact of Distributed Generation on Electric Power System** P. Vieira, T. Peres, P. Mandal, *UTEP*
Session 1-D: Thin Films & Coatings Session Chair: Chintalapalle Ramana, UTEP	Room: Orchid Wyndham El Paso Airport

9:30 am	**Evaluation of the Chemical Properties and the High Temperature Oxygen Sensing Capabilities of W-Doped Ga_2O_3 Thin Films** E. J. Rubio, A. Miranda-Gallardo, C.V. Ramana, *UTEP*
9:50 am	**Study of Tungsten-Yttrium Based Coatings for Nuclear Applications** G. Martínez, J. Chessa, S. Shutthanandan, T. Tevuthasan, M. Lerche, C.V. Ramana *UC Davis, UTEP, PNNL-EMSL*
10:10 am	**Preparation of Dielectric/Metal/Dielectric Thin Films for Transparent Heat Mirrors** J. Gomez, M. Vargas, C.V.Ramana, *UTEP*

PARALLEL TECHNICAL SESSIONS II

Session 2-A: Additive Manufacturing Session Chair: Pavana Prabhakar, UTEP	Room: Walnut Wyndham El Paso Airport
10:50 am	**Electron Beam Melting Additive Manufacturing of Niobium** P.A. Morton, J. Mireles, A. Hinojos, P. Frigola, R. B. Wicker, *UTEP*
11:10 am	**Fabrication of Ceramic Components using Binder Jetting Additive Manufacturing Technology** J. A. Gonzalez, J. Mireles, Y. Lin, R. B. Wicker, *UTEP*
11:30 am	**Smart Part Fabrication using Electron Beam Melting Additive Manufacturing Technology** M. S. Hossain, J. A. Gonzalez, J. Mireles, Y. Lin, A. Choudhuri, R. B. Wicker, *UTEP*
Session 2-B: MHD Power Generation Session Chair: Norman Love, UTEP	Room: Sandalwood Wyndham El Paso Airport
10:50 am	**Preliminary Design of an Oxy-Fuel Open-Cycle MHD Combustor System** M. Hernandez, L. Cabrera, and N. Love, *UTEP*
11:10 am	**Review of MHD Power Generation Systems** J. Rosero, G. Enriquez, J. Aboud, B. Lovich, C. Gamboa, N. Love, *UTEP*
11:30 am	**Spectral Radiation Analysis of Premixed Oxy-Syngas and Oxy-Methane Flames** N. J. Afrose, A. S. M. Chowdhury, M. de la Torre, N. D. Love, *UTEP*
Session 2-C: SMARTGRIDS-II Session Chair: Paras Mandal, UTEP	Room: Satinwood Wyndham El Paso Airport
10:50 am	**Vulnerability Assessment and Risk Management (VARM) for Critical Operational Technology** E. Obregon, *UTEP*
11:10 am	**Optimal Operation Strategy for Grid Connected Wind/PV and Energy Storage System** E. Galvan, P. Mandal, *UTEP*
11:30 am	**Hybrid Intelligent Method for Very Short-Term Power Output Prediction of Wind Farm** R. M. Peri, P. Mandal, B. Tseng, *UTEP*
Session 2-D: Energy Storage Session Chair: Binata Joddar, UTEP	Room: Orchid Wyndham El Paso Airport
10:50 am	**Porous Carbon/CEO2 Composites for LI-Ion Battery Application** H. Karim, M. A. I. Shuvo, Md T. Islam, G. Rodriguez, A. Sandoval, M. I. Nandasiri, A. M. Schwarz, A. Devaraj, J. C. Noveron, M. Vijayakumar, Y. Lin *UTEP, PNNL*
11:10 am	**High-Performance Hybrid Super-Capacitors for Energy Storage** M. A. I. Shuvo, H. Karim, G. Rodriguez, Y. Lin, *UTEP*
11:30 am	**Characterization of Smart Sensors** R. Martinez, *UTEP*

PARALLEL TECHNICAL SESSIONS III

Session 3-A: Composites Session Chair: Pavana Prabhakar, UTEP	Room: Walnut Wyndham El Paso Airport
1:10 pm	**Experimental Investigation of Woven Composites as Potential Cryogenic Tank Materials** Md S. Islam, E. Melendez-Soto, P. Prabhakar, *UTEP*
1:30 pm	**Experimental Investigation of Thermal Shock Effects on Carbon-Carbon Composites** A. Leanos, P. Prabhakar, *UTEP*
1:50 pm	**Stiffening of Woven Composites for Enhancing Mode-I Interlaminar Fracture Toughness** A. Castellanos, Md S. Islam, S. Quevedo, M. A. I. Shuvo, Y. Lin, P. Prabhakar, *UTEP*
2:10 pm	**Sandwich Core Design for Naval Hull Structures using Additive Manufacturing** S. A. Quevedo, P. Prabhakar, *UTEP*
Session 3-B: Coatings, Explosives & Composite Synthesis Session Chair: Deidra Hodges, UTEP	Room: Sandalwood Wyndham El Paso Airport
1:10 pm	**Low Cost Spin Coating Fabrication of Efficient Perovskite Thin Film Layers** J. Galindo, D. Kava, S. Shahbriar, D. R. Hodges, *UTEP*
1:30 pm	**Development of Novel Method to Manufacture Mock Polymer Bonded Explosives** C. Catzin, C.M. Stewart, *UTEP*
1:50 pm	**Spin Coating Thin Film CZTs for Efficient, Low-Cost Solar Cells** D. Kava, S. Shahbriar, J. Galindo, D. R. Hodges, *UTEP*
2:10 pm	**Optical Properties of Cu2ZnSnS4 (CZTS) Thin Films Deposited by Non-vacuum Liquid-based Techniques** C. Sana, S. Shahriar, D. Kava, J. Gallindo, D. Hodges *UTEP*
Session 3-C: Heterogeneous combustion Session Chair: Evgeny Shafirovich, UTEP	Room: Satinwood Wyndham El Paso Airport
1:10 pm	**Reaction Mechanisms in Mixtures of Lunar and Martian Regolith Simulants with Magnesium** A. Delgado, S. Cordova, E. Shafirovich,*UTEP*
1:30 pm	**Fabrication of Magnesium Silicide via Mechanically Activated SHS followed by Shockwave Consolidation** S. Cordova, A. Delgado, D. Nemir, E. Shafirovich, *UTEP*
1:50 pm	**Mechanically Activated SHS of Molybdenum Borosilicides for Ultrahigh-Temperature Structural Applications** A. Esparza, E. Shafirovich, *UTEP*
2:10 pm	**Thermite Mixtures for Rapid Generation of Iodine** S.E. Guerrero, E.L. Dreizin, E. Shafirovich, *UTEP*

Session 3-D: Creep, Fatigue & Corrosion Session Chair: Calvin Stewart, UTEP	Room: Orchid Wyndham El Paso Airport
1:10 pm	**Limitations of Classic Local Approach Kachanov-Rabotnov Creep Damage Model** Creep Damage Model M. S. Haque, C. M. Stewart, *UTEP*
1:30 pm	**Tensile Properties of Polylactic Acid (Pla) Additive Manufactured Parts** J. Cardenas, C. M. Stewart, *UTEP*
1:50 pm	**Near Surface Layer Microstructural Investigation of a Highly SCC Susceptible Grade A Steel Vintage Gas Transission Pipeline** M. Torres, S. Stafford, J. Lope, *UTEP*
2:10 pm	**Theory of Unified Viscoplastic Models** Luis A. Varela J. and Calvin M. Stewart, *UTEP*

PARALLEL TECHNICAL SESSIONS IV

Session 4-A: Turbulent Combustion and Propulsion Session Chair: Vinod Kumar, UTEP	Room: Walnut Wyndham El Paso Airport
2:50 pm	**Flow Characterization of Liquid Fueled High Velocity Oxy-Fuel Thermal Sprays** D. Mohamed, L. Cabrera, A. Rios, N. D. Love, A. Choudhuri, *UTEP*
3:10 pm	**Design and Water Flow Testing of a LOX/LCH4 Pintle Injector** I. Lopez, A. Johnson, A. Patel, R. Ponce, M. Lopez, E. Flores, G. Martinez, Ahsan Choudhuri, *UTEP*
3:30 pm	**The Design of a LOX/LCH4 Reaction Control System Thruster** A. Johnson, I. Lopez, A. Patel, R. Ponce, M. Lopez, E. Flores, Ahsan Choudhuri, *UTEP*
Session 4-B: Optimization Studies Session Chair: Eric Smith, UTEP	Room: Sandalwood Wyndham El Paso Airport
2:50 pm	**A Design Stage Optimization Method of Wind Farm Placement Layout on Non-Flat Terrains** C. A. Rosales, T.-L. Tseng, *UTEP*
3:10 pm	**Data-Driven Forecasting on Building Energy Consumption** C. Cui, T. Wu, J. Weir, J. Wen, K. Lewis, H. Kim, B. Tseng UTEP, ASU, Drexel, U of Buffalo, AFIT
3:30 pm	**Stress Truss Optimization by Genetic Algorithm & FEA** M. Tauhiduzzaman, P. Prabhakar, *UTEP*
Session 4-C: Pavements Session Chair: Yirong Lin, UTEP	Room: Satinwood Wyndham El Paso Airport
2:50 pm	**Effect of Friction Course on the Performance of Asphalt Pavement** M. R. Islam, R.A Tarefder, UNM
3:10 pm	**Effects of Input Parameters while Back Calculating Layer Stiffness of Pavement** M.R. Islam, M.M. Hasan, R.A. Tarefder, UNM
3:30 pm	**Measured Versus Generated Temperature and Rainfall Data in a Pavement Section in New Mexico** M.R Islam, M.A Hasan, R.A Tarefder, UNM
Session 4-D: Computational Modeling & Analysis Session Chair: Calvin Stewart, UTEP	Room: Orchid Wyndham El Paso Airport
2:50 pm	**Design and Numerical Analysis of Helical Shaped Tubular Solar Receiver for Concentrated Solar Power Plant** N. Hossain, S. Afrin, V. Kumar, *UTEP*

3:10 pm	**A Polynomial Chaos Approach to Ensemble Kalman Filter SLAM for Autonomous Robot Motion** P. Delgado, V. Kumar, *UTEP*
3:30 pm	**Computational Modeling of Isentropic Flow through a Conical Nozzle** O. Vidaña, M. Chaidez, N. D. Love, *UTEP*

ENTROPY AND PROPERTY ANALYSIS OF A SUPERCRITICAL COMBUSTION PROCESS

L. Bugarin[1], A.S.M. Chowdhury[1], A. Badhan[1], N. Afrose[1], N. D. Love[1]*, and A. Choudhuri[1]
[1] Department of Mechanical Engineering, UTEP, El Paso, TX 79968, USA;
* Corresponding author (ndlove@utep.edu)

Keywords: *Supercritical, thermodynamic properties, combustion*

ABSTRACT

Implementation of supercritical fluids into power cycles has become an attractive solution to increase power plant efficiency. In order to implement a complete cycle analysis of the working fluid, the thermodynamic properties should be further analyzed. More specifically the determination of the specific heat is necessary at supercritical conditions. This will aid in the generation of pressure-specific volume and temperature and entropy diagrams for complete systems.

1 Introduction

The demand for more efficient and environmentally safe power cycles has always been a continuous challenge for engineers over the last few years. In recent years exploration of cycles operating in fluids in the supercritical region has been an attractive solution to implement in power cycles [1]. In addition to higher plant efficiencies, these systems have the capability to implement carbon dioxide recirculation in the system, which can in turn increase the power plant efficiencies [2]. For the current project, the final goal is to design a combustor that is capable of operating at a pressure of 300 bar and at a temperature limit of approximately 1400K. At these conditions the thermodynamic properties of the working fluid is of great importance. Extensive analysis has been conducted to evaluate the amount of CO_2 that should be recirculated in the cycle to be able to generate combustion at a maximum temperature of 1400K [3]. The combustion products generated by this research will be implemented to evaluate the thermodynamic properties at this range and composition.

2 Background

2.1 Combustion reaction

In order to fully understand the implications of the thermodynamic properties of a power cycle at supercritical conditions, an initial analysis was completed. Initially the specific heat of the fluids of interest was estimated from a temperature of 260 K to 1400K, based on estimated maximum temperature experienced during combustion. [3]

The balanced chemical reaction of the combustion that is to be analyzed is as follows. [3]

$$CH_4 + 2O_2 \rightarrow 2H_2O + CO_2 \quad (1)$$

2.2 Thermodynamic Relations

An equation for entropy as a function of temperature was obtained. According to the Principle of Clausius, the change in entropy in a system can be found as the change in the heat exchange in a reversible process over the temperature [4]. The change in heat can be estimated as the change in specific heat which is a function of temperature, as seen in Equation (2) [4].

$$dS = \frac{\delta Q_{rev}}{T} \tag{1}$$

$$S(T_2) - S(T_1) = \int_{T1}^{T2} \frac{Cp(T)}{T} dT \tag{2}$$

Where in the formulas above temperature (T) is in kelvin, molar entropy (S) and specific heat (C_p) is in units of Joules per mole Kelvin (J/mol•K).

For this study, the products of the reaction and their respective molar fraction and molecular weight were used to calculate the mixtures' entropy, as shown in Equation (3). Where mass entropy (s) of the mixture is the sum of the product of the molar mass (M), molar fraction (x) and the change in molar entropy between two temperatures for all of the species present in the product, which leave the mass entropy in units of kJ/kg•K.

$$s_{mix}(T) = \frac{1}{1000} \sum_i M_i x_i \left(S_i(T_1) + \int_{T_1}^{T} \frac{Cp_i(T)}{T} dT \right) \tag{3}$$

2.3 Critical Point

The critical point is of interest because of the drastic property changes near fluids' critical point. The critical points of the fluids considered for the products in the chemical reaction can be seen in Figure 1 (a). Water is an example of this drastic change, which can be seen in Figure 1 (b).

(a)

Fluid	Critical temperature (K)	Critical Pressure (bar)
H2O	647	221
CO2	304	74
CH4	191	46
CO	133	35

(b)

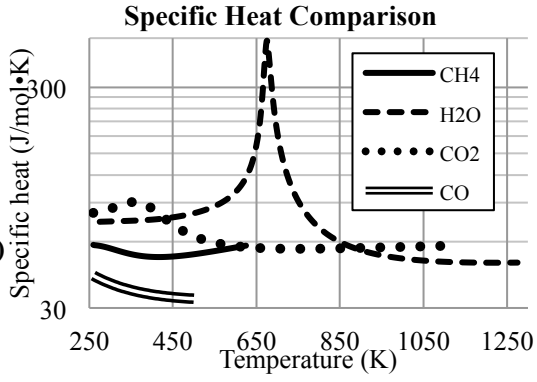

Fig. 1: (a) Critical Points of Fluids of interest (b) Specific heat comparison of products at 300 bar

3. Specific Heat Evaluation Methods

To evaluate the specific heat two approaches were implemented 1) use of the Shomate equations and 2) the values of specific heat from the online database provided by NIST. The Shomate equation is an approximation of specific heat as a function of temperature, seen in Equation (4). The coefficients seen in Equation (4) vary at different temperature ranges and between materials; which were extracted from NIST.

$$Cp = A + bt + Ct^2 + Dt^3 + E/t^2 \quad (4)$$

In Equation (4) t is the temperature of interest, in Kelvin, divided by a thousand, and specific heat is in units of Joules per mole kelvin (J/mol•K)).

4. Results and Conclusions

The Shomate equation has a good correlation with the data obtained in the isobaric tables in the NIST database the temperature of the fluid moves away from the critical temperature. Due to the limited data at a higher temperature range in some of the fluids, the Shomate equation was utilized mainly at high temperatures; low temperatures only for water. With a combination of both methods this yielded in a more accurate depiction of how entropy varied with temperature, as seen in Figure 2. A comparison with the simulation done by [3] yielded a percent difference of approximately 6.76%. Further expansion of this work will simplify the generation of the complete T-s and P-v diagrams for the complete cycle.

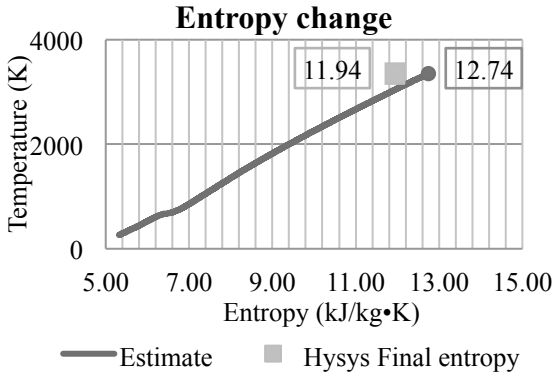

Fig. 2: Change in entropy as a function of temperature during combustion [3]

References

[1] A. McClung, K. Brun, L. Chordia "Technical and economic evaluation of supercritical oxy-combustion for power generation," *The 4th International Symposium-Supercritical CO2 Power Cycles*, Pittsburg, PA, 2014.

[2] C. Oh. "*Development of a superciritical carbon dioxide Brayton cycle: improving VHTR efficiency and testing material compatibility*." Final report. Idaho National Laboratory.2006

[3] Y, Çengel and M. Boles "Thermodynamics: an engineering approach." 7th edition, McGraw Hill, 2011.

[4] National Institute of Standards and Technology "NIST Chemistry WebBook", 2011, URL <http://webbook.nist.gov/chemistry/>

THERMODYNAMIC CYCLE ANALYSIS OF DIRECTLY HEATED SUPERCRITICAL OXY-FUEL GAS TURBINE

A S M Arifur Chowdhury[1], Antara Badhan[1], Luz Bugarin[1], Naznin Jahan Afrose[1], N. D. Love * and Ahsan R. Choudhuri
[1]*Department of Mechanical Engineering, The University of Texas at El Paso*
* Norman. D. Love (ndlove@utep.edu)
Keywords: *Oxy-fuel Combustion, Supercritical Phase, Brayton Cycle*

ABSTRACT

Directly heated supercritical oxy-fuel gas turbines have potential to be an important addition to current power generation systems. It provides a higher thermal efficiency and effective capture techniques than current gas turbine systems. Nevertheless, to achieve super-critical condition at the working fluid, combustion needs to be conducted under enormous amounts of pressure, which is about 10 times those found in existing power generation systems. Motivated by the advantages of supercritical gas turbine, this paper focuses on the thermodynamic cycle analysis of the directly heated supercritical gas turbine system. The analysis was conducted using ASPEN HYSYS® simulation package at two different phases of combustion feeding system: Gaseous Phase and Liquid Phase. Finally, the P-v diagram for both cycles is generated and compared to achieve better understanding of the power generation process. The analysis revealed that the liquid phase feeding system produced more net power than the gaseous phase feeding system.

1 Introduction

The motivation of this project is to develop a high-pressure oxy-fuel combustion system that can produce supercritical working fluid to drive a turbine to produce 300 MW net power. The usage of indirectly heated sCO_2 as a working fluid in a power cycle has been increasing in recent years on solar thermal and nuclear power plants applications [1]. The directly heat supercritical oxy-fuel gas turbine can be an influential addition to the super critical phase power generation system since it demonstrates higher thermal efficiency and provides option to recapture more than 90% of exhaust CO_2[2]. Nevertheless, thermodynamic cycle analysis of directly heated super critical power generation system is yet to be determined. Furthermore, widespread research was conducted on existing high performance turbo-machineries that can possibly meet the system requirements. However, due to high power densities of super critical combustion product as well as high operating temperatures and pressures, several key components must be advanced to meet the system requirements.

A full cycle analysis of 300 MW directly heated supercritical gas turbine is performed using ASPEN HYSYS® simulation package and compared. The cycle analysis was performed at 30 MPa pressure using two different feeding systems, which incorporate a compressor for gaseous phase feeding system and a cooler as well as a pump for liquid phase feeding system. Finally, the P-v diagram is plotted for both cases to visualize the total thermodynamic cycle. Furthermore, a brief discussion is also provided about existing turbo-machinery that can be fitted to the directly heated supercritical gas turbine.

2 Parameter Determinations and Assumptions

Extensive research was conducted to determine the inlet parameters for the thermodynamic stages. The goal for this project is to produce supercritical working fluid at the turbine inlet. For this study, CH_4 is used as the fuel, which reaches the supercritical phase at 4.5 MPa pressure and 190 K temperature; on the other hand, oxygen reaches super critical phase at 5 MPa pressure and 154 K temperature [3]. For the cycle analysis, it is assumed that the reactants are fully combusted and produce CO_2 and H_2O.

$$CH_4+2O_2=CO_2 + 2\ H_2O$$

From literature it is found that, critical pressure for CO_2, and H_2O are 7.4 MPa and 22 MPa respectively and the critical temperature for CO_2, and H_2O are 304 K and 647 K respectively [3,4]. To achieve super critical working fluid, the combustion needs to be conducted above 22 MPa, which is the critical pressure for water vapor. Currently there is a material constraint that determines the maximum pressure and temperature that can be produced during power generation. Significant amount of CO_2 can be recirculated to keep the temperature within the range of operating point. Fuel inlet pressure and temperature is considered 3 MPa and 313 K, which are obtained from a DoE Report [5]. On the other hand, oxidizer inlet pressure and temperature is considered at 250 KPa and 288 K which are obtained from Deepak Kumar Bhunya at el. [6].

Further research is conducted to achieve better understanding about current gas turbines. It is found that, currently the maximum efficiency for single cycle gas turbines are around 40-41 % [5]. For this project, the goal is set to achieve around 50 % efficiency for single cycle directly heated supercritical oxy fuel gas turbine. The mass flowrates for the fuel and oxidizer are calculated assuming 50% overall efficiency for the cycle. Conventional power generation follows Brayton Cycle which includes four major stages: Compression, Combustion, Expansion, and Heat Rejection. For this case study, isentropic condition is assumed for compression as well as expansion process and constant pressure for combustion stage. The isentropic efficiency for compressor and turbo-expander is assumed 75%. Additionally, the combustion is assumed to be happened at stoichiometric condition and any pressure loss is neglected between any stages.

3 Turbomachinery

Directly heated supercritical gas turbines are fairly new for use in power generation processes and it is still limited to the research stage. For that reason, the turbomachinery which are available in the market cannot fulfill all the requirements for the super critical power generation process. Most of the turbomachinery needs to be modified and redesigned to make it withstand the very high pressure combustion process. Wide range research is conducted to achieve ideas about existing high performance turbomachineries. Atlas Copco Inc. manufactures high performance CH_4 compressor that operates at minimum inlet pressure around 3 MPa and maximum outlet pressure 30 MPa accomplishes the project requirements. Moreover, it satisfies the CH_4 mass flow rate required for the process. High end oxygen compressors can be found from the same manufacturer that operates at 8 MPa minimum inlet pressure and 20 MPa maximum outlet pressure. However, it requires significant modifications for it to fit within the system. On the other hand, for the liquid feeding system, reactants can be cooled using refrigeration cycle and pressurized using a pump. There are numerous high performance pumps available that fulfill the design requirements. Nevertheless, there is no turbine available in the market that can withstand this high-pressure environment. Extensive research and development needs to be performed to design a turbine that can withstand this immense amount of pressure for power generation.

4 Results and Discussion

The P-v diagram for both the liquid feeding system and the gaseous feeding system is plotted based on the assumptions discussed earlier. The power required for running turbomachinery is highly dependent on the efficiency of that particular machine. Since all the key components are not available in the market, estimated assumptions are made based extensive literature review and project goal. Ideal directly heated super critical gas turbine cycle P-v diagram is plotted in Figures 1 and 2. They key advantage of super critical combustion is, the drastic change in density during the expansion process delivers significant amount energy to drive the turbine than conventional power generation systems. From both P-v diagram it can be seen that the expansion process starts from very low specific volume and ends up in high

specific volume. This phenomenon can be explained by the significant change in density during the process. The work done by a cycle can be calculated from area under the curve in P-v diagram. From the plots it can be seen that, area under the curve for liquid feeding system is higher than gaseous feeding system, which implies more work can be obtained by the liquid feeding system for this particular cycle.

Conclusion:

The purpose for this paper was to generate P-v diagrams for an ideal directly heated supercritical gas turbine that can demonstrate the thermodynamic processes included in the cycle. Due to the lack of required turbomachinery the analysis was conducted based on simplified assumptions. From the plot it can be concluded that, more net work can be extracted from the liquid feeding system compared to a gaseous feeding system. Nevertheless, proper turbomachinery needs to be developed to fit with a directly heated supercritical gas turbine, which will also help to generate P-v diagrams that can include all the facts involved during each process.

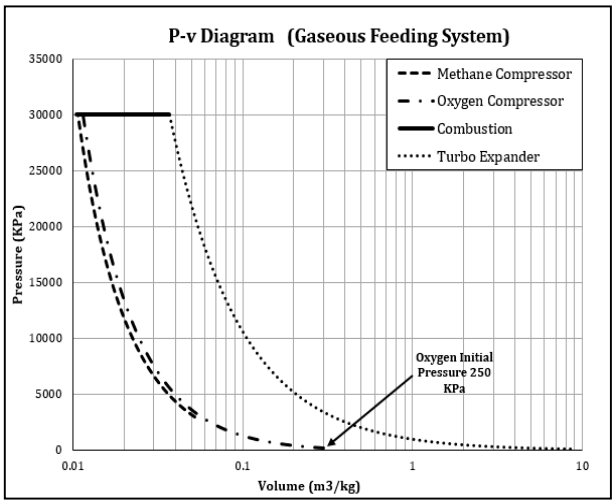

Figure 1 P-v Diagram (Gaseous Feeding System)

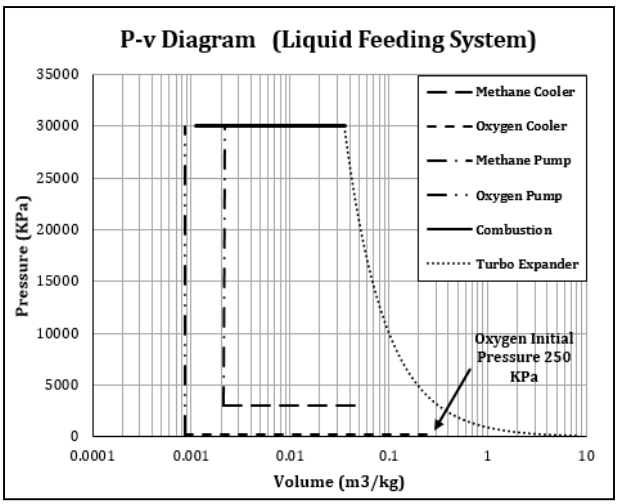

Figure 2 P-v Diagram (Liquid Feeding System)

References

[1] Nassar, Abdul, et al. "Designing Supercritical Co2 Power Plants Using an Integrated Design System." *Proceedings of ASME 2014 Gas Turbine India Conference*, New Delhi, India GTINDIA2014-8225, 2014.

[2] Wall, Terry F. "Combustion Processes for Carbon Capture." Proceedings of the Combustion Institute: 31-47. Print.

[3] NIST Database

[4] Seth Root, John H. Carpenter, Kyle R. Cochrane, Thomas R. Mattsson "Equation of state of CO2: experiments on Z, density functional theory (DFT) simulations, and tabular models"

[5] DOE/NETL Report-"Current and Future Technologies for Natural Gas Combined Cycle (NGCC) Power Plants".

[6] Deepak Kumar Bhunya, et al. 'Simulation Study of Cryogenic Air Separation Unit Using Aspen Hysys At Rourkela Steel Plant"

CONCEPTUAL DESIGN OF A SUPERCRITICAL OXYFUEL COMBUSTOR BASED ON LOX/METHANE ROCKET ENGINE TECHNOLOGIES

A S M Arifur Chowdhury, John F Chessa*,N. D. Love * and Ahsan R. Choudhuri*
[1] [1]*Department of Mechanical Engineering, The University of Texas at El Paso*, El Paso, TX 79968, USA;
* Norman. D. Love (ndlove@utep.edu)

Keywords: *Oxy-fuel Combustion, Supercritical Phase*

ABSTRACT

Directly heated Supercritical Carbon Dioxide (SCO_2) Power cycles have the potential to achieve high thermal efficiencies and provide options for more than 90% CO_2 capture. However, the realization of a directly heated SCO_2 cycle requires combustion systems to be designed to operate in supercritical conditions. Despite a linear increase in gas turbine combustion pressures over the last few decades, the current operating pressure range (~ 30 atm) is significantly below the > 100 atm chamber pressure needed for directly heat SCO_2 power cycles. In contrast rocket combustion chambers are often designed to operate in well excess 100 atm. Thus, they may offer proven legacy technologies for the development of future supercritical oxyfuel combustors. The overarching goal of this project is to design a supercritical combustor based on a Liquid Oxygen (LOX)/Methane Rocket Engine. The proposed conceptual design of directly heated SCO2 gas turbine on this paper is focusing on operating envelop determinations, system design and modeling of the proposed combustor based on two different types of injectors: Pintle, and Modified Shear Co-axial injectors.

1. Introduction

The motivation of this project is to develop a conceptual design of a directly heated Supercritical Carbon Dioxide (SCO2) gas turbine that can produce supercritical working fluid to drive a turbine to produce 300 MW net power. The usage of indirectly heated SCO2 as working fluid in a power cycle has been growing in recent years on solar thermal and nuclear power plants applications [1]. The directly heated Supercritical Carbon Dioxide (SCO2) gas turbine can be an influential addition to the super critical phase power generation system since it demonstrates higher thermal efficiency and provides option to recapture more than 90% of exhaust CO_2[2,3]. Nevertheless, the conceptual design of the directly heated Supercritical Carbon Dioxide (SCO2) gas turbine needs to be developed. The proposed design adopted the conventional rocket engine concept. Four separate powerheads will be used to inject fuel and oxidizer mixer to combustion chamber. Powerheads are designed to fit for both Pintle, and Modified Shear Co-axial injectors. Furthermore, proposed combustion chamber has bell shape geometry which maximize the mixing of supercritical combustion product from four separate powerheads.

3. Conceptual Design:

3.1 Combustor: Figure 1(a) shows the LOX/Methane, rocket engine derived, O_2-CO_2/Natural Gas supercritical combustor. Each engine is a complete combustion module and connected to a transition piece to form the entire supercritical combustor unit. The schematic in Figure 1(a) shows a four-module configuration, however, three- and five module configurations will be considered as well for scaling analysis.

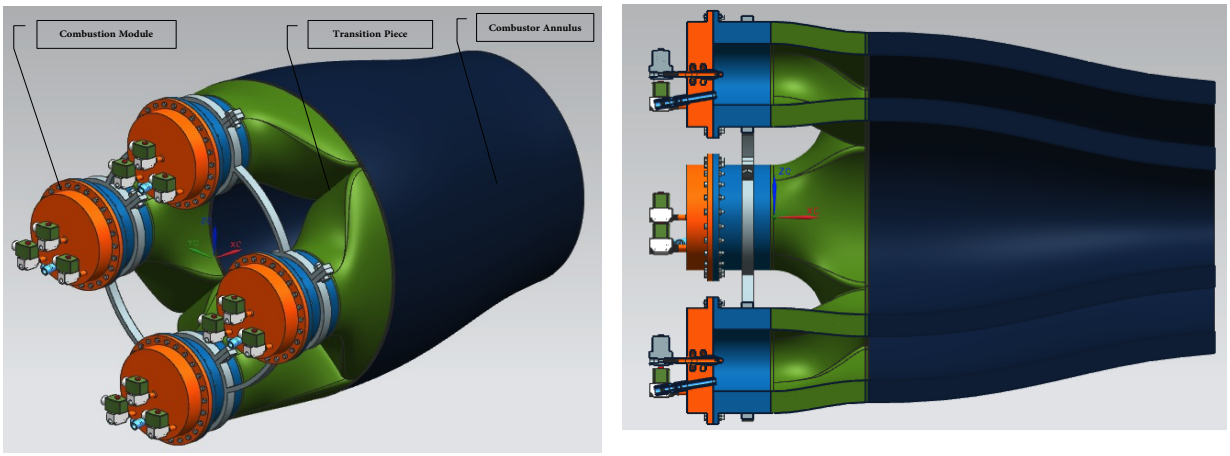

(a) (b)

Figure 1 a) 9kN LOX/Methane rocket engine derived O2/CO2/Natural Gas combustor, b) Cut away of system showing power-head, combustors, and transition sections

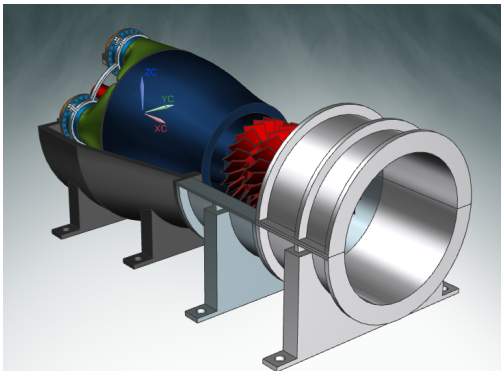

Figure 2 Integration of the proposed combustor with turbine components

This particular combustor design has two primary advantages: (1) direct implementations of LOX/Methane engine technologies and (ii) modularity and compatibility with current power turbine layouts. Each combustion module is included a power-head, a combustor-body, and a transition piece to mesh with the combustor annulus (**Fig. 1 (b)**). The power-head consists of injector elements, valves, and a torch igniter assembly **(Fig. 4 (a)).**

The proposed combustor is designed to use two types of LOX/Methane injectors: (i) Pintle hole and (ii) modified shear-coaxial (Choudhuri et al., 2013a). The transition piece is designed to translate the flow from each combustor module to the primary annulus flow. The design shown in Fig. 1 is preliminary in nature, and has not been scaled or optimized.

3.2 Powerhead Design

Figure 4 (a,b,c) shows the powerheads and modified injectors where accommodations are made to introduce CO_2 into the combustor. Another component which is critical to the proposed combustor development is the torch igniter assembly. UTEP cSETR has two LOX/Methane igniter technologies: (i) a coaxial swirl based igniter and (ii) LOX/Methane reaction control system (RCS) derived igniters (**Fig. 3**) [4,5]. These igniters are high TRL and have been tested with a wide range of propellant conditions. Therefore, no major modifications is needed for their integration in the proposed combustor. Nonetheless, a limited number of validations tests are needs to be tested at their extended operability in proposed supercritical combustor conditions.

Figure 3 Reaction Control System Based Igniter

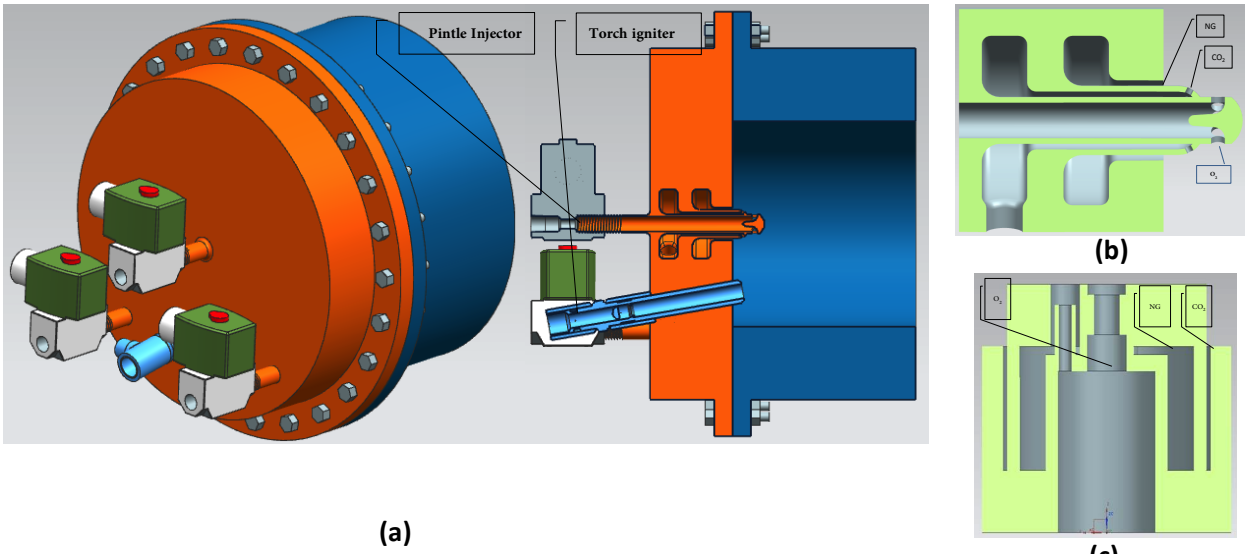

Figure 4 a) Power-head showing injector, valves, and igniter systems b) modified pintle injector c) modified shear coaxial injector

References

[1] Nassar, Abdul, et al. "Designing Supercritical Co2 Power Plants Using an Integrated Design System." *Proceedings of ASME 2014 Gas Turbine India Conference*, New Delhi, India GTINDIA2014-8225, 2014.

[2] Wall, Terry F. "Combustion Processes for Carbon Capture." Proceedings of the Combustion Institute: 31-47. Print.

[3] NETL, Technology Development for Supercritical Carbon Dioxide (SCO2) Based Power Cycles, retrieved from http://www.netl.doe.gov/research/coal/energy-systems/turbines/supercritical-co2-power-cycles, 2014.

[4] Acosta-Zamora, A. and Choudhuri, A., Development of Propellant Feed, Thrust Measurement, and Automation Control Systems for Testing LOX/LCH4 Reaction Control Thruster, 2013c, 49th AIAA/ASME/SAE/ASEE Joint Propulsion Conference & Exhibit, AIAA 2013-3839. (ITAR Restricted Paper)

[5] Flores, J., Sanchez, L., Dorado, V. and Choudhuri, A, Experimental Studies of Uni-Element Shear Coaxial Injector for LOX/LCH4 Propulsion Research, 2013a, 49th AIAA/ASME/SAE/ASEE Joint Propulsion Conference & Exhibit, AIAA 2013-3851

CONCEPT AND PRELIMINARY TESTING OF A METAMATERIAL BASED PASSIVE WIRELESS TEMPERATURE SENSOR

Hasanul Karim[1], Diego Delfin[1], Luis A Chavez[1], Mohammad Arif Ishtiaque Shuvo[1], , Ryan B Wicker[1,2], Yirong Lin[1], Ahsan Choudhuri[1]
* Corresponding author (ylin3@utep.edu)

Keywords:*Metamaterial, wireless sensor, passive, temperature sensor*

ABSTRACT

The recent development of metamaterials has inspired substantial amount of research in many fields. The temperateure dependent resonance properties of metamaterial makes it suitable for use as a temperature sensor. In this paper we propose a passive wireless temperature sensor suitable for harsh environments. The resonance frequency of this structure depends on the temperature and enables its functionality as a temperature sensor.

1 Introduction

Metamaterials are man-made materials, which can display properties that are otherwise absent in nature. The materials are usually arranged periodically to duplicate the structure of an atom. Depending on the shape, size, orientation, and arrangement, metamaterials can show different exclusive properties such as negative refractive index [1], cloaking [2], and reverse Doppler effect [3].

Wireless passive sensors are getting more and more attentions in the industries. Optical based wireless sensors were developed but the accuracy of these sensors was not satisfactory. Metamaterials were introduced to remove these limitations. Ekmekci et al. demonstrated the feasibility of different types of SRR structures for different types of sensors. They suggested broadside-coupled SRR structure for temperature, humidity and concentration sensor application. The objective of this paper is to propose a metamaterial-based temperature sensor that is able to work in harsh environments such as combustion chambers and will be cheap and easy to replace.

The proposed sensor has two closed metal ring resonators embedded in a dielectric material matrix, which separates the two resonators as depicted in Figure 1(a). The dielectric matrix surrounding the metal rings helps protect the metals from harsh and corrosive environments. The whole structure acts as an LC resonance circuit. The equivalent circuit is also suggested in Figure 1(b). The resonance frequency of the structure can be expressed as:

$$f = \frac{1}{2\pi\sqrt{LC}} \tag{1}$$

where, f is resonance frequency. The simplest expression for capacitance can be given as:

$$C = \varepsilon_0 \varepsilon_r \frac{A}{d} \tag{2}$$

where, ε_0 is the relative permittivity of vacuum, ε_r is the relative permittivity of the dielectric matrix, A is the area of one ring resonator and d is the distance between the two resonators. The detailed modeling and parameter evaluation of the sensor can be found elsewhere.

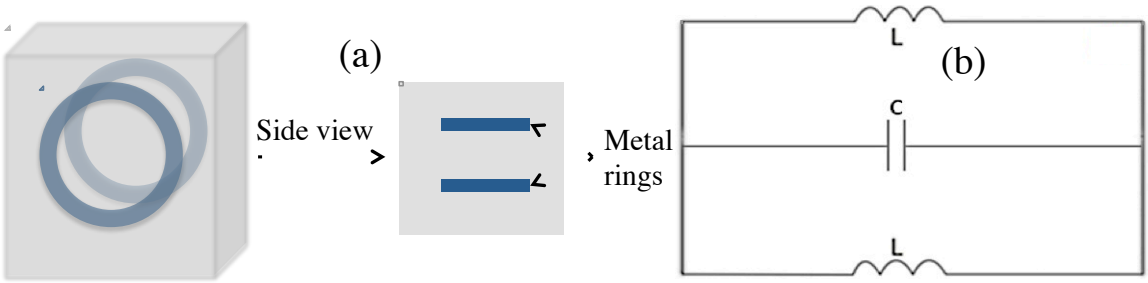

Fig.1. (a) Proposed model of the temperature sensor (b) Equivalent circuit

2 Fabrication

Barium Titanate ($BaTiO_3$) was selected as the dielectric material and Polyvinyl alcohol (PVA) was chosen as the binder because of their linear dielectric properties with temperature. Samples of different thickness and sizes as well as with different configurations of Cu washers were fabricated and tested to find out the optimal performance. Fabricated sample are shown in Figure 2.

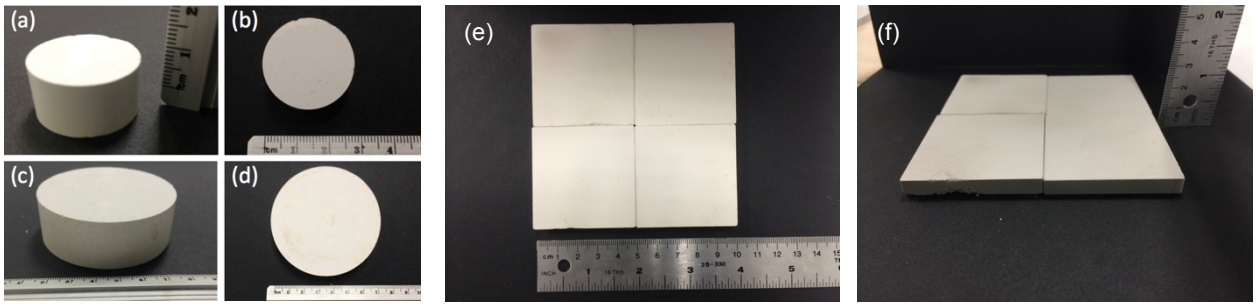

Figure 2: Die punch fabricated samples, (a) diameter=1 inch, side view (b) diameter=1 inch, top view, (c) diameter=2.75 inch, side view, and (d), diameter=2.75 inch, top view; (e) and (f) represent a set of four 2 inches/side samples in top and front view, respectively.

3 Testing and results

Free space measurements were performed on the fabricated samples in the cSETR facility by utilizing a set of Gaussian beam antennas, a vector network analyzer and two co-axial cables, as seen in Figure 3. Additionaly, Styrofoam was used as supporting material due to its transparency to electromagnetic waves. The frequency range used was 7 – 16 GHz. The transmission spectrum of the sample was obtained by sending an electromagnetic wave from the interrogating antenna and after material-wave interaction, received by the second antenna. The testing results can be observed in Figure 4.

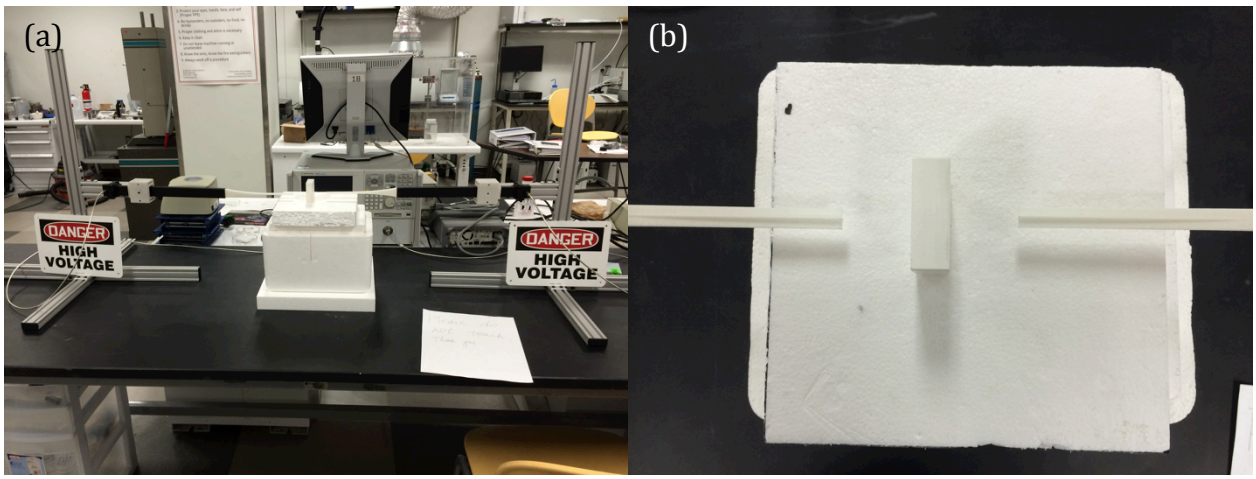

Figure 3. Free space testing setup: (a) overview of the setup, (b) sample placement

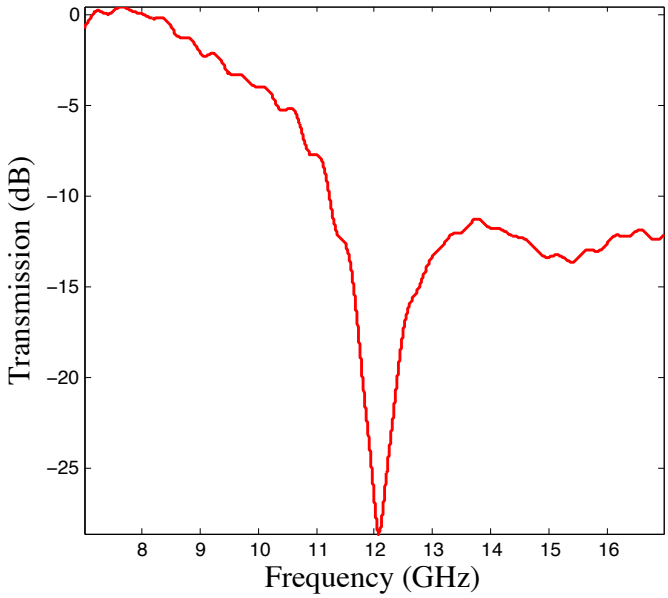

Figure 4: Room temperature response of the temperature sensor unit

4 Conclusion

In this paper the concept of a passive wireless temperature sensor using metamaterial has been discussed. A cheap method of fabrication using traditional die-punch was used. The room termpeature characterization of the sensor shows a defined resonance peak at 12 GHz. The future work will involve testing at different temperature and measuring the sensitivity.

References

[1] Smith, D. R., J. B. Pendry, and M. C. K. Wiltshire. "Metamaterials and negative refractive index." *Science* 305.5685 (2004): 788-792.

[2] Cai, Wenshan, et al. "Optical cloaking with metamaterials." *Nature photonics* 1.4 (2007): 224-227.

[3] Lee, Sam Hyeon, et al. "Reverse Doppler effect of sound." *arXiv preprint arXiv:0901.2772* (2009).

A PASSIVE, WIRELESS TEMPERATURE SENSOR FOR HARSH ENVIRONMENT APPLICATIONS BASED ON FREQUENCY SELECTIVE SURFACE STRUCTURES

D. Delfin[1], H. Karim[1], L. A. Chavez[1], J. A. Romero[1], R. E. Enriquez[1], R. Martinez [1], R. Sarker[1], M. A. I. Shuvo[1], R. Rumpf[2], Y. Lin [1,*]
[1] Department of Mechanical Engineering, The University of Texas at El Paso, El Paso, TX 79968, USA;
[2] Department of Electrical Engineering, The University of Texas at El Paso, El Paso, TX 79968, USA;
[*] Corresponding author: Yirong Lin (ylin3@utep.ed)

Keywords: *Frequency selective surface, wireless temperature sensors, guided mode resonance, harsh environments*

ABSTRACT

Wireless sensing has become of main research interest for harsh environment applications due to its direct impact on the performance of several thermal systems and the drawbacks of current sensing solutions. In this research work, a frequency selective surface passive, wireless temperature sensor based on sandwiched structures is proposed. The FSS based sensor is composed of metallic screens and a dielectric substrate. The chosen geometry for the periodic unit cell was circular apertures. An infinitely periodic simulation was performed using Ansoft's HFSS. Simulation results show a resonance frequency of 10.05 GHz in the reflection spectrum with an intensity of -16.74 dB. This resonance frequency can be utilized to measure temperature do the sensor's temperature dependent dielectric constant.

1 Introduction

Wireless temperature sensing has attained increasing attention in recent years due to the need of precisely predicting temperature conditions in several thermal, electronic and energy conversion systems for performance and safety reasons. Particularly, precise temperature monitoring is of utter importance in power generation systems, such as coal-based power plants and gas turbines, due to its influence on the combustion process and overall operating conditions of the system. Accurate temperature control can lead to higher thermal efficiencies and, as a consequence, less pollutant agents released to the atmosphere. Furthermore, wireless temperature sensing is critical in preventing thermally induced failures and preserving the structural integrity of the system's components [1]. However, these systems typically operate in high temperature, high pressure, and corrosive atmospheres [2]. These conditions can negatively impact the performance of current sensing solutions due to the presence of semi-conductor materials, energy storage devices and welded joints in their configuration. Therefore, there is a growing need to develop next generation sensing solutions for harsh environment applications. Frequency selective surfaces (FSSs) are spatial filters composed of single or multilayered periodic arrays with the ability to filter specific frequency bands [3]. FSSs are typically used to filter electromagnetic interference and allow for certain information-carrying frequency bands to pass through the device. However, recent

research efforts have focused on utilizing the properties of FSSs for chemical, mechanical and biological sensing solutions. Jang et al. developed FSS based on a cross geometry capable of structural health monitoring sensor able to operate in harsh environment applications [4]. Moreover, Kaja, et al. devised a sub-wavelength FSS for detecting absolute and relative protein levels for ovarian cancer [5]. This project presents a wireless, passive temperature sensor based on frequency selective structures for harsh environment applications.

2 Concept and Modeling

The proposed wireless temperature sensor is composed of a multilayered sandwiched structure by utilizing two metal plates and a dielectric slab. A circle geometry aperture was chosen as the periodic element of the sensor. The periodic geometrical array will serve as a diffraction grating responsible for separating the incoming plane wave into discrete modes. Furthermore, the dielectric slab and both the plates function as a slab waveguide, producing a guided wave phenomenon inside of the sensor, allowing for the resonance to take place. Due to the temperature dependent dielectric constant of the dielectric slab, a relationship can be drawn between the peak shift and the temperature of the sensor. Titanium and aluminum were chosen as the metal screens for the sensor, while aluminum oxide (Al_2O_3) was selected as the dielectric ceramic. A schematic diagram of the top and side views of the sensor can be observed in Figure 1.

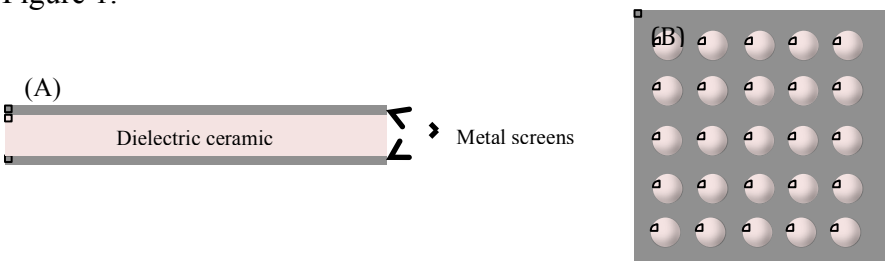

Fig.1. (A) Side and (B) front views of the proposed wireless temperature sensor.

3 Simulation

3.1 Unit Cell Simulation

The simulation was performed using Ansoft's High Frequency Structure Simulator (HFSS) with the objective of proving the feasibility of the sensor and determining its geometry. An infinitely periodic unit cell simulation was performed to evaluate the performance of the sensor. Master/slave periodic boundary conditions (PBCs) were utilized to simulate an infinitely periodic structure, while Floquet ports were used as the excitation method. The former were added on surfaces present on the XZ and YZ planes, while the latter were placed on the surfaces present on the XY plane, with the excitation direction being the Z-axis. The model can be observed in Figure 2.

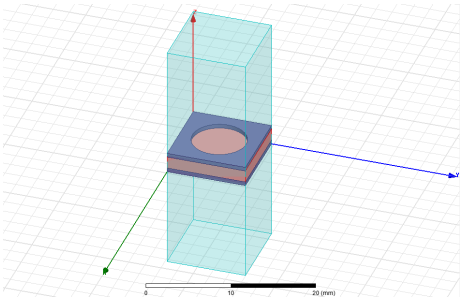

Fig.2. Unit cell model of the proposed sensor

4 Results

The simulation results display a resonance frequency of 10.05 GHz, which is in concordance with the design frequency of the sensor. Furthermore, an intensity of -16.75 dB was observed for the reflection spectrum. This frequency response is visible in the X-band allowing for a feasible temperature sensor application for the circular aperture FSS. The simulation results can be observed in Figure 3.

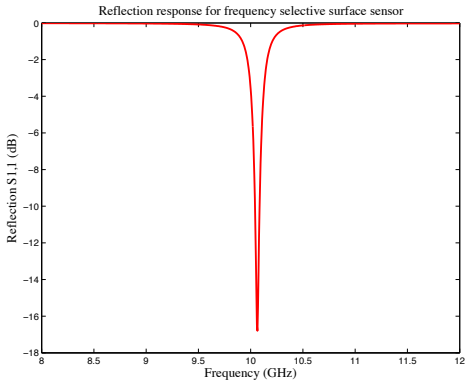

Fig.3. Reflection results for proposed sensor

5 Conclusion

The concept and model for a frequency selective surface based wireless temperature sensor has been presented. The model was based on a metal-dielectric-metal sandwiched structure with periodic circular apertures. A model was developed in Ansoft's HFSS and a resonance frequency for the reflection spectrum of 10.05 GHz was achieved. The proposed design can work as a temperature sensor due to its temperature dependent resonance frequency behavior.

References

[1] Wang, Y., Yi J., Quiushi C., and Yang Y. "A Passive Wireless Temperature Sensor for Harsh Environment Applications." *Sensors*, no. 8. 2008: 7982-7995.

[2] Zhang, .Y., Pickrell, G. R., Qi, B., Saafi-Jazi, A., Wang, A. "Single-Crystal Sapphire-Based Optical High Temperature Sensor for Harsh Environment Applications" *Opt. Eng.*, no. 43(1). 2004: 157-164.

[3] Munk, B. A., "Frequency Selective Surfaces Theory and Design", Wiley, 2000

[4] Jong, S. D., Kang, B. W., Kim, J. "Frequency Selective Surface Based Passive Wireless Temperature Sensor for Structural Health Monitoring" *Smart Mater. Struct,* vol. 22, 2013.

[5] Kaja S., Hilgenberg, J. D., Collins, J. L., Shah, A. A., Wawro, D., Zimmerman, S., Magnusson, R., Koulen, P. "Detection of Novel Biomarkers for Ovarian Cancer with an Optical Nanotechnology Detection System Enabling Label-Free Diagnostics", *J of Biomed Opt*., vol. 17, no. 8. 2012.

TEMPERATURE MEASUREMENTS USING A LITHIUM NIOBATE PYROELECTRIC CERAMIC

Md Rashedul H. Sarker[1], Hasanul Karim[1], Ricardo Martinez[1], Diego Delfin[1], Rodrigo Enriquez[1], Mohammad Arif Ishtiaque Shuvo[1], Norman Love[1*], Yirong Lin[1*]
[1]Department of Mechanical Engineering, UTEP, El Paso, TX-79968, USA;
* Norman Love (ndlove@utep.edu); Yirong Lin (ylin3@utep.edu)
Keywords: *Pyroelectricity, Sensor, Lithium Niobate, Temperature Measurement*

ABSTRACT

Temperature measurement of an operational power generation system could improve its overall safety and efficiencies. Real time temperature measurement could lead to the opportunity of qualitative assessment of the power generation system. In this paper, a pyroelectric ceramic material (Lithium Niobate, $LiNbO_3$) capable of sustaining high temperatures, is considered as the temperature sensing material. $LiNbO_3$ is a pyroelectric material that generates current proportional to the rate of temperature change with time. This property is sustained by $LiNbO_3$ until it reaches its Curie temperature (1210 °C). The generated current could be used for temperature sensing. This paper presents the temperature measurement results using a $LiNbO_3$ pyroelectric ceramic.

1. Introduction

Efficient operation and management of energy systems could improve power generation and reduce the harmful emission of pollutants, which include greenhouse gases such as CO_2 and NO [1]. Among the different processing parameters needed to accomplish this goal, an important parameter is the precise temperature monitoring of the system. The most commonly used intrusive temperature measurement methods are thermocouples and resistance thermometry with a wide measurement range. However, these types of devices have a limited life cycle for particular applications where they are exposed to chemical reactions and erode due to long term exposure to the high temperature environment [2-3]. The work presented in this paper shows the measurement of temperature within the range between room temperature and 100 °C using the pyroelectric property of lithium niobate ($LiNbO_3$) as sensing material. This type of material exhibits strong temperature variation dependent spontaneous polarization and loses its pyroelectric property when it is heated above its Curie temperature [4-5]. $LiNbO_3$ has a high Curie temperature (1210 °C) compared to any other pyroelectric ceramic materials hence it is promising for high temperature and harsh environment applications. Generated current (I) through a homogenous pyroelectric material with temperature (T) at any time (t) is presented in Eq. (1): [6]

$$I = \frac{dQ}{dt} = -pA\frac{dT}{dt} \tag{1}$$

By integrating Eq. (1) for a certain period of time the generated charge (Q) can be found, Eq. (2) [7]:

$$Q = \int_{t_i}^{t_f} I dt = \int_{t_i}^{t_f} -pA\frac{dT}{dt}dt = \int_{T_i}^{T_f} -pA dT = -pA(T_f - T_i) \tag{2}$$

The focus of this study is to provide a measurable amount of current after applying a heating and cooling cycle to the $LiNbO_3$ and the temperature of the sample at any time (T_f) can be calculated from Eq. (2) by considering the initial temperature (T_i) as room temperature.

2. Experimental Procedures

In this experiment the generated current output of the pyroelectric ceramic material $LiNbO_3$ due to heating and cooling was characterized. Small samples of $LiNbO_3$ (1 cm x 1 cm) with two different thicknesses (2 mm and 1 mm) were used for testing. Electrodes were made for the top and bottom surfaces of the sample by using high purity silver paint (SPI Supplies, CAS #: 7440-22-4, Structure Probe, Inc.). Two electrical leads were attached to the top and bottom surfaces of the sample with non-conductive paste. A silicon heating pad was used to apply 14.5 W/cm^2 heat flux to the bottom of the sample for 210 s and then allowed to cool naturally for the following 300 s. An increasing rate of temperature change of the sample by silicon heating pad with 14.5 W/cm^2 heat flux was found for the first 210 s and then the rate of temperature change started to decrease and becomes near zero. A K-type surface thermocouple was mounted on top of the sample. Two electrical leads from the sample were connected to an auto ranging picoammeter (KEITHLEY 485). The analog output voltage from the picoammeter was measured with LabVIEW Program at 500 Hz sample rate through data acquisition board. The schematic diagram of the experimental setup is shown in Fig.1

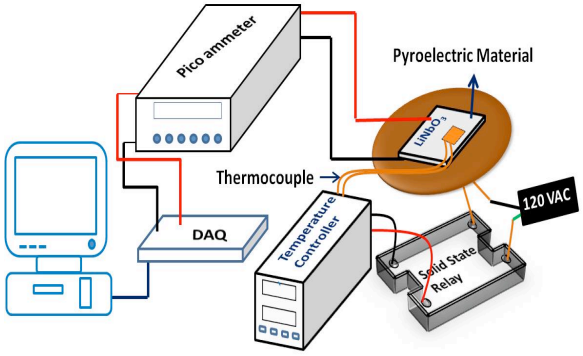

Fig.1.Schematic diagram of the experimental setup

3. Results and Discussions

Fig.2 shows the experimental results for 2 mm thick $LiNbO_3$ sample with temperature profile, rate of temperature change and generated current. Sample generates current with rate of temperature change (Fig.2 (b)) within experimental uncertainties satisfying Eq. (1). Fig.2 (d) shows the comparison between temperatures measured by thermocouple and $LiNbO_3$. Experimental results for 1 mm thick $LinbO_3$ shows the same tend and profile. Maximum of 8 % and 6.7 % differences were found for the 2 mm and 1 mm thick sample, respectively. These differences are caused as the surface thermocouple is mounted on top of the sample. The top surface of the $LiNbO_3$ and the thermocouple is open to the atmosphere, which causes a heat loss due to natural convection and resulting in low measurements by the surface thermocouple than the $LiNbO_3$ is actually experiencing. Therefore, in Fig.2 (d), the differences between the temperatures measured by thermocouple and $LiNbO_3$ are observable where the dashed line represents the measurement by thermocouple.

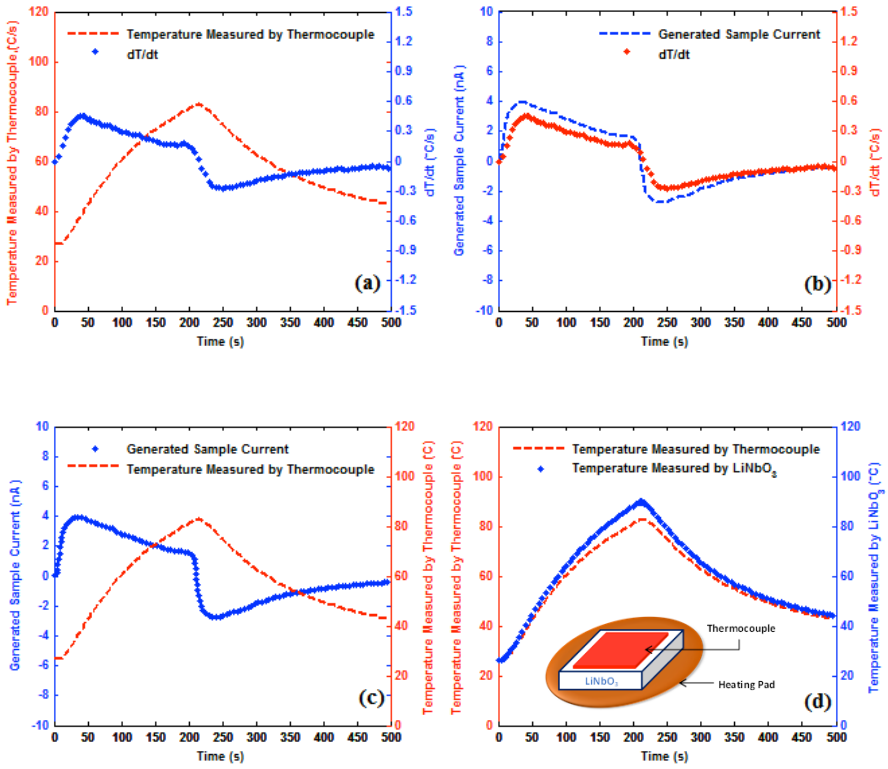

Fig.2.(a) Temperature profile (b) Generated current with rate of temperature change (c) Temperature profile with generated current (d) Temperature measured by thermocouple and 2 mm thick $LiNbO_3$

4. Summary and Conclusions

Current responses of lithium niobate ($LiNbO_3$) material for two different thicknesses were experimentally measured by picoammeter. Numerical integration with Simpson's one-third rule was applied to the pyroelectric current profile to calculate the total amount of current for a certain period of time. Maximum 8% and 6.7% differences were found between the temperature measurement by thermocouple and $LiNbO_3$ for 2 mm and 1 mm thick sample, respectively. The difference between temperature measurements is due to the low measurement by the surface thermocouple.

References

[1] Wang, Ya, Yi Jia, Qiushui Chen, and Yanyun Wang. "*A passive wireless temperature sensor for harsh environment applications*" Sensors 8, no. 12 (2008): 7982-7995

[2] Bentley, Robin E., ed. Handbook of Temperature Measurement Vol. 3: *The Theory and Practice of Thermoelectric Thermometry*. Vol. 3. Springer, 1998

[3] Childs, P. R. N., J. R. Greenwood, and C. A. Long. "*Review of temperature measurement*" Review of scientific instruments 71, no. 8 (2000): 2959-2978

[4] Whatmore, R. W. "*Pyroelectric devices and materials*" Reports on progress in physics 49, no. 12 (1986): 1335

[5] Srinivasan, M. R. "*Pyroelectric materials*" Bulletin of Materials Science 6, no. 2 (1984): 317-325

[6] Hossain, Akram, and Muhammad H. Rashid. "*Pyroelectric detectors and their applications*." Industry Applications, IEEE Transactions on 27, no. 5 (1991): 824-829

[7] Cuadras, A., M. Gasulla, and Vittorio Ferrari. "*Thermal energy harvesting through pyroelectricity*." Sensors and Actuators A: Physical 158, no. 1 (2010): 132-139

INTERDISCIPLINARY CENTER OF RESEARCH EXCELLENCE IN DESIGN OF INTELLIGENT TECHNOLOGIES FOR SMARTGRIDS (ICREDITS): RESEARCH AGENDA

S. Brahma[1], H. Cao[2], R. Galves[2], S. Misra[2], E. Pontelli[2]*, S. Ramade[1], T. Son[2], W. Yeoh[2]
[1] Dept. Electrical & Computer Eng., New Mexico State Univ., Las Cruces, NM 88003, USA;
[2] Dept. Computer Science, New Mexico State University, Las Cruces, NM 88003, USA;
* Corresponding author (epontell@cs.nmsu.edu)

Keywords: *energy delivery, agents coordination, communication, monitoring*

ABSTRACT

In this short abstract, we provide a summary of the research agenda explored by the recently established interdisciplinary Center of Research Excellence in Design of Intelligent Technologies for Smartgrids (iCREDITS).

1 Introduction

The traditional view of the electric grid is that of a "centralized" and uni-directional system, where a relatively small number of generation systems (e.g., power plants) supply power to a large number of customers. The availability of electric monitoring facilities, broadband communication networks, computational intelligence, and customer-driven electricity storage and generation capabilities, have posed the foundations for the next generation power grids: the *smartgrids*. Three key aspects distinguish the smart grid from the more traditional electric grid: *(1)* producers and consumers have access to *information* (e.g., production costs, customers' electricity needs, time distribution of demands); *(2)* continuous access to information and communication is possible (e.g., producers and consumers can negotiate prices); and *(3)* energy can be produced not only by power plants, but also by customers (e.g., via solar panels) and stored for later use (or redistribution).

The *interdisciplinary Center of Research Excellence in Design of Intelligent Technologies for Smartgrids (iCREDITS)* has been established at New Mexico State University with the goal of advancing the state of the art in smartgrids through a coordinated research agenda. The rest of this abstract provides a brief overview of the principal research threads being pursued.

2 Research Agenda

The goal of iCREDITS is to investigate and develop the fundamental science and engineering necessary to develop an energy-delivery paradigm, and thus realize the promise of the smart grid. The domain of this work is the conventional power system as it evolves into an energy-delivery system using smart grid concepts. These concepts are applicable to a small *microgrid*, a larger *customer-driven microgrid (CDMG)* in a distribution feeder and, ultimately, the *smart grid*, which includes the generation,

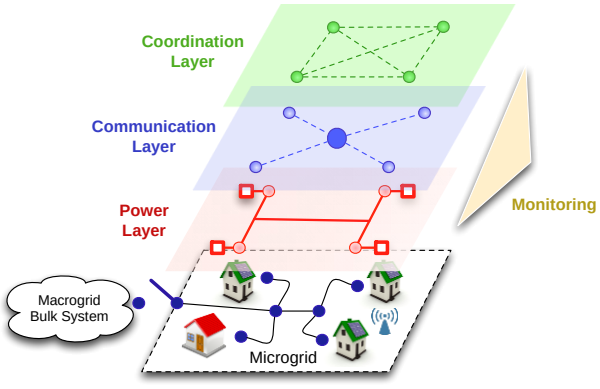

Fig. 1: Microgrid Layers

transmission, and distribution of the entire power system. Enabled by the electric utility, we see an evolution in which renewable and conventional distributed energy sources proliferate, energy storage systems and electric vehicles are accommodated, and consumer demand is controllable. Microgrids represent the evolution of conventional electric utility distribution feeders, in which the customers invest in resources and the utility becomes an enabler for reliable energy transfer. We view microgrids as cyber-physical systems, consisting of both distributed energy sources (including renewable sources and energy storage) and energy demands with differentiated reliability expectations and with communication and computation capabilities. The microgrid integrally ties together the utility, distributed generation, storage, operation, control, and market and economic participants for energy services. In the normal operation, the microgrid is connected to a traditional power grid (macrogrid). The users in a microgrid can generate low voltage electricity using distributed generation, e.g., solar panels, wind turbines, and fuel cells. The single point of common coupling with the macrogrid can be disconnected, with the microgrid functioning autonomously. Different from today's centrally-controlled microgrids, where all devices support a global objective, microgrids also consider individual objectives of participants, which enable the dynamic load participation and differentiated reliability. Inherent in this paradigm are important *social and behavioral issues* (e.g., resource management by microgrid participants, level of cooperation between participants in accepting a global objective vs. satisfying individual objectives).

Figure 1 shows a simplified microgrid, which can connect to a bulk system or a macrogrid; the organization is the core of the recently proposed *Smart Grid Architectural Model*. The bottom layer shows the physical structure of the microgrid (e.g., homes, renewable sources, network access). The red power layer shows the power flow within the microgrid; the blue communications layer shows the information flow; the green coordination layer shows the coordination interactions, where the agents collectively (or antagonistically) determine the appropriate power generation and loads. The yellow component represents the monitoring infrastructure, using data collected from various sources (e.g., meters, phasor measurement units) to model exceptions and support protection and recovery.

The challenge is to provide holistic approaches that integrate the co-dependent issues deriving from the above architecture together. Without such inter-disciplinary integration, it is impossible to effectively achieve the science of the energy-delivery paradigm and the engineering of the smart grid. iCREDITS explore this challenge through four inter-twined research strands: fundamental science in *energy delivery*, *communication systems*, *disturbance modeling and monitoring*, and *agent-based coordination mechanisms*.

Energy Delivery: The shift in paradigm from power to energy delivery requires a change in the design and operation of the system, since they are formulated on the paradigm of continuously meeting instantaneous loads. In order to establish the energy-delivery paradigm for system operation, we will build on our seminal work to define several models and related optimization problems. The core problem can be formulated as follows: Determine a series of energy deliveries over a specified time horizon and time increments that allow load points to meet their demand, while optimizing global and local objectives (e.g., energy costs, CO_2 emissions). The development of the optimization problems, its solution and implementation will require investigating the requirements in terms of design and capabilities of smart devices (e.g., energy storage, electric vehicles, demand controllers), architectural

requirements (e.g., inverters, switches, transformers) and electrical communication infrastructure (e.g., control and state parameters). The focus of this subproject will also be to provide validation of models through their deployment in simulations and concrete testbeds.

Communication: The microgrids/smart grids of today still depend on standard master/slave protocols, which rely on simplifying assumptions on the communication network - and commonly assume the topology of the power and data networks to be the same - which cannot scale to meet the real-time, bandwidth intensive communication requirements of the future grid. The architecture will need to meet the bandwidth, delay, and jitter requirements for communication; it will need to satisfy other quality of service requirements, especially pertaining to handling real-time and non-real-time traffic and different reliability requirements in both types of traffic; and it needs to address concerns of security and privacy. Our research will design frameworks for the communication architecture for a microgrid which uses the Internet infrastructure, leverages the information-centric networking paradigm, and extends proposed standards for communication in electric power systems. The motivation behind our design is to create a framework that can support the information-flow requirements of microgrids, that is compatible with communication primitives and devices that are already in use in the grid, and at the same time can scale seamlessly to other microgrids and to future information-heavy smart grids.

Monitoring: In this subproject, we assume that each home, office building, factory, or power plant has an agent that is able to control its power load, consumption, and transmission. Given this network of agents, our goal is to design and develop agent-based coordination mechanisms that allow the agents to come to an agreement on how much power should be generated, consumed, and transmitted between the agents, such that some objective is achieved. We will investigate **(1)** constraint-based mechanisms, which are well suited for cooperative agents (e.g., a military base or a college campus); **(2)** knowledge-based negotiation mechanisms, which are well suited for self-interested agents to arrive at long-term agreements (e.g., long-term contracts with producer agents); and **(3)** utility-based negotiation mechanisms, which are well suited for self-interested agents to reach a short-term agreement (e.g., short-term exchange of energy).

Coordination: Disturbances in a power system that can have impact on system operation and stability consist of loss of generation or load, loss of lines, faults, and reclosures. Other phenomena, like switching of large reactive resources or connection of large loads, can create variations in voltages to be tagged as disturbances by the measuring devices. These events can affect the optimized operation of a power system. The goal of this subproject is to classify in real time different disturbances occurring in transmission and distribution networks in power systems, so that system operators can respond to maintain system integrity. We address several issues for the classification of disturbances: **(1)** how to characterize the nuances of the data for different disturbance events; **(2)** how to learn different disturbance events from data with incomplete information; and **(3)** how to classify disturbances from streaming and large-scale data in real-time with lack of complete disturbance events. We explore workflows with such components as: semi-supervised clustering techniques to learn unknown disturbance events from known disturbances, unsupervised pattern discovery algorithms to characterize nuances of different disturbances, and real-time classification of disturbances using learned events and patterns.

CYBER SECURITY MODEL FOR POWER SYSTEM BASED ON GAME THEORY

Goutham Krishna Chalamasetty[1], Paras Mandal[1*], and Bill Tseng[2]
[1]Department of Electrical and Computer Engineering [2]Department of Industrial, Manufacturing and Systems Engineering University of Texas at El Paso, El Paso, TX 79968, USA *Corresponding author (pmandal@utep.edu)

Keywords: *Cyber security, game theory, intrusion detection, SCADA, vulnerability.*

ABSTRACT

This paper discusses the vulnerabilities of supervisory control and data acquisition (SCADA) system. Furthermore, this paper proposes a cyber-security model to detect and defend cyber-attacks on power system. The proposed model follows the principle of game theory approach for an effective decision making to defend the attack by calculating the impact on system. The impact of an attack will be calculated from the information send by intrusion detection system (IDS) and vulnerability monitoring system (VMS).

1. Introduction

Cyber security is one of the key requirements for reliable operation of smart grid, which can perform multiple functions such as generation, transmission, and distribution of power with the help of information technology. Smart grid operation is regulated by the supervisory control and data acquisition (SCADA) system by creating an interface with humans [1], [2]. SCADA contains a communication network, sensor network, and many other intelligent electronic devices (IEDs), and a software that is used to provide an interface with humans. SCADA system controls all the electronic and communication devices in the system by gathering the information from sensor network and IEDs, and transfers the received data to control center. All these interactions between different units are carried over a two-way communication path. Cyber-attack on the key components, such as sensor network, regional terminal unit (RTU), and master terminal unit (MTU) in the SCADA system, lead to failure in the entire system [3]-[5].

This paper mainly focuses on analyzing vulnerabilities in SCADA system and proposes a cyber-security model to protect SCADA system and other major components of power system such as power generation plants and substations. The proposed model uses the principle of game theory, which helps defenders to calculate the impact of an attack on the system with the help of information from intrusion detection system (IDS) and vulnerability monitoring system (VMS).

2. Vulnerability assessment of SCADA system

The three main important security parameters in cyber security are *confidentiality, integrity and availability* [1]-[5]. Without any one of these security parameters following attacks may occur:

- If sensor network and nodes are attacked, the sensor information can be compromised and helps the attackers to perform eavesdropping and data injection.

- If the system is attacked, attackers may change the information displayed to human machine interface (HMI), which leads to incorrect operation by human operator.
- If the attacker gains control on the SCADA system, they can route packages to other destinations, which results in denial of service (DOS) attack.

3. Proposed cyber security architecture for power system

The proposed work presents a development of cyber security architecture as shown in Fig. 1. The proposed model monitors network security, infrastructure security, and data security that flow through communication channels. IDS and VMS send the information of power generation plants, SCADA system, and substations to control center, which then functions on the provided information and sends the commands to power generation plants, SCADA system, and substations accordingly. The communication between the units is carried out by SCADA communication channel. IDS detects any attack on the smart grid, IEDs, sensor network, RTU, and MTU, and then sends the information to control center. VMS identifies the vulnerabilities in components, and sends the information of such vulnerable components in the system to the control center, which receives information from IDS and VMS to avoid any damage to the system by making decisions in time. The control center consists of different components, namely *access network, proxy server, firewall, phasor data concentrator (PDC), and anti-virus server*. Access network provides secure login to employees by using dial-up virtual private network (VPN); proxy server helps secure connection between client and server; firewall controls the incoming and outgoing traffic by blocking the information from unauthorized servers; PDC collects the information from phasor measurement units (PMU) and stores as a backup data to be analyzed in case of emergency, and anti-virus server is used to block unwanted data and helps in secure communication.

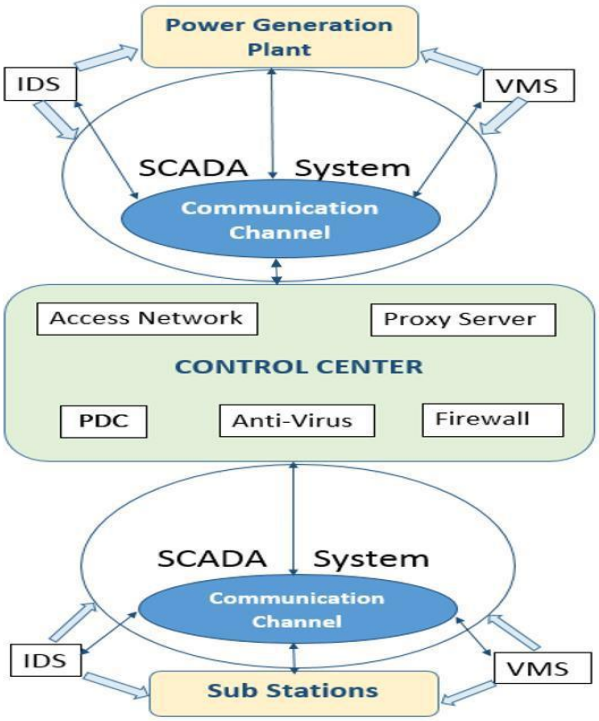

Fig. 1. Proposed cyber security model for power system.

4. Decision making using game theory approach

Control center has to take decision and defend the attack before the entire system is affected. Game theory approach [5] can be applied to the proposed cyber security model (see Fig. 1) to calculate the impact of an attack and helps the defender to take action before the whole system is attacked. The game theory will have two players in the game: attacker and defender. Attacker is the one who attacks the system and defender is control center who defends the attack. Before implementing this method, defender has to give priority for the security of the system. For example, consider the SCADA system with the priority of confidentiality as 0.2, priority for

integrity as 0.5, and 0.3 for availability on the scale of 1. IDS and VMS provide the information about the intensity of attack on confidentiality, integrity, and availability on the scale of 10. Furthermore, the attacks on SCADA network follows the sequence: initially attacker attacks the sensor network or node assumed with the intensity of 2 on confidentiality, 0 on integrity, and 0 on availability followed by attacker performing eavesdropping and data injection attacks with the assumption of eavesdropping intensity on confidentiality as 1, integrity as 3, and availability as 6. Later assuming the data injection intensity on confidentiality as 1, integrity as 8, and availability as 1. Fig. 2 shows the applied game theory model with the assumed parameters. In general, the mathematical model used to calculate impact of attack is given by [5]:

$$Impact\ of\ Attack = (pC \times aC) + (pI \times aI) + (pA \times aA) \quad (1)$$

Where *C, I, A, p, and a* are confidentiality, integrity, availability, priority given, and attack intensity, respectively.

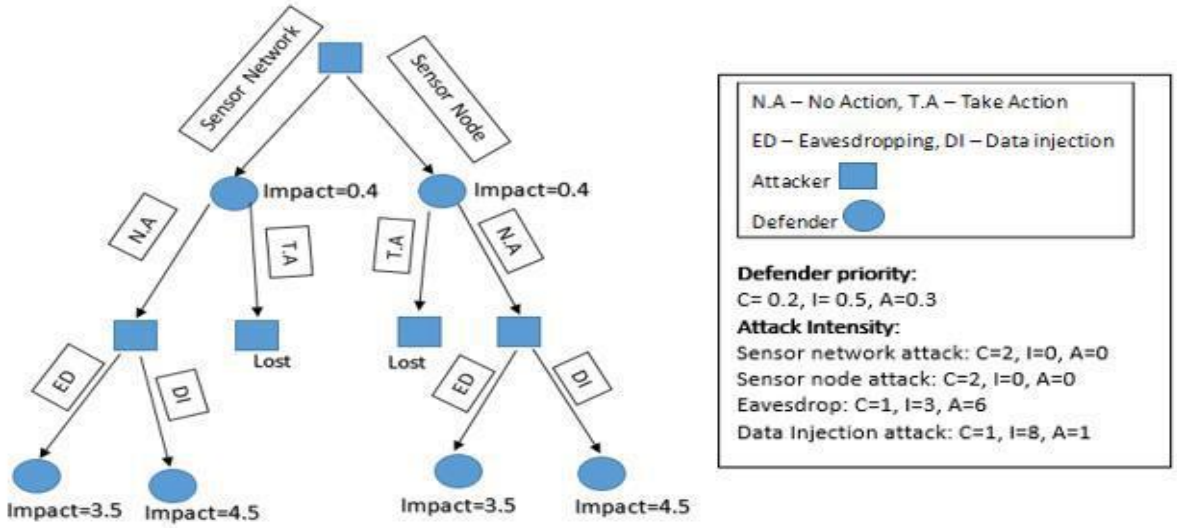

Fig. 2. Game theory approach to prevent cyber-attacks on power system.

5. Conclusion

This paper proposed a security model to prevent cyber-attacks on power system based on game theory approach that helps the control center to calculate the impact of attack on the system and take decisions in time in order to avoid further damages to the system. Future work will concentrate on internal system of the proposed model, i.e. to develop an architecture for IDS and VMS.

References

[1] V. Sridharan, "Cyber Security in Power Systems". A Thesis Presented to the Academic Faculty, Georgia Institute of Technology May 2012.

[2] T. Lu, J. Zhao, L. Zhao, Y. Li, X. Zhang, "Security Objectives of Cyber Physical Systems," in *Proc.* 7th International Conference on Security Technology 2014.

[3] W. Wang and Z. Lu, "Cyber security in the Smart Grid: Survey and challenges," Computer Networks, Vol. 57, No. 5, pp. 1344–1371, 2013.

[4] Y. Yan, Y. Qian, H. Sharif, and D. Tipper, "A survey on cyber security for smart grid communications." *IEEE Communications Surveys and Tutorials*, vol. 14, no. 4, pp. 998-1010, Jan. 2012.

[5] S. Rudrapattana, "Cyber-Security Analysis in Smart Grid SCADA Systems: A Game Theoretic Approach". A Thesis Report submitted to Texas Tech University Faculty December 2013.

IMPACT OF DISTRIBUTED GENERATION ON ELECTRIC POWER SYSTEM

Paulo Vieira, Thais Peres, and Paras Mandal*
Department of Electrical and Computer Engineering
University of Texas at El Paso, El Paso, TX 79968, USA
*Corresponding author (pmandal@utep.edu)

Keywords: *Active power, distributed generation, distribution system, power system.*

ABSTRACT

This paper presents dynamic aspects of the connection of distributed generation (DG) into electric power distribution system and discusses the impact of active power on power system. Simulation results are produced using Electrical Transient Analysis Program (ETAP).

1. Introduction

An alternative to meet the increasing electricity demand is by the use of DG, which are the small generating units (10 MW or less) installed at strategic points of electrical system and especially close to consumption centers. In general, the technologies applied in DG comprise of small gas turbines, micro turbines, fuel cells, generators wind, and solar. Distributed Generation can be used in an isolated mode supplying the local demand or in an integrated manner providing power to the rest of the electrical system. In distribution systems, DG can provide benefits for both consumers and businesses suppliers, especially in the places where the central generation is impractical or when deficiency exists in the power transmission system. The main reasons for the increasing use of DG are [1]:

- DG units are closer to the consumer so that the cost of transmission are reduced,
- Flexibility to choose the most appropriate combination of cost and reliability,
- Opportunities for new producers agents,
- Reduction of electric losses, and
- Reducing emissions of pollutants.

With an introduction of DG to the power system, this shift may significantly impact the performance of electric utilities and protection equipment, e.g., load current redistribution, increase in fault currents, and overvoltage problems [2]. This will require a new measure to be adopted in order to ensure its proper operation. This is a fundamental requirement to approve their connections and coordination between the protection schemes of the independent generators and the utility [2]. This paper applies ETAP to demonstrate the impact of the DG on the load flow in the power system.

2. System Description

Barsoum and Lee [3] analyzed dynamic aspects of the insertion of DG using ETAP to simulate a distribution system with and without DG. In this paper, a small 60 Hz grid system

of nine buses is constructed using ETAP as shown in Fig. 1. There are two buses at high voltage level in main system representing the transmission system. The transmission line connecting the 138 kV to the step-down transformer T1. The induction motor M1 is connected at the bus Sub2A, M2 is connected at the bus Sub2B (both buses of 13.8 kV) and the M3 is connected at the bus Sub3 (0.44 kV). The current and power flow simulations are based on Newton-Raphson method.

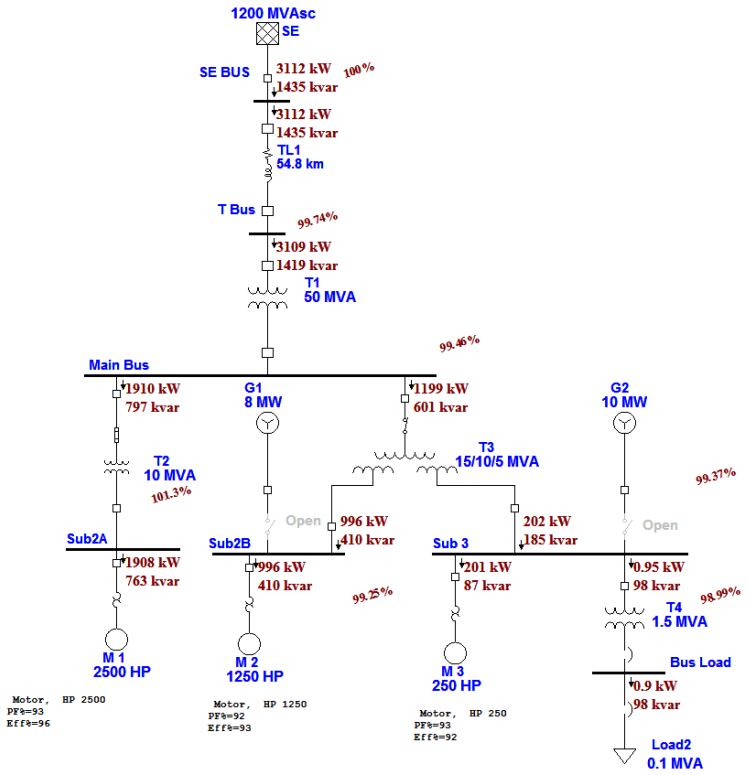

Fig. 1. Example of grid system developed in ETAP.

3. Simulation and Results

Two generator are connected into the system in order to study the impact of an insertion of DG on the power system. Generators G1 and G2 are inserted at Sub2B and Sub3, respectively. The specifications of generators are presented in Table I below.

Table I. Specifications of generators.

Generator	S (MVA)	P (MW)	PF
G1	9.41	8	0.85
G2	11.76	10	0.9

The values of power injection into the grid without generators, with G1 at the bus Sub2A, with G2 at the bus Sub2B, and with both G1 and G2 at bus Sub2A and Sub2B, respectively, are presented in Table II. In Fig. 2, the output power from the swing generator is analyzed and it is found to be reduced due to an injection of G1 and G2. It is observed that in every scenario,

the output power from the swing generator reduces in proportion to the increase in distributed generation G1 and G2 injection.

Table II. Power generation and demands for each DG.

Swing Generator (Bus 1)	Swing w/o DG	Swing with DG 1	Swing with DG 2	Swing with DG 1 & DG 2
MVAR- Generator SE	3112kW+1435 kvar	1284 kW +560 kvar	1768 kW +693 kvar	843 kW +316 kvar
Power Demand at Sub2A	1908 kW +763 kvar	1908 kW +763 kvar	1908 kW +763 kvar	1908 kW +763 kvar
Power Demand at Sub2B	996 kW +410 kvar	1825 kW +410 kvar	996 kW +410 kvar	1534 kW +655 kvar
Power Demand at Sub3	201 kW +87 kvar	202 kW +186 kvar	1342 kW +725 kvar	732 kW +248 kvar
Power Demand at Bus Load	0.95 kW +98 kvar	0.91 kW +99 kvar	0.91 kW +99 kvar	0.91 kW +99 kvar

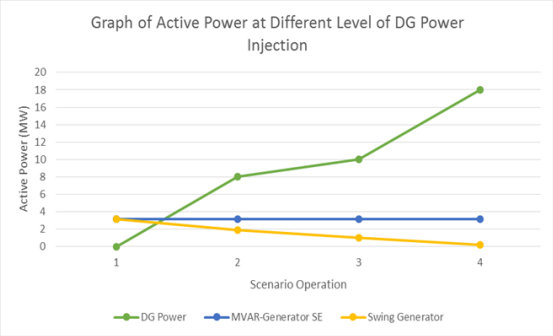

Fig. 2. Reduction of output power from generator in proportion to the increase in DG injection.

4. Conclusion

This paper presented the preliminary studies in order to foresee the consequences of inserting distributed generators into an existing feeder in the power system. This paper discussed one of the several dynamic aspects that should be analyzed in order to adapt the existing power network to choose the best location for the installation. The simulation results demonstrated that the insertion of distributed generation would result into a reduction in the output power of swing bus.

References

[1] E. E. Spier, F. A. B. Lemos, and A. S. Bazanella, "Evaluation of the independent producer's connected to radial feeders in distribution systems." *VI11 Simposium of Specialists in Electric Operational and Expansion Planning*, Brasilia, Brazil, 2002 (In Portuguese).

[2] M. T. Doyle, "Reviewing the impacts of distributed generation on distribution system protection," in *Proc. IEEE Power Engineering Society Summer Meeting*, 2002.

[3] N. Barsoum and C. Z. Lee. "Simulation of power flow and protection of a limited bus grid system with injected solar power," *Energy and Power Engineering,* vol. 5, pp. 59-69, 2013.

EVALUATION OF THE CHEMICAL PROPERTIES AND THE HIGH TEMPERATURE OXYGEN SENSING CAPABILITIES OF W-DOPED GA_2O_3 THIN FILMS,

Ernesto J. Rubio[1], Alejandro Miranda-Gallardo[1], and C.V. Ramana[1*]
Department of Mechanical Engineering, University of Texas at El Paso, El Paso, TX 79968, USA;
* C.V. Ramana (rvchintalapalle@utep.edu)

Keywords*: Oxygen Sensor, Gallium Oxide, Thin Films, High Temperature*

ABSTRACT

The search towards reliable materials that can withstand high temperature without any effect on the intrinsic properties of the material is highly necessary, especially for material employed in energy systems which uses fossil fuels as the main source of power generation. The optimization of energy system which depend on the combustion of fossil fuels can be achieve by determine the ideal quantities of air-to-fuel ratio (λ), and doing it while exposed to extreme environments such high temperature and high pressures, without any presence of structure, electrical or morphological change. Materials for oxygen sensors for high temperature (>700 °C) are also under extensive research due to their importance inside combustion processes. Several type of oxygen sensors have being explored, but the use of metal oxide semiconductors (MOS) have shown promising results, and easy industrial processes fabrication [2]. Nevertheless, many MOS can be employed as oxygen sensors, but the number of material capable of working at >700 °C is reduced to CeO2, Ga2O3 and TiO2 [2]. In this work, the effect that tungsten have in the different intrinsic properties of Ga2O3, such as microstructure, morphology, optical properties and the oxygen sensor capabilities, which were deposited using rf-magnetron sputtering technique. The films were deposited as a function of W-sputtering power varying the concentration of W inside Ga2O3 films, which was confirmed using Rutherford Backscattering Spectroscopy (RBS). The power for the W-target was varied from 50W to 100W, while the substrate temperature in all case was kept constant at 500 °C, the films were deposited on silicon and sapphire. In order to evaluate the sensor performance of the films, the evaluated samples were introduced to a vacuum chamber at temperatures of 800 °C, and the partial pressure of oxygen introduced into the chamber was controlled using a mass flow controller. The change in electrical resistivity was recorded as a function of oxygen partial pressure and the results will be shown. The chemical valance of the films was evaluated using X-ray Photoelectron Spectroscopy (XPS) as deposited and after an annealing process of 700 °C for 1 hours. The results obtained from RBS in conjunction with XPS showed evidence of tungsten diffusion from the surface of the films to the bulk portion after the films were annealed. XPS spectra is shown in Figure 1.

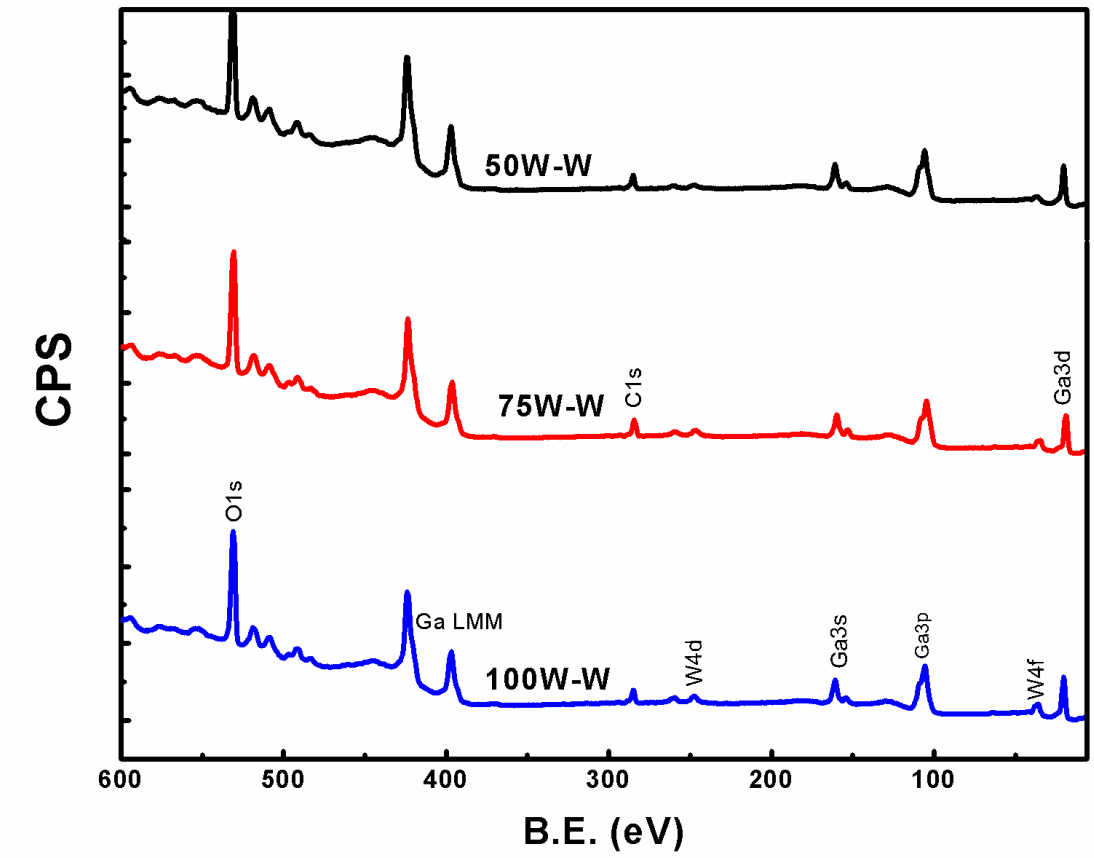

Figure 1. XPS spectra for W-doped Ga_2O_3 after annealing at 700 °C for 1 hours.

References

[1] Liu, Y., Parisi, J., Sun, X., Lei, Y.; *J. Mater. Chem. A.* **2014**, 2, 9919.
[2] Ramamoorthy, R., Dutta, P. K., Akbar, S. A.; J. Mater. Sci. **2003**, 38, 4271.

STUDY OF TUNGSTEN-YTTRIUM BASED COATINGS FOR NUCLEAR APPLICATIONS

Gustavo Martínez[1], Jack Chessa[1], Shuttha Shutthanandan[2], Theva Tevuthasan[2], Michael Lerche[3] and C.V. Ramana[1*]

[1].Department of Mechanical Engineering, The University of Texas at El Paso, El Paso, TX, 799682.
[2].Environmental Molecular Sciences Laboratory (EMSL), Richland WA, 080341
3.McClellan Nuclear Research Center, UC Davis, One Shields Avenue, Davis, CA 95616*
*Corresponding author (rvchintalapalle@utep.edu)

Keywords*: Tungsten, Yttrium, Structural*

ABSTRACT

The 5th Southwest Energy Science and Engineering Symposium will be held by the University of Texas El Paso at Wyndham Airport Hotel and Water Park El Paso on Saturday, **April 4th, 2015**. The purpose of the symposium is to encourage communication among the engineers and scientists in and around the El Paso area's universities and industries. You are invited to participate by helping organize a session, chairing a session, presenting a paper, and/or attending presentations to listen and discuss the papers with the authors. The symposium provides a great opportunity for students to attend and present papers. The registration fee is only $10 for students and $15 for other professionals. The symposium will have parallel morning technical sessions and will end after a luncheon with an invited speaker. Word limit for abstract is 300.

1 Introduction

Recently it is in the research community the fundamental structure-property evaluation of Tungsten and Tungsten-Yttrium (W-Y) films variable with dependent sputtering pressure PAr. It was found that the sputtering pressure can tailor the phase structure of the film. A transformation from body centered cubic (α-W) was favored at sputtering pressures greater than 0.63E-2 mbar whereas a metastable A15 phase (β-W) was favored when sputtering pressures of 0.46E-2 or lower where used. In order to achieve an isotropic, crack-resistant material, mechanical W-Y allow a fundamental understanding of mechanical and electrical properties must be investigated. This quarter was devoted to grow comparable W-Y samples with a variable content of Y in the lattice and its electrical and mechanical properties were compared to pure W, W 95 –Y 5 wt. % and W 90 –Y 10 wt. %.It is well known that the mechanical properties of nanocrystalline metals apparently differ from those of the conventional polycrystalline materials [1,5]. In the case of hard metal films, some studies have re- ported that the very high hardness of Ta [6] and Mo[7] films were obtained as 11.6

and 11.8 GPa, respectively, which are much higher than those of bulk Ta and Mo. Tungsten (W) and W-based alloyed films possess many attractive properties, such as high melting temperature, high mechanical strength, and good metal barrier performance [8,9]. Taking account of the fact that bulk W is harder than corresponding Ta and Mo, W films is anticipated to be of great scientific and technological interest. In this work, W films were prepared by magnetron sputtering onto Si (100) substrates. In order to improve the adhesion properties between W films and Si substrates, 30 nm Cr sticking layers was deposited prior to the W deposition for a set of samples. Nano-indentation was used to characterize the hardness and modulus of W films. Surprisingly, the ultrahigh hardness (24.5 GPa, 21.3 GPa) which are significantly higher than that of coarse-grained W in bulk form (3.92 GPa[10]) are obtained for the deposited and annealed W films with the average grain size of about 26.9 and 32.5 nm, respectively. The relationship between hardness enhancement and the microstructure features is discussed.

2 Experimental Methodology

Nano-crystalline tungsten coatings were deposited onto Silicon (100) and Sapphire (C-plane) using DC sputtering technique. The parameters used for this deposition fallow the DEC 2013 growth parameters. The film thickness was varied from 2 min of sputtering time deposition to 10 min in order to investigate crystallographic formation and texture with respect to film thickness. In general one of the many advantages of using physical vapor deposition processes is the ability to manipulate phase and microstructure with not only sputtering time, but also with deposition pressure, depositing power, substrate orientation. Something to consider is phase change due to exposition of the sample to external environments such as substrate interference. A more detailed table describing the film growth condition parameters is described in table 1.

2.1 Microstructure Characterization of the films

Depending on the growth conditions, W thin films are usually made up of either the stable a phase (bcc lattice), the metastable B phase (A15 cubic lattice), or a mixture of both phases [12]. As it can be appreciated in figure 1 corresponding to pure W samples with variable deposition pressure, all the peaks in XRD data can be correlated to either bcc α or A15 β structure. The occurrence of dominant $\beta(210)$ is observed at sample W-Y 1 as highly crystalline with a mixture of $\alpha(200)$ phase at PAr =0.46x102 mbar. As the deposition pressure increases to PAr =0.63x102 the dominant peak corresponds to a phase change in $\alpha(110)$ and also a mixture with $\alpha(200)$ plane. For the samples W-Y 3-6 the phase changes to a dominant $\alpha(110)$ with different intensities of the peak. In plot 1B obviously, the effect of Yttrium content in the lattice affects the crystallite size making bigger crystals when compared to pure tungsten. Overall phase change can be considered the same for both when increasing the deposition pressure, the behavior is the same. Therefore it is concluded that the desired phase with less than 5% of Y wt. % can be tailored with the sputtering pressure as the appearance of the metastable β-W phase is related to the lowered deposition flux of W atoms, increased film porosity and correspondingly to the higher probability of oxygen incorporation

all this related to sputtering pressure. This same behavior was previously observed by K. Salomon et al in pure W films prepared by magnetron sputtered films.

2.2 Tables and Figures

Table 1

Deposition Parameters	
Substrate	Si (100), Sapphire (C plane)
Temperature	200°C
Sputtering Gas	Ar (40 sccm)
Deposition Time	2min-10min

Table.1. Table 1 Depicts growth parameters conditions for W films

Figure 1

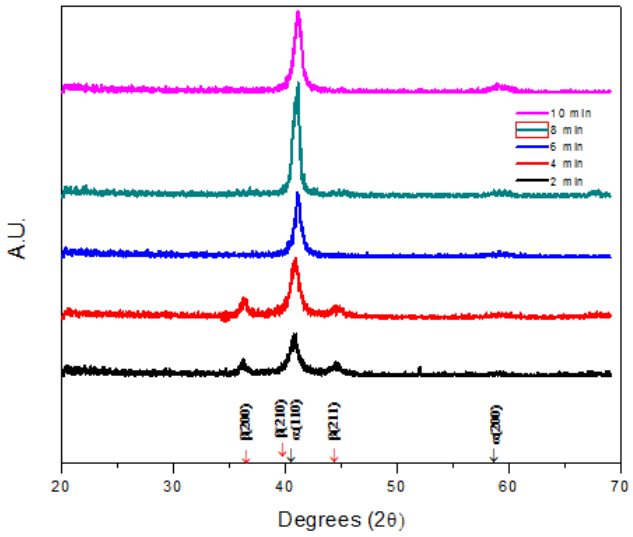

3. References

[1]A.H. Chokshi, A. Rosen, J. Karch and H. Gleiter. Scripta Mater., 1989, 23, 1679.
[2] C.A. Schuh, T.G. Nieh and H. Iwasaki: Acta Mater.,2003, 51(2), 431.
[3] J. Schiotz and K.W. Jacobsen: Science, 2003, 301,1357.
[4] H. Gleiter: Acta Mater., 2000, 48(1), 1.
[5] K.S. Kumar, H.V. Swygenhoven and S. Suresh: Acta Mater., 2003, 51(19), 5743.
[6]M. Zhang, B. Yang, J. Chu and T.G. Nieh: Scripta Mater., 2006, 54(7), 1227.
[7] K.B. Yoder, A.A. Elmustafa, J.C. Lin, R.A. Hoffman and D.S. Stone: J. Phys D: Appl. Phys., 2003, 36,884.
[8] K.Y. Ahn: Thin Solid Films, 1987, 153(1-3), 469
[9] V.G. Glebovsky, V.Y. Yaschak, V.V. Baranov and E.L. Sackovich: Thin Solid Films, 1995, 257(1), 1.
[10] S. Eroglu, H. Ekren and T. Baykara: Scripta Mater.,1997, 38(1), 131.
[11]M. Gutierrez, H. li and J. Patton. J. Thin Film Surface resistivity and Materials Engineering, 0-24 (2002)[12]S.M. Rossnagel, I.C.

PREPARATION OF DIELECTRIC/METAL/DIELECTRIC THIN FILMS FOR TRANSPARENT HEAT MIRRORS

J. Gomez[1], M. Vargas[1], R. Chintalapalle[1]*
[1] Mechanical Engineering, The University of Texas at El Paso, El Paso, TX 79968, USA;
* Corresponding author (rvchintalapalle@utep.edu)

Keywords*: Thin films, heat mirrors, D/M/D, transmittance, reflectance.*

ABSTRACT

Transparent heat mirrors are defined as transparent multilayered structures of different compositions that have several uses for energy savings. The sought application in this experiment is to produce efficient windows which effectively absorb visible light and reflect the infrared radiation of the light spectrum which represents the main generator of heat coming from sun light [5]. Subsequently, a three layered structure of thin films composed of $Hf0_2$/Mo/HfO_2 (dielectric/metal/dielectric or D/M/D) of 40 nm, 20 nm, and 40 nm thick respectively were deposited by the use of electron beam physical evaporation and sputtering systems on transparent sapphire substrates. First, the optical properties of each film such as (%) transmittance, (%) reflectance and refractive index coefficient will be investigated and compared to the properties of the final multilayered structure in order to analyze possible improvements for the final structure. The films will be characterized using X-ray diffraction (XRD) to analyze the microstructural characteristics. With the experimentation on the selected multilayered D/M/D structure it is expected to achieve a high solar transmittance in the visible region and a low thermal emittance in the infrared region in order to achieve the required properties for efficient windows that allow the absorption of more visible light while reflecting the infrared light spectrum which reduces the heat absorbed in buildings coming from solar light.

1 Introduction

Transparent heat mirrors are devices made of different material coatings that generate a high visible transmittance of light ($400<\lambda<700$ nm) and high infrared reflectance ($700< \lambda<3000$ nm), where λ represents the wavelength of light [4]. From this film technology several industrial uses can be seized but one of the most important optical application of these coatings is for efficient insulated glass windows in buildings which can help to save significant amounts of cooling and illumination energy in buildings. Transition metals oxides such as HfO_2 represent an important contributor in the efficiency of transparent heat mirrors since it possesses good mechanical, thermal and chemical stability, as well as a relatedly high dielectric constant and a high refractive index [3]. The wide band gap of HfO_2 (5.5 eV) [1]

provides transparency over a wide spectral range which is extended from ultraviolet to the mid-infrared range. Furthermore, a dielectric/metal/dielectric (D/M/D) structure is used in heat mirrors due to embedding a metal mirror layer between two dielectric transparent oxides can suppress the reflection from the metal layer in the visible region and show a selective high transparent effect which represents a key factor in controlling the reflectance of infrared radiation [2]. In addition, the degree of crystallinity, nonstoichiometry, impurities and defects in oxide film also influence the optical properties of the heat mirror structure [2]. A large variety of coating techniques are used in the preparation of these D/M/D films. Among the most used techniques are included conventional electron beam evaporation, ion-assisted electron beam evaporation, sputtering, chemical vapor deposition and atomic layer epitaxy. The main objective of this project is to generate and analyze D/M/D thin films on transparent sapphire substrates by the following methodology: First, the HfO_2 films are grown at room temperature on the substrate using conventional electron beam deposition. From this point the optical properties of the hafnium oxide films will be determined and studied. Second, the HfO_2 layers will be employed to make a sandwich D/M/D structure with a metallic layer prepared with Mo using sputtering. The final heat mirror structure will be studied optically and chemically for future improvement purposes.

2 Experimental Procedure.

Hafnium oxide films of 40 nm thick were grown at an overall deposition rate of 0.3 nm/s on unheated transparent sapphire substrates using electron beam deposition. The overall dimensions of the substrates were 1.5 cm by 1.5 cm. The samples were kept during deposition at an average vacuum pressure of $2.8x10^{-6}$ torr. After the first layer was grown, the properties of the samples such as transmittance and reflectance were determined. Then, a metal layer of 20 nm thick composed of Molybdenum was grown on the unheated samples using sputtering deposition. The optical properties specified above were determined as well for the multilayered structure made. Finally, the last HfO_2 was grown on the samples following the same procedure specified at the beginning using electron beam deposition. The optical properties of the final D/M/D structure will be analyzed and compared with the obtained optical properties data from the first two layers. A schematic of the desired heat mirror structure is shown in figure 1.

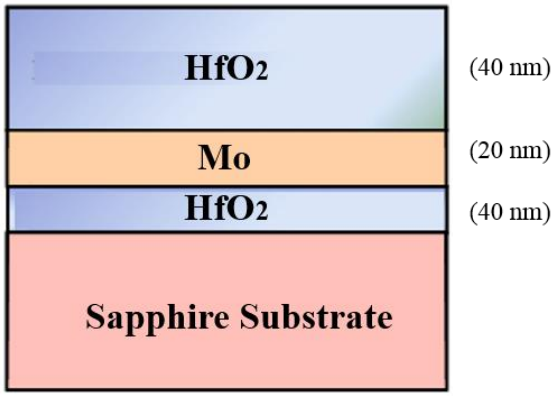

Figure 1. Schematic diagram of final heat mirror structure

3 Discussion

From this experiment, it is first expected from the final selected D/M/D structure to have a high transmittance in the visible region area of light ($400<\lambda<700$ nm) due to influence of the dielectric HfO_2 films which help to improve the amount of visible light absorbed by windows. Second, it is expected to achieve a high infrared reflectance from the light ($700<\lambda<3000$ nm) due to the combination of the reflective metal film (Mo) embedded in the two dielectric layers. Finally, with the achieved optical properties it is expected to generate effective heat mirrors that absorb as much as possible visible light reflecting the heat generating infrared light spectrum.

References

[1] N. Selvakumar, H. C. Barshilia, K. S. Rajam and A. Biswas, "Structure, optical properties and thermal stability of pulsed sputter deposited high temperatue HfO/Mo/HfO solar selective absorbers," *Solar Energy Materials & Solar Cells,* vol. 94, pp. 1412-1420, 2010.

[2] M. Al-Kuhaili, "Optical properties of hafnium oxide thin films and their application in energy-efficient windows," *Optical Materials,* vol. 24, pp. 383-387, 2004.

[3] M. Ramzan, A. Rana, E. Ahmed, A. Bhatti, M. Hafeez, A. Ali and M. Nadeem, "Optical description of HfO/Al/HfO multilayer thin film devices," *Current Applied Physics,* vol. 14, pp. 1854-1860, 2014.

[4] M. Al-Kuhaili, A. Al-Aswad, S. Durrani and I. Bakhtiari, "Energy-saving transparent heat mirrors based on tungsten oxide-gold WO/Au/WO multilayer structures," *Solar Energy,* vol. 86, pp. 3183-3189, 2012.

[5] "Transparent heat mirrors based on tungsten oxide-silver multilayer structures," *Solar Energy,* vol. 83, pp. 1571-1577, 2009.

Electron beam melting additive manufacturing of niobium

P.A. Morton[1, 2*], J. Mireles[1, 2], A. Hinojos[1, 3], P. Frigola[4], R. B. Wicker[1, 2]

1 W.M. Keck Center for 3D Innovation, the University of Texas at El Paso (UTEP), El Paso, TX 79968, USA;
2 Department of Mechanical Engineering, UTEP, El Paso, TX 79968, USA;
3 Department of Metallurgical and Materials Engineering. UTEP, El Paso, TX 79968, USA;
4 RadiaBeam Technologies, Santa Monica, CA 90404, USA

* Corresponding author (pmorton@miners.utep.edu)

Keywords: additive manufacturing, niobium, electron beam melting

ABSTRACT

Electron beam melting (EBM) is a class of powder bed fusion additive manufacturing technologies that is uniquely capable of processing high-melting temperature, refractory, and reactive materials. This research focused on the processing of high-purity grade niobium precursor powder to allow freeform design of components for superconductive applications, specifically, superconductive resonating frequency (SRF) cavities. Material purity and part density post fabrication were used as benchmarks to gauge manufacturing quality. Purity was tracked through all processing steps (i.e. ingot, wire, powder, EBM processing) and it was found that a reduction of titanium content occurred after EBM processing, while all other impurities maintained levels comparable to those measured prior to processing with EBM. A density of 8.58g/cc (wrought density 8.6g/cc) was measured in EBM-fabricated structures. Re-engineered SRF cavities were successfully fabricated whose complex design was intended to overcome stresses during operation. Successful fabrication of niobium suggests that other refractory materials such as niobium alloys (e.g. C-103) as well as highly conductive materials such as copper can be fabricated which widens the application space of EBM AM technology for space applications (e.g. rocket engine components) and energy conservation and efficiency (e.g. heat exchangers).

1. Introduction

Additive manufacturing (AM) gives engineers of today unprecedented design freedom that has enabled the re-engineering of high-value components, which are embodied today in GE's fuel nozzle and SpaceX's SuperDraco rocket engine. Limitations of AM are no different than any new processing/manufacturing method. Quality control concerns and rapid growth of these technologies to new applications and materials are currently limiting the widespread adoption of AM by industry. Difficulties when forming or processing certain alloys (e.g. C-103 and Inconel 718) have been facilitated by AM technologies. Specifically, electron beam melting (EBM) has shown promise in fabricating high melting temperature alloys that result in parts with mechanical properties comparable to conventional manufacturing methods. This research was focused on the fabrication of high purity grade niobium precursor powder for superconductive applications where density and material purity were the criterion for part quality. The ultimate part fabrication successes using niobium create an exciting narrative for the future applications of high melting temperature, refractory, and reactive materials.

1.1 Motivation

Niobium is of particular interest for its extremely high melting point (2468°C) in propulsion applications and liquid helium superconducting critical temperature (T_c = 9k). Conventional fabrication of superconducting resonating frequency (SRF) cavities require months of fabrication time and introduces impurities that can hinder the end product's electrical performance [1]. EBM is seen as an ideal processing platform for high purity grade niobium

due to the high vacuum (up to 10^{-5}torr) processing environment and high powder bed temperature (up to 1500°C) [2]. Moreover, design freedom of SRF cavities will allow for enhanced product life and in turn will lower operating costs of medical imaging equipment (e.g. MRI and CT scanning).

Other applications such as rocketry that operate at temperatures up to 3000°C benefit greatly when using refractory niobium alloys to maintain strength at high temperatures, unfortunately, these type of alloys are difficult to process. Design freedom enabled by AM can further increase the operating temperatures of niobium alloys by incorporating complex heat rejecting features. Thus, utilizing EBM technology to process niobium alloys can enable fabrication of rocket components that allow an oxidizer to fuel mixture closer to the stoichiometric ratio, creating a hotter flame, increasing efficiency, and increasing the net thrust of the rocket engine.

1.2 Background

Additive manufacturing is seen as beneficial and useful for a wide range of applications, specifically for the fabrication and design of complex parts whose conventional manufacturing methods are costly and require long time to market. Rocket engines have been previously additively manufactured out of Inconel using selective laser melting (SLM) by SpaceX (SuperDraco Engine). Benefits of this engine include internal regenerative cooling channels, complex throttling mechanism and injector head which are enabled by the design freedom of AM. Moreover, the lead time of manufacturing these engines was reduced from months to two days with improved mechanical properties when compared to that of cast parts. Furthermore, the latest launch engines designed by SpaceX (Merlin 1D) are radiatively cooled niobium alloy engines. With the recent advancements by the W.M. Keck Center for 3D innovation in the AM processing of niobium [1, 3], advanced designs with niobium alloys similar to the SuperDraco engine are possible.

Currently, C-103 (a niobium based alloy containing 10% Hf and 0.7 – 1.3% Ti) is of great interest in rocket applications due to its high operating temperature (~1400°C), roughly 700°C higher than nickel alloys. Difficulties of manufacturing this alloy can be overcome when utilizing AM while also reducing the need for milling or turning. Furthermore, utilizing C-103 in high and cryogenic temperature service conditions require less material to maintain strength and in turn save money by reducing payload and increasing efficiency.

2. Methodology

2.1 Electron beam melting (EBM)

Electron beam melting (EBM) uses a 60kV electron beam to selectively melt 50-70 μm layers of metallic precursor powder. A substrate material (sized 150x150x10mm) is placed within a powder bed to work as an anchor and thermal energy storage for the fabricated object. The substrate material helps achieve and maintain an elevated powder bed temperature during fabrication that helps lower thermally induced residual stress in the final product. After reaching an elevated powder temperature (760°C for Ti-6Al-4V), the build platform is lowered one layer thickness. A rake is then used to evenly deposit powder that is selectively melted using an electron beam. The process is repeated and continues in a layer-by-layer fashion until part fabrication is complete.

2.2 Characterization

Metallography and density measurements were performed to characterize the EBM-fabricated niobium. A metallographic preparation procedure developed at the W.M. Keck Center for 3D Innovation was used to examine the EBM-fabricated niobium. Etching between polishing steps

was used to remove excess polishing media to prevent scratching. A mixture of 30ml HF, 15ml HNO_3, and 30ml HCl was used to reveal the microstructure. Density measurements were taken following ASTM B311-13 standard.

3. Results

High purity grade niobium was successfully processed via EBM. Material purity was tracked following ASTM B393, and found EBM processing reduced titanium impurity levels with all other impurities remaining constant. EBM microstructure (Figure 1) resembles directional solidification with columnar grains perpendicular to the build platform (Figure 1b) while an equiaxed microstructure was evident in the plane parallel to the build platform (Figure 1a). Optimization of density was achieved through process parameter changes and was measured to be around 99.8% relative density compared to the wrought product.

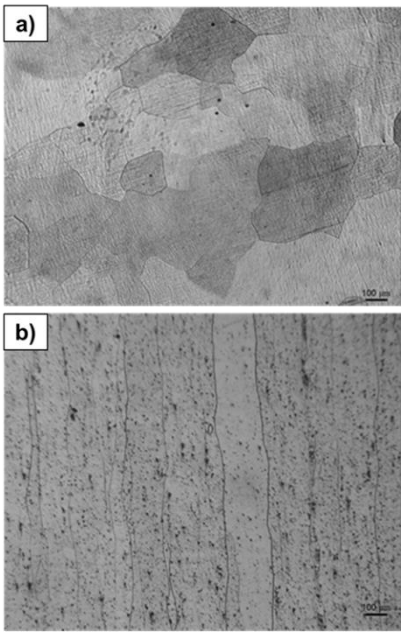

Figure 1. EBM fabricated Niobium a) horizontal plane b) vertical plane

Part fabrication of complex geometries was successfully achieved using EBM. Figure 2 shows the results pertaining to the successful fabrication of an SRF cavity that contains a lattice structure (Figure 2a) meant as structural support during operation. Figure 2b shows a substrate with various complex parts showing the full capabilities developed in this research for part fabrication using niobium.

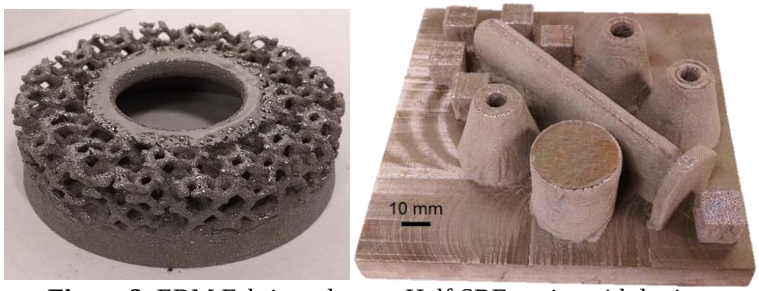

Figure 2. EBM Fabricated parts. Half SRF cavity with lattice structure (Left) and substrate with various complex parts (Right)

4. Discussion & Conclusion

Expanding EBM processing capabilities to new high temperature alloys (e.g. C-103) is exciting for the vast potential to the energy and aerospace industries. Similarities in density, specific heat, and thermal conductivity of pure niobium wrought product give confidence for EBM processing of refractory alloys. EBM processing of high temperature conductive ceramics may also be possible since melting temperatures of up to 2400°C have been achieved with materials like niobium.

The authors are grateful for the support of DOE NP STTR Grant: DE-SC0007666.

References

[1] C.A. Terrazas, S.M. Gaytan, J. Mireles, P. Frigola, D. Espalin, R.B. Wicker, "EBM Fabrication and Characterization of High Purity Niobium for Superconductor Applications" *SFF Symposium 2014*, Austin, TX, pages 500-513.

[2] Gibson, I., Rosen, D.W., and Stucker, B. "Additive Manufacturing Technologies." NY: Springer, 2010.

[3] E. Martinez, L.E. Murr, J. Hernandez, X. Pan, K. Amato, P. Frigola, C. Terrazas, S. Gaytan, E. Rodriguez, F. Medina, R.B. Wicker, "Microstructures of Niobium Components Fabricated by Electron Beam Melting," *Metallography, Microstructure, and Analysis*, Volume 2, 2013, pages 183-189.

Fabrication of ceramic components using binder jetting additive manufacturing technology

J. A. Gonzalez[1 2*], J. Mireles[1,3], Y. Lin[3], R. B. Wicker[1,3]

1 W.M. Keck Center for 3D Innovation, The University of Texas at El Paso, El Paso, TX 79968, USA
2 Department of Metallurgical and Materials Engineering, The University of Texas at El Paso, El Paso, TX 79968, USA
3Department of Mechanical Engineering, The University of Texas at El Paso, TX 79968, USA
* Corresponding author (jagonzalez24@miners.utep.edu)

Keywords: *binder jetting, additive manufacturing, ceramics, alumina, barium titanate, sensor packaging*

ABSTRACT

Binder jetting technology is a form of additive manufacturing that uses precursor powder material to create complex, three-dimensional components in a layer-by-layer fashion. Binder jetting has a wide range of commercial materials that can be fabricated, including metals and ceramics (316 SS, 420 SS, Inconel 625, Iron, Silica). In this project, Barium titanate ($BaTiO_3$) and aluminum oxide (Al_2O_3) were built using an ExOne M-Lab machine. Various build parameters (e.g. layer thickness, saturation, particle size) were modified and different sintering profiles were investigated to achieve nearly fully dense parts. The materials were characterized to analyze density, shrinkage in all directions, and dielectric properties. The capabilities shown in this research suggest that ceramic parts can be fabricated that can be useful in a wide range of industries including biomedical, automotive, and aerospace. The materials chosen in this research were selected for the fabrication of sensor packages that can house health monitoring electronic components within aerospace and energy generating systems. The complexity that can be offered by the additive process can be extended to manufacture high value energy and environmental components for environmental systems (e.g. filters and membranes) as well as energy conservation and efficiency (e.g. heat exchangers).

1. Introduction

Ceramics have a wide range of applications that range from biomedical implants (i.e. osseointegrated implants) to filters for industries in oil and gas production. Such materials have high temperature resistance and can survive in harsh environments where polymers and metals cannot survive without premature failure. Ceramic components are currently being manufacturing by machining, slip casting or applied by vacuum evaporation, sputtering, laser ablation, and plasma sputtering. However, such methods have been known to cause cracking or peeling of layers during operation and use at high temperatures. In this project, a novel way of processing ceramics using additive manufacturing (AM) was explored. AM is a method of part fabrication that occurs in a layer-by-layer fashion and is comprised of seven different technologies [1]. The technology of focus in this research is binder jetting, which is an AM technology led by the ExOne company that uses precursor powder for the layer-by-layer fabrication of parts ranging from polymers and metals to ceramics and composites [1]. An ExOne M-Lab binder jetting system was used in this research to demonstrate the feasibility of fabricating ceramic components.

Two ceramic materials were explored in this research including barium titanate (BaTiO3), or BTO, and alumina oxide (Al_2O_3). BTO has applications varying from chip capacitors to dynamic random access memories (RAM), and embedded capacitance in printed circuit boards to piezoelectric devices like sensors, heaters and transducers. Other applications that use BTO for ferroelectric and piezoelectric properties include semi-conductors with positive temperature coefficient of resistivity (PTCR), dynamic random access memories (DRAM), and infrared sensors. Alumina, on the other hand, has applications ranging from dental, ear, and hip implants, to sensors. [2,3]. Both ceramic materials have potential to revolutionize current fabrication methods for sensor packaging and health monitoring sensors. Highly complex ceramic structures can be enabled by binder jetting to create sensor packages such as packages integrated with porous structures that have gas and liquid permeability for humidity sensors. The complexity that can be offered by ExOne's binder jetting process can be extended to manufacture high value energy and environmental components for environmental systems (e.g. filters and membranes) as well as energy conservation and efficiency (e.g. heat exchangers).

2. Materials and Methodology

The binder jetting process was used in this research was an ExOne M-Lab system. The process involves the use of precursor powder material that is added to a powder bed in a layer-by-layer fashion using a stationary roller. The precursor powder is selectively bonded layer-by-layer using an inkjet head that deposits a binding substance as directed by instructions from a computer-aided design (CAD). After the binder is deposited, the powder bed moves below a heater that helps cure the deposited binder. After the heating cycle is complete, the part is prepared for a new layer and the process continues until the part is complete. After fabrication, the product is transferred to an oven that helps to fully cure the part by completely burning off the binder used during the process. The resulting product is a rigid green body that, if needed, can be used as a core for casting operations. If an end-use part is desired, the green body is then sintered using the appropriate sintering profile for the material being used. [1]

ExOne's M-Lab binder jetting system was used and allows the control of certain build parameters to achieved appropriate fabrication of non-commercial materials. The process parameters that can be controlled include: (1) binder saturation, (2) layer thickness, and (3) powder packing density. Experiments were conducted using these process parameters to achieve the appropriate fabrication that allowed highly dense and rigid green bodies. Different sintering profiles were also explored after part fabrication using a vacuum furnace. For BTO, the sintering profiles were explored to achieve the required crystal structure for sensing applications, para-electric (cubic; a1⁄44.031 A˚) or ferroelectric (tetragonal; a 1⁄4 3.994 A˚ and c 1⁄4 4.038 A˚). For alumina, the change in sintering profile was used to achieve process parameters that produced nearly fully dense components. Although fully dense ceramic components allows a wide range of applications to be realized, control over part density enabled by AM technology can be achieved to create biomedical implants with improved osseointegration or environmental components such as filters with pores of desired shape and size [2,3].

3. Results

Successful fabrication was achieved using BTO precursor powder. The green bodies were sintered at three sintering profiles: 1) 1260°C, 2) 1330°C, and 3) 1400°C for 12 hours. Changes in geometry were evaluated and Figure 1 illustrates a plot of how the shrinkage varies as the

sintering temperature was increased. Work is being conducted to optimize the process in order to limit shrinkage and improve density. The relative density achieved was 65% density when compared to the theoretical value of BTO. Successful fabrication results demonstrate the feasibility to use BTO with binder jetting for 3D printed dielectric structures, ceramic capacitors and gas and pressure sensors.

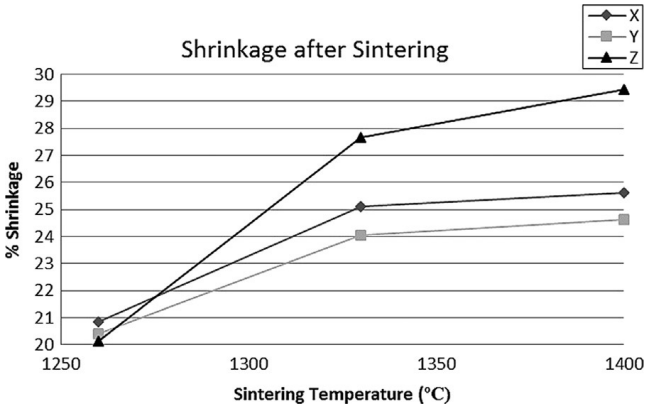

Figure 1. Percent shrinkage at different orientation when sintering at different temperatures

Successful part fabrication using alumina was achieved with binder jetting technology. Figure 2a shows the alumina powder used in this research and Figure 2b and 2c show the fabrication results. Figure 2b shows the capabilities achieved to produce complex geometries while Figure 2c shows the alumina components fabricated for sensor packaging applications. Current work is being performed to measure density and shrinkage upon sintering. Preliminary results show that a density of 3.81g/cm^3 can be achieved which is translated to a 96.5% relative density.

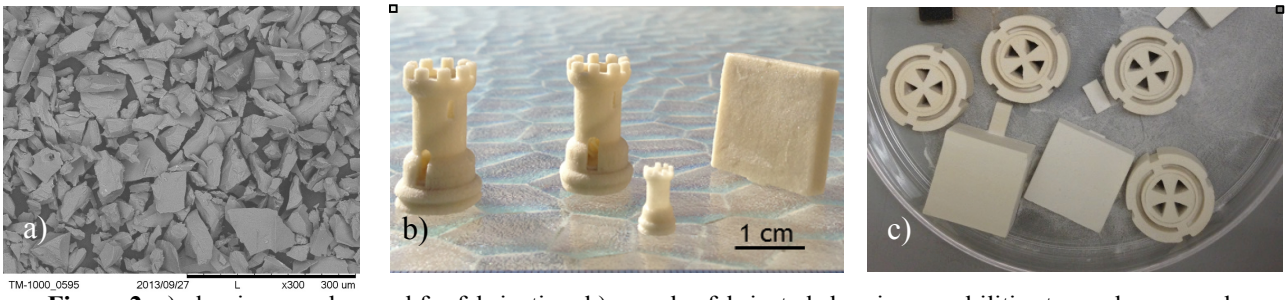

Figure 2. a) alumina powder used for fabrication, b) samples fabricated showing capabilities to produce complex geometries, and c) alumina components for sensor packaging

4. Conclusions

ExOne's binder jetting technology was shown to be a feasible method for fabrication of ceramics components. The layerwise process allows highly complex parts to be fabricated, which widen the application of the process to industries such as environmental, energy, and biomedical. The successful fabrication of different ceramics shown in this research suggests that other ceramic materials that are traditionally difficult to process can be used with binder jetting technology for the seamless fabrication of complex parts. ExOne's binder jetting technology has enormous research potential in the fabrication and characterization of high value components that can be used in environmental systems (e.g. filters and membranes) as well as for energy conservation and efficiency (e.g. heat exchangers).

References

[1] Gibson, I., Rosen, D.W., and Stucker, B. "Additive Manufacturing Technologies." New York: Springer, 2010.

[2] Gaytan , S. M., Cadena, M. A., Karim, H., Delfin, D., Lin, Y., Espalin, D., MacDonald, E., Wicker, R.B., (2015). Fabrication of barium titanate by binder jetting additive manufacturing technology. *Ceramics International* .

[3] Murphy, S. B., Ecker, T. M., & Tannast, M. (2006). Two- to 9-Year Clinical Results of Alumina Ceramic-on-Ceramic THA. *Clinical Orthopaedics and Related Research* (453), 97-102.

Smart part fabrication using electron beam melting additive manufacturing technology

Mohammad S. Hossain[1, 2*], Jose A. Gonzalez[1, 3], Jorge Mireles[1, 2], Yirong Lin[2], Ahsan Choudhuri[2], and Ryan B. Wicker[1, 2]

[1] *W.M. Keck Center for 3D Innovation, The University of Texas at El Paso (UTEP), TX 79968, USA;*
[2] *Department of Mechanical Engineering, UTEP, TX 79968, USA;*
[3] *Department of Metallurgical and Materials Engineering, UTEP, TX 79968, USA;*
* Corresponding author (mshossain@miners.utep.edu)

Keywords*: smart parts, electron beam melting, piezoceramic sensor, Ti-6Al-4V, additive manufacturing*

ABSTRACT

The use of embedded sensors within energy system components, or smart parts, can be useful to obtain real-time performance feedback during operation. The fabrication of smart parts using additive manufacturing technology allows for the flexibility of placing a sensor within any desired position without affecting part performance. This flexibility allows the non-intrusive placement of sensors for proper part operation as well as sensor placement to monitor specific critical areas that are exposed to high temperatures and pressures. This paper focuses on the fabrication process of smart parts using electron beam melting (EBM) additive manufacturing technology. This research involved the development of a "stop and go" procedure that consisted of pausing the part fabrication process to allow the placement of piezoceramic sensors into cavities designed within the part and resuming part fabrication thereafter. The final product resulted in a fully enclosed and non-intrusive sensor within a metal component. The project suggests that smart parts can be fabricated with non-intrusive and fully enclosed sensors to monitor component performance during operation at high temperatures and pressures.

1. Introduction

Additive manufacturing (AM) consists of seven different processes that allow the layerwise manufacture of complex geometries [1]. Electron beam melting (EBM) is a class of powder bed fusion AM technologies that is capable of fabricating parts from precursor powder using an electron beam. Previous research has shown that EBM can be used to fabricate parts useful to the biomedical, automotive, and biomedical industries [1]. With the capability to manufacture energy components such as turbine blades and fuel nozzles, the specific area of interests in this research is using the added complexity allowed by EBM to create smart parts with embedded sensors (e.g. piezoceramics) within a part's structure. Currently, sensor placement in energy system components (e.g. turbine blades, pressure tubes, etc.) consists of adding thermocouples or pressure sensors to the outer surface of a part using pastes or assembled post-fabrication within a machined cavity. A problem with the placement of sensors within a part's wall is the risk of interference with part performance. For example, thermocouples on the outer vane of a turbine blade may affect aerodynamic performance. Another issue arises in the life of a sensor when such a component is placed in operation due to high temperature, high pressure, or corrosive conditions. That is, a sensor may not withstand the same operating conditions as the energy component, causing sensor failure and loss of health monitoring data.

The methods investigated in this paper involve embedding of a sensor within a metallic part to allow *in situ* monitoring of the energy system components during operation. A procedure was developed here using an EBM system that involved pausing part fabrication to allow the

placement of a piezoceramic sensor and continuing part fabrication until completion. As a proof of concept, a cylindrical shaped part was fabricated, and the sensor assembly was placed within the part. The embedding process of functional electronics into engineering components is of great interest with additive manufacturing technologies. Previously, Aguilera *et al*. [2] fabricated an electromechanical device that included manual insertion of electrical components within thermoplastic material using material extrusion technology by implementing the stop and go methods investigated in this research. Terrazas *et al.* [3] showed that the stop and go process was possible in EBM by demonstrating the capability of fabricating a single component using two different materials: Ti-6Al-4V and copper. The process introduced the pausing of EBM part fabrication to continue building onto a set of previously built parts. The resulting smart parts will ensure the proper funcitonality of a system component enabled by prolonged sensor life and monitoring information that is more closely related to critical sensor areas. A combined approach of Aguilera's and Terrazas's research was explored in this research to achieve the placement of a piezoceramic sensor into cavities designed within a part's volume. The main challenge in fabricating smart parts using EBM technology is selecting sensing components that endure the high temperature farbrication process characteristic of EBM. This paper emphasizes on the fabrication process using EBM technology, and addresses improvements options. Preliminary results show that sensors can be embedded within parts fabricated using EBM to achieve the fabrication of smart parts. This research suggests that AM using EBM can revolutionize the design of energy system components by allowing the embedding of sensors within component critical areas that are exposed to high temperatures and pressures. The resulting smart parts will ensure the proper funcitonality of a system component enabled by prolonged sensor life and monitoring information that is more closely related to critical sensor areas.

2. Materials and Methodology

This research was performed using EBM additive manufacturing technology from ARCAM AB to fabricate parts using Ti-6Al-4V precursor powder. Layers of powder are deposited in a layer-by-layer fashion onto a powder bed where an electron beam is focused to selectively melt areas within the powder bed. A raking mechanism spreads new powder layers and the process continues until part fabrication is complete. Parts were designed using CAD software to include cavities for sensor placement. The sensor assembly included the piezoceramic sensor (in this experiment, $LiNbO_3$ was used) as temperature and pressure sensor, titanium electrode for signal transfer, and alumina plate for insulation purpose.

Procedures were developed in this research to achieve the insertion of a piezoceramic sensor that required the pause of part fabrication at specific heights. It is important to note that the continuation of part fabrication can only proceed on top of a planar surface. Thus, sensor placement was achieved by designing cavities in which part fabrication would start

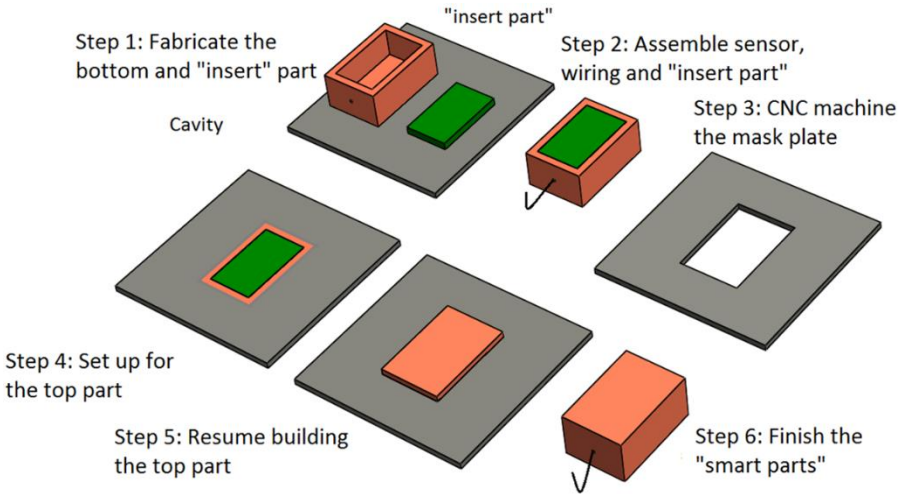

Figure 1. Fabrication of smart parts using "stop and go" process

onto a planar surface. The process was stopped at the desired height for sensor placement and allowed to continue. The "stop and go" process can be divided into six steps shown in Figure 1 by an example smart part of simple geometry. The first step consisted of fabricating the desired component along with an insert part. The insert part is meant to hold the sensor assembly within the cavity of the bottom part as well as to allow the continuation of part fabrication onto a planar surface. Step 2 consisted of assembling the smart part and step 3 consisted of machining a mask plate to ensure a planar fabrication surface and assist in part registration. The setup was completed and fabrication was allowed to continue until a final product was achieved.

3. Results

Figure 2 shows the results achieved from the developed procedures where Figure 2a illustrates the exploded view of the internal components of the fabricated part. Figure 2b shows the actual parts fabricated using the "stop and go" process.

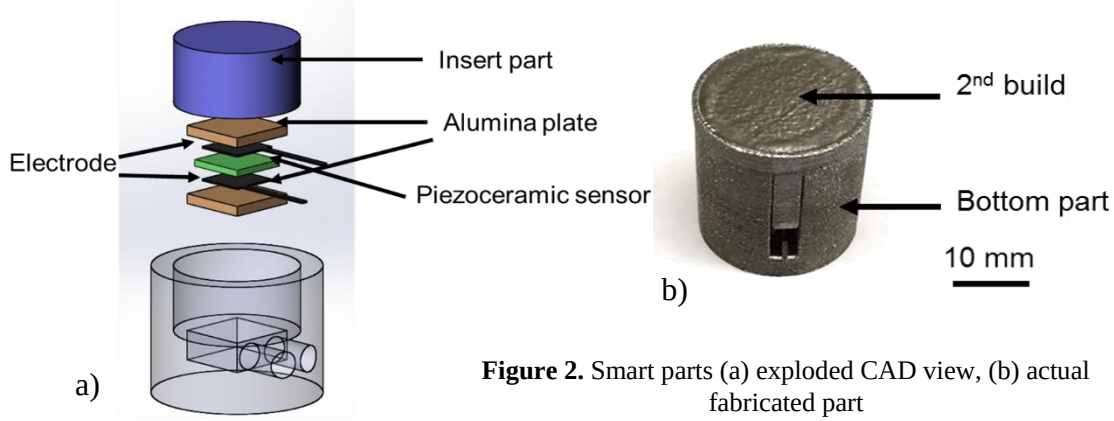

Figure 2. Smart parts (a) exploded CAD view, (b) actual fabricated part

4. Conclusions

The work presented in this paper showed the feasibility of fabricating energy system components with fully embedded non-intrusive health monitoring sensors. Certain issues such as part registration and bonding at the separate fabrication interfaces are still being investigated to further optimize the smart part fabrication process. Nonetheless, this research demonstrated that sensors could be placed within metal components that are non-intrusive to system operation and can be placed in inaccessible areas within a part's volume, which further isolates the sensor from harsh operating conditions. Eventually, the resulting smart parts will ensure the proper funcitonality of a system component enabled by prolonged sensor life and monitoring information that is more closely related to critical sensor areas. Results from this research suggests that AM using EBM for the manufacturing of energy system components can revolutionize part design by allowing the embedding of sensors within component critical areas which are exposed to high temperatures and pressures.

This research was supported by the U.S. Department of Energy (DOE) (award No. DE-FE0012321). Findings, opinions, conclusions, or suggestions herein are those of the authors, and do not necessarily reflect the views of the DOE.

References

[1]. Gibson, I., Rosen, D.W., & Stucker, B. "Additive Manufacturing Technologies." NY: Springer, 2010.

[2]. E. Aguilera, J. Ramos, D. Espalin, F. Cedillos, D. Muse, R. Wicker, and E. MacDonald, " 3D Printing of Electro Mechanical Systems", 2013 Solid Freeform Fabrication Symposium, Austin, TX, USA.

[3]. C.A. Terrazas, S.M. Gaytan, E. Rodriguez, D. Espalin, L.E. Murr, F. Medina, and R.B. Wicker, "Multi-material metallic structure fabrication using EBM", Int J Adv Manuf Technol, Vol 71, pp 33-45, 2014.

PRELIMINARY DESIGN OF AN OXY-FUEL OPEN-CYCLE MHD COMBUSTOR SYSTEM

M. Hernandez[1], L. Cabrera[1], and N. Love[1]*
[1] Department of Mechanical Engineering, University of Texas at El Paso, El Paso, TX 79968, USA;
* Norman D. Love (ndlove@utep.edu)

Keywords: *open-cycle MHD, combustor design, steady-state heat exchanger design*

ABSTRACT

A low-pressure configuration of an open-cycle, constant-pressure oxyfuel (O_2/CH_4), lab-scale MHD combustor was developed to yield 2800 K and 2000 m/s. A systems engineering design approach was used. The required heat load to remove via convection, a steady-state process, was determined to sustain the design for a given firing duration. Initial parameters yield a coolant convective heat transfer of 50,000 W/m^2-K. It is concluded that an optimization of the solution will lie in the study of coolant, wall material, and geometry options. A future investigation will follow in the subject, establishing options for its resolution.

1 Introduction

Seeded-combustion plasma induces a motional electromotive force if interacting with a magnetic field, which can generate an electrical current. Plasma electrical conductivity is a function of temperature, wherein a suggested claim of temperature range is 3000-3500 K[1]. Oxyfuel combustion reactions accelerated to supersonic velocities may resolve the low conductivity property of gas-fired seeded combustion plasmas [1]. The purpose of this study is to present the design of a lab-scale oxy-fuel fed MHD combustor.

2 Open-cycle MHD combustor design and configuration

The preliminary design approach of the MHD combustor and heat exchanger design is delineated. The processes in this design can be described by mathematical constructs of ideal one-dimensional nozzle theory. This theoretical description is the core of the MHD design approach, which approximates the actual thermochemical behavior. The open -cycle MHD engine design solution space was defined using this description. The postulated assumptions of the process are:

- The chemical reactions reach equilibrium state and the combustion products are gaseous, homogeneous, and conform to the ideal gas law;
- Isentropic processes are ubiquitous throughout the flow direction, i.e. adiabatic and reversible attributes;
- Constant steady-flow with constant and uniform properties; and
- The normal exit-plane yields an axial momentum vector [2,3].

The design objective is to yield a supersonic plasma state. The design constraints of 2000 m/s and near 3000 K were placed on the exit property conditions, where the critical plasma behavior must interface with an MHD collector. The static temperature was selected based on a claimed upper operating range[1]. A lab-scale engine was designed for sea-level operation, steady-state flow, 3.68 mm throat diameter, 1.63 contraction area ratio, and constant-pressure gas-gas combustion mixture of O_2 /CH_4, subjected O/F mixture ratio of 3.5. The preprocessing step was to investigate, generate, and analyze a myriad of constant-pressure chemical equilibrium data sets for the given reactant conditions. This analysis yielded the initial system solution subspace. The NASA CEA computer program was employed to

compute the equilibrium mixture compositions and properties. Stagnation properties of the combustion products are defined at the prescribed boundary value conditions upon the nozzle inlet. For a given stagnation condition set, a one-dimensional stagnation-static nozzle flow description of an isentropic flow process provided the exhaust gas solutions, in an iterative process. The accepted solution options were vetted to verify if the solution satisfied the design requirements and if the solution yielded an under-, ideal-, or over-expansion state. The latter over-expanded state induces undesired shockwaves or discontinuities in the flow, and was avoided. The injection-end interface was defined, i.e. the total maximum permitted mass flow rate or choked mass flow condition for the given throat area and the injector-end pressure was defined for interface requirements to the pressure-feed subsystem. A low-pressure configuration was selected for the initial design – since under higher chamber pressures, the confinement geometry would require thicker walls, a possible heat sink, which may lead to plastic deformation or failure of wall materials from excessive temperatures, and may not be suitable for a steady-state heat transfer process. The subsequent process that ensued was the characterization of the combustor volume and internal solid boundary contour. The upstream combustor geometry, was established from previous experimentally tested characteristic chamber length data – this accounts for the residence time of the chemical reacting gases[3] – and theoretical engine performance parameters. The final process was to define the exit section, which dictates the acceleration efficacy and exit behaviors of the flow. A gradual near-axial, supersonic momentum vector was designed to ensure no
discontinuities or possible stagnation points. Two exit nozzle contour concepts were examined, a standard 15-degree half-angle cone contour and a parabolic-bell contour [2,3]. The
preliminary engine operating parameters, design conditions, and findings of the lab-scale MHD combustor are denoted in Table 1. The design concept is presented in Figure 1.

3 Open-cycle MHD heat exchanger design

Due to the nature of the project, the MHD setup is required to operate in steady-state conditions, akin to an industrial arrangement. According to existing literature, high heat fluxes are to be expected, requiring the test instrument to be properly cooled in order to avoid plastic deformation[3]. The steady state heat flux in the system outlined above can be approximated through Bartz's correlation. This equation combines both nozzle gas flow properties (e.g. heat capacity and viscosity) and engine parameters, given in the form of chamber pressure and throat diameter. This relationship establishes that the maximum heat flux occurs at the throat of a nozzle, enabling the investigation to focus on this critical point. Once the convective heat transfer coefficient has been established by the former relationship, finding the heat flux reduces to determining the maximum allowable wall temperature of the system. This can be estimated through Newton's law of cooling. As an initial assumption, the maximum wall temperature is set to be 1273 K or 1000 ^{o}C, based on existing literature on the subject[3]. A correction factor corresponding to a 30% reduction is added to this equation, to account for the over estimation of Bartz's equation. This results in a heat flux of 7.06 MW/m^2 . The initial material taken for this study corresponds to SS304, which has an approximate high temperature thermal conductivity of 20 W/m-K [5]. Additionally, an initial thickness of 3.5 mm is assumed for this study. Using Fourier's Law for conduction, the maximum allowable cool-side wall temperature corresponds to 481 K, or 208 ^{o} C, which is well within the limits of most high-temperature heat transfer fluids. The final step in this procedure corresponds to the convective heat transfer between the coolant-side wall and the cooling fluid. The required convective heat transfer coefficient can be estimated through the assumption of a coolant bulk temperature. Initially, the coolant is assumed to have a bulk temperature of 291 K, or 20 ^{o}C. This value yields a required coolant convective heat transfer coefficient 'h_g' of 50,000 W/m^2-K. Using the Sieder-Tate correlation to relate the former to required hydraulic diameter

and velocity, it becomes apparent that such a high value is unreasonable in terms of real dimensions. Thus, a minimization of this number is required. Due to the fact that the heat flux magnitude has been fixed to a certain value only the coolant bulk temperature and maximum coolant-side temperature are variables. It is then concluded that an investigation on the optimization of wall material, thickness and coolant selection is required to finalize the design in this matter. The preliminary findings of the forced convective steady-state heat exchanger concept and conditions are denoted in Table 1.

References

[1] N. Kayukawa, "Open-cycle magnetohydrodynamic electrical power generation: a review and future perspectives," *Progress in Energy and Combustion Science*, vol. 30, no. 1, pp. 33–60, Jan. 2004.

[2] G. P. Sutton and O. Biblarz, *Rocket Propulsion Elements*, 8 ed. Hoboken, NJ: John Wiley & Sons, 2010, pp. 1–764.

[3] D. K. Huzel and D. H. Huang, *Modern Engineering for Design of Liquid Propellant Rocket Engines*. Washington DC: AIAA (American Institute of Aeronautics & Ast.), 1992, pp. 1–431.

[4] Y. A. Cengel and J. M. Cimbala, *Fluid Mechanics*. McGraw-Hill Science/Engineering/Math, 2004, pp. 1– 2036.

[5] Y. A. Cengel and A. J. Ghajar. *Heat and Mass Transfer: Fundamentals & Applications*. 4th Ed. New York: McGraw-Hill, 2011. Print.

Table 1. The principal operating conditions of the lab-scale open cycle MHD combustor and heat exchanger.

Mixture Properties	**Value**	**Units**	**Heat Exchanger Parameters**	**Value**	**Units**
Propellant combination	CH_4-O_2		Critical Heat Flux	7.06	MW/m^2
O/F mixture ratio	3.5		Maximum wall temperature	1273	K
Stagnation chamber pressure	785.9	kPa	Coolant Bulk Temperature	291	K
Stagnation chamber temperature	3320	K	Maximum coolant-side temperature	481	K
Specific heat ratio	1.12		Estimated Wall Thickness	3.5	mm
Molecular weight of gas mixture	20.984	1/n	SS304 Thermal Conductivity	20	W/m-K
Total choked mass flow rate	4.753E-03	kg/s	Coolant heat transfer coefficient	50000	W/m^2-K
Compressible Flow Parameters			**MHD Engine Parameters**		
Throat diameter	3.683	mm	Thrust	10.4	N
Area contraction ratio	1.63		Design characteristic velocity	1776	m/s
Area expansion ratio	2.07		Design coefficient of thrust	1.18	
Nozzle exit temperature	2660	K	Design TC specific impulse	215	s
Nozzle exit pressure	100.13	kPa	Injector-throat length	50.14	mm
Nozzle exit velocity	2204	m/s	Cylindrical chamber length	48.26	mm
			Parabolic-bell nozzle length	0.094	mm

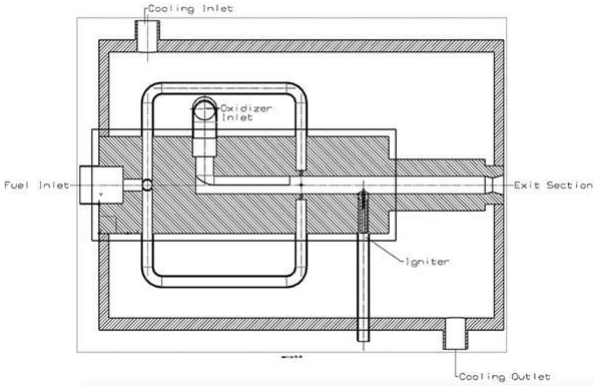

Fig.1. The preliminary concept of an open-cycle MHD combustor and heat exchanger is shown.

REVIEW OF MHD POWER GENERATION SYSTEMS

J. Rosero[1], G. Enriquez[1], J. Aboud[1], B. Lovich[1], C. Gamboa[1], N. Love[1]*
[1] Department of Mechanical Engineering, University of Texas at El Paso, El Paso, TX 79968, USA;
* Norman Don Love (ndlove@utep.edu)

Keywords*: MHD generators, Review, Open-cycle, Seeded & Unseeded, Electrodes,*

ABSTRACT

A literature review of magnetohydrodynamic (MHD) power generation systems is performed. Topics such as what MHD power generation is, what different types of MHD generators exist, typical setups for MHD systems, properties important to this type of research, the difference between seeded or unseeded systems, different types of electrodes and MHD channels, as well as potential efficiencies of these systems is discussed. A large variety of methods for MHD power generation were found, but some key principles were noticed such as high temperatures, high velocities, and similar strengths of magnetic fields. While many simulations of MHD research were found, a lack of experimental open-cycle MHD generator research was observed. More research is recommended in order to fully understand the potential of MHD systems in use in large-scale power generation efforts.

INTRODUCTION

1 What is MHD?

MHD power generation works by converting the enthalpy from a high temperature working fluid to electrical power using Faraday's Law of electromagnetic induction [1]. This type of energy generation could have the potential of becoming the next wave of high efficiency energy conversion systems since they can convert thermal energy directly to electrical power. Most power generation systems used today usually involve the conversion to mechanical energy first, where much of the energy is lost leading to low efficiencies. Some advantages of these MHD systems are potentially higher efficiencies and decreased maintenance due to the smaller number of moving parts [3].

2 Different Types of MHD Generators

There are two main classifications for MHD generators with gas plasma as the working fluid: open and closed cycle. For open-cycle systems the working fluid is typically a fossil fuel combustion gas plasma such as carbon dioxide and water [5]. Closed-cycle systems usually use a noble gas non-equilibrium plasma such as argon [10,12]. Although the setup for an MHD power generator can vary slightly, it was noticed that a typical MHD open-cycle system consists of a combustion chamber, a nozzle, an MHD channel/duct, and a diffuser [3,4]. In the combustion chamber, the feeding fuel is oxidized by either air or oxygen-enriched air; in the nozzle, the plasma is accelerated; in the MHD duct, which has a magnetic field and electrodes on the surrounding walls, the electric power is extracted; finally, in the diffuser we obtain energy pressure by converting the kinetic energy of the plasma [3]. Figure 1 below illustrates a typical MHD power generator setup.

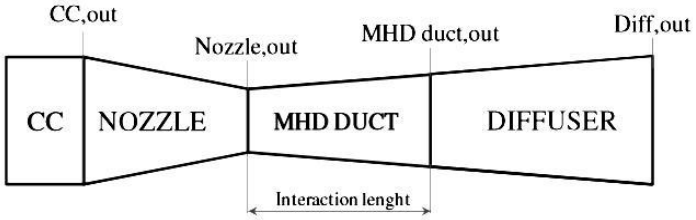

Figure 1. Typical MHD Setup [3]

3 Properties

With MHD systems there does tend to be a wide range of variability; however, some properties have shown to be fairly constant. In general, higher velocities at the entry point of the magnetic field are preferred since higher velocities generate higher currents according to Faraday's Law of induction. Higher velocities of course come with higher Mach numbers being achieved as the fluid enters the magnetic field, approximately 1 to 5 Mach [5,7,12]. In order to achieve such high speeds a strong combustion event is needed which in turn leads to higher temperatures ranging from 1500 to 3100 K [2,4,5,10] at the nozzle throat. Lastly, the magnetic induction produced by the magnetic field ranges has been noticed to range from 2 to 6 T [5,10,12]. This is shown in several attempts at MHD power generation such as the Sakhalin, a pulsed large-scale open-cycle MHD generator with a Faraday MHD channel. The generator achieved velocities of 2050 m/s, a Mach number of 2.4, temperatures as high as 2750 K, and a maximum magnet induction of 2.5 T at the inlet of the electrode section [11]. The Mark II generator, which used segmented Faraday MHD channels showed lower velocities by contrast at only 887 m/s but it did show temperatures of 2971 K and a maximum magnetic field of 2.12 T [4].

4 Seeded and Unseeded MHD Generators

For both open-cycle and closed-cycle MHD generators it is not uncommon to seed the fluid with an alkali metal such as potassium or cesium. Alkali metals have high ionizing potential and therefore the introduction of these elements into the flow field increases the electrical conductivity of the fluid. Seed fraction, which is the percentage of seed found in the working fluid, vary greatly depending on the geometry and size but are normally of the order of 0.1% for noble-gas and 1.0% for combustion MHD plasmas. [8] Unseeded fluid ionization is possible as shown in a power recovery experiment conducted at Princeton University [7]. This method uses high voltage pulsars to ionize the air only for the time that its fluid will be passing through the MHD channel, which is the only time the fluid needs to be ionized. There have also been other attempts at unseeded ionization using high temperature plasma. An experiment using a disk-shaped Hall-type MHD generator demonstrated that it is possible to change the plasma structure from inhomogeneous and unstable to homogeneous and stable by increasing the total inlet temperature. This homogeneous stable plasma showed high generator performance comparable to that obtainable with seeded MHD generators [11].

5 Electrodes and MHD Channels

Electrodes are the main source of extracting power from MHD systems. However, since configurations for MHD generators tend to vary, this leads to different types of electrodes being used. There are 4 main types: Faraday [10], Hall [9], diagonal [9], and disk [5]. A finite segmented Faraday generator fundamentally differs in electrical connection from the diagonal connected generators and the Hall connected generators, and each separated electrode is individually connected to an external load. The disk-type channel consists of two insulator disks with inner and outer ring electrodes. Testing has found that the Faraday electrodes are best in a wide range of areas including efficiency, voltage drop, and maximum power output.

However, the complexity of these types of electrodes greatly increases maintenance; for this reason the diagonal electrodes are preferred.

6 Efficiency

MHD power generation systems' efficiency is usually described in terms of enthalpy extraction ratio, which is ratio of power output over thermal input [6]. Extraction ratios can range from 10 – 30% [5,6]. Open-cycle generators, as recently as 2004, had experimentally demonstrated a 15% enthalpy extraction ratio for a shock-driven disk channel and 11% for a linear Faraday channel which had a 3.2 T of magnetic field. This last come from the Arnold Engineering Development Center (AEDC) in Tullahoma, Tennessee, using 300 MW of heat input [5]. Sakhalin also showed enthalpy extraction ratios at this range at 12 % [12]. These low efficiencies are potentially due to the lack of research in this area. More experimental research into MHD generators may produce higher enthalpy extraction ratios.

CONCLUSION

Although much work has been done, there are still many unanswered questions regarding open-cycle MHD generation systems. Due to the nature of the project, open-cycle MHD generators do not tend to lend themselves well to small scale testing. This has led to many teams opting for theoretical calculations instead of expensive large scale experiments. Because of these factors, a lack of experimental research on open-cycle MHD generators was noted. There is also little understanding of how well MHD experiments when going from small to large scale experiments or how efficiencies may change when using higher energy working fluids such as oxy-fuel. In order to further advance this technology there is a major need for more experimental research in open-cycle MHD generators.

References

[1] Ajith Krishnan, R., and B. S. Jinshah. "Magnetohydrodynamic Power Generation." International Journal of Scientific and Research Publications 3.6 (2013): 1.

[2] Brogan, T. R., et al. *A review of recent MHD generator work at the Avco-Everett Research Laboratory*. No. 2352. AVCO EVERETT RESEARCH LAB INC EVERETT MA, 1962.

[3] Cicconardi, Salvatore P., and Alessandra Perna. "Performance Analysis of Integrated Systems Based on MHD Generators." *Energy Procedia* 45 (2014): 1305-1314.

[4] Liu, BL, et al. "Three-Dimensional Analysis of the IEE MARK II MHD Generator". *9th International Conference on Magnetohydro-dynamic Electric Power Generation.* Web.

[5] Kayukawa, Naoyuki. "Open-cycle magnetohydrodynamic electrical power generation: a review and future perspectives." *Progress in Energy and Combustion Science* 30.1 (2004): 33-60.

[6] Murakami, Tomoyuki, Yoshihiro Okuno, and Hiroyuki Yamasaki. "Achievement of the highest performance of a CCMHD generator: an isentropic efficiency of 63% and an enthalpy extraction ratio of 31%." *Plasma Science, IEEE Transactions on* 32.5 (2004): 1886-1892.

[7] Murray, Robert C., et al. "Observation of MHD effects with nonequilibrium ionization in cold supersonic air flows." Paper AIAA 2004 1025.42 (2004): 5-8.

[8] Rosa, Richard J., Charles H. Krueger, and Susumi Shioda. "Plasmas in MHD power generation." *Plasma Science, IEEE Transactions on* 19.6 (1991): 1180-1190.

[9] Takahashi, Toru, Takayasu Fujino, and Motoo Ishikawa. "Comparison of Generator Performance of Small-Scale MHD Generators with Different Electrode Dispositions and Load Connection Systems." *Journal of International Council on Electrical Engineering* 4.3 (2014): 192-198.

[10] Tanaka, Daijiro, and Yoshio Hattori. "Characteristics of resistive electrode in MHD generator duct and a minimizing technique for internal power loss."*Journal of Nuclear Science and Technology* 12.11 (1975): 687-694.

[11] Tanaka, Manabu, Tomoyuki Murakami, and Yoshihiro Okuno. "Plasma Characteristics and Performance of Magnetohydrodynamic Generator With High-Temperature Inert Gas Plasma." (2014).

[12] Velikhov, EP, et al. "Pulsed MHD Power System SAKHALIN-the World Largest Solid Propellant Fueled MHD Generator of 500MWe Electric Power Output". Proceedings of 13th International Conference on MHD Power Generation and High Temperature Technologies. Web.

[13] Yiwen, L. I., et al. "Preliminary Experimental Investigation on MHD Power Generation Using Seeded Supersonic Argon Flow as Working Fluid." *Chinese Journal of Aeronautics* 24.6 (2011): 701-708.

SPECTRAL RADIATION ANALYSIS OF PREMIXED OXY-SYNGAS AND OXY-METHANE FLAMES

Naznin Jahan Afrose[1], A S M Arifur R. Chowdhury[1], Martin de la Torre[1], and N. Love*
Department of Mechanical Engineering, University of Texas at El Paso, El Paso, Texas 799681
* Norman Love (ndlove@utep.edu)

ABSTRACT

In this experimental study, spectral radiation of premixed oxy-syngas and oxy-methane data was collected from 1.2μm to 5μm wavelengths with varying firing inputs, equivalence ratios, and CO_2 recirculation ratios. The study finds that oxy-fuel combustion flame displays 3 to 5 time stronger spectral intensity than a conventional air combustion flame. It is also found from this experimental study that spectral intensity increases with the increase of CO_2 in emission and with the increase of firing input for both oxy-syngas and oxy-methane combustion. This is very important for combustion system designing.

1 Introduction

The primary focus of this experimental study is to investigate the spectral radiation emission of premixed oxy-syngas and oxy-methane flames. In the present study radiation data was measured for varying firing inputs, equivalence ratios, and CO_2 recirculation ratios. The two main byproducts produced in oxy-fuel are CO_2 and H_2O, which emit in the infrared region at 2 and 4.4 μm ranges for CO_2 and 1.4, and 1.8 μm ranges for H_2O with an overlap in the 2.7 μm range [1], [2]. In a gas turbine the banded spectra from H_2O and CO_2 reach its strongest heat transfer emission at temperatures of up to 3000 K. The flame is much stronger due to the high concentrations of CO_2 in this process [3].

2 Experimental Methodology

A small radiative surface (A_s) observed from a long distance can be approximated as a differential area for solid angle calculations [4]. In that case solid angle (Ω) is a function of only radiative area normal (A_n) to the source light rays, and the distance (r) between radiative source and the detector. The formulas used to calculate spectral intensity (I) are defined in equations. (1-4)[5]:

$$I = \frac{\text{Radiative Energy Flow}}{t \times A_n \times \Omega \times \lambda} \tag{1}$$

$$\text{Radiative Power} = \frac{\text{Radiative Energy Flow}}{\text{Time(t)}} \tag{2}$$

$$I = \frac{\text{Radiative Power}}{A_n \times \Omega \times \lambda} \tag{3}$$

$$\Omega = \frac{A_s}{r} \tag{4}$$

Recirculation ratio (RR) is defined as the mass fraction of CO2 in the oxidizer stream.

$$RR_{CO_2} = \frac{\dot{m}_{CO_2}}{\dot{m}_{O_2} + \dot{m}_{CO_2}} \tag{5}$$

3 Results and Discussion

For this experimental study, spectral intensity is measured and plotted with respect to wavelength for premixed oxy-syngas as well as oxy-methane flames to investigate the spectral radiation emission.

3.1 Comparison between Oxy-Combustion and Air-Combustion Flames

To assess the spectral intensity of oxy-fuel combustion and air-fuel combustion, radiation data are recorded from 1.2 μm to 5 μm wavelengths at 500 W stoichiometric combustion conditions. It is known from the literature review that in oxy-fuel combustion, products are dominated by CO_2 and H_2O; where in air combustion, combustion products are dominated by NOx gases due to the higher

concentration of the nitrogen in air[6],[7]. A similar trend can be seen from Figs. 3 and 4. Figures 3 and 4 are showing the comparison between oxy-combustion and air-combustion for syngas and CH_4, respectively. It can be seen from the graph that oxy-combustion emits significantly higher radiation than conventional air-combustion in the CO_2 and H_2O spectral radiation band.

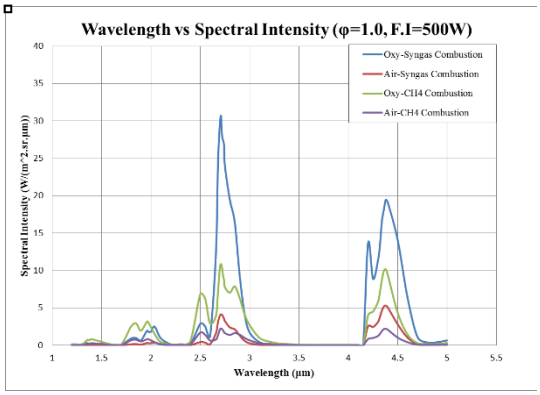

Fig.1. Spectral Intensity of oxy-fuel and air-fuel flames at φ=1.0 and F.I. =500 W

3.2 Effects of Equivalence Ratio on Spectral Radiation

The effect of equivalence ratio on spectral radiation for premixed oxy-syngas and oxy-methane at a constant firing input is presented in this section. For this particular set of studies, firing input is kept constant at 500 W and equivalence ratio is set to 0.8,0.9,1.0 and 1.5. Furthermore, no extra CO_2 is recirculated during the combustion process. It can be seen from Figs. 8 and 9 that spectral intensity for oxy-syngas combustion increases at 2.71 μm as equivalence ratio increases, however, spectral intensity marginally decreases at 4.38 μm as equivalence ratio increases. On the other hand, for oxy-methane combustion, overall spectral intensity decreases as the equivalence ratio increases. Moreover, for oxy-syngas combustion, the change in equivalence ratio affects on radiation at 2.71 μm and 4.38 μm; on the contrary for oxy-methane combustion, change in equivalnce ratio affects the whole spectrum from 1.2 μm to 5 μm.

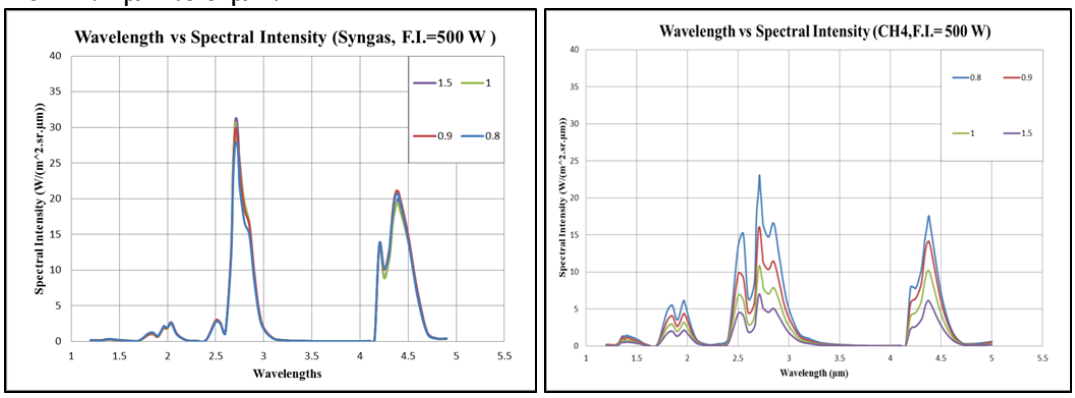

Fig.2. Effects of equivalence ratio for (a) oxy-syngas flames and (b) oxy-methane flames at F.I=500 W.

3.3 Effects of Firing Input on Spectral Radiation

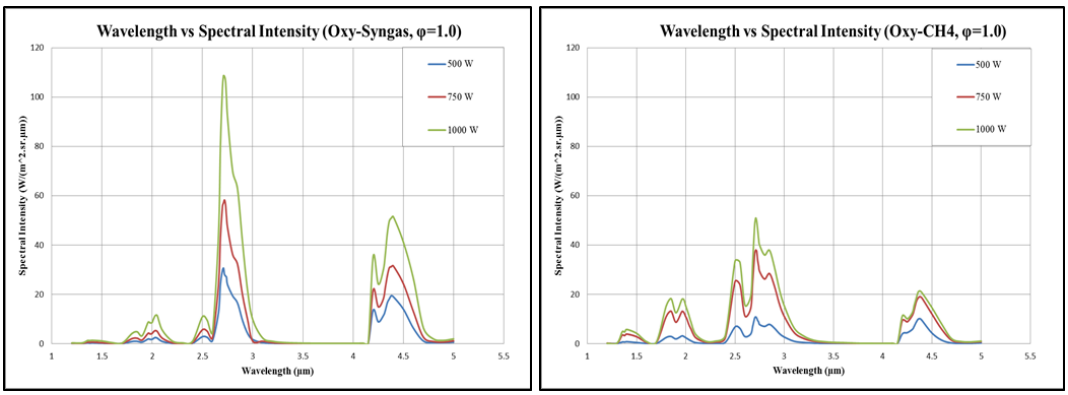

Fig.3. Effects of Firing Input in (a) oxy-syngas flames and (b) oxy-Methane flames

Figure 3 demonstrates the effect of firing input on spectral radiation for oxy-syngas combustion. The results show that spectral intensity at CO_2 as well as H_2O wavelengths increase as the firing input increases for both oxy-syngas and oxy-methane combustion. Moreover, spectral radiation increases at the highest wavelengths corresponding to 2.71 μm. This can be explained by the presence of increasing amounts of CO_2 and H_2O due to the increment of firing input.

3.4 Effects of Recirculation Ratio on Spectral Radiation

For this section the spectral radiation data is measured at a stoichiometric combustion condition while varying CO_2 recirculation ratio at 500 W firing inputs. It can be seen from the Fig. 4 that radiation increases significantly at CO_2 emission wavelengths as CO_2 recirculation ratio increases. Furthermore, radiation increases at 2.71 μm with the increment of RR_{CO2} which is the overlapping of CO_2 and H_2O emission wavelength; this phenomenon can be explained by the increment of CO_2 in the combustion process due to CO_2 recirculation. The H_2O radiation remained constant throughout the emission band.

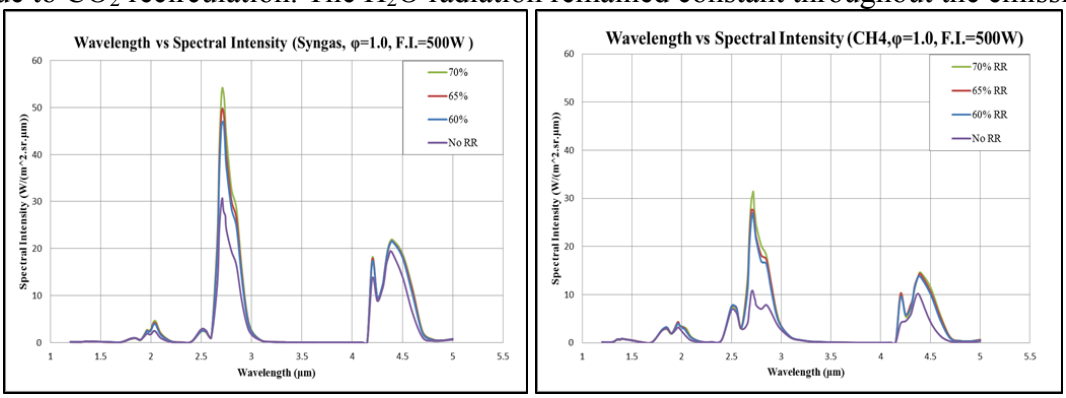

Fig.4. Effects of recirculation ratio on (a) oxy-syngas flames and (b) oxy-methane flames at F.I=500 W

4 Summary and Conclusion

The purpose of this experimental study is to demonstrate the spectral radiation behavior of premixed oxy-syngas and oxy-methane combustion. It is observed from the experiment that oxy-combustion displays significantly higher radiation than conventional combustion for both syngas and methane flames. Spectral radiation data for premixed oxy-syngas and oxy-methane combustion is collected varying equivalence ratio, firing input and CO_2 recirculation ratio. It is detected that oxy-syngas and oxy-methane combustion display opposite trends for change in the equivalence ratio. For oxy-syngas combustion spectral radiation increases as the equivalence ratio increases, on the contrary, for oxy-methane combustion equivalence ratio decreases as the equivalence increases. Moreover, for oxy-syngas combustion radiation change occurs mostly at 2.71 μm. Oxy-methane combustion radiation changes throughout the entire spectrum from 1.2 μm to 5 μm. It is also determined from the experimental study that spectral radiation increases with the firing input for both oxy-syngas and oxy-methane combustion. For CO_2 recirculation ratio variation, it is observed that radiation significantly increases at the CO_2 emission wavelength as the recirculation ratio increases for both oxy-syngas and oxy-methane combustion. Furthermore, it is also noted from the experimental study that oxy-syngas combustion exhibits higher overall radiation than oxy-methane combustion.

References

[1] Ellis, Joseph. "Emission and Absorption Bands of Carbon Dioxide in the Infrared."Physical Review 26.4 (1925): 469-474. Print.

[2] Depraz, S., M.y. Perrin, Ph. Rivière, and A. Soufiani. "Infrared emission spectroscopy of CO2 at high temperature. Part II: Experimental results and comparisons with spectroscopic databases." Journal of Quantitative Spectroscopy and Radiative Transfer 113.1 (2012): 14-25. Print.

[3] Andersson, Klas, et al. "Radiation Intensity of Propane-Fired Oxy-Fuel Flames: Implications for Soot Formation." Department of Energy and Environment, Division of Energy Technology

[4] Çengel, Yunus A.. Heat and mass transfer: a practical approach. 3rd ed. Boston: McGraw-Hill, 2007. Print.

[5] Modest, M. F.. Radiative heat transfer. 2nd ed. Amsterdam: Academic Press, 2003. Print.

[6] Brink, Anders, et al. "Modeling of oxy-natural gas combustion chemistry." Journal of Propulsion and Power 16.4 (2000): 609-614.

[7] Buhre, B. J. P., et al. "Oxy-fuel combustion technology for coal-fired power generation." Progress in energy and combustion science 31.4 (2005): 283-307.

VULNERABILITY ASSESSMENT AND RISK MANAGEMENT (VARM) FOR CRITICAL OPERATIONAL TECHNOLOGY

Eduardo Obregon
Regional Cyber and Energy Security Center
The University of Texas at El Paso
El Paso, TX 79902, USA;
eaobregon@utep.edu

Keywords*: cyber security, vulnerability, threat, impact, risk*

ABSTRACT

Continual evolution in technology has allowed enterprises to operate more efficiently with the introduction of automated processes and advanced equipment that result in better quality of products and services. At the same time, going forward at such a rapid pace has created cyber security gaps that have increased the possibility of compromising critical Operational Technology equipment through a cyber-attack. Currently, there is a major need to address newly created cyber security requirements for Operational Technology (OT) to ensure the continuous and safe operation of these enterprises and the infrastructures that depend on them. The Vulnerability Assessment and Risk Management (VARM) process is a non-intrusive, interdisciplinary methodology created to help address cyber security of Operational Technology by identifying and prioritizing the critical operational assets of an enterprise and providing risk management guidance through the analysis of impact, vulnerability and threat.

1. Background and Overview

Current operational technologies throughout different enterprises utilize increased monitoring and control mechanisms to improve reliability and efficiency. Operational technology comprises critical event-driven infrastructure required for systems support that include physical devices and equipment with software applications that are used to ensure system integrity and 24/7 running operations for enterprises such as utilities and manufacturing plants.

Technology modernization has increased dependency of information and communication technologies in order to integrate more accurate physical parameter measurements and intelligent controller devices. However, the increased dependency on information technology (IT) and Operational Technology, such as Industrial Control Systems (ICS), has introduced a higher risk in cyber security based on the vital necessity for these systems and the evolving and dynamic approaches for cyber-attacks.

2. VARM Process

The Vulnerability Assessment and Risk Management (VARM) process for Critical Operational Technology is defined as a non-intrusive methodology created for identifying, estimating and prioritizing cyber security risks by analyzing physical and cyber threat and recognized vulnerability information to determine the extent to which physical and cyber circumstances or events could adversely impact a critical operational asset from any given enterprise. Once an assessment is conducted, a risk profile is generated to document the results and possibly lead to a creation of a risk management process by the enterprise. Risk management is defined as the process utilized to avoid and mitigate the risks and involves the continuous monitoring of vulnerabilities and threats [4].

The VARM Process is composed of four major stages:

2.1 System Characterization and Criticality Analysis

The system characterization includes the identification of both cyber and physical assets that are critical for operation of an enterprise. This step identifies criticality paths in an infrastructure. A criticality path is a group of individual components, which if compromised, can directly affect a critical asset of interest. Critical assets are initially identified at the enterprise level, i.e. assets of high value due to their importance to day-to-day operations, monetary, safety, or specific factors. In order to customize the criticality factors, several types and volumes of data have to be collected and correlated using specific equations because each enterprise has different criticality priorities depending on their mission or business.

Given that some OT assets might serve possibly large numbers of enterprise assets, it is a challenge to prioritize the interconnections of OT assets to the critical enterprise assets and to other OT assets. Critical OT assets are typically accessed through Human Machine Interfaces (HMI) and computer terminals that might be remotely accessible. Such access points, along with the associated communication channels, have to be analyzed as well. The combination of identified critical assets and their connections captures the criticality paths.

2.2 Vulnerability Assessment

The vulnerability assessment includes the analysis of each critical OT asset to identify potential vulnerabilities. This step includes careful examination of policy and procedures, personnel cyber security practices, control software, physical protection, and OT communication networks. Cyber vulnerability data associated with each critical asset is collected from different sources such as online repositories and/or results from previous assessments that included penetration tests. A challenge derived from this step is that part of the vulnerability assessment depends on third party vulnerability repositories, which if compromised, can prevent the vulnerability assessment from taking place or might provide inappropriate results due to lack of data.

2.3 Threat Assessment

The threat assessment quantitatively estimates the likelihood of threats on critical assets. This step identifies possible threat sources and likelihood of cyber-attacks specific to a given enterprise based on historical data and reported threats of the business sector to which the enterprise belongs to i.e. education, health, manufacturing, etc. A major issue with threat is that is difficult to predict a behavior and to obtain a near real time value since it is based on historical data and/or reported attacks.

2.4 Risk Analysis

The last primary step of the VARM process is the calculation of the risk of a critical asset being compromised. Risk is a function of a **threat** exercising a potential **vulnerability** on a critical OT asset, and the resulting **impact** of that adverse event on the overall enterprise. The magnitude of the risk is directly dependent on the values for the obtained impact (criticality), threat, and vulnerability scores. The goal of this step is to identify areas of opportunity for Risk Mitigation and Risk Management that can be created and implemented by the enterprise based on the following criteria:

- Risk Acceptance – An implicit decision not to take an action that would affect a particular risk.
- Risk Avoidance – A strategy which effectively removes the exposure of an organization to a risk.
- Risk Control – Deliberate actions taken to reduce a risk's potential for harm or to maintain the risk at an acceptable level.
- Risk Transfer – Shifting some or all of the risk to another entity, asset, system, network, or geographic area.

3. Summary

The modernization of technology has improved operational functions of enterprises, but has also increased the possibility of cyber-attacks. The VARM process can be used as a starting point for risk mitigation for cyber security of Operational Technology by identifying and prioritizing the critical operational assets of an enterprise and providing risk management guidance through the analysis of impact, vulnerability and threat. This work provides a high level overview of the VARM process and its major steps that an enterprise can perform periodically to address cyber security.

References

[1] Department of Homeland Security, "Risk management fundamentals," April 2011.
[2] J. Dagle, "Vulnerability assessment activities," Pacific Northwest National Laboratory, 2001.
[3] National Institute of Standards and Technology. "Guide for conducting risk assessments," September 2011.
[4] S. Cordero, R. Martinez, I. Gallegos, E. Obregon, "Patent No. 61/725,474. "System, method and apparatus for assessing a risk of one or more assets within an operational technology infrastructure." 2012

OPTIMAL OPERATION STRATEGY FOR GRID CONNECTED WIND/PV AND ENERGY STORAGE SYSTEM

Eric Galvan and Paras Mandal*
Department of Electrical and Computer Engineering
University of Texas at El Paso, El Paso, TX 79968, USA
*Corresponding author (pmandal@utep.edu)

Keywords: *Economic dispatch, energy storage, renewable energy, unit commitment.*

ABSTRACT

This paper discusses an approach for modeling a two-phase short-term scheduling considering renewable energy sources (RES) and energy storage system (ESS). The first-phase is the day-ahead model, which determines the unit commitment (UC) operational decisions, and feeds them into the second-phase, which is a real-time economic dispatch (ED). The proposed model is applied to 8-bus system that uses a real-time data with a sampling time of five minutes. The results indicate that the application of photovoltaic (PV) and wind/ESS can impact the overall power losses and reduce peak load demand.

1. Introduction

The increase in demand for electrical energy coupled with increased awareness of the environmental impacts associated with conventional power production creates an urgency to explore non-conventional energy supply sources. Among these non-conventional sources, wind and solar hold the most potential, particularly if their large-scale utilization can be exploited. Assessing the impact of wind/PV power on UC and ED is a fundamental issue when integrating intermittent RES into power grid. One possibility to achieve higher system flexibility is the use of ESS. In this paper, sodium-sulfur (NaS) batteries are considered to store the excess electricity from the RES during off-peak hours and discharging during peak hours. Several studies are available concerning the short-term coordination of conventional thermal generation with RES. In [1], short-term coordination between battery bank systems/PV with thermal generation was studied. More recent studies include demand response, which allows customers to respond to varying prices in different periods of time [2], [3]. Other studies have utilized a model predictive control approach to allocating the resources needed to supply fluctuating load while considering the tradeoffs between the environmental and economic costs. This is also known as the load-following problem [4].

This paper discusses an approach for modeling a two-phase short-term scheduling with intermittent RES and ESS. UC is executed in the first-phase in order to commit generating units and leave them on line. The ED is applied in the second-phase to optimally dispatch the power system units with real-time demand and RES/ESS production.

2. Proposed short-term coordination model

The algorithm to solve the short-term coordination problem with intermittent RES is depicted in Fig. 1 and can be implemented as follows: *Step-1)* forecast load, wind, PV, and ESS power output in hourly basis for the day-ahead operation, and define the initial conditions for the thermal generators; *Step-2)* subtract RES and ESS power output from the forecasted demand; *Step-3)* solve the UC problem with the modified demand; *Step-4)* forecast real-time (5 minutes in advance) load, wind, PV, and ESS power output; *Step-5)* update the system load by subtracting the wind, PV, and ESS power outputs from the real-time load; *Step-6)* solve the ED problem with real-time data; *Step-7)* run power flow to determine losses, overloads, and nodal voltage magnitudes; and *Step-8)* if this is the last 5-minute period stop, otherwise, go to step-5.

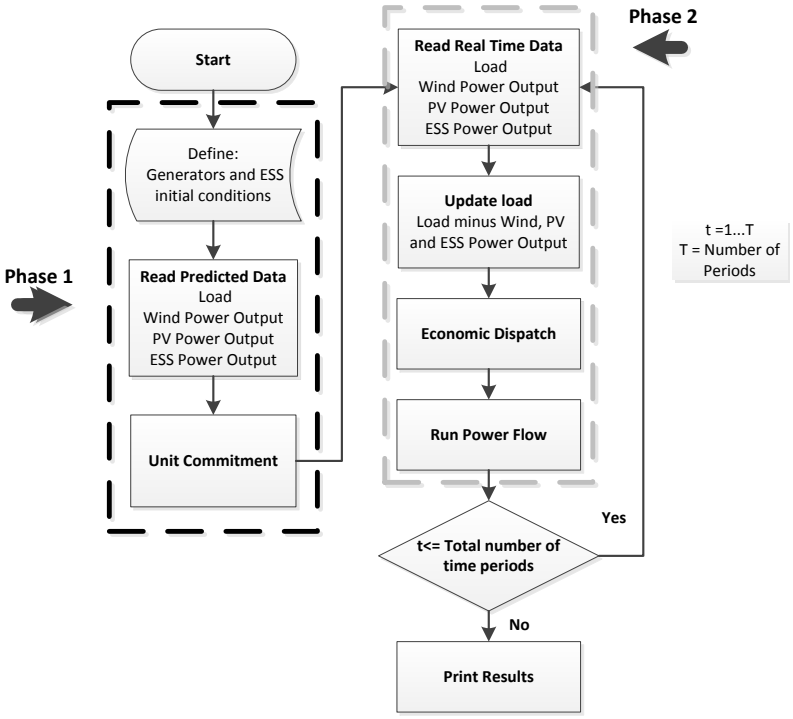

Fig. 1. Flowchart of the proposed model to solve short-term coordination utilizing RES/ESS.

3. Numerical results

The test system consists of 8 buses with a maximum demand of 344.11 MW [3]. It has (i) a 6 MW PV system connected to bus 8; (ii) a 36 MW wind farm interconnected with a 5 MW (NaS) ESS, connected at bus 3, and (iii) five thermal units based on coal and natural gas are connected to buses 1, 4, 5, 6 and 7, respectively. The line diagram of the 8-bus system is shown in Fig. 2. The results of the case study based on the 8-bus test system are presented in Figs. 3 and 4. From Fig. 3, it can be observed that the application of PV/wind/ESS can reduce peak load. The ESS increases the value of electricity generated from RES by making it available regardless of when it was generated. ESS can provide peak-shaving capability or reduce peak load by storing energy during off-peak hours from the grid or RES, and release it on peak hours. In Fig. 4, a comparison of the overall power losses of the system under two scenarios is

presented: the first one is without the RES/ESS integrated, and the second scenario considers the integration of the RES/ESS. The results show that the overall power system losses are reduced by the addition of RES/ESS. These benefits are dependent on the megawatt size of the PV/wind/ESS and their location on the power grid, which may increase or decrease their impact.

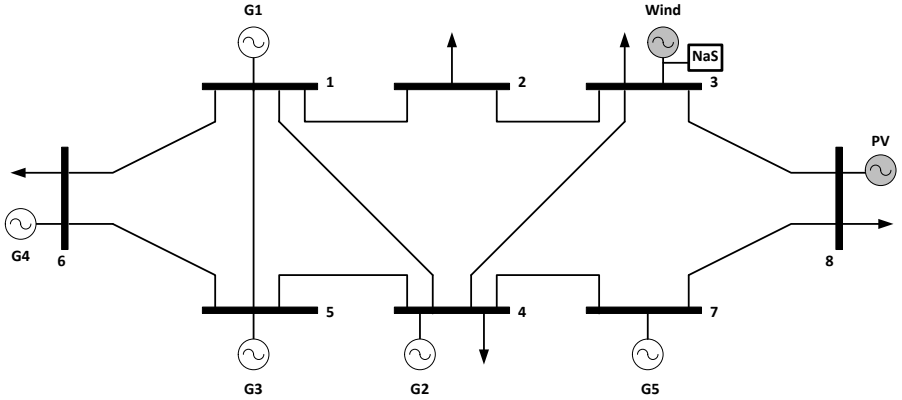

Fig. 2. 8-bus test system.

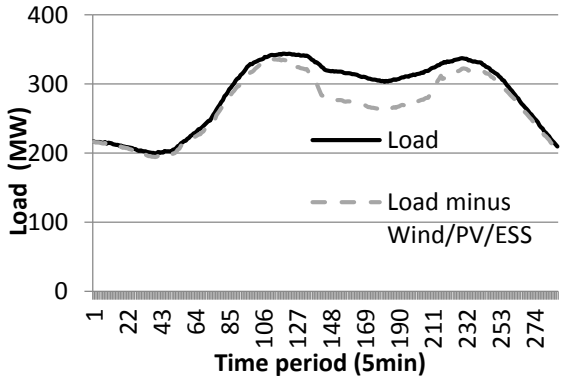

Fig. 3. Load vs load minus RES/ESS.

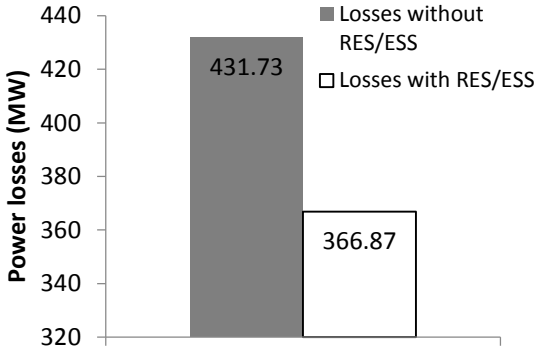

Fig. 4. Comparison of total system power losses with and without RES/ESS.

4. Conclusion

This paper proposed a short-term coordination model allowing the resolution of UC and ED problems in an electrical power network integrating RES and ESS. The proposed model can be used for day-ahead and real-time power system operations as well as long-term planning of electric power systems considering RES/ESS. The future work could be the development of an intelligent algorithm to optimally size and locate the RES/ESS in the power grid.

References

[1] B. Lu and M. Shahidehpour, "Short-term scheduling of battery in a grid-connected PV/battery system," *IEEE Trans. on Power Systems*, vol. 20, no. 2, pp. 1053-1061, May 2005.

[2] A. Khodaei, M. Shahidehpour, and S. Bahramirad, "SCUC with hourly demand response considering intertemporal load characteristics," *IEEE Trans. on Smart Grid*, vol. 2, no. 3, pp. 564-571, Sept. 2011.

[3] B. Zeng and L. Zhao, "Robust unit commitment problem with demand response and wind energy," University of South Florida, Technical Report 2010.

[4] L. Xie and M. D. Ilic, "Model predictive economic/environmental dispatch of power systems with intermittent resources," *in* Proc. IEEE Power & Energy Society General Meeting, 2009.

HYBRID INTELLIGENT METHOD FOR VERY SHORT-TERM POWER OUTPUT PREDICTION OF WIND FARM

Ramya M. Peri[1], Paras Mandal[2*], and Bill Tseng[1]
[1]Department of Industrial, Manufacturing and Systems Engineering
[2]Department of Electrical and Computer Engineering
University of Texas at El Paso, El Paso, TX 79968, USA
*Corresponding author (pmandal@utep.edu)

Keywords: *neural networks, similar day method, wind power forecasting, wavelet transform.*

ABSTRACT

This paper presents an improved hybrid intelligent forecasting model for very short-term (10-minute-ahead) wind power forecasting (WPF). The proposed hybrid intelligent model utilizes similar day (SD) method, which is combined with a data filtering technique based on wavelet transform (WT) and an artificial intelligence technique based on radial basis function network (RBFN).

1. Introduction

Wind energy is the fastest growing alternative power generation source throughout the world. Due to its stochastic nature, integration of wind power into power system faces several challenges, such as voltage instability and power flow reliability, which results in increment in power system operational costs. An accurate forecasting of wind power can tackle these challenges and help in efficient scheduling of dispatching, which results in reduction of spinning reserve capacity of the system and also decrease in the operating costs of power system [1]. Several techniques are available to predict wind power, such as, persistence method, physical models, statistical models etc. However, application of Neural Networks (NN) has received special attention in forecasting wind power generation [1], [2]. Haque *et al*. [2], proposed a hybrid intelligent framework for WPF engine which uses combination of wavelet, NN, support vector machine and grid search algorithm.

This paper proposes a hybrid intelligent technique for very short-term (few seconds to 30-minute-ahead) WPF that utilizes the combination of data filtering technique based on wavelet transform (WT), an intelligent model based on radial basis function neural network (RBFNN) and similar day (SD) method. The proposed hybrid WT+SD+RBFNN method involves two forecasting procedures: (i) forecasting using SD method only, and (ii) forecasting using an integration of SD and WT+RBFNN in which the RBFNN refines the output of SD forecasts.

2. Description of similar day method and proposed hybrid intelligent technique

2.1. Similar day method

SD method is a similarity technique that selects similar wind power days corresponding to forecast day based on Euclidean Norm [3]. To evaluate the similarity between forecast day and

searched previous days, Euclidean norm with weighted factors are used in this paper. We select SD wind power data by considering a time framework that utilizes past 10 days *(d)* from the day before a forecast day, and past 10 days before and after the forecast day in the previous year. In order to find the value of *d*, sensitivity analysis was performed by considering different values for *d*, e.g., *d= 5, 10, 15, and 45* days, and it was found that *d=10* produced the best and optimized results. In this paper, the SD based forecast data is obtained by taking an average of 200 Euclidean norm values. The Euclidean norm equation is adopted from [3] that considers three weighted factors.

2.2. Proposed hybrid intelligent model

Fig. 1 shows the flow of forecast process. The forecasting procedure is described below.

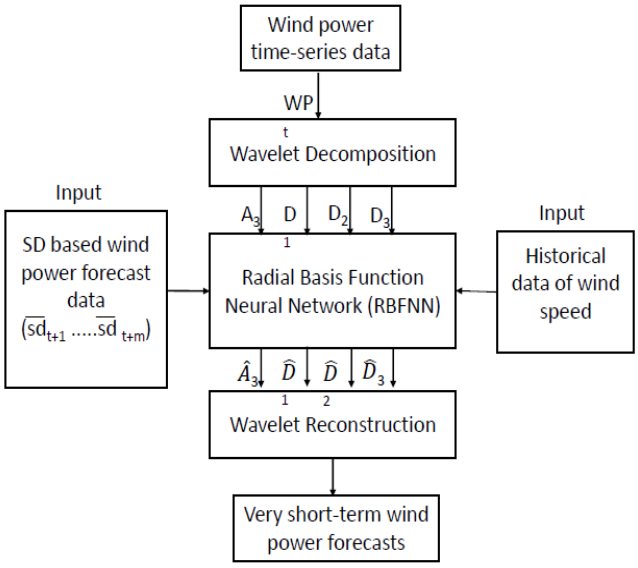

Fig. 1. Flow of the forecast process using proposed hybrid WT+SD+RBFNN model

Step-1: Only wind power time-series data is passed through the WT decomposition process.

Step-2: Individual decomposed wind power signals from step-1 (A_3, D_1, D_2, and D_3) along with wind speed and SD wind power forecast data ($\overline{sd}_{t+1}$, $\overline{sd}_{t+2}$,…., $\overline{sd}_{t+m}$, where m is 10-minute-ahead) are then fed into the RBFNN. Here, A_3 is a decomposed approximation signal, and D_1, D_2, and D_3 are the detailed coefficients.

Step-3: The output of the RBFNN model is the forecasted output of the individual decomposed signals, i.e., $\hat{A}_3$, $\hat{D}_1$, $\hat{D}_2$, and $\hat{D}_3$ which will then go through the WT reconstruction process, and thus produces the very short-term (10-minute-ahead) wind power forecasts.

3. Simulation results and discussion

This paper considers the data acquired from a wind farm located near Midland, Texas [4]. To evaluate the effectiveness of the proposed model, the results are compared with other soft computing models (SCM) such as back propagation neural network (BPNN), generalized regression neural network (GRNN) and the persistence method. Table I presents the results obtained from all the chosen forecasting models. The seasonal average mean absolute error (MAPE)s as defined by (1), obtained from the persistence method is 11.06%, and those obtained from the SD, WT+SD+ BPNN, GRNN and RBFNN models are 10.32%, 9.7%, 11.19% and 8.9% respectively. It can be observed that with the application of SD, the average seasonal MAPE are greatly improved (11.06% to 10.32%), and with the integration of WT with SD+RBFNN, the prediction error is found to be further improved (8.9%). The test results demonstrate that the proposed model outperformed the benchmark persistence method as well as displayed superior performance over tested alternatives. Table I also presents mean absolute error (MAE) and root mean square error (RMSE), as defined by (2) and (3). It is also observed that the MAE and RMSE of lower values are obtained from the proposed hybrid

WT+SD+RBFNN intelligent model in all the simulated cases. The results are simulated using built-in house code written in MATLAB.

$$MAPE = \frac{1}{N}\sum_{i=1}^{N}\frac{\left|WP_t^f - WP_t^a\right|}{\overline{WP_t^a}} * 100\% \quad (1)$$

$$MAE = \frac{1}{N}\sum_{i=1}^{N}\left|WP_t^f - WP_t^a\right| \quad (2)$$

$$RMSE = \sqrt{\frac{1}{N}\sum_{i=1}^{N}\left(WP_t^f - WP_t^a\right)^2} \quad (3)$$

where N is the total number of data points, e.g., for 10-minute-ahead WPF over a time period of 6 hours, N=36; WP_i^f is the forecasted wind power, WP_t^a is the actual wind power data and $\overline{WP_i^a}$ is an average of the actual wind power.

Table I. Comparison of 10-minute-ahead WPF performance of chosen models over a period of 6 hours.

Season	Error	P	BPNN	RBFNN	GRNN	SD	Hybrid 1	Hybrid 2	Proposed
Winter	MAPE	5.97	7.44	6.38	7	6.96	5.52	7.24	5.41
	RMSE	10.3	12.85	10.68	11.56	11.14	10.4	11.59	10.36
	MAE	8.45	10.53	9.03	9.91	9.84	7.81	9.33	7.66
Spring	MAPE	7.04	6.66	6.99	9.09	6.46	6.41	9.04	6.2
	RMSE	11.66	10.69	11.61	14.92	10.66	11.14	16.91	10.83
	MAE	9.34	8.84	9.28	12.07	8.58	8.51	12	8.23
Summer	MAPE	9.91	8.48	9.13	9.98	9.08	7.49	9.75	6.69
	RMSE	7.97	5.87	6.96	7.72	7.56	5.53	7.36	4.9
	MAE	5.75	4.9	5.29	5.79	5.27	4.34	5.65	3.88
Fall	MAPE	21.35	18.43	20.6	21.35	18.79	19.41	18.73	17.33
	RMSE	10.79	9.3	10.54	10.63	9.12	9.87	9.29	9.56
	MAE	7.72	6.66	7.45	7.72	6.8	7.02	6.77	6.27

P: persistence, hybrid 1: WT+SD+BPNN, hybrid 2: WT+SD+GRNN; proposed: WT+SD+RBFNN; MAPE in %, RMSE and MAE in MW.

4. Conclusion

This paper presented a hybrid intelligent model for predicting very short-term wind power generation of a wind farm. The proposed hybrid WT+SD+RBFNN intelligent model outperformed the persistence method, individual SCMs, and other WT+SD+SCMs. In particular, an improvement of 19.5% in forecasting error over the standard persistence method is observed using the proposed hybrid model. Forecasting very short-term wind power with a higher rate of accuracy is very important for the power system operators as they face challenges associated with variability in wind power production. Future work would be to perform probabilistic wind power forecasting that provides an uncertainty in wind power forecasts.

References

[1] G. Giebel, L.Landberg, and G. Kariniotakis, "State-of-the-art on methods and software tools for short-term prediction of wind energy production," *European Wind Energy Conference & Exhibition*, Madrid, Spain, 2003.

[2] A.U. Haque, P. Mandal, H.M. Nehrir, A. Bhuiya, and R. Baker, "A hybrid intelligent framework for wind power forecasting engine," *Electrical Power and Energy Conference*, 2014, 184-189.

[3] P. Mandal, T. Senjyu, N. Urasaki, T. Funabashi, and A. K. Srivastava, "A novel approach to forecast electricity price for PJM using neural network and similar days method," *IEEE Trans. on Power Syst*., vol. 22, no. 4, pp. 2058-2065, Nov. 2007.

[4] National Renewable Energy Laboratory (2015, Mar.). NREL: Western Wind Resources Dataset [Online]. Available: http://wind.nrel.gov/Web_nrel/

POROUS CARBON/CeO_2 COMPOSITES FOR LI-ION BATTERY APPLICATION

Hasanul Karim[1], Mohammad Arif Ishtiaque Shuvo[1], Md Tariqul Islam[2], Gerardo Rodriguez[1], Armando Sandoval[1], Manjula I Nandasiri[3], Ashleigh M Schwarz[3], Arun Devaraj[3], Juan C. Noveron[2], M. Vijayakumar[3], and Yirong Lin[1]
[1]Department of Mechanical Engineering, University of Texas at El Paso, El Paso, TX 79968
[2]Department of Chemistry, University of Texas at El Paso, El Paso, TX 79968
[3]Pacific Northwest National Laboratory, Richland, WA 99352

ABSTRACT

Li-ion batteries are widely used in modern technologies because of their high energy density and extended cycle life. Among anode materials for Li-ion batteries, porous carbon is of particular interest because it provides high lithiation and excellent cycling capability by shortening the transport length for Li^+ ions with large electrode/electrolyte interface. It has also been demonstrated that transition metal oxide nanoparticle can enhance surface electrochemical reactivity and increase the capacity retention capability for higher number of cycles. Here we investigate porous carbon/ceria (CeO_2) nanoparticles composites as an anode material. The high redox potential of ceria is expected to provide a higher potential window as well as increase the specific capacity and energy density of the system. Scanning Electron Microscopy (SEM), X-Ray Diffraction (XRD), Transmission Electron Microscopy (TEM) is used for material characterization, while battery analyzer is used for measuring the electrochemical performance of the battery.

Keywords: Li-ion battery, energy storage, porous carbon, ceria

1. INTRODUCTION

The ever-increasing demand for portable electronic devices is the drive force behind the technological improvements in electrochemical energy storage devices such as batteries[1,2]. Lithium-ion batteries are widely considered as the technology of choice owing to its high energy density, lightweight and flexible design and longer lifespan. Although Li is the most electropositive metal[2] (-3.04V), Li metal batteries suffered from dendritic Li growth, which led to explosion hazards, and it was necessary to find an alternative solution. Use of carbonaceous material for anode and Li_xMO_2 for cathode material solved the issue as Li is present as Li ion rather than the metal form[2,11], however the specific capacity and specific energy is considerably lower than the Li metal batteries. Numerous investigations have been being carried out to address this issue. Porous carbon is considered one of the most promising materials for anode application as it has a high specific surface area (2000 m^2/g), which enables higher charge-discharge rate along with high charge capacity. It has been also demonstrated that use of metal oxides nanowires or nanoparticles can increase the reversible capacity and rate capacity of a Li-ion battery (LIB)[12].

Cerium oxide (CeO_2) or Ceria is a rare earth oxide that has high oxygen storage capacity, high electrical conductivity and diffusivity and high thermal stability[13,14]. It offers high potential as an anode material for LIB due to its fast transformation between Ce(III) and Ce(IV) oxalates which have relatively low decomposition temperature in air, good structural stability and are of low cost[12]. In this work, a facile one step hydrothermal method is used to synthesize Ceria nanoparticles on Porous Carbon for LIB electrodes and the performance is compared with bare porous carbon electrodes.

2. EXPERIMENTAL DETAILS

The PC/CON hybrid synthesis is a one-step hydrothermal method. At first Porous Carbon was dispersed in deionized (DI) water. Then Ammonium Cerium Nitrate $(NH4)_2Ce(NO_3)_6$ was added to the solution and the solution was sonicated. The mixture was then separated by centrifugation. At this stage $Ce(OH)_4$ was formed on the pores and surfaces of the porous carbon. Then the product was mixed with a NaOH solution and transferred into a Teflon lined autoclave. After heating the mixture for 45 hours at 180° C, the solution was separated by centrifugation, and washed with DI water for three times. Then the remnant was dried at 70° C. At last the product was heated at 450° C in Argon for 2 hours.

For making anodes for both PC and PC-CON electrodes, Polyvinylidene Fluoride (PVDF) was used as the binding material. PVDF was dissolved in N-Methyl-2-pyrrolidone (NMP). Later 80 wt% active material and 10 wt% activated carbon were dispersed in 10 wt% PVDF with excess NPM to prepare homogenous slurry using a homogenizer. Then the slurry was coated on Copper foil and dried at 100 °C on a hot plate. Next, a precision disc cutter was used to cut anodes with 13 mm diameter. Later the anodes were kept overnight in vacuum oven.

Coin cells (CR 2032) were assembled using either PC anodes or PC-CON anodes inside an Argon filled glovebox. One molar LiPF6 in ethylene carbonate (EC), dimethyl carbonate (DMC), and diethyl carbonate (DEC) organic solvent at 1:1:1 volume ratio was used as electrolyte. Celgard 2500 was used as the separator.

3. RESULTS AND DISCUSSION

Scanning Electron Microscopy (SEM) and Transmission Electron Microscopy (TEM) were used to determine the size and the morphology of the PC-CON hybrids. The crystal structures of the PC/CON hybrid were determined via X-ray diffraction (XRD) using Cu Kα radiation. XRD confirmed that the products were well crystallized and in accordance with the JCPDS file for Porous carbon and CeO_2.

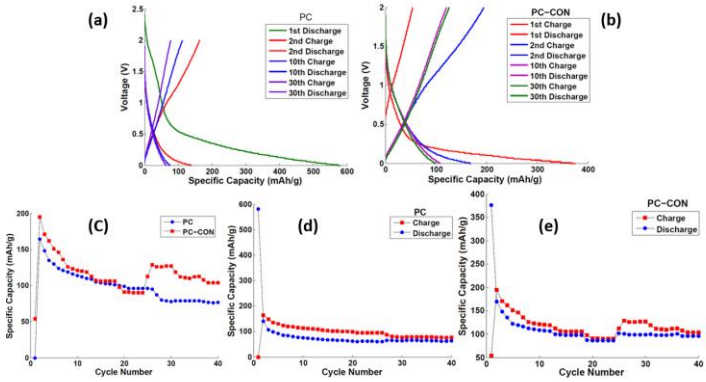

Fig. 5. Measurements of capacity and rate capability, (a) charge/discharge curve for PC anode, (b) charge/discharge curve for PC-CON anode, (c) comparison of specific capacity of the two anode materials as a function of cycle number: PC anode was cycled at 100mA/g for 40 cycles; PC-CON was varied among 100mA/g, 200mA/g, 300mA/g and 500mA/g consecutively after every 5 cycles (d) cycling performance of PC anode at 100mA/g for 40 cycles (e) specific capacity of PC-CON at 100mA/g, 200mA/g, 300mA/g and 500mA/g consecutively after every 5 cycles

To evaluate the electrochemical performance of the anodes an eight-channel battery analyzer form MTI Corporation was used. Fig. 5 (a) and (b) shows the galvanostatic charge-discharge curves for

PC and PC/CON anodes respectively at the voltage window between 0.01 to 2 V in the 1st, 2nd, 10th and 30th cycles. The current density used for the PC electrodes is 100 mA/g while for PC/CON electrode it was varied from 100mA/g, 200 mA/g, 300 mA/g and 500mA/g in a cyclic manner. It can be seen that while the electrode with only PC shows a capacity of 64 mAh/g at the 30th cycle, the PC/CON electrode retained capacity around 100 mAh/g after that cycle. Fig. 5 (c) compares the specific capacity of the PC and PC/CON electrodes as a function of cycle number from 2nd cycle to the 40th cycle at different current densities. The capacity of PC electrode decreased from 164 mAh/g to 77 mAh/g while PC/CON showed a higher capacity of 195 mAh/g in the 2nd cycle and it went down to 146 mAh/g and then successively to 90 mAh/g with further increase in current densities. However, when the current density was returned to the 100 mA/g the electrode recovered to 113 mAh/g capacity. After the 40th cycle, PC/CON electrode showed significantly higher capacity (104 mAh/g) over the PC electrode (77 mAh/g) although it was measured at five times higher current density (500 mA/g).

4. CONCLUSION

A single step hydrothermal synthesis technique was utilized to synthesize Ceria nanoparticles on porous carbon to develop a high performance LIB anode material. The growth and presence of Ceria was confirmed using SEM, XRD and TEM. Electrodes with bare PC and PC/CON was prepared and tested using a battery analyzer. The PC/CON electrode showed significantly higher specific capacity and better capacity retention up to forty cycles. The investigation shows the potential of using metal oxide nanoparticles on carbonaceous materials as an intriguing way of improving the performance of Li ion batteries.

ACKNOWLEDGEMENTS

The synthesis and analysis part of the work is supported by Chemical Imaging Initiative, under LDRD program at Pacific Northwest National Laboratory (PNNL). PNNL is a multi-program laboratory operated for DOE by Battelle under Contract DE-AC05-76RL01830. The XPS work is carried out at the Environmental and Molecular Sciences Laboratory, a national scientific user facility sponsored by DOE's Office of Biological and Environmental Research. A portion of this work is supported by the National Science Foundation (NSF) under NSF-PREM Grant No. DMR-1205302. The authors would like to thank Dr. Peter H. Cooke, CURRL director at New Mexico State University for TEM facility.

REFERENCES

[1] Armand, M. and J.M. Tarascon, "Building better batteries," *Nature*. 451(7179): p. 652-657(2008).
[2] Tarascon, J.M. and Armand M., "Issues and challenges facing rechargeable lithium batteries," *Nature* 414(6861): 359-367(2001)
[3] Rajib, M., Shuvo, M. A. I., Karim, H., Delfin, D., Afrin, S., & Lin, Y., "Temperature influence on dielectric energy storage of nanocomposites." *Ceram. Int.*, *41*(1), 1807-1813(2015)
[4] Zhou, H., Zhu, S., Hibino, M., & Honma, I. "Electrochemical capacitance of self-ordered mesoporous carbon," *J. Power Sources*, *122*(2), 219-223(2003)
[5] Mendoza, M., Rahaman Khan, M. A., Ishtiaque Shuvo, M. A., Guerrero, A., & Lin, Y., "Development of lead-free nanowire composites for energy storage applications," *ISRN*, (2012).
[6] Futaba, D. N., Hata, K., Yamada, T., Hiraoka, T., Hayamizu, Y., Kakudate, Y., ... & Iijima, S., "Shape-engineerable and highly densely packed single-walled carbon nanotubes and their application as super-capacitor electrodes," *Nat. Mater*, *5*(12), 987-994(2006)

HIGH-PERFORMANCE HYBRID SUPER-CAPACITORS FOR ENERGY STORAGE

Mohammad Arif Ishtiaque Shuvo[1], Hasanul Karim [1], Gerardo Rodriguez[1], & Yirong Lin[1]*
[1]Department of Mechanical Engineering, University of Texas at El Paso, El Paso, TX 79968;
* Yirong Lin (ylin3@utep.edu)

Keywords*: super-capacitor; energy storage; ceria; organic electrolyte*

ABSTRACT

Increasing demand for energy storage devices has propelled researchers for developing efficient super-capacitors (SC) with long cycle life and ultrahigh energy density. Carbon-based materials are commonly used as electrode materials for SC. Herein we report a new approach to improve the SC performance utilizing porous carbon /Cerium oxide nanoparticle (PC-CON) hybrid as electrode material synthesized via low temperature hydrothermal method and tetraethyl ammonium tetrafluroborate in acetonitrile as organic electrolyte. Through this approach, charges can be stored not only via electrochemical double layer capacitance (EDLC) from PC but also through pseudo-capacitive effect from CeO_2 NPs. The excellent electrode-electrolyte interaction due to the electrochemical properties of the ionic electrolyte provides a better voltage window for the SC. Scanning Electron Microscopy (SEM), Transmission Electron Microscopy (TEM) and X-Ray Diffraction (XRD) measurements were used for the initial characterization of this PC/CeO_2 NPs hybrid material system. Electrochemical measurements of SCs will be performed using a potentio-galvanostat.

1 Introduction

Herein, we report a simple one step hydrothermal method for synthesizing porous carbon/CeO_2 nanoparticle (PC-CON) hybrids for super-capacitor electrode. To our best knowledge no previous research has been done with porous carbon and ceria (CeO_2) in the past. The prepared PC-CON hybrid electrodes were investigated for super-capacitor applications within organic electrolyte and compared against bare porous carbon electrodes. PC-CON electrode showed better performance than bare porous carbon electrode in super-capacitor application.

2 Experimental Details

2.1 Porous Carbon/Cerium oxide nanoparticle (PC-CON) hybrids Synthesis

The PC/CON hybrid synthesis is a one-step hydrothermal method. At first 100mg porous carbon (ACS Material, LLC) was dispersed in 200mL of deionized water (DI) water. Then 150mL of 0.02M Ammonium Cerium Nitrate $(NH4)_2Ce(NO_3)_6$ was added to the solution and the solution was sonicated for 45 minutes. The mixture was then separated by centrifugation. At this stage $Ce(OH)_4$ was formed on the pores and surfaces of the porous carbon. Then

product was mixed with 100mL 5M NaOH solution and transferred into a Teflon lined autoclave. After heating the mixture for 45 hours at 180° C, the solution was separated by centrifugation, washed with DI water for three times. Then the remnant was dried at 70° C. At last the product was heated at 450° C in Argon for 2 hours [1].

2.2 Electrode fabrication

A two electrode testing set up was prepared using coin cells (CR 2032) because it provides most accurate measure for an electrode's performance for electrochemical capacitors

[1]. For making both PC and PC-CON electrodes, polyvinylidene fluoride (PVDF, MTI corp., purity ≥99.5%) was used as binding material. PVDF was dissolved in N-Methyl-2-pyrrolidone (NMP, MTI corp., purity ≥99.5%) at a 1:2.5 weight ratio by heating at 80 °C.

Later 80 wt% active material and10 wt% activated carbon were dispersed in 10 wt% PVDF with excess NPM to prepare homogenous slurry using a homogenizer. Then the slurry was coated on Aluminum foil and dried at 100 °C on a hot plate. Then a precision disc cutter from MTI Corporation was used to cut anodes with 13 mm diameter. Next the pieces were kept overnight in vacuum oven.

2.3 Coin Cell Assembly

Coin cells (CR 2032) were assembled using either PC electrodes or PC-CON electrodes inside an Argon filled glovebox (Unilab, MBraun). One molar Tetraethylammonium tetrafluoroborate ($TEABF_4$) (Sigma Aldrich) in acetonitrile was prepared inside the glovebox for the electrolyte. Polypropylene membrane (Celgard) was used as separator. Oxygen and moisture level were kept less than 0.1 ppm inside the glovebox.

3 Results and discussion

Scanning Electron Microscopy (SEM) and Transmission Electron Microscopy (TEM) were used to determine the size and the morphology of the PC-CON hybrids as shown in Figure 1. As indicated by the figure, CeO_2 particles were formed on the surfaces and nooks of the porous carbon. The nanoparticles had a diameter between 6 to 8 nm. Clear lattice fringes were observed in HRTEM image which confirms the formation of crystalline particles formed in the hydrothermal reaction.

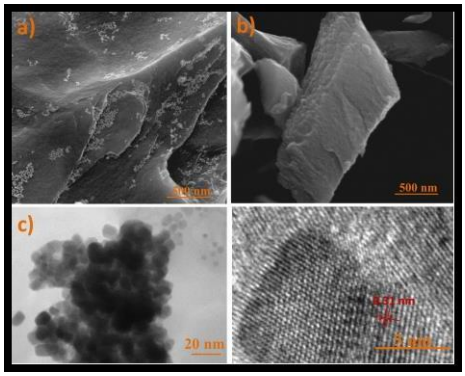

Fig.1. (a) SEM image of CeO2 nanoparticles on porous carbon, (b) morphology of porous carbon, (c-d) TEM & HRTEM images of CeO2 nanoparticles.

The crystal structures of the PC/CON hybrid were determined utilizing a Bruker D8 Discover XRD using Cu Kα radiation. The asterisk (*) marked peak represents porous carbon and rest of the XRD peaks indicate that the products were well crystallized and have a cubic fluorite structure of CeO_2 (space group: Fm3m) with lattice constant a=5.411Å, which is in agreement with the JCPDS file for CeO_2 (JCPDS 34-0394). No extra peaks corresponding to any other secondary phases were observed.

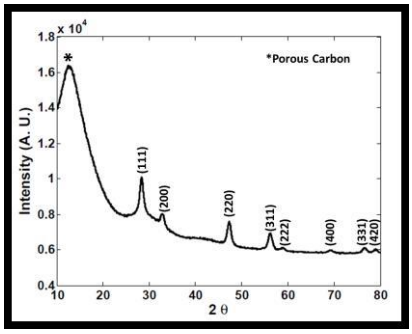

Fig.2. XRD result for CeO_2 nanoparticle with porous carbon. Asterisk (*) peak is for carbon. The rest of the peaks belong to CeO_2 nanoparticle.

The area under each CV curve suggests that all fabricated super-capacitor have good electrochemical stability and capacitance. Figure 3 (a) shows the comparison of CV plot at 100mV/s scan rate for both samples and the area under the CV curve for PC-CON sample is larger than the PC sample which suggests that the PC-CON sample has higher specific capacitance. Moderate leakage resistance of each sample was perceived as low leakage resistance would skew all CV curves vertically. Pseudo-capacitive behavior of all samples had been observed which can be ensured by the mirror like image at the anodic and cathodic regimes [1].

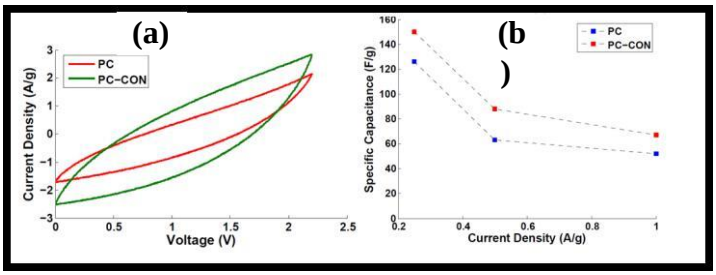

Fig.3. (a) comparison of CV plot for PC and PC-CON at 100mV/s scan rate, (b) specific capacitance of PC and PC-CON at different current density

3 Conclusion

This hybrid electrode combination allows for the hybridization of the best attributes of each singular electrode material. Based on the electrochemical results, it is obvious that PC-CON hybrid electrodes have promising future for electrochemical energy storage. This simple method can be utilized for making high performance super-capacitor for next generation aerospace, automobile and electronic application.

References

[1] Shuvo, M. A. I., Tseng, T. L. B., Khan, M. A. R., Karim, H., Morton, P., Delfin, D., & Lin, Y. "Nanowire modified carbon fibers for enhanced electrical energy storage," J. Appl. Phys., 114(10), 104306 (2013).

CHARACTERIZATION OF SMART SENSOR: PART I

R Martinez[1]
[1] Mechanical Engineering, University of Texas, El Paso, TX 79968, USA;

Keywords: *sensor, piezoelectric, simulation*

ABSTRACT

Characterization of smart parts fabricated using Electron Beam Melting (EBM) 3D printing technique with built-in piezoceramic sensors is presented. The sensor is fabricated in two stages: building of the base and embedded cavity (first fabrication) and closing the cavity (second fabrication). Simulation includes a thermal-stress analysis for the piezoceramic after the second fabrication and a thermal analysis during the second fabrication of the sensor. The response of a piezoceramic after first fabrication is done using an Instron fatigue machine. Results show the baseline responses for future design and improvement during the second fabrication.

1 Simulation of the Smart Parts

Simulation was designed to obtain an approximation of the behavior of the sensor under combined conditions of temperature, pressure, and time. The main objective is to estimate an electrical response that will support the calibration results as well as tracking the performance of the sensor during operation.

For this report, a 3D model simulation is being done in ABAQUS under the assumptions that perfect contact and zero thermal resistivity exist on the interface. Mechanical and piezoelectric properties of the different materials were obtained in literature. The simulation assumes transient heat transfer, which depends on the temperature conditions – starting at room temperature and raising it up to 1000°C.

Transient heat transfer, as well as coupled thermal displacement response was achieved at this stage of the simulation. The thermal rate was 19.5°C/s from 25°C to 1000°C. Further studies will include the implementation of piezoelectric properties to obtain a relationship between voltage and temperature, and the inclusion of the other parts of the sensor.

To study the temperature profile across the whole "smart parts", a transient heat transfer simulation in Abaqus 6.13 was performed to investigate the heat profile of the components during the second fabrication in the Arcam S12 (EBM). The objective of the analysis was to determine the maximum temperature of the piezoceramic, and to compare the possible evaporation of alloy components that were being coated inside the cavity.

The simulation consisted in five steps that were taken from the temperature reading of the thermocouple positioned beneath the mask plate during the actual fabrication. The reading consists in preheating until 500 °C (~700s), holding section for degasing during 750s, preheating continues until 736 °C (~450s), building (~1900s), and cooling (~2600s). The electron beam provides power at 30 kV and alternating current during preheating and building sections.

The simulation included a stainless steel mask plate, two alumina plates, a LiNbO3 plate, and a Ti64 cavity. The simulation consisted in five transient steps:

1. Preheating by heat flux of 28.5 kW/m2 located at the top surface of assembly for 700s.
2. Removal of heat flux for 12.5 min.
3. Preheating continues with parameters of no. 1.
4. Building by specifying temperature of 1700 °C on the center point at the top surface of the cylinder.
5. Removal of all heat sources.

All steps included constant heat loss from the bottom and side surfaces with a film surface coefficient of 2.5 (W/m^2C). It is observed that the variation of temperature achieved by the preheating stage, remain throughout the components of the sensor cavity. The deviation is a consequence of the optimization process. Although accuracy on the assumptions should be addressed, the results shows that from a concentrated heat source on a single point during fabrication, is not enough to reach Curie temperature of $LiNbO_3$.

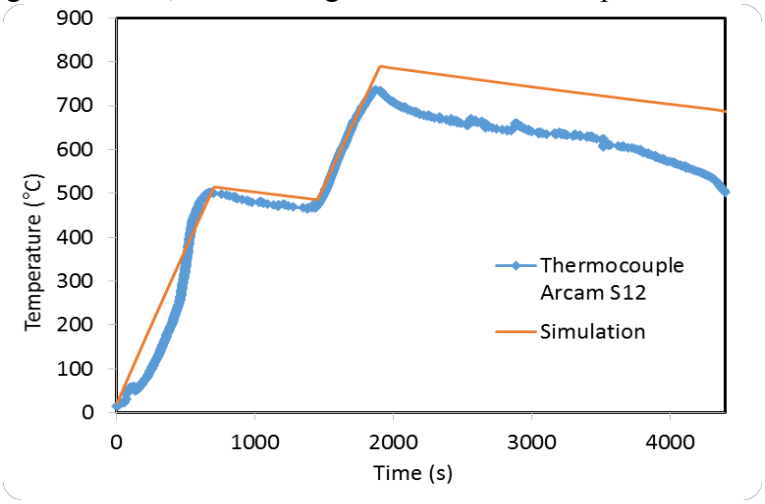

Figure 1: Comparison of temperature between the thermocouple and simulation.

2 Smart Parts Stress/Pressure Sensing Demonstration

The sensor was designed to be built by a layered assembly. The assembly contains six layers of different materials stacked into the cavity of the fabricated base. These materials are alumina (AI203) plates (1st and 5th layer), electrodes built by joining titanium wires (Aldrich GF69168662-1EA) and titanium foils (2nd and 4th layer), a piezoceramic (3rd layer; PZT) element that acts as sensing material for temperature and pressure, and the insert part (6th layer) that closes the cavity that is fabricated with EBM technology. Ideally, the insert part would be pressed fitted into the cavity, but for this demonstration, the edges were reduced for better handling and facilitate corrections during fabrication.

The electrodes and the piezoceramic were cut in smaller sizes hence no contact would

be caused between the walls of the cavity. Electrical insulation of the titanium wires was achieved by using insulation tape. Two sensors with same layered procedure were fabricated and tested for the response under cyclic displacement.

The sensors were tested in a Low-Capacity 8800 Servohydraulic Fatigue Testing Instron machine. Preliminary testing was done to find the relationship between load and displacement, since a displacement control is more stable; this testing determined safe values of parameters for displacement control. The experiments methodology included two modes:

1. Single step displacement control method, cyclic amplitude (compression-compression, compression-release), and different frequencies (0.25 Hz, 0.5 Hz, 1 Hz, 2 Hz, 4Hz, 10Hz) for 10 cycles.
2. Three multi-step displacement control method, cyclic amplitude (compression-compression, compression-release) - decreasing amplitude by half each step, and different frequencies (0.25 Hz, 1 Hz, and 10Hz) with 10 cycles each step.

To record voltage response, an oscilloscope (RIGOL DS1102E) was used. Because of the layered and the testing setup, a predefined stress was needed on the sensor before testing. This stress was defined previously by calculating the mean line of the sinusoidal function of force, thus the peaks fell in the compressive-compressive stress region, and the compressive-release region.

The results obtained from the experiments showed good agreement in the frequency and very low noise for the Instron machine outputs. Contrarily, human error and noise levels were presented in the voltage readings. The shifting caused by the human synchronization of the oscilloscope was reduced by correcting the time axis of the voltage with the first peak of the force output. Additionally, a smooth process was done in the voltage signal using a smooth ratio of 0.005 to preserve true peaks heights and widths.

The analysis is focused on studying the ratio between amplitude of force to voltage. The results showed that the sensitivity of the piezoceramic reduces as the frequency of loading increases. The intensity of the response is attributed to the mass of the piezoceramic, since the peak force deviation is only 5% for both samples. The trend would be explained by an exponential decay, but the discrepancy of the sample 2 at 4 Hz requires further testing to demonstrate the mathematical correlation.

For Multi step method a similar behavior was observed when frequency of the cyclic displacement was increased. The results were processed by tens of cycles. The deviation was reduced, resulting a maximum standard deviation at 0.25 Hz at the 21-30 cycles of 15%.

To further investigate the trend in the results, the samples averages were compared using hypothesis testing. The analysis showed, for each experiment, that each set of 10 cycles were independent of the other two (with at least 95% confidence) except at 0.25 Hz between the first set (1-10) and second set (11-20) with 88% confidence that they were different.

The results showed no clear trend among results. There is an equal increase at 0.25 Hz of sample 1, but at higher frequencies variation occurs to 6%. In contrast, the exception of 7% and the high deviation occurring at the 3rd set of 0.25 Hz of sample 2, impedes a good comparison with sample 1.

Experimental Investigation of Woven Composites as Potential Cryogenic Tank Materials

Md Shariful Islam, Enrique Melendez-Soto and Pavana Prabhakar
Department of Mechanical Engineering, University of Texas, El Paso, TX

1 Introduction

The field of composite materials has gained importance within the study of engineering in the recent years. Developments in material science and the study of novel materials have allowed engineers to consider the use of alternate and less traditional materials in their designs. Composite materials have been known for providing good strength to weight ratios, improved thermal and mechanical properties, and many other desirable aspects which are obtained through the combination of different constituent materials. Among myriad applications for composite materials, their use in cryogenic fuel tanks could result in an increase in the efficiency of the vehicles. In the field of aerospace technology, National Aeronautics and Space Administration (NASA) recently completed a major space technology development milestone by successfully testing a pressurized, large cryogenic propellant tank made of composite material[1].

Cryogenic tanks are devices which are commonly used to store extremely low temperature fluids, usually in their liquid state. This type of tank, generally comprised of different layers of insulators and some type of metal, is exposed to an extremely cold temperature in its interior and to ambient temperature on its external surface. This large temperature gradient across the thickness of the wall results in a thermal phenomenon defined as thermal shock. Thermal shocks occur when high thermal gradients cause a differential expansion and contraction across the tanks walls, resulting in an uneven expansion or contraction of the material. If the stress caused by this differential expansion exceeds the strength of the material at some point, then, cracks will form and propagate in the direction of least resistance. In addition, if the boundaries of the material at the molecular level do not impede crack propagation, this will ultimately cause the tanks structure to fail, resulting in an undesirable leakage [2]. This will consequently lead to the catastrophic fuel tank failure in the case of a rocket or spacecraft being launched into space. Documented research work about the thermal characteristics of hybrid composites at cryogenic temperatures is limited. Hybrid polymeric matrix composites are formed by the use of two or more types of fibers in a polymer matrix. Hybridization enhances the capability of a material to me modified in order to get desired properties in comparison with mono-fiber materials [3]. NASA's Composite Overwrapped Pressure Vessel (COPV) is a well-established cryogenic tank with metallic liner and continuous fiber/matrix system wrapped around it. The overarching goal of the study conducted in this paper is to design cryogenic tanks without the extra metallic lining or insulators, where the cryogenic pressure vessels can sustain cryogenic temperatures and subsequent loading on the tanks. Towards that, the feasibility of using textile composites is investigated in this paper.

2 Experimental Details

The Vacuum Assisted Resin Transfer Molding (VARTM) process is an advanced fabrication process for polymer-matrix composite structures which is used to produce textile composites. For the current study, composites with four layers each of Carbon and Kevlar fabric are manufactured using the VARTM process. Tensile tests on the two types of composites (Carbon and Kevlar

reinforced) were conducted in this section. A total of 16 samples (8 of each types) were prepared for the tensile tests according to ASTM D3039 standard [4]. Tensile tests are simple, relatively inexpensive, and fully standardized. Tensile loading tests frames are utilized to conduct the tensile test of these specimens. During the test, specimens were loaded in the Instron 8801 Servo hydraulic Fatigue Testing System until failure at a loading rate of 1 mm/min. The load-displacement curves were determined for each case, and the corresponding tensile stress-strain responses were calculated using the area of cross-section and the gage length of the extensometer. Four specimens of each type were tested as pristine and the other four were exposed to liquid Nitrogen at a temperature of -196^{0}C for 6 hours and then tested.

3 Results and Discussions

Woven composites with Carbon and Kevlar as stiffeners were investigated in this paper. Prior to trying to combine layers of carbon fiber and Kevlar, these two materials were analyzed separately in order to understand individual mechanical behaviors after cryogenic exposure. Fig. 1 display the tensile stress vs. strain responses, which served to compare samples in both, pristine and cryogenic conditions. From these figures, it is observed that the cryogenic exposure does not have any significant effect on the initial stiffness and ultimate tensile strength for both Carbon and Kevlar fiber laminates.

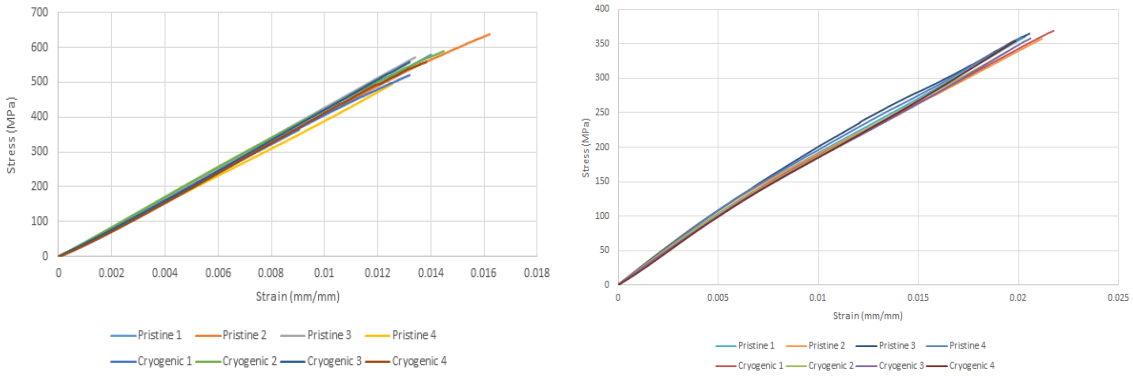

(a) (b)

Fig.1. Tensile response of (a) Carbon fiber and (b) Kevlar fiber composites.

The main characteristic of thermal shock is that a materials structure is damaged due to crack creation or propagation. Carbon fiber and Kevlar samples in, both, pristine and cryogenic conditions were analyzed with the use of Scanning Electron Microscope to observe any crack growth or propagation for both pristine and cryogenic conditions, but as it can be seen from figures 2 and 3, there were no growth or propagation of cracks in either case. Which confirms that after cryogenic exposure, the mechanical properties of laminate does not degrade.

4 Conclusions and Future Work

Within the effort to design a hybrid composite material for its use in cryogenic propellant tanks, the failure of such tanks due to thermal shock was thoroughly investigated. Experimental approaches were followed in order to properly determine the thermo-mechanical properties of Kevlar and Carbon fiber. Properly designing this hybrid material would allow for lighter, stiffer, tougher and damage resistant propellant tanks. The results and studies reported in this paper

demonstrate that woven textile composites materials are definitely candidates to be used in cryogenic propellant tanks.

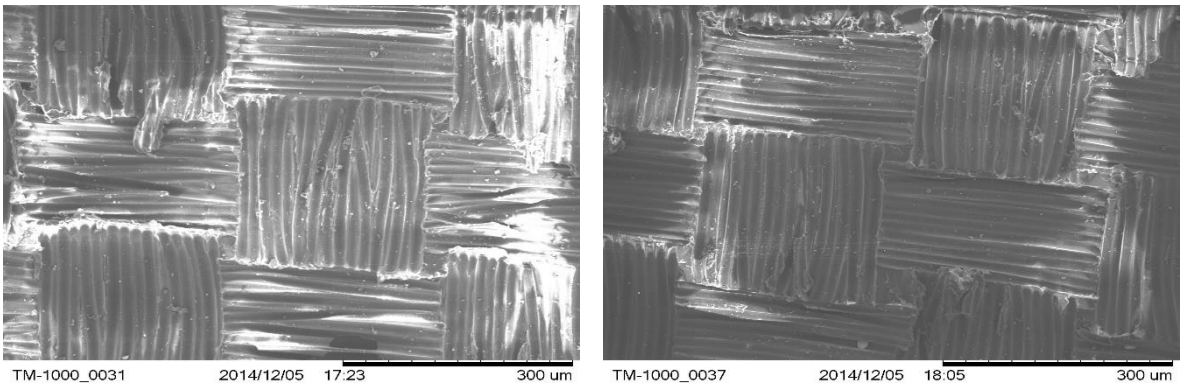

(a) (b)

Fig.2. Scanning Electron Microscope (SEM) Images of Carbon Composite (a) at Room Temperature and (b) after Cryogenic Exposure.

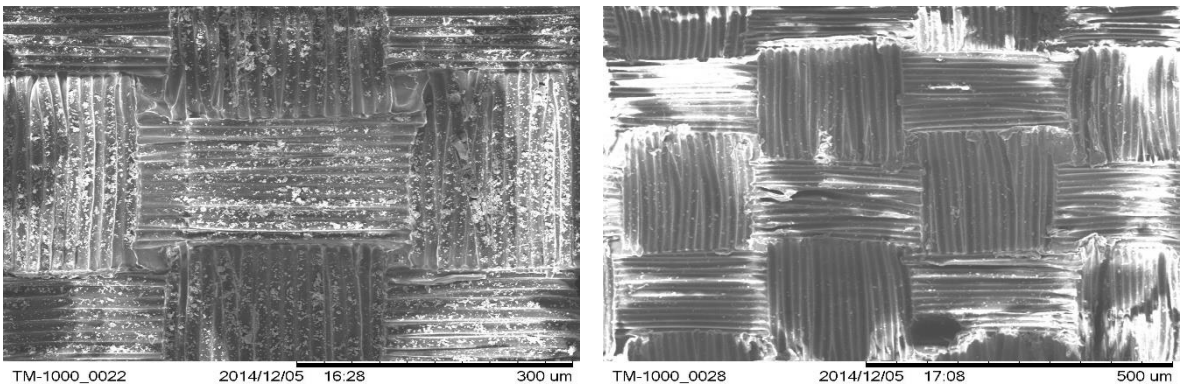

(a) (b)

Fig.3. Scanning Electron Microscope (SEM) Images of Kevlar Composite (a) at Room Temperature and (b) after Cryogenic Exposure.

References

1. Steitz, D.E., Nasa tests game changing composite cryogenic fuel tank. NASA Web., 16 Dec. 2013.

2. Choi, S. and B.V. Sankar, Fracture toughness of transverse cracks in graphite/epoxy laminates at cryogenic conditions. Composites Part B: Engineering, 2007. **38**(2): p. 193-200.
3. Praveen, R., et al., Hybridization of carbon–glass epoxy composites: An approach to achieve low coefficient of thermal expansion at cryogenic temperatures. Cryogenics, 2011. **51**(2): p. 95-104.
4. ASTM Standard. D3039/d3039 m, standard test method for tensile properties of polymer matrix composite and a.i. materials, west conshohocken, pa, 2003, doi: 10.1520/d3039 d3039m-08.

EXPERIMENTAL INVESTIGATION OF THERMAL SHOCK EFFECTS ON CARBON-CARBON COMPOSITES

Alma Leanos[1]*, Pavana Prabhakar[1]
[1] Department of Mechanical Engineering, University of Texas at El Paso, El Paso, TX 79968, USA;
* Corresponding author (alleanosortiz@miners.utep.edu)

Keywords*: Carbon-Carbon Composite, Thermal Shock, Mechanical Properties, Compressive Response, Carbon Degradation*

ABSTRACT

In this paper, both compressive stiffness and oxidation behavior of pristine and thermal shock exposed 2D C/C composite specimens were examined. Pristine test specimens were exposed to thermal shock conditions with temperatures ranging from 400ºC to 1000ºC in an oxidizing environment, followed by compression tests on pristine and thermal shock exposed specimens to obtain their compressive stiffness. The experimental results showed that 2D C/C composite compressive stiffness decreased with increasing thermal shock temperature. Also, upon exposure to thermal shock, the stress-strain response displayed a plasticity type behavior prior to failure as compared to the pristine C/C composite that failed in a brittle manner. Furthermore, it was observed by microstructural analysis that at low temperatures, i.e. 400ºC, the oxidation attack was uniform through the interior of the composite. On the other hand, at high temperatures, i.e. above 400ºC, oxidation occurred rigorously at the surface of the composite, except for test specimens exposed to 1000ºC, which experienced the two aforementioned oxidation mechanisms. Therefore, it was concluded that carbon matrix degraded rapidly when exposed to thermal shock conditions in oxidizing environments and protective coating is required to maintain the quality of the composite under such conditions.

1 Introduction

Carbon fiber reinforced carbon matrix composites retain exceptional thermal and mechanical properties at high temperatures in non-oxidizing environments. However, in oxidizing environments the carbon constituents burn away rapidly under temperatures as low as 450ºC [10]. Zhao et al. [26] demonstrated that oxidation has a strong effect on the C/C composite mechanical properties, nevertheless, limited studies have been conducted to analyze the properties and microstructure of unprotected C/C composites under thermal shock conditions in oxidizing environments ([10] [1]). Similarly, numerous studies have investigated the tensile and flexural strength of C/C composites at high temperatures ([3] [4] [5]), but there is seldom information available about through-thickness compressive properties of 2D C/C composites after being exposed to thermal shock conditions. Therefore, there is a great interest in analyzing the effects of oxidation on the properties and microstructure of C/C composites in order to assure their good performance in high temperature structural applications.

2 C/C Composite Oxidation and Compressive Response

Several previous research efforts have been made to understand the oxidation kinetics of unprotected C/C composites ([11] [2] [7] [6]). Bacos [1] affirms that for 2D C/C composites, carbon matrix degradation prevails during an oxidation process. This author also states that at low temperatures, oxidation damage is distributed uniformly throughout the interior of the

composite and swollen cracks/voids are observed more frequently in the tows. On the other hand, at high temperatures, Bacos [1] declares that only the first layers of the composite are extensively oxidized, while the fiber tows and matrix within the exposed surfaces remain unoxidized. Through-thickness compressive stiffness of fiber reinforced composites has been measured by Lodeiro et al. [9], however, there is seldom information available regarding the failure analysis of 2D C/C composite specimens under compressive loads.

4 Experimental Procedure

In the present work, a 2D woven C/C composite was investigated. The composite plate, having an average thickness of 0.2067 inches, was sectioned into square specimens with sides of 0.5±0.05 inches. Test specimens were heated from room temperature (25±5ºC) to the desired thermal shock temperature at a constant heating rate of 12.5±2ºC/min. Peak temperatures were reached with a tolerance of ±2ºC and the cooling rate ranged from 3±0.5ºC/min for 400ºC cycle to 1.6±0.5ºC/min for 1000ºC cycle. One pristine specimen were exposed to each of the five thermal shock condition (one cycle), with temperatures of 400ºC, 600ºC, 700ºC, 800ºC and 1000ºC, respectively. Then, five pristine specimens were exposed to each of the aforementioned temperatures, but following a three cycle thermal shock condition. Five pristine specimens were subjected to through-thickness compression loading to determine the pristine compressive stiffness. Besides this, compression tests were performed on one test specimen for each thermal shock condition (one cycle) and on five test specimens exposed to each of the three cycles thermal shock condition. Next, the measured compressive properties were compared with those of the pristine specimens.

5 Results and Conclusion

Microstructural examination of the 400ºC test specimens resulted in good agreement with Bacos [1], since the C/C composite showed uniform oxidation attack within the interior of the composite, as shown in Figure 1 (a) for three cycles thermal shock conditions. In this case, oxidation mechanisms as cracks/voids growth and cracks propagation were observed, suggesting that the matrix was more susceptible to degrade than the fibers, as shown by circles in Figure 1 (a). On the other hand, at high thermal shock conditions, i.e. above 400ºC, test specimens degradation was strictly located at the surface and the fiber tows and matrix between the exposed surfaces showed limited oxidation, as shown in Figure 1 (b) for 700ºC thermal shock condition (three cycles). It was observed that by increasing the thermal shock temperature, exposed fibers became more glossy and sharp than the rest of the fibers within a tow, representing oxidized and misaligned fibers along the tow direction, as shown by a rectangle in Figure 1 (b).

The average compressive stiffness of pristine 2D C/C composite specimens were determined to be 1.7±0.14 GPa. Through-thickness stress-strain responses of specimens exposed to one cycle of thermal shock displayed a brittle type of failure, as shown by a dashed line in Figure 2 (a) for a 400ºC thermal shock condition. Likewise, the stress-strain responses obtained for the 400 ºC thermal shock configuration (three cycles) are shown in Figure 2 (a), which illustrates some plasticity in the stress-strain response, observing good agreement between repeated tests. The rest of the stress-strain responses (600ºC, 700ºC, 800ºC and 1000ºC) are not displayed in this paper, however, the compressive stiffness measured for each of these thermal shock conditions (one and three cycles) is summarized in Figure 2 (b). The figure

shows that the compressive stiffness degraded with increasing thermal shock temperatures for one and three cycles. Besides this, it is concluded that the compressive stiffness was lower for three cycle thermal shock conditions as compared to one cycle.

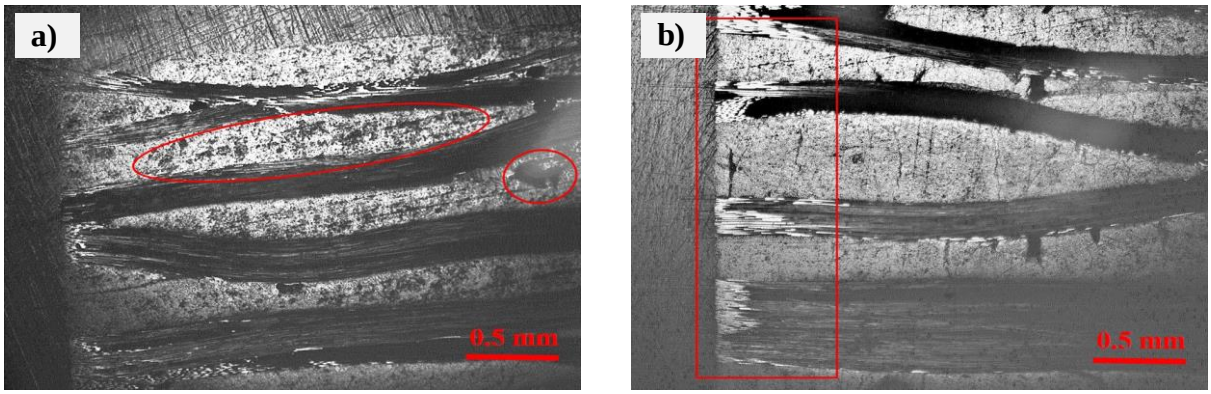

Fig.1. Optical micrograph of (a) 400ºC and (b) 700ºC polished 2D C/C composite test specimens (3 Cycles). Cracks/voids growth is shown by circles and surface oxidation by a rectangle.

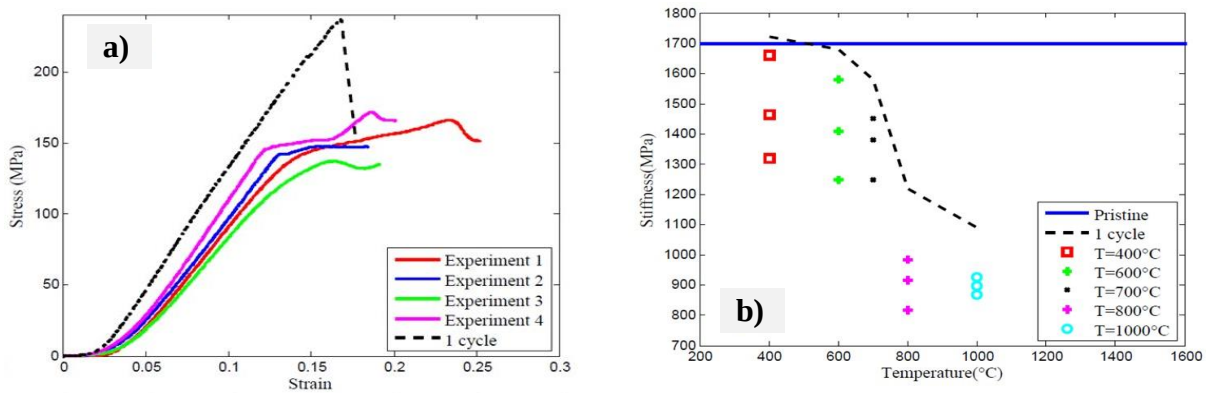

Fig.2. Stress-strain responses of 400ºC thermal shock condition (1 and 3 Cycles) (a); and comparison of compressive stiffness between pristine and exposed test specimens (1 and 3 Cycles) (b).

References

[1] M. Bacos. Carbon-carbon composites, oxidation behavior and coatings protection. Journal de Physique IV, 3(7):1895-1903, 1993.

[2] P. Crocker and B. McEnaney. Oxidation and fracture of a woven 2d carbon-carbon composite. Carbon, 29(7):881-885, 1991.

[3] S.R. Dhakate, T. Aoki, and T. Ogasawara. High temperature tensile properties of 2d cross-ply carbon-carbon composites. Adv Mater Lett, 2:106, 2011.

[4] F. Dillon, K.M. Thomas, and H. Marsh. The influence of matrix microstructure on the mechanical properties of CFRC composites. Carbon, 31(8):1337-1348, 1993.

[5] E. Fitzer and M. Heym. High temperatures-high pressures. pages 10-29, 1978.

[6] W.H. Glime and J.D. Cawley. Oxidation of carbon fibers and films in ceramic matrix composites: A weak link process. Carbon, 33(8):1053-1060, 1995.

[7] J.C. Han, X.D. He, and S.Y. Du. Oxidation and ablation of 3d carbon-carbon composite at up to 3000ºC. Carbon, 33(4):473-478, 1995.

[9] M.J. Lodeiro, W.R. Broughton, and G.D. Sims. Understanding limitations of through thickness test methods. Plastics, Rubber and Composites, 28(9):416-424, 1999.

[10] L.M. Manocha. High performance carbon-carbon composites. Sadhana, 28(1-2):349-358, 2003.

[11] D.W. McKee. Oxidation behavior and protection of carbon/carbon composites. Carbon, 25(4):551-557, 1987.

STIFFENING OF WOVEN COMPOSITES FOR ENHANCING MODE-I INTERLAMINAR FRACTURE TOUGHNESS

A. Castellanos[1], Md S. Islam[1], S. Quevedo[1], M. A. I Shuvo[1], Y. Lin[1], P. Prabhakar[1]*
[1] Mechanical Engineering, The University of Texas at El Paso, El Paso, TX 79968, USA;
* Corresponding author (pprabhakar@utep.edu)

Keywords*: Mode I, ZnO nanowires, Interlaminar fracture toughness, Woven composites, DCB*

ABSTRACT

The objective of this research is to explore the feasibility of using Zinc Oxide nanowires as potential interlaminar stiffeners textile polymer based composites. A comparison between the fracture toughness of a regular carbon fiber composite and a nanowire stiffener composite was performed to evaluate if the ZnO nanowires enhance or decrease the fracture toughness. In this paper, both mode-I and mode-II fracture toughnesses of the interfaces within carbon fiber woven polymer matrix composites are investigated. Different methods have been proposed to calculate the fracture toughnesses experimentally and computationally. The interlaminar mode-I fracture toughness of a woven carbon/epoxy composite was measured using double cantilever beam (DCB) test. Eight woven carbon laminate specimens were tested, where each specimen had 8 layers of dry fabric of carbon fiber. A 0.002 in thick Teflon sheets were inserted in the mid-plane of the composite to simulate a crack. Thickness-reinforcement by ZnO nanowires were added to three specimens. The fracture toughness of the eight specimens were calculated. The value of G_{IC} was compared between the specimens with and without ZnO nanowires. The initiation and propagation of the crack was recorded, and every specimen showed a stable crack growth during the tests. The results showed that the fracture toughness of the specimens with ZnO nanowires increased between 25-50% in comparison to the specimens without ZnO nanowires. Mode-II fracture toughness of the two laminates is currently being pursued to explore the influence of nanowire stiffeners on the interlaminar interfaces of the woven composites.

1 Introduction

Composite materials have become an attractive replacement of conventional materials such as steel or aluminum for high performance structures. The benefits are their tailorable mechanical properties, reliability and fatigue resistance that make them suitable for use in aerospace vehicles, marine structures and automobiles. Fiber-reinforced polymer matrix composites (FRPCs) consist of layers of long fibers reinforced in polymer matrix material. Fibers have superior tensile properties and matrix possess better compressive response, with relatively weaker interfaces between the layers. These interfaces, commonly referred to as interlaminar regions are highly susceptible to damage resulting in premature failure of the composite. Therefore, the interfaces play an important role on the overall strength of the laminate [1] .

The life expectancy of a composite structure requires a clear understanding of the material's response to growth of interlaminar delamination under mode I, mode II and mixed modes. Fracture toughness, which is characteristic of the interface, is related to the amount of energy required to create fracture surfaces [2]. The interlaminar performance is characterized by the susceptibility to fail under both tensile and shear stresses. There are various failure mechanisms that occur in FRPCs subject to complex loading, such as, delamination or interlaminar facture, matrix cracking, matrix-fiber debonding, fiber breaking, fiber pullout, etc.[3] Delamination or interlaminar fracture is one of the predominant mechanisms of damage in composite structures[4] that weakens the composite strength resulting in global failure. The focus of this research is on pure Mode-I interlaminar fracture of textile composites made of carbon woven fabric.

Carbon woven composites are primarily studied in this paper. ZnO nanowires are grown on dry fabric, and the composites are manufactured using Vacuum Assisted Resin Transfer Molding (VARTM) process. The interlaminar Mode-I fracture toughness with and without nanowire stiffening are compared using double cantilever beam (DCB) tests. Significant improvement in Mode-I fracture toughness of the interfaces was observed due to ZnO nanowire stiffening.

2 Determining Fracture Toughness of the Interfaces

DCB test was used to determine the Mode-I interlaminar fracture toughness, which is the critical strain energy release in J/m^2, of continuous fiber-reinforced composite materials. The DCB specimen typically consists of a rectangular uniform thickness laminated composite with a non-adhesive insert on the mid-plane that serves as a delamination initiator [5]. Opening forces are usually applied to the DCB specimen by means of hinges or loading blocks bonded on the top and bottom surfaces at one end of the specimen. The ends of the DCB specimen are opened by controlling either the opening displacement or the crosshead movements, while the load and delamination length are recorded [5]. In the current study, hinges were used for the tests. According to the ASTM Standard D5528-13[5], the dimensions of each specimen were 127 mm (5.0 in) long, 25.4 mm (1.0 in) wide and 2.54 mm (0.1 in) thickness. A Teflon sheet of 50.8 mm (2.0 in) long x 25.4 mm (1.0 in) wide x 0.0508 mm (0.002 in) thickness was inserted to simulate a crack. A pre-crack (about 2 mm) was propagated by pulling the hinges with the Instron machine. Tests were performed on an Instron 8801 at a loading rate of 5 mm/min. Eight specimens were tested in total (4 specimens without ZnO nanowires and 4 with ZnO nanowires). Fig. 1. shows the dimension of the samples used for testing.

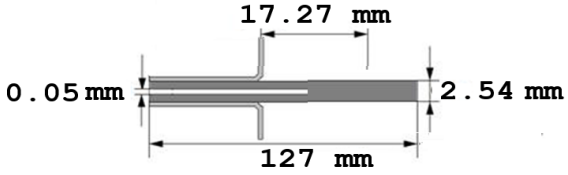

Fig. 1. Sample dimensions for DCB test

3 Results and Discussion

Fig. 2 shows the load-displacement response along with a series of deformed shapes of Test-1 corresponding to the loading history. Point A corresponds to the initial loading point, Point B to the peak force and Point C lies in the softening regime. Point D represents the last point of the curve. It is observed that the crack growth primarily starts at Point B and goes all the way to Point D.

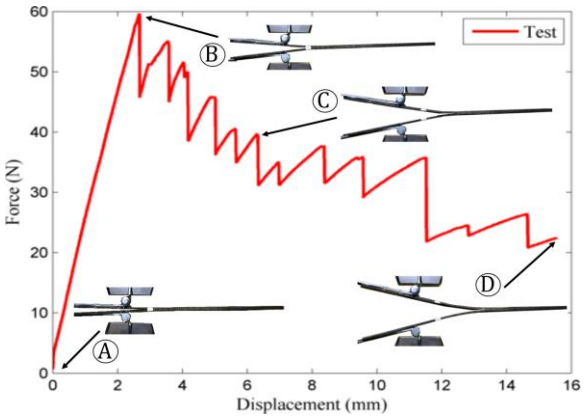

Fig. 2. Load displacement response along with a series of deformed shapes.

The peak force reached by the specimens prior to crack extension for the specimens with ZnO nanowires were approximately 55 N. While the specimens without ZnO nanowires showed a peak force of approximately 60 N. A stable crack growth was observed on both cases. An increase in the fracture toughness was observed by introducing ZnO nanowires. This increase is attributed to the bridging effect of ZnO nanowires at the laminate interfaces by reducing the ease of creating new fracture surfaces.

4 Conclusion

G_{IC} values were calculated with two reduction methods: MBT and MCC. The MBT method showed an increase of approximately 42\% in the fracture toughness when ZnO nanowires were added while the MCC method showed an increase of 44%. Therefore, ZnO nanowires appear to greatly improve the Mode-I interlaminar fracture toughness of carbon woven composites.

References

[1] U. Galan, Y. Lin, G. J. Ehlert and H. Sodano. "Effect of {ZnO} Nanowire Morphology on the Interfacial Strength of Nanowire Coated Carbon Fibers," *Composites Science and Technology*, vol. 71, no. 7, pp. 946-954, 2011.

[2] S. Prasad, C.S. Venkatesha and T. Jayaraju "Experimental Methods of Determining Fracture Toughness of Fiber Reinforced Polymer composites under Various Loading Conditions," *Journal of Minerals \& Materials Characterization & Engineering*, vol. 10, pp. 1263-1275, 2011.

[3] C. K. H. Dharan, "Fracture Mechanics of composite materials.," *Journal of Engineering materials and technology*, vol. 100, pp. 223-247, 1978.

[4] A. Szekrenyes, "Overview on the Experimental Investigations of the Fracture Toughness in Composite Materials," *Journal of Engineering materials and technology*, vol. 100, pp. 1-19, 2011.

[5] A. International, "Standard Test Method for Mode I Interlaminar Fracture Toughness of Unidirectional Fiber-Reinforced Polymer Matrix Composites," *D5528 − 13,* Vols. ASTM International.

Sandwich Core Design for Naval Hull Structures using Additive Manufacturing

S. A. Quevedo, P. Prabhakar Ph. D[1]*
[1] Mechanical Engineering Department, Assistant Professor, El Paso, TX 79968, USA;
* Corresponding author (pprabhakar@utep.edu)

Keywords: *Sandwich structure, Woven composites, Additive manufacturing*

ABSTRACT

Sandwich core designs were analyzed with the intention of studying their mechanical behavior for designing low-weight, high-strength core structures. Normal and shear stress, as well as bending, were the factors endured in the designs. With the use of NX and additive manufacturing, the designs were able to be 3D printed and tested. Carbon fiber reinforced with polymer will be the chosen material for the sandwich outer layers. 3-point bending and impact tests were executed to determine the experimental response of the various designs. In conclusion, optimized designs with least weight and highest stiffness and strength were obtained..

Introduction

Historically, ships have been one of the largest means of transportation and have been used for commercial, recreational or military purposes. One of the most important parts of a ship is the hull that makes the ship float. The design of the hull depends on the intended weight carried by the ship, stability, ship dimensions, speed, power, cost, and ship motion. One of the major concerns in the hull is the effect of the cyclic impact of waves on it. In order to improve the structural efficiency of the ships' hull, the most efficient material and an optimized structural geometry must be used. Until recently, sandwich structures have become a very attractive solution to replace steel and aluminum in the ship's hull. Figure 1 shows the configuration of a sandwich structure. Advantages from sandwich structures to consider include its capability to reach high strength and stiffness while remaining relatively lightweight compared to metals. Composite materials (carbon fiber reinforced in polymer) are used for the skins and the materials that are used for the core are polymers, aluminum or composite [1]. The separation created by the honeycomb core between the carbon fiber skins makes the structure resistant to bending and to buckling loads. This structure is capable of transmitting shear and axial load to and from the core.

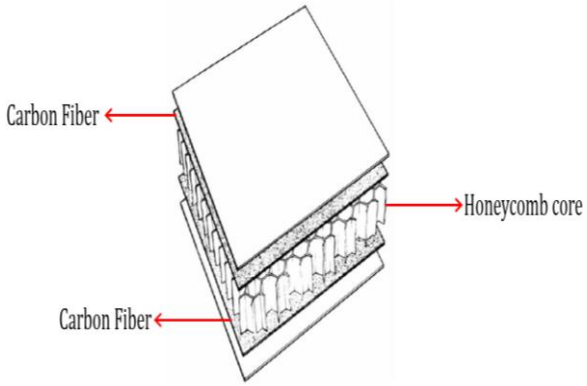

Fig. 1. Sandwich structure configuration

Methodology

Carbon fiber textile composites are typically manufactured using the Vacuum Assisted Resin Transfer Molding (VARTM) process. In this process, composites are made by placing dry fiber reinforced fabrics into a mold, enclosing the mold into a vacuum bag, and drawing it into a vacuum in order to ensure a complete infiltration with resin [3]. In the last stage of the process, the mold is heated until the material is fully cured resulting in a high-quality part.
The current research effort focuses on the design of core of the sandwich structures. Towards that, different structures of sandwich cores were modeled using CAD software (NX 8.5) and fabricated through additive manufacturing. The responses of these cores under different loading conditions were conducted, e.g. tension, compression, and bending. Test results of the different sandwich cores were then compared to select the best core design to be used in the sandwich structure. Static and Impact tests on the sandwich structures will be conducted to determine the behavior of the material, which will aid in designing better sandwich structures for hulls. For example, dynamic impact tests will be conducted on the sandwich structure made up of the textile composites and the core to simulate the impacted force of the sea water.
The 3-Point bending test results on the fabricated core designs were obtained through the usage of the next two formulas:
Calculate the core shear ultimate stress:

$$F_{ult} = P_{max} /(d+c)b \quad (1)$$

Where:

F_{ult} = core shear ultimate stress, MPa [psi],

P_{max} = maximum force prior to failure, N [lb],

d = sandwich thickness, mm [in.],

c = core thickness, mm [in.],

b = sandwich width, mm [in.]

Calculate the facing stress:

$$\sigma = [P_{max} * S] /[2t(d+c)b] \quad (2)$$

Where:

σ = facing stress, MPa [psi]

t = facing thickness, mm [in.]

S = span length, mm [in.]

Computational Design of Core Structure

Figures 2 and 3 demonstrate a design with the purpose to highly resist shear stress. In contrast with figures 4 and 5 which show a design more suited to withstand normal stresses. Additive Manufacturing (AM) enabled the production of the designs. Although the presence of support material inside the material allows the design to be created accurately, the support material is difficult to take off from inside the specimen. The versatility of AM proved to be a quality tool in research. As designs were created on NX, a file format change into a Makebot 3D printer compatible file quickly allowed the design to be printed. Noticeable trends in the failure of the designs in tests, allowed the team to generate higher quality designs that are able to withstand higher amounts of stress while maintaining low weight.

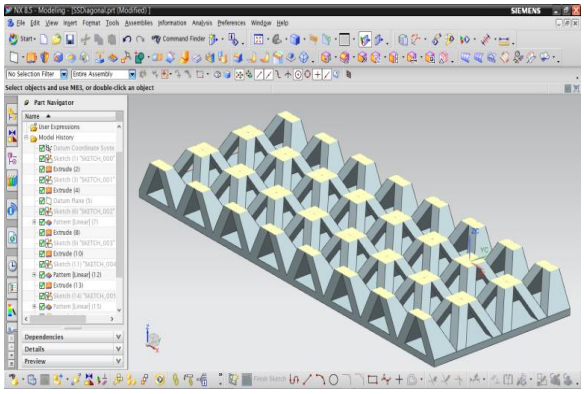

Fig. 2. Diagonal NX truss design

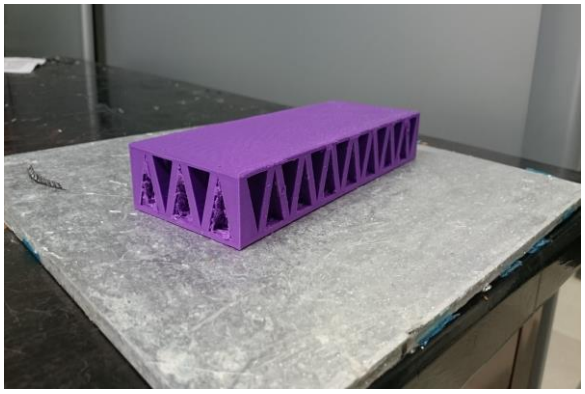

Fig. 3. Diagonal truss design after being 3D printed

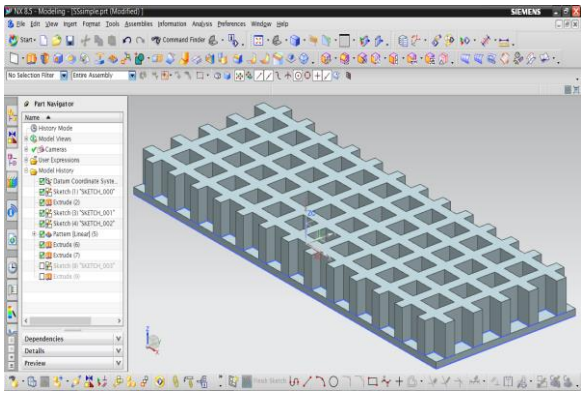

Fig. 4. Normal NX Truss Structure

Fig. 5. Normal NX Truss structure after being 3D printed

References

[1] D'Mello. "*Compression response and energy absorption of filled circular cell honeycombs*." Dissertation. The University of Michigan, 2014.

[2] Lomov, Stephan V., and Ignaas Verpoest. "Textile Composite Materials: Polymer Matrix Composites." *Encyclopedia of Aerospace Engineering*: n. pag. Print. 2010

[3] Chittajallu, Krishna. "Computational Modeling of the Vacuum Assisted Resin Transfer Molding (VARTM) Process." Thesis. Clemson University, Print. 2004

LOW COST SPIN COATING FABRICATION OF EFFICIENT PEROVSKITE THIN FILM LAYERS

Jose Galindo[1], Donato Kava[1], Shaimum Shahbriar[1], Deidra R. Hodges[1]
[1] Electrical Engineering, University of Texas at El Paso, El Paso, TX 79902, USA;

Keywords*: Perovskite thin film solar cells, deposition, spin coating.*

ABSTRACT

Development of fabrication techniques to produce efficient Perovskite absoroption layers via spin coating and deposition techniques. The methyl ammonium lead iodied (CH3NH3PbI3) perovskite was deposited on top of Molybdenum (mo)-caoted glass. Two ways of synthesizing CH3NH3PbI3 were explored. Different parameters will be explored in spin coating the perovskite solution. Thickness, resistance, mobility, concentration type, crystal structure, and fingerprint of each element will be measured. Various instruments will be used to characterize the perovskite absorption layer including: Veeco Dektak 150 Profilometer, Zeiss NEON 40 Scanning Electron Microscope, UV-Vis-NIR Spectrophotometer (Carry 5000), HMS3000 Hall Effect Measurement System (SEM), and a 4 point probe from Lucas Labs. Achieving an efficient perovskite layer, while having simple fabrication methods, is the top concern at this moment.

1 INTRODUCTION

Hybrid organic-inorganic perovskite materials have recently had an increase in attention due to breakthroughs in efficiency of over 15 per cent. [1] Perovskite based solar cells are considered to be a favorable upcoming technology for efficient and economic thin film solar cells due to their ease of fabrication and economical fabrication. [2] This shows that perovskite based absorption layer can be easily manufactured without having a complex nanostructure of the whole solar cell device. Ease of fabrication is the most important aspect of a solar cell when pushing it to be fabricated for wide consumer use.

Fabrication of the perovskite layer was achieved by mixing together two solutions, PbI2 and CH3NH3I, which will result in a solution of CH3NH3PbI3 which will then be spin coated onto soda lime glass (SLG) that will be used as a substrate. Different parameters and methods of spin coated were explored to achieve the best possible properties in the perovskite absorption layer.

The analysis and characterization of the perovskite layer was performed using the Philipps X'Pert X-Ray Diffraction (XRD) and Zeiss NEON 40 Scanning Electron Microscope (SEM) to determine the crystal structure, orientation, and crystal size. The resistance, thickness, mobility, concentration type, and absorption were measured using the Veeco Dektak 150 Profilometer, 4 Point Probe from Lucas Labs, Ecopia Hall Effect Measurement System

HMS300, and Cary 5000 UV-Vis-NIR Spectrophotometer. Raman Spectroscopy identifies the fingerprint for each element.

2 EXPERIMENTAL

The perovskite absorption layer was deposited on Soda Lime Glass (SLG), which were used as substrates. The SLG substrates were cleaned using acetone and rinsed with deionized water. They were then dried with nitrogen (N2). This insured that hydrocarbons and other contaminates were mostly removed. The CH3NH3PbI3 solution was synthesized by mixing together two solvents, PbI2 and CH3NH3I. [1][3] The CH3NH3PbI3 solution was achieved by dissolving PbI2 and CH3NH3I in γ-butyrolactone for 24 hours while stirring. The solution was then spin coated and heated at 100°C with different parameters, in order to determine which one would yield the most efficient perovskite layer. [4]

Another way the perovskite solution was synthesized was by first synthesizing CH3NH3I. It was made by reacting 20-25 mL of methylamine and 10 mL of hydroiodic acid in a 250 mL round-bottom flask at 0°C for 2 hours while stirring. The resulting precipitate was recovered by putting the solution on top of a rotary evaporator and carefully removing it at 50°C. The solution was then dissolved in 80mL of absolute ethanol and precipitate with 300 mL diethyl ether. The solution was then filtered and the process repeated again. The resulting solid was collected and dried at 60°C in a vacuum oven for 24 hours. [5]

After each layer was fabricated, thickness was measured using the Veeco Dektak 150 Profilometer. When the thickness was known, use of the 4-point probe and the Hall Effect measurement system could be used to find various properties needed to determine if the set parameters would yield an efficient absorption layer such as mobility and conductivity.A example of figure format is shown in Fig.1.

2.1 Equations

The optical properties of perovskite thin film layers were analyzed with the Carry 3000 UV-VIS photo spectrometer. The energy band gap can be determined (1).

$$\alpha = A\,(h\upsilon - E_g)^{1/2} \tag{1}$$

3 FUTURE WORK

Future work will include the development of a full solar cell device. The perovskite layer will rest on top of a TiO2 layer, which will rest on Molybdenum (Mo)- coated glass. Other glass options will be explored such as Corning Ultra-slim Willow glass, which will explore flexible solar cell possibilities.

4 ACKKNOLEDGMENTS

This work was supported by: The University of Texas at El Paso (UTEP) School of Engineering, Electrical and Computer Engineering, Electrical and Computer Engineering Department, Chemistry Department, Partnerships Research Education Materials (PREM), the National Science Foundation (NSF), and the Microelectronics Research Center (MRC) at the University of Texas at Austin.

References

[1] J. Burschka, N. Pellet, S. J. Moon, R. Humphry-Baker, P. Gao, M. K. Nazeeruddin, et al., "Sequential deposition as a route to high-performance perovskite-sensitized solar cells," Nature, vol. 499, pp. 316-9, Jul 18 2013A. Green, B. Red and C. Blue "The title of the conference paper". *Proceedings of* C*onference Title*, where it took place, Vol. 1, paper number, pp 1-11, 2004.

[2] K.-C. Wang, P.-S. Shen, M.-H. Li, S. Chen, M.-W. Lin, P. Chen, et al., "Low-Temperature Sputtered Nickel Oxide Compact Thin Film as Effective Electron Blocking Layer for Mesoscopic NiO/CH3NH3PbI3 Perovskite Heterojunction Solar Cells," ACS Applied Materials & Interfaces, vol. 6, pp. 11851-11858, 2014/08/13 2014W. Ke, G. Fang, J. Wang, P. Qin, H. Tao, H. Lei, et al., "Perovskite solar cell with an efficient TiO(2) compact film," ACS Appl Mater Interfaces, vol. 6, pp. 15959-65, Sep 24 2014.

[3] K. Wojciechowski, M. Saliba, T. Leijtens, A. Abate, and H. J. Snaith, "Sub-150 °C processed meso-superstructured perovskite solar cells with enhanced efficiency," Energy & Environmental Science, vol. 7, p. 1142, 2014.

[4] M. Liu, M. B. Johnston, and H. J. Snaith, "Efficient planar heterojunction perovskite solar cells by vapour deposition," Nature, vol. 501, pp. 395-8, Sep 19 2013.

DEVELOPMENT OF NOVEL METHOD TO MANUFACTURE MOCK POLYMER BONDED EXPLOSIVES

C. Catzin[1], C.M. Stewart[1]*
[1] Department of Mechanical Engineering, The University of Texas at El Paso, El Paso, TX 79968, USA;
* Calvin M. Stewart (cmstewart@utep.edu)

Keywords: *Manufacturing, Novel method, Plastic bonded explosives, Mock PBX.*

ABSTRACT

Polymer bonded explosives (PBXs) are composite materials that are typically a mixture of explosive crystals and a polymeric binder. The elastic modulus of the particles, at room and at elevated temperatures is frequently three to four times higher than that of the binder material. Furthermore, the ratio of the explosive component to the binder varies from one material to the next depending on the explosive material specifications; but, typically, the energetic material comprises 80-95% of the mass of the composite. Both experimental and numerical determination of macroscopic properties of these composites is difficult. Such difficulty relies in the heterogeneous nature of the PBX, the issue of obtaining the explosives, the high cost of the crystal explosives, and the safety regulations that need to be enforced while testing the PBX. Mock PBXs provide means of safe and relatively inexpensive experimentation and validation of numerical approaches to determine the mechanical properties of these type of composite materials. This paper will focus on a method to manufacture a Mock PBX.

1. Introduction

Polymer bonded explosives are extensively used by the engineers, specifically in the aerospace industry for solid rocket propellant. Many innovative applications for polymer bonded explosives can be developed, but a lack of research inhibits the innovative applications. The high cost of gathering the constituent materials and the arduous task of following safe handling procedures of explosives are some of the main issues that slow down research. Therefore a precise and well developed method of manufacturing a standard mock PBX specimen that closely resembles the mechanical behavior of PBXs is required in order to safely study the mechanical behavior of PBXs. Few methods of manufacturing Mock PBX have been proposed in literature. Many of the proposed methods lack the high volume fraction of the mock energetic material or details connecting the proper manufacturing process. Contrary to literature in the current study, the manufacturing process will be carefully described to facilitate the repeatable production of mock PBX. The manufacturing process of the mock PBX will closely resemble the one used in industry; specifically in the volume fraction of the mock energetic material to polymer binder. The final product is expected to be a cylindrical shaped specimen of mock PBX (1 inch diameter, 1 inch length) with a heterogeneous arranged volume shown in figure 1[1]. The spheres represent the energetic mock material that are encased in a polymer binder material.

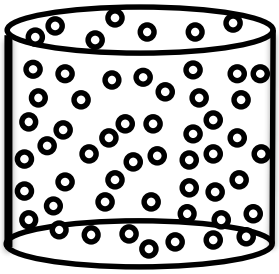

Figure 1. Final specimen sketch

2. Materials

In the explosives industry, many different constituent materials are use in the manufacturing process of the different types of PBX. Due to this diversity, the selection of the constituent materials for a new mock PBX presented was a challenge. Table 1 shows the different energetic materials used in the explosives industry and their respective dimension. Also, it shows the different possible simulants of the energetic mock and their dimensions. From an extensive and

careful literature review, it was determined that the optimal simulant for an energetic particle will be a standard soda lime glass bead because they closely resemble the particle size and have a similar mechanical behavior[2]. Contrary to the energetic material simulant selection, the selection of the matrix or binder material was stochastic. The literature review revealed that the most commonly used binders among industry and academia are estate, fluoropolymers, polyethylene, polyurethane, plasticized polystyrene, among different customized binders. All the previous binders have different properties in terms of thermal stability, lubrication, friction sensitivity, etc., but they share a crucial property essential to this application, good adhesive properties. Therefore, the selection of the binder material was based on their ability to have a strong adhesion. Table 2 shows the different binder material used in the explosive industry for PBX applications and their respective composition with their characteristic adhesive properties. HDPE was selected as the binder because it has excellent adhesion properties and is more accessible and inexpensive when compared to the other excelling binders. Summarizing, the mock polymer bonded explosive will be compose of standard spherical soda lime glass beads contained in a high density polyethylene resin(HDPE) binder.

Table 1. Composition of Energetic Material and common mocks

Energetic Material	**Size (µm)**	**Mock Energetic Material**	**Size (µm)**
TATB (1,3,5-triamino-2,4,6-trinitrobensene)	50-70	Sperical Soda Lime glass beads	200±50
HMX (Octahydro-1,3,5,7-tetranitro-1,3,5,7-tetrazocine)	3, 100,8	Pink Salt	1000 coarse
RDX (cyclotrimethylenetrinitramine)	1.4-124	Sea Salt	2000 coarse
HNS(Hexanitrostilbene)	8.8	Sand	2000 coarse
PETN Pentaerythritol tetranitrate	850 - 44		

Table 2. Common binders for PBXs used in the explosives industry

Matrix Materials	**Matrix composition(wt. %)**	**Energetic Material(wt.%)**	**Adhesive Properties**
Estane 5703	5	95	Good
Fluoropolymer Binders	15	85	Average
Polyisobutylene	5	95	Good
Methyl-methacrylate	5	95	Good
Viton A	5	95	Excellent
Fluorel	5	95	Good
Poly(ester urethane)	8	92	Good
Hydroxyl-terminated polybutadiene (HTPB)	5	95	Good
Polyethylene (HDPE)	10	90	Excellent
Polyurethane	5	95	Good
Plasticized Polystyrene	5	95	Excellent

2.1. HDPE HD 7800P (Binder Material)

The HDPE was obtained from Premier Polymers in pellet form. This specific binder provides an excellent combination of stiffness and crack resistance, besides having excellent adhesive properties. This binder has a melt index of .25 grams per 10 min. Melting temperature around 190 Celsius.

2.2. Glass beads (Energetic Mock)

The glass beads were manufactured by Jaygo Incorporated as a standard soda lime glass with an average diameter of 200 µm ± 50 µm. These glass beats are completely spherical and have a high impact and crush strength.

3. Manufacturing Process

The techniques that are going to be used during the manufacturing process are blending and compression molding, which will provide specimens that are heterogeneous and after simple machining can be used in experimentation to the desired application. The following steps describe

the manufacturing process for a mock PBX [3]. Figure 2 shows a diagram of the manufacturing process of the mock PBX.

- **Blend the constituent materials in a heating mixer.**
  A mixer is going to be used in this manufacturing process to melt and mix the constituent materials to form a heterogeneous dough which later will be compress to the desired shape. It is recommended to start melting the binder material before adding the energetic simulant.
- Add the HDPE into the mixer. (Remember that the quantity of the binder material depends in the chosen binder, the respective composition can be found in table 2.)
- Heat the HDPE until an elastic dough consistency is obtained (Keep in mind the properties of your selected binder material to avoid coating the mixing blades.)
- Proceed to add the soda lime glass beats to the mixture chamber. (Maintain constant temperature.) Allow the sample to mix for 10 minutes in order to ensure a heterogeneous arrangement along the volume.
- **Densify and give shape to the composite using compression molding.** The compression molding can be done using any hydraulic press with heating capabilities. For the purpose of this paper, the compression molding will be done using the Instron 8801, a barrel heater and a customized cylindrical mold.
  - Place the specimen inside the cylindrical mold. Turn on the barrel heater and heat the mold to 190 Celsius for 5 min to allow the heat reach the specimen.
  - Proceed to apply a compressive force to increase the pressure to about 600 psi for 5min to allow the densification and give the desired shape to the specimen.

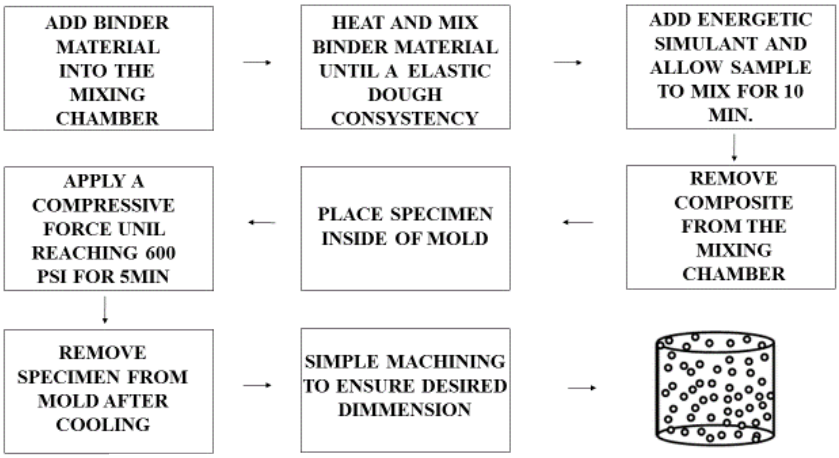

Figure 2. Manufacturing Diagram of a Mock PBX

4. Conclusion

The final product or specimen provides means of safe and relatively inexpensive experimentation and validation of numerical approaches to determine the mechanical properties of plastic bonded explosives. This product can be considered reliable because it contains the high volume fraction of energetic crystal that are so commonly used in industry as well as a widely used binder material.

References

[1] Xu, X., Mares, J., Groven, L. J., Son, S. F., Reifenberger, R. G., and Raman, A., 2015, "Nanoscale Characterization of Mock Explosive Materials Using Advanced Atomic Force Microscopy Methods," Journal of Energetic Materials, **33**(1), pp. 51-65.

[2] Ferranti Jr, L., Gagliardi, F. J., Cunningham, B. J., and Vandersall, K. S., 2010,"Measure of Quasi-Static Toughness and Fracture Parameters for Mock Explosive and Insensitive High Explosive LX-17,"Proceeding of the 14th International Detonation Symposium, Coeur d'Alene, Idaho, pp. 11-16.

[3] Banerjee, B., Cady, C.M., Adams, D.O., 2003,"Micromechanics simulations of glass-estane mock polymer bonded explosives,' Modelling and Simulation in Materials Science and Engineering, **11**(4), pp. 457–475.

SPIN COATING THIN FILM CZTS FOR EFFICIENT, LOW-COST SOLAR CELLS

Donato Kava, Shaimum Shahbriar, Jose Galindo, and Deidra R. Hodges
Electrical Engineering, University of Texas at El Paso, El Paso, TX 79902, USA;

Keywords*: CZTS Thin films, spin coating, and photovoltaic cells.*

ABSTRACT

The development of Cu2ZnSnS4 (CZTS) thin film solar cell using non-vacuum ,liquid-based spin coating techniques have been previously investigated. The focus of this paper is optimization of CZTS thin film solar cell created using a non-vacuum spin coater (WS650 spin processor, Laurell Technologies) using a ink sol–gel method to deposit thin films onto soda lime glass (SLG). Characterization and analysis of the thin films were performed using Raman spectroscopy, Scanning Election Microscope (Zeiss NEON 40), X-ray diffraction (Philipps X'Pert), proflimeter (Veeco Dektak 150), UV-Vis-NIR Spectrophotometer (Carry 5000), Hall Effect measurement system (HMS3000) and 4 point probe (Lucas Labs) measurements. Ultimately the goal is to create a record efficiency cell using earth abundant non-toxic elements leading to low cost solar cells.

1 INTRODUCTION

Research in thin film solar cells continues to make substantial progress towards developing not only an economically viable and high-efficiency photovoltaic (PV) devices but CZTS allows for a solar cell that is environmentally non-toxic. If Earth abundant element thin film solar cells can be developed with equal or better efficiency to CIGS or CdTe, they will likely be the long-term solution of choice for low-cost terawatt scale PV[1]. Besides the issue of abundance, the heavy metal cadmium has experienced resistance towards adoption in some countries because of the toxicity issue[2].

The first CZTS solar cell was constructed from a heterostructure with cadmium tin oxide, yielding an open circuit voltage of 165 mV under AM1.5 illumination (no efficiency reported)[2]. Work on this technology has since improved. Previously reported by Katagiri et al. CZTS thin films prepared from thermally evaporated elements and binary chalcogenides in high vacuum, have resulted in a solar cell with a conversion efficiency of 6.7% after a preferential etching in deionized water (DIW) [3]. Using vacuum raises costs for large scale manufacturing, thus making spin coating CZTS efficiencies economically viable. Additionally as of today a 12.6% efficiency was reported by Wang et al. using a hydrazine-based CZTSe approach[4]. As hydrazine is toxic, handling procedures make large scale manufacturing a problem. Using methoxyethanol as a solvent can solve this problem.

Multiple physical manufacturing procedures have been studied. Optimized spin speed have been reported to be 3000 rpm [5]. Reported CZTS layers have shown optimize grain structures when annealed at 550° C resulting in densely packed grains with a few large 1 micron grains [6].

The microstructure of the films is mainly determined by the substrate temperature, the lattice match of the compound, the substrate properties, the growth process direction, and the growth rate and pressure during deposition of the films[6]. By optimizing these properties CZTS thin films have been produced using non-vacuum liquid-based spin coating procedures.

2 EXPERIMENTAL

This work builds off on prior established procedures known to yield optimized results. Soda Lime glass (SLG) is to be used as a substrate. SLG are to be cleaned with acetone and deionized water rinses and dried with nitrogen (N2), to remove hydrocarbons and other contaminates, prior to the film deposition. Film preparation begins with a CZTS precursor created by mixing copper (II) acetate monohydrate, zinc (II) acetate dehydrate, and tin (II) chloride dehydrate of 4.375 x 10-2, 2.1875 x 10-2 and 2.1875 x 10-2 mol, respectively, in a 50 ml solvent of 2-methoxyethanol. Sulfur precipitated power is to be added as the sulfur source at 8.75 x 10-2 mol. 5ml of monethanolamine is added and used as a stabilizer. The solution is stirred and heated at 45° C for 1 hour to dissolve metal sources. The solution is deposited on SLG substrates using a spin coating technique. The film is dried in air at 300° C for 15 minutes on a hot plate. This process is repeated 4 additional times and results in 5 layers of coated and dried films. After the fifth layer is complete the samples are to be annealed varying the temperature from 400°C to 600°C.
The created thin films are characterized by X-ray diffraction (XRD), scanning electron microscope (SEM), Raman spectroscopy, transmission and absorption spectroscopy, 4 point probe, Hall effect measurements, and Dektak profilometer.

3 RESULTS AND DISCUSSION

Based on the work Hergert and others [6-8], Cu_2ZnSnS_4 can be formed rapidly in a one step reaction from three binary chalcogenide compounds (1):

$$Cu_2S + ZnS + SnS_2 \rightarrow Cu_2ZnSnS_4 \quad (1)$$

or in two successive reactions with Cu_2SnS_3 as an intermediate production (2) and (3):

$$Cu_{2-x}S + SnS_2 \rightarrow Cu_2SnS_3 \quad (2)$$

$$Cu_2SnS_3 + ZnS \rightarrow Cu_2ZnSnS_4 \quad (3)$$

3.1 Structural Properties

The thin films structural properties were analyzed. Problems investigated include poor grain formation, delamination due to volume expansion (formation of metal sulfides from metals), and formation of binary compounds [1]. Because of the direct band gap (and corresponding high absorption coefficient of ~10^4 – 10^5 cm^{-1}), material utilization can be reduced, with 1–2 µm layer thickness generally being enough to absorb most of the incident solar radiation[2]. XRD and Raman spectroscopy was used for investigation of CZTS thin films. A prolifimeter was used to measure the thickness of the thin films. A 4 point probe for resistivity of the film, a hall was used for conductivity and mobility.

X-ray diffraction was used in the determination of a single phase kesterite CZTS thin films. Due to overlapping peaks, Raman spectroscopy measurements were made in the CZTS thin films.

3.2 Morphological Properties

The morphology of CZTS thin films is important to producing large, densely packed and uniform grains [3]. To obtain larger CZTSSe grains, most fabrication procedures require high temperature annealing in a sulfur or selenium atmosphere[9].

3.3 Optical Properties

The optical properties of the CZTS thin film layer were analyzed using the Carry 3000 UV-VIS photo spectrometer. Using the transmittance data from the absorption spectra, the energy band gap can be determined (4):

$$\alpha = \mathrm{A}\left(h\upsilon - \mathrm{E_g}\right)^{1/2} \qquad (4)$$

where α is the absorption coefficient, A is a constant, E_g is the energy band gap and *hv* is the incident photon energy[6, 10].

4 ACKNOWLEDGEMENTS

This work was supported by The University of Texas at El Paso (UTEP) School of Engineering, Electrical and computer engineering, Microelectronics Research Center (MRC) at The University of Texas at Austin, the National Science Foundation (NSF) National Nanotechnology Infrastructure Network (NNIN), and Partnerships Research Education Materials (PREM).

References

[1] W. Ki and H. W. Hillhouse, "Earth-Abundant Element Photovoltaics Directly from Soluble Precursors with High Yield Using a Non-Toxic Solvent," *Advanced Energy Materials*, vol. 1, pp. 732-735, 2011.

[2] D. B. Mitzi, O. Gunawan, T. K. Todorov, K. Wang, and S. Guha, "The path towards a high-performance solution-processed kesterite solar cell," *Solar Energy Materials and Solar Cells*, vol. 95, pp. 1421-1436, 6// 2011.

[3] K. Hironori, J. Kazuo, Y. Satoru, K. Tsuyoshi, M. Win Shwe, F. Tatsuo, *et al.*, "Enhanced Conversion Efficiencies of Cu 2 ZnSnS 4 -Based Thin Film Solar Cells by Using Preferential Etching Technique," *Applied Physics Express*, vol. 1, p. 041201, 2008.

[4] W. Wang, M. T. Winkler, O. Gunawan, T. Gokmen, T. K. Todorov, Y. Zhu, *et al.*, "Device Characteristics of CZTSSe Thin-Film Solar Cells with 12.6% Efficiency," *Advanced Energy Materials*, vol. 4, pp. n/a-n/a, 2014.

[5] Y. Yue, G. Jie, T. Prabhakar, and Y. Yanfa, "Effects of Spin Speed on the Properties of Spin-coated Cu_2ZnSnS_4 Thin Films and Solar Cells Based on DMSO Solution," in *Photovoltaic Specialist Conference (PVSC), 2014 IEEE 40th*, 2014, pp. 0448-0451.

[6] B. J. Deidra Hodges, Toussaint Moseley, Aaron Love, Caleb Burke, Edward Jones, Irina Tyx, Manoj Chaulogain, and Ophelia Johnson, "Development of CZTS Thin Films by Non-vacuum, Liquid-based Techniques for Efficient, Low-cost CZTS Solar Cells," *IEEE Transactions on Device and Materials Reliability* vol. 13, p. 4, 2013.

[7] F. Hergert and R. Hock, "Predicted formation reactions for the solid-state syntheses of the semiconductor materials Cu2SnX3 and Cu2ZnSnX4 (X," *Thin Solid Films*, vol. 515, pp. 5953-5956, 2007.

[8] T. B. Massalski, J. L. Murray, L. H. Bennett, and H. Baker, *Binary Alloy Phase Diagrams*. Metals Park: American Society for Metals, 1986.

[9] C.-J. Hsu, H.-S. Duan, W. Yang, H. Zhou, and Y. Yang, "Benign Solutions and Innovative Sequential Annealing Processes for High Performance Cu2ZnSn(Se,S)4 Photovoltaics," *Advanced Energy Materials*, vol. 4, pp. n/a-n/a, 2014.

[10] M. Snure and A. Tiwari, "$CuBO_2$: A p-type transparent oxide," *Applied Physics Letters*, vol. 91, pp. 092123-092123-3, 2007.

Optical Properties of Cu_2ZnSnS_4 (CZTS) Thin Films Deposited by Non-vacuum Liquid-based Techniques

Cheik Sana, Shaimum Shahriar, Donato Kava, Jose Galindo, and Deidra Hodges

University of Texas at El Paso, El Paso, TX 79968, USA

Keywords*: CZTS thin films, optical properties, bandgap energy*

ABSTRACT

Cu2ZnSnS4 has been considered a material of choice for an absorber layer in thin film solar cells due to its large absorption coefficient of over 104 cm-1 in the visible range, its optimal optical band gap of ~1.5 eV, the earth abundance and eco-friendliness of its constituents. CZTS polycrystalline thin films were prepared by a non-vacuum liquid-based coating method. Optical characterization and band gap analysis of thin films were performed by transmission using Cary 5000 UV-Vis spectrophotometer, DXR SmartRaman spectrometer and Dektak 150 surface profilometer. Results show the photon energy bandgap decreases as the annealing temperature increase, the bandgap energy also decrease as the annealing time increases.

1 Introduction

Prominent thin-film photovoltaic (PV) solar cells such as Cu(In,Ga)Se2 and CdTe have attracted a lot of attention because of their respective power conversion efficiency over 20.1%[1] and 20.9% [2] in laboratory conditions . However, these thin film solar cells are made of chalcogenides and other materials that are both scarce in the earth's crust (In and Ga) [3, 4] and toxic (Cd and Se) [3]. It is therefore imperative to synthetize new materials for solar cells that could compensate for the current limitations. The materials for CZTS are low cost, abundant in the crust of earth, environmental friendly and suitable to be applied for thin film solar cell absorber layer.

CZTS is one of the most promising absorber layer semiconductor materials that could make the technology competitive. CZTS has a suitable optical band gap of ~1.5 eV and a large optical absorption coefficient of over 104 cm-1 in visible wavelength region for photovoltaic application [5, 6]. These optical characteristics can yield a theoretical power conversion efficiency of 30% according to Shockley-Queisser theory [7].

There are two main approaches to synthetize CZTS, specifically vacuum based processes and non-vacuum solution based processes [8]. The vacuum based processes include RF magnetron sputtering, thermal evaporation, pulsed laser deposition, electron beam evaporation and the non-vacuum processes include spray pyrolysis, photochemical deposition, sol-gel method, spin-coating method and electrodeposition. The non-vacuum solution processes are considered the low cost route for fabricating solar cells [5].

The optical characteristics of CZTS depend on the processing conditions and deposition parameters. Crystal growth and thin film techniques are carried out at high temperatures. It is important for the determination of the stoichiometry of the compounds to control the vapor

pressure of the components at these temperatures. The microstructure of the films is mainly determined by the substrate temperature, the lattice match of the compound, the substrate properties, the growth process direction, and the growth rate and pressure during deposition of the films. In this paper, we present the results of a non-vacuum spin coating deposition of CZTS thin films. CZTS was prepared in a two-step reaction of Cu2S, ZnS and SnS. The optical properties were studied by transmission, and absorbance in the visible wavelength.

2 EXPERIMENTAL

2.1 Preparation of CZTS solution

In this study, film preparation began with the preparation of CZTS precursors by mixing of the metal sources copper (II) acetate monohydrate, zinc (II) acetate dehydrate, and tin (II) chloride dehydrate of 4.375 x 10-2, 2.1875 x 10-2 and 2.1875 x 10-2 mol, respectively, in a 50 ml solvent of 2-methoxyethanol. Sulfur precipitated powder was added as the sulfur source at 8.75 x 10-2 mol. Monethanolamine was used as a stabilizer and 5 ml was added to the solution. The solution was stirred and heated at 45°C for 1 hour to dissolve metal sources.

2.2 Preparation of CZTS solution

Soda lime glass (SLG) was used as substrates. SLG substrates were cleaned with acetone and deionized water rinses, and dried with nitrogen (N2), to remove hydrocarbons and other contaminants, prior to the film deposition. The solution was deposited on SLG substrates by spin coating. The film was dried in air at 300°C for 15 minutes on a hot plate. This process was repeated 4 additional times resulting in a total of 5 layers of coated and dried films. After the fifth layer, samples were annealed varying the temperature from 400°C to 600°C.

2.3 Characterization

Thin films were characterized by Raman spectroscopy, surface profilometry, transmission and absorption spectrophotometry. DXR SmartRaman was used to analyze the molecular structure and perform phase analysis of the thin films. Veeco Dektak 150 was used to analyze the surface profile of the films. Cary 5000 UV-Vis spectrophotometer wavescans in the range of 200 nm to 1200 nm was used to analyze the optical properties including the energy band gap, transmission and absorption of the samples.

3 RESULTS

Based on the work Herbert others [9], Cu_2ZnSnS_4 was prepared in a two-step reaction from three binary chalcogenide compounds:

$$Cu_2S + ZnS + SnS_2 \rightarrow Cu_2ZnSnS_4 \qquad (1)$$

Important dependencies in the formation of stoichiometric kesterite CZTS in these reactions include annealing temperature and time. Higher annealing temperatures improve the crystallinity of the CZTS thin films, but affect the formation of stoichiometric kesterite CZTS due to the volatility of Zn, Sn and sulfur at the higher temperatures [3, 10].

Bandgap analysis

The optical properties of the CZTS thin films were analyzed using Cary UV-VIS optical transmission spectroscopy measurements and Scanning electron microscopy at room temperature. The optical absorption coefficient(α) was determined from the measured transmittance (T) using the formula

$$\alpha = A\left(h\upsilon - E_g\right)^{1/2} \qquad [11]$$

where α is the absorption coefficient, A is a constant, Eg is the energy band gap and hν is the incident photon energy [11].Below are the plots of (αhν)2 as a function of incident photon energy for CZTS thin films. The estimated direct optical band gap were obtained by extrapolation of the (αhν)2 versus hν plot at α=0.

Fig. 1 show the absorption coefficient spectrum of the sample annealed at 490°C, for 30 minutes, 60 minutes and 90 minutes with respective bandgap energy 1.65 eV, 1.50 eV and 1.47 eV. Fig. 2 show the absorption coefficient spectrum of the sample annealed at 500°C, for 30 minutes, 60 minutes and 90 minutes, 1.6 eV, 1.45 eV and 1.42 eV. Fig. 3 show the absorption coefficient spectrum of the sample annealed at 510°C, for 30 minutes, 60 minutes and 90 minutes, 1.52 eV, 1.45 eV and 1.40 eV. It can be observed that the bandgap energy decreases as the temperature increases. This is consistent with observations made by Hodges [12] and Emrani [13].

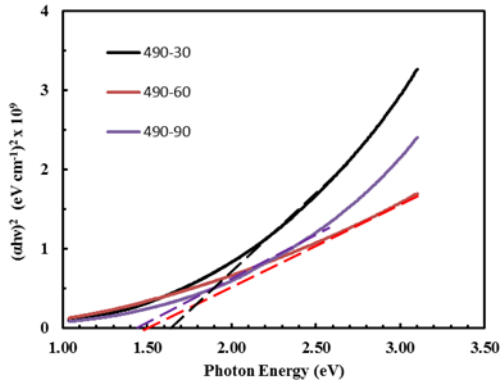

Fig. 1. Absorption coefficient spectrum of sample annealed at 490°C.

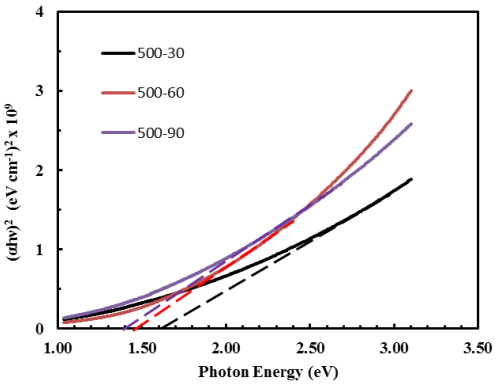

Fig. 2. Absorption coefficient spectrum of sample annealed at 500°C.

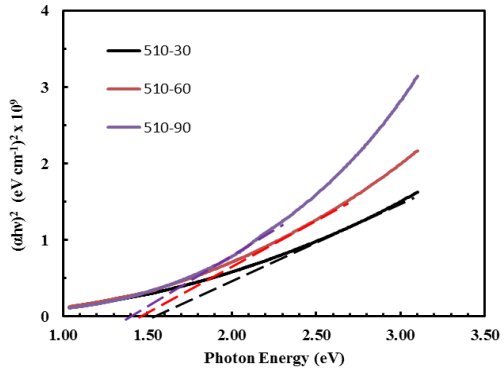

Fig. 3. Absorption coefficient spectrum of sample annealed at 510°C.

Fig. 4 show the absorption coefficient spectrum of the sample annealed for 30 minutes, at 490°C, 500°C and 510°C. Fig. 5 show the absorption coefficient spectrum of the sample annealed for 60 minutes, at 490°C, 500°C and 510°C. Fig. 6 show the absorption coefficient spectrum of the sample annealed for 90 minutes, at 490°C, 500°C and 510°C. It can be observed that the photon band gap energy decreases as the annealing time increases

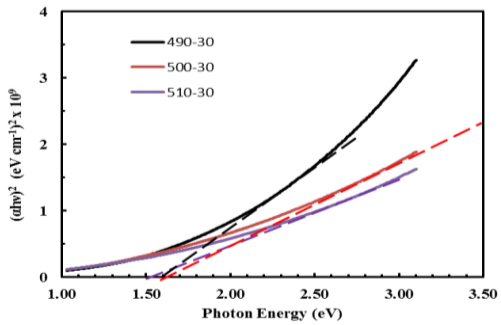

Fig. 4. Absorption coefficient spectrum of sample annealed for 30 minutes.

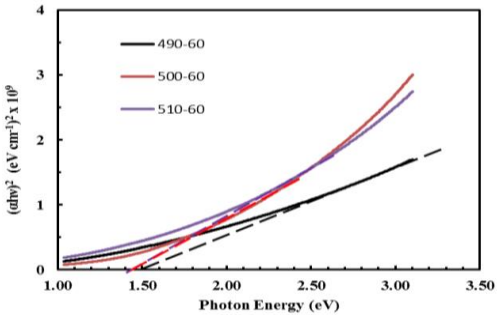

Fig. 6. Absorption coefficient spectrum of sample annealed for 60 minutes.

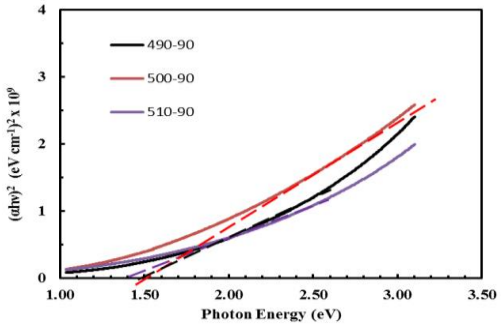

Fig. 6. Absorption coefficient spectrum of sample annealed for 90 minutes.

4 CONCLUSION

A low cost approach for the development of CZTS thin films using a liquid-based, non-vacuum technique has been demonstrated. The sample have been annealed at 490°C, 500°C and 510°C for 30, 60 and 90 minutes. It has been shown that there is an inverse correlation between the bandgap energy and both the annealing temperature and the annealing time. The annealing times and temperatures values for this process that yield the optimum bandgap of ~1.5 eV are 500°C and 30 minutes, 500°C and 60 min, 490°C and 60 min.

ACKNOWLEDGEMENTS

This work was supported by The University of Texas at El Paso (UTEP) School of Engineering, Microelectronics Research Center (MRC) at The University of Texas at Austin and the NSF National Nanotechnology Infrastructure Network (NNIN).

References

1. Jackson, P., et al., *New world record efficiency for Cu(In,Ga)Se2 thin-film solar cells beyond 20%.* Progress in Photovoltaics: Research and Applications, 2011. **19**(7): p. 894-897.
2. Green, M.A., et al., *Solar cell efficiency tables (version 44).* Progress in Photovoltaics: Research and Applications, 2014. **22**(7): p. 701-710.
3. Jimbo, K., et al., *Cu2ZnSnS4-type thin film solar cells using abundant materials.* Thin Solid Films, 2007. **515**(15): p. 5997-5999.
4. Tanaka, K., et al., *Cu2ZnSnS4Cu2ZnSnS4 thin film solar cells prepared by non-vacuum processing.* Solar Energy Materials and Solar Cells, 2009. **93**(5): p. 583-587.
5. Ennaoui, A., et al., *Cu2ZnSnS4 thin film solar cells from electroplated precursors: Novel low-cost perspective.* Thin Solid Films, 2009. **517**(7): p. 2511-2514.
6. Ito, K. and T. Nakazawa, *Electrical and Optical Properties of Stannite-Type Quaternary Semiconductor Thin Films.* Jpn. J. Appl. Phys., 1988. **27**.
7. Shockley, W. and H.J. Queisser, *Detailed Balance Limit of Efficiency of p-n Junction Solar Cells.* Journal of Applied Physics, 1961. **32**(3): p. 510.
8. Mitzi, D.B., et al., *The path towards a high-performance solution-processed kesterite solar cell.* Solar Energy Materials and Solar Cells, 2011. **95**(6): p. 1421-1436.
9. Hergert, F. and R. Hock, *Predicted formation reactions for the solid-state syntheses of the semiconductor materials Cu2SnX3 and Cu2ZnSnX4 (X.* Thin Solid Films, 2007. **515**(15): p. 5953-5956.
10. Weber, A., R. Mainz, and H.W. Schock, *On the Sn loss from thin films of the material system Cu-Zn-S-S in high vacuum.* J. Appl. Phys., 2010. **107**(1): p. 6.
11. Weber, A., et al., *In-situ XRD on formation reactions of Cu2ZnSnS4 thin films.* Phys. Status Solidi C, 2009. **6**(5): p. 1245-1248.
12. Hodges, D., et al. *Development of CZTS thin films by non-vacuum, liquid-based techniques for efficient, low-cost CZTS solar cells*. in *Photovoltaic Specialists Conference (PVSC), 2013 IEEE 39th*. 2013.
13. Emrani, A., P. Vasekar, and C.R. Westgate, *Effects of sulfurization temperature on CZTS thin film solar cell performances.* Solar Energy, 2013. **98**: p. 335-340.

REACTION MECHANISMS IN MIXTURES OF LUNAR AND MARTIAN REGOLITH SIMULANTS WITH MAGNESIUM

A. Delgado[1], S. Cordova[1], E. Shafirovich[1]*
[1] Department of Mechanical Engineering, The University of Texas at El Paso, El Paso, TX 79968, USA;
* Corresponding author (eshafirovich2@utep.edu)

Keywords: *Combustion synthesis, Thermites, Differential scanning calorimetry*

ABSTRACT

Previous research has shown that lunar and Martian regolith simulants form thermite mixtures with magnesium, combustion of which produces ceramics that could be used as construction materials on the Moon and Mars. The present paper focuses on the mechanisms of reactions that occur during combustion of these mixtures.

1 Introduction

In-situ resource utilization (ISRU), i.e., the use of lunar and planetary resources for the production of oxygen, propellants, and other materials is an attractive concept for future space exploration missions. Previous research has shown that lunar and Martian regolith simulants form thermite mixtures with magnesium. Once these mixtures are ignited, they exhibit a self-sustained combustion that leads to the formation of ceramic products that could be used as construction materials on the Moon and Mars[1-3]. The present work focused on the mechanisms of reactions that occur during combustion of these mixtures. This was achieved using differential scanning calorimetry and X-ray diffraction analysis.

2 Experimental

JSC-1A lunar regolith simulant and two Martian regolith simulants (JSC-Mars-1A and Mars Mojave) were studied in the present research. These powders were milled in a planetary ball mill as described elsewhere [2] and then mixed with magnesium powder (−325 mesh, 99.8% pure, Sigma-Aldrich) at different mixture ratios in a three-dimensional inversion kinematics tumbler mixer (Bioengineering Inversina 2L).

Thermal analysis of mixtures was conducted using a differential scanning calorimeter (Netzsch DSC 404 F1 Pegasus). The mixture samples placed in alumina crucibles were heated in an argon flow (20 mL/min) at heating rates of 5 °C/min or 10 °C/min, depending on the test. In some tests, the heating process was terminated at different temperatures and the condensed products were cooled in argon for subsequent XRD analysis (Bruker D8 Discover XRD).

3 Results

Figure 1 shows the DSC curve obtained for the mixture of 26 wt% Mg and 74 wt% JSC-1A at a heating rate of 10°C/min. The curve has a distinct exothermic peak at 560°C, which indicates that the reaction occurs at temperatures below the melting point of magnesium (650°C).

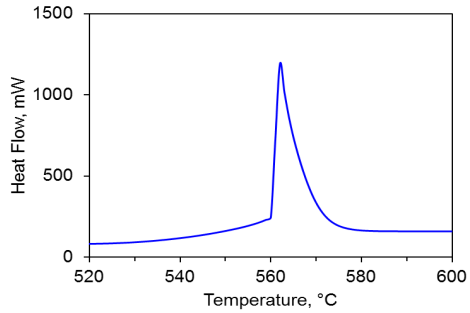

Fig. 1. DTA curve for 74 wt% JSC-1A/26 wt% Mg.

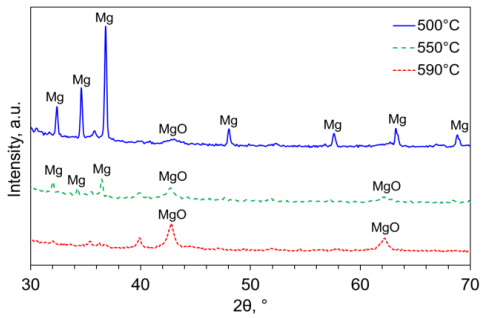

Fig. 2. XRD patterns of 74 wt% JSC-1A/26 wt% Mg.

To further investigate this reaction, the heating process, conducted at 5°C/min, was stopped at 500°C, 550°C, and 590°C. XRD of the obtained products (Fig. 2) revealed that there was no MgO at 500 °C, while all Mg was converted to MgO at 590°C. At 550°C, a partial conversion of Mg to MgO was observed. These results confirm that the reaction between JSC-1A and Mg occurs when Mg is still solid.

Mixtures of JSC-1A, JSC-Mars-1A, and Mojave Mars simulants with 26 wt% Mg were heated to 650°C at a heating rate of 10 °C/min. Figure 3 shows the DSC curves for these mixtures. It is seen that the temperature of the peak is the highest for the mixture based on JSC-Mars-1A and the lowest for the mixture based on Mojave Mars. The concentrations of silica and iron oxide in the composition of each simulant (Table 1) explain the order of the peaks. It is seen that the order of the DSC peaks in Fig. 3 correlates with the SiO_2–Fe_2O_3 ratio: an increase in this ratio decreases the temperature of the peak.

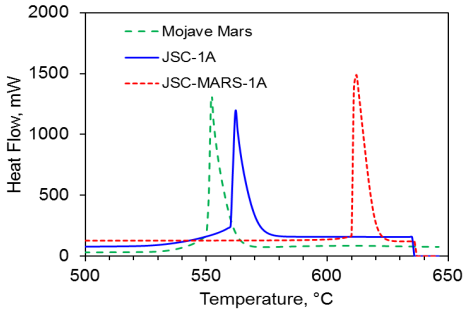

Fig. 3. DSC curves for mixtures of JSC-1A, JSC-Mars-1A, and Mojave Mars simulants with Mg.

Table 1. SiO_2 and Fe_2O_3 concentration in regolith simulants

Compound	Concentration, wt%		
	JSC-1A[4]	JSC-Mars-1A[5]	Mojave Mars[5]
SiO_2	45.7	43.48	49.4
Fe_2O_3	12.4	16.08	10.87

DSC tests with binary Fe_2O_3/Mg and SiO_2/Mg mixtures were conducted under the same conditions. Figure 4 shows that the peak in the mixture based on iron oxide is at about the same temperature as for the mixture based on JSC-Mars-1A (higher iron oxide concentration), while the peak in the mixture based on silica is at a lower temperature than for mixtures with two other simulants. This implies that iron oxide plays a dominant role in the reaction between JSC-Mars-1A and Mg, while for two other regolith simulants the increased concentration of silica decreases the temperature of the reaction.

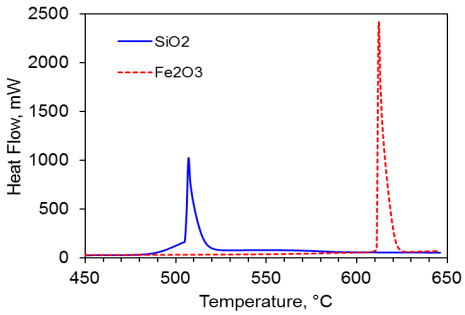

Fig. 4. DSC curves for Fe_2O_3/Mg and SiO_2/Mg mixtures.

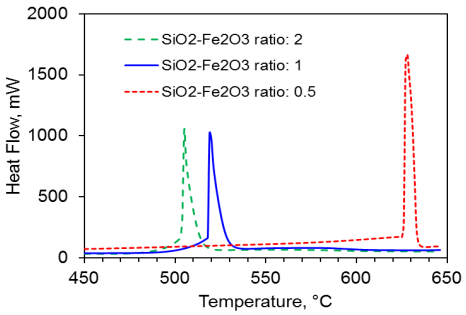

Fig. 5. DSC curves for SiO_2/Fe_2O_3/Mg mixtures with SiO_2–Fe_2O_3 mass ratios of 2, 1, and 0.5.

DSC tests were conducted with ternary SiO_2/Fe_2O_3/Mg mixtures to verify this conclusion. Three ternary mixtures had different SiO_2–Fe_2O_3 mass ratios (2, 1, and 0.5), while the concentration of Mg was determined to simultaneously provide stoichiometry for both reactions. Figure 5 shows DSC curves obtained for the three mixtures. It is seen that the temperature order of the peaks correlates with the SiO_2–Fe_2O_3 mass ratio. This confirms the conclusion that iron oxide plays a primary role in combustion of iron-rich JSC-Mars-1A simulant with Mg, while the effect of silica is significant in combustion of iron-lean JSC-1A and Mojave Mars simulants.

4 Conclusions

Thermoanalytical studies have shown that iron oxide plays a dominant role in the combustion of JSC-Mars-1A simulant with magnesium. For Mojave Mars material and JSC-1A lunar regolith simulant, which include more silica and less iron oxide, silica exhibits a significant effect on the combustion, promoting reactions at lower temperatures.

5 Acknowledgements

This research was supported by the NASA Office of Education (Group 5 University Research Centers). The differential scanning calorimeter was acquired owing to support by the U.S. Department of Defense (Grant No. W911NF-14-1-0034; Grant Officer's Representative: Dr. Ralph A. Anthenien of the Army Research Office; Co-GOR: Dr. Clifford D. Bedford of the Office of Naval Research).

6 References

[1] C. White, F. Alvarez, and E. Shafirovich, "Combustible mixtures of lunar regolith with metals: Thermodynamic Analysis and Combustion Experiments," *Journal of Thermophysics and Heat Transfer*, Vol. 25, 2011, pp. 620-625.

[2] F. Álvarez, C. White, A.K. Narayana Swamy, and E. Shafirovich, "Combustion wave propagation in mixtures of JSC-1A lunar regolith simulant with magnesium," *Proceedings of the Combustion Institute*, Vol. 34, 2013, pp. 2245–2252.

[3] A. Delgado, and E. Shafirovich, "Towards better combustion of lunar regolith with magnesium," *Combustion and Flame*, Vol. 160, 2013, pp. 1876-1882.

[4] C.S. Ray, S.T. Reis, S. Sen, and J.S. O'Dell, "JSC-1A Lunar Soil Simulant: Characterization, Glass Formation, and Selected Glass Properties," *Journal of Non–Crystalline Solids,* Vol. 356, 2010, pp. 2369–2374.

[5] G.H. Peters, W. Abbey, G.H. Bearman, G.S. Mungas, J.A. Smith, R.C. Anderson, S. Douglas, and L.W. Beegle, "Mojave Mars simulant—Characterization of a new geologic Mars analog," *Icarus,* Vol. 197, 2008, pp. 470–479.

FABRICATION OF MAGNESIUM SILICIDE VIA MECHANICALLY ACTIVATED SHS FOLLOWED BY SHOCKWAVE CONSOLIDATION

S. Cordova[1], A. Delgado[1], D. Nemir[2], E. Shafirovich[1]*
[1]Department of Mechanical Engineering, The University of Texas at El Paso, El Paso, TX 79968
[2]TXL Group Inc., 2000 Wyoming Ave., El Paso, TX 79903
*Corresponding Author (eshafirovich2@utep.edu)

Keywords: Combustion synthesis, Mechanical activation, Shockwave consolidation, Thermoelectric materials

1 Introduction

Harvesting energy from exhaust gases would have a tremendous impact on the economy and the environment. The materials based on magnesium silicide (Mg_2Si) are promising for high-temperature thermoelectric conversion as they could be used at 300–600°C [1].

Mg_2Si-based compounds are typically synthesized on a small scale via melt synthesis or casting. Scaling up these methods is problematic due to the high vapor pressure and reactivity of Mg, which can lead to the loss of Mg and poor control over stoichiometry [2]. Mechanical alloying has been considered, but this method requires long milling times, leading to contamination from the milling media [3]. One promising alternative is self-propagating high-temperature synthesis (SHS), also called combustion synthesis and recognized as a cost-effective, efficient, and clean method for the production of advanced materials [4]. Unfortunately, it is difficult to ignite Mg/Si mixture because the reaction between Mg and Si is not very exothermic. Also, materials fabricated by SHS have a low density and high porosity.

The problems caused by the low exothermicity can be overcome using the so-called mechanically activated SHS (MASHS) [5]. The method adds a short-duration, high-energy ball milling step before the combustion.

To yield a useful thermoelectric material, SHS products must be densified. This can be done using shockwave consolidation, where densification and interparticle bonding occur so quickly that grain growth can be suppressed and the material retains its nano- or amorphous structure [6].

The objective of the present paper is to explore the feasibility of fabricating dense Mg_2Si by MASHS followed by shockwave consolidation.

2 Experimental

Magnesium and silicon powders were mixed in the stoichiometric proportion, milled in a planetary ball mill (Fritsch Pulverisette 7 Premium Line), and cold-pressed into 8-g cylindrical pellets with a 3-g Ti/B booster pellet at the top using a uniaxial hydraulic press at a force of 30 kN. The combustion synthesis was conducted inside a windowed stainless steel chamber, filled with argon at 1 atm pressure. The pellet was ignited at the top with a tungsten coil.

For shockwave consolidation experiment, Mg_2Si powder was compacted into a steel tube in an argon-filled glovebox. The tube was sealed and placed coaxially within a larger-diameter "explosive" tube, which was then filled with ammonium nitrate fuel oil (ANFO), an explosive material (Fig. 1). A third, "confinement" tube of a larger diameter was installed coaxially and the gap between the explosive and confinement tubes was filled with sand. A detonator at the top was used to initiate the explosion which applied a symmetrical high-pressure pulse that moved inward and down the inner tube, causing the tube to deform and the interior powders to consolidate into a dense, well bonded bulk material.

Fig.1. Shockwave consolidation setup.

After consolidation, thermal diffusivity and specific heat of the densified products were investigated using a laser flash apparatus (Netzsch LFA 457 MicroFlash).

3 Results and Discussion

Thirteen combustion experiments with mechanically activated Mg/Si mixtures were conducted. In each experiment, a steady propagation of the combustion front was observed. Figure 2 shows images of the reaction propagation over mechanically activated Mg/Si mixture. The first image shows a heated tungsten coil and the second image shows combustion of the booster pellet. The reaction propagation over the pellet is seen on images 4 – 8 (36 s – 40 s). It is seen that the surface of the pellet remains rather dark and the reaction manifests itself through the twofold increase in the volume of the material. The obtained product was very porous and fragile.

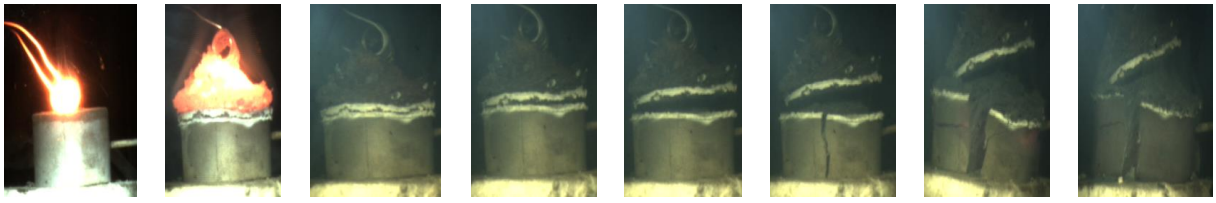

Fig. 2. Self-sustained propagation of the reaction wave over mechanically activated Mg/Si mixture.

One shockwave consolidation experiment was performed with commercial Mg_2Si powder and two experiments were conducted with the Mg_2Si powder produced by MASHS. The commercial Mg_2Si

was compacted to a density of 1.75 g/cm^3, which is 88% of the theoretical density (1.99 g/cm^3). Figure 3 shows the thermal conductivity of the shockwave-consolidated commercial Mg_2Si sample, which was calculated using the thermal diffusivity and the specific heat, both determined by laser flash analysis in the temperature range from 50°C to 225°C. The obtained values of the thermal conductivity are lower than those reported for hot-pressed Mg_2Si [7], which may be associated with insufficient densification in the test.

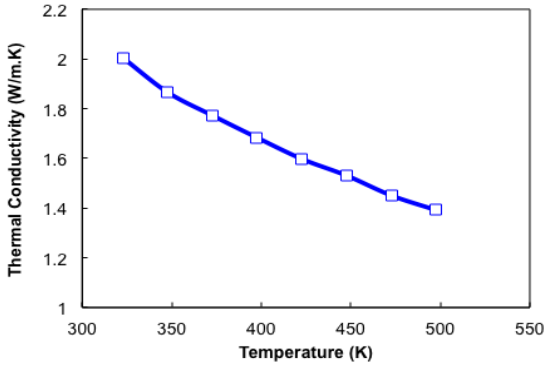

Fig. 3. Thermal conductivity of a shockwave-consolidated Mg_2Si sample vs. temperature.

4 Conclusions

Magnesium silicide has been fabricated from magnesium and silicon powders via mechanically activated self-propagating high-temperature synthesis (MASHS). The obtained powder was densified using shockwave consolidation.

5 References

[1] S.K. Bux, J.P. Fleurial, R.B. Kaner, "Nanostrucured materials for thermoelectric applications," *Chemical Communications*. 46 (2010) 8311–8324.

[2] S.K. Bux, M.T. Yeung, E.S. Toberer, G.J. Snyder, R.B. Kaner, J.P. Fleurial, "Mechanochemical synthesis and thermoelectric properties of high quality magnesium silicide," *Journal of Material Chemistry* 21 (2011) 12259–12266.

[3] X. Niu, L. Lu, "Formation of magnesium silicide by mechanical alloying," *Advanced Performance Materials* 4 (1997) 275–283.

[4] K. Morsi, "The diversity of combustion synthesis processing: a review," *Journal of Materials Science* 47 (2012) 68–92.

[5] M.S. Alam, E. Shafirovich, "Mechanically activated combustion synthesis of molybdenum silicides and borosilicides for ultrahigh-temperature structural applications" *Proceedings of the Combustion Institute* 35 (2015) 2275–2281.

[6] R.A. Pruemmer, T. Balakrishna Bhat, K. Siva Kumar, K. Hokamoto, *"Explosive Compaction of Powders and Composites,"* Science Publishers, Enfield, NH, 2006.

[7] Q.S. Meng, W.H. Fan, R.X. Chen, Z.A. Munir, "Thermoelectric properties of Sc- and Y-doped Mg_2Si prepared by field-activated and pressure-assisted reactive sintering," *Journal of Alloys and Compounds* 509 (2011) 7922–7926.

MECHANICALLY ACTIVATED SHS OF MOLYBDENUM BOROSILICIDES FOR ULTRAHIGH-TEMPERATURE STRUCTURAL APPLICATIONS

A. Esparza[1], E. Shafirovich[1]*
[1]Department of Mechanical Engineering, The University of Texas at El Paso, El Paso, TX 79968, USA;
*Corresponding author (eshafirovich2@utep.edu)

Keywords*: Combustion synthesis, SHS, Mechanical activation*

ABSTRACT

The thermal efficiency of gas-turbine power plants could be dramatically increased by the development of new structural materials based on molybdenum silicides. A major challenge, however, is to simultaneously achieve high oxidation resistance and acceptable mechanical properties at high temperatures. The addition of boron to Mo-rich silicides improves their oxidation resistance through the formation of a borosilicate surface layer. In particular, Mo_5SiB_2 (called T_2) phase and alloys based on this phase are promising materials that offer favorable combinations of high temperature mechanical properties and oxidation resistance. In the present paper, alloys of T_2 phase with Mo_3Si, Mo, and TiB_2 have been obtained using mechanically activated self-propagating high-temperature synthesis (MASHS). Self-sustained combustion of Mo/Si/B mixtures for the formation of Mo_5SiB_2–TiB_2 materials became possible because of adding more exothermic reactions of Mo and Ti with B. The "chemical oven" technique was used to fabricate α-Mo/Mo_5SiB_2/Mo_3Si (Mo-12Si-8.5B) materials.

1 Introduction

The thermal efficiency of gas-turbine power plants could be increased by the development of new structural materials based on molybdenum silicides and borosilicides[1-3]. A promising approach focuses on adding boron to Mo-rich silicides[3]. The addition of boron improves oxidation resistance because of the formation of a borosilicate surface layer[1]. This has promoted interest in fabricating Mo_5SiB_2 (called T_2) phase. Boron addition, however, makes silicides brittle. One way to toughen these mixtures is to add molybdenum phase. A three-phase α-Mo/Mo_5SiB_2/Mo_3Si (Mo-12Si-8.5B) this material is considered as an attractive option[2, 3]. Another method for improving the mechanical properties of Mo_5SiB_2 materials involves the addition of titanium carbide (TiC). It has been shown that this improves the compression strength of Mo-Si-B material at high temperatures[4]. However, the properties of titanium diboride (TiB_2) are even better than those of TiC with a melting point of 3230 °C and elastic modulus equal to 534 GPa at 1000 °C. Thus, the addition of TiB_2 to T_2 phase is worth of investigation. It would be attractive to use self-propagating high-temperature synthesis (SHS) for the fabrication of T_2 phase based alloys. A major problem, however, is low exothermicities of mixtures for producing these materials through combustion reactions, but those problems can be mitigated with the so-called mechanically activated SHS (MASHS)[5]. Sometimes, the use of mechanical activation is insufficient for ignition. Such mixtures can be used for SHS if

either external heat is applied or their exothermicity is increased by adding more energetic components. One method for providing external heat is the so-called "chemical oven," where the sample is surrounded by a layer of a highly exothermic mixture. Recently, this method has been successfully employed for fabrication of a single T_2 phase[6]. The objectives of the present paper are to investigate the feasibility of using MASHS for the fabrication of materials based on Mo_5SiB_2 phase, including α-Mo/Mo_5SiB_2/Mo_3Si (Mo-12Si-8.5B) and Mo_5SiB_2/TiB_2 materials.

2 Experimental

To enable reactions in Mo-12Si-8.5B mixtures, the "chemical oven" technique was used. The pellets consisted of Mo-12Si-8.5B mixture core inside a shell made of Ti/B (1:2 mole ratio) mixture. The combustion was performed in a 30-L stainless steel reaction chamber and the chamber was evacuated and filled with ultrahigh purity argon at 1 atm. The composite pellet was heated by a tungsten wire connected to a DC power supply. To fabricate Mo_5SiB_2/TiB_2 materials, four compositions were tested. Different amounts (10 wt%, 20 wt%, 30 wt%, and 40 wt%) of stoichiometric Ti-B (1:2 mole ratio) mixture were added to Mo-Si-B (5:1:2 mole ratio) mixture. The resulting mixture was compressed into cylindrical pellets (diameter: 13 mm, height: 12-15 mm). Ti/B (1:2 mole ratio) mixture was used as a booster pellet, which was ignited by a tungsten wire. The as-milled powders and combustion products were analyzed using X-ray diffraction (Bruker D8 Discover XRD).

3 Results and Discussion

3.1 Synthesis and characterization of α-Mo/Mo_5SiB_2/Mo_3Si (Mo-12Si-8.5B) materials

The chemical oven experiments for fabrication of Mo−12Si−8.5B alloy produced the expected phases**.** The density was 7 – 7.6 g/cm^3. XRD analysis of the combustion products has shown (Fig. 1) that each sample consisted of the desired three phases α-Mo, Mo_5SiB_2, and Mo_3Si, with no other phases. Analysis of the obtained XRD patterns shows that Mo has the highest peaks. Considering the highest peak for each phase, Mo : Mo_3Si : Mo_5SiB_2 intensity ratio is 6.84 : 2.23 : 1. Note that in the desired Mo-12Si-8.5B material, Mo : Mo_3Si : Mo_5SiB_2 mole ratio is 8.23 : 4.51 : 1. Thus, the results of XRD analysis indicate that the desired sequence of phase contents has been obtained.

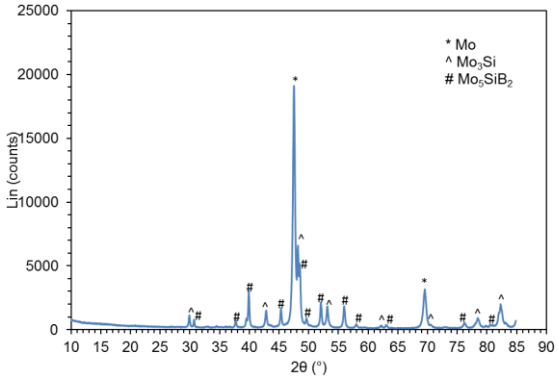

Fig.1. XRD pattern of products obtained by combustion of Mo-12Si-8.5B mixture.

3.2 Synthesis and characterization of Mo_5SiB_2/TiB_2 materials

Combustion of Mo/B/Si/Ti mixtures occurred in the spin combustion regime and was accompanied by cracking. XRD analysis has shown that the best product was obtained for the mixture with 40 wt% Ti/B. Figure 2 shows the XRD pattern for the products obtained by combustion of this mixture. It is seen that along with desired Mo_5SiB_2 and TiB_2 phases, there are also $MoSi_2$, Mo_3Si, and Mo_5Si_3. A decrease in the concentration of Ti/B in the initial mixture from 40 to 30 wt% led to the appearance of TiB in the mixture. Further decrease resulted in the appearance of Mo.

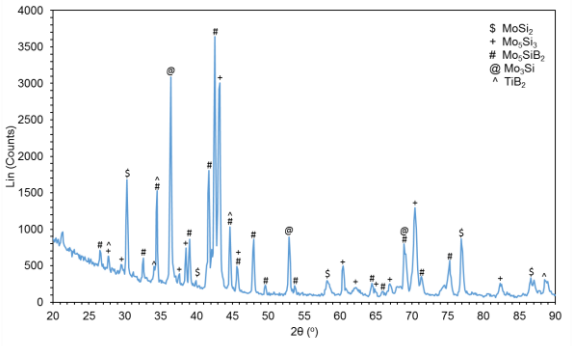

Fig.2. XRD pattern of products obtained by combustion of Mo-Si-B-Ti mixture designed for 60% Mo_5SiB_2 and 40% TiB_2.

4 Conclusions

Materials based on Mo_5SiB_2 phase have been obtained by mechanically activated SHS. Self-sustained combustion of Mo/Si/B mixtures for the formation of Mo_5SiB_2 phase materials became possible when the composition was designed for adding reactions that lead to the formation of TiB_2. The products, however, contained several Mo-Si-B phases and not only the desired Mo_5SiB_2, and TiB_2. The chemical oven technique has enabled fabrication of α-$Mo/Mo_5SiB_2/Mo_3Si$ (Mo-12Si-8.5B) alloys, which are considered as promising materials for ultrahigh-temperature structural applications.

5 Acknowledgement

This research was supported by the U.S. Department of Energy (Grant DE-FE-0008470) and Climax Molybdenum, Inc.

6 References

[1] J.H. Perepezko, Science 326 (2009) 1068–1069.
[2] J.H. Perepezko, R. Sakidja, K.S. Kumar, in: W. Soboyejo (Ed.), Advanced Structural Materials: Properties, Design Optimization, and Applications, CRC Press, Boca Raton, FL, 2007, p. 437.
[3] J.A. Lember, R.O. Ritchie, Adv. Mater. 24 (2012) 3445–3480.
[4] S. Miyamoto, K. Yoshimi, S.-H. Ha, T. Kaneko, J. Nakamura, T. Sato, K. Maruyama, R. Tu, T. Goto, Metall. Mater. Trans. A 45A (2014) 1112−1123.
[5] C. Gras, E. Gaffet, F. Bernard, Intermetallics 14 (2006) 521–529.
[6] E.A. Levashov, Yu.S. Pogozhev, A.Yu. Potanin, N.A.Kochetov, D.Yu. Kovalev, N.V. Shvyndina, T.A. Sviridova, Ceram. Int. 40 (2014) 6541–6552

THERMITE MIXTURES FOR RAPID GENERATION OF IODINE

S.E. Guerrero[1], E.L. Dreizin[2], E. Shafirovich[1]*

[1]Department of Mechanical Engineering, The University of Texas at El Paso, El Paso, TX 79968
[2]Department of Chemical, Biological, and Pharmaceutical Engineering, New Jersey Institute of Technology, Newark, NJ 07102
*Corresponding Author (eshafirovich2@utep.edu)

Keywords: Combustion, Reactive materials, Thermites, Laser ignition

ABSTRACT

Halogen-containing reactive materials could be used for mitigating the spread of hazardous biological microorganisms aerosolized as a result of explosion. In the present work, mechanically alloyed Al·I_2 powder was mixed with oxides of iron, bismuth, and copper. Combustion of the obtained thermite mixtures was studied using laser ignition. The experiments were conducted in air, in a sealed chamber designed to enable laser ignition and collection of condensed products for chemical analysis. Mixtures of mechanically alloyed Al·I_2 powder with Bi_2O_3 and Fe_2O_3 did not exhibit rapid ignition and steady combustion, while its mixtures with CuO readily ignited and burned rapidly and steadily, similarly to Al/CuO mixtures.

1 Introduction

Halogen-containing reactive materials could be used for mitigating the spread of hazardous biological microorganisms aerosolized as a result of explosion. Different methods of incorporating halogens in reactive materials have been considered. Recently, reactive compositions including halogen-containing thermites have been explored [1-3]. The tested mixtures included metal powders and halogen-containing oxides such as I_2O_5 and $AgIO_3$. These compositions are typically very easy to ignite so that their handling and storage may be challenging. The approach explored in this research effort involves incorporating halogens into metal fuel, which then can be mixed with metal oxides, leading to the formation of combustible (thermite) mixtures. Specifically, mechanically alloyed Al·I_2 powder, recently developed at NJIT [4-6], was studied in the present work. The objectives were to prepare mixtures of mechanically alloyed Al·I_2 powder with Fe_2O_3, Bi_2O_3, and CuO, and investigate their combustion in comparison with mixtures of conventional Al powder with the same oxides.

2 Experimental Procedure

Mechanically alloyed Al·I_2 (20 wt% I_2) powder was fabricated by ball milling at the liquid nitrogen temperature. Details are given in [6]. Commercial Al powder (97.5% pure, spherical, 3.0-4.5 μm, Alfa Aesar) was used in experiments conducted for comparison. Bi_2O_3 (99.9% pure, 80-200 nm, Alfa Aesar), CuO (>99.0% pure, Alfa Aesar), and Fe_2O_3 (>99% pure, <5 μm, Sigma Aldrich) were used for the preparation of thermite mixtures with Al and Al·I_2 powders. Both Al and Al·I_2 powders were mixed with the oxides according to the stoichiometries of Al-oxide reactions, i.e., I_2 was assumed to be an inert additive (this is based on thermodynamic calculations). Wet (with hexane) mixing was accomplished using an acoustic mixer (Resodyne LabRAM). The mixing was conducted with an intensity of 40% for 2 min. After removing hexane in a vacuum chamber, a

fine, uniformly mixed powder was compressed into pellets (diameter 6 mm, length 5-20 mm) using a uniaxial hydraulic press (the pressing force 14.7 kN).

The experiments were conducted in a laser ignition facility, recently used for studies on combustion of mixtures for generation of oxygen [7] and hydrogen [8]. In the present work, experiments were conducted in air, in a sealed 0.5-L chamber (inner diameter 70 mm, length 160 mm, Fig. 1) designed to enable laser ignition and collection of condensed products for chemical analysis. The chamber is equipped with two window ports, which can be easily removed for installation of the pellet and collection of solid products. A ZnSe window is use for introducing the laser beam. This window is installed at the top end of a vertical tube, the purpose of which is to remove the window from high-temperature products released during combustion.

Fig. 1. Chamber for combustion of iodine-generating mixtures.

A brass sample holder with a pellet was placed inside the chamber directly under the ZnSe window and the window ports were bolted onto the chamber. An infrared beam (diameter: 2.0 ± 0.3 mm) of a CO_2 laser (Synrad Firestar ti-60) was introduced into the chamber vertically and directed to the top of the sample. A laser diode pointer (Synrad) was used for alignment. The power of the beam after passing the beam delivery system and ZnSe window was measured with a powermeter (Synrad PW-250) and controlled using a laser controller (Synrad UC-2000), while the duration of the laser pulse was controlled using LabVIEW (National Instruments) software. The combustion of each pellet was recorded with a high-speed video camera (Vision Research Phantom v1210). After the combustion process, the chamber was let to cool off for about 15 min.

3 Results and Discussion

Experiments with Al/Bi_2O_3, Al/Fe_2O_3, and Al/CuO mixtures, conducted for comparison with iodine-generating thermites, have shown stable and rapid combustion in all tests (Fig. 2). In contrast, combustion of thermites based on mechanically alloyed Al·I_2 powder was strongly dependent on the oxidizer. The pellets consisting of Al·I_2/Bi_2O_3 mixture did not ignite. Laser heating led to light emission and ejection of some material (Fig. 3a), which stopped immediately after the end of the laser pulse. Laser heating of Al·I_2/Fe_2O_3 pellets was accompanied by the ejection of relatively large fragments from the top end of the pellet. The ignition did occur (Fig. 3b), but the combustion front propagated much slower than in the case of Al/Fe_2O_3 mixture

and it was accompanied by the formation of a large bubble. In contrast with $Al{\cdot}I_2/Bi_2O_3$ and $Al{\cdot}I_2/Fe_2O_3$ mixtures, rapid and steady combustion of $Al{\cdot}I_2$/CuO pellets was observed (Fig. 3c), resembling that of Al/CuO mixture (Fig. 2c).

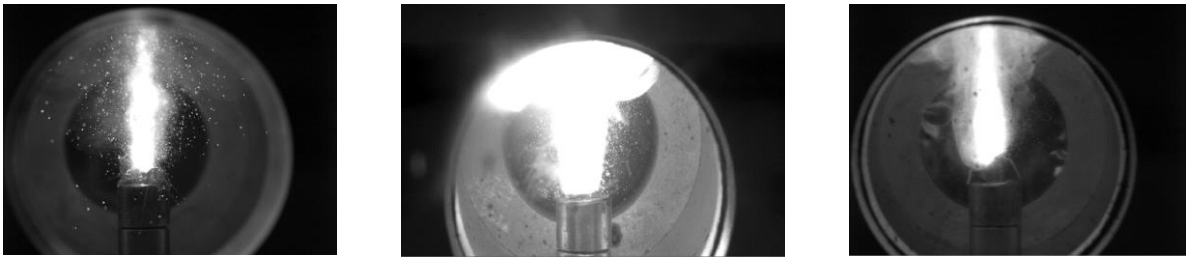

(a) (b) (c)

Fig. 2. Combustion of mixtures of Al with (a) Bi_2O_3, (b) Fe_2O_3, and (c) CuO.

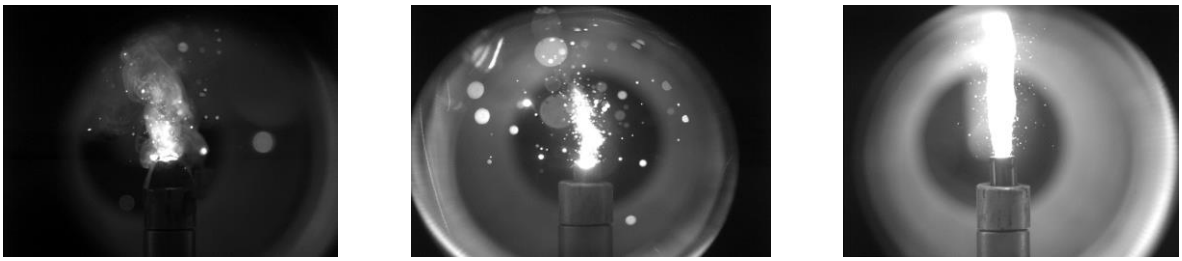

(a) (b) (c)

Fig. 3. Combustion of mixtures of $Al{\cdot}I_2$ with (a) Bi_2O_3, (b) Fe_2O_3, and (c) CuO.

4 Conclusions

Mixtures of mechanically alloyed $Al{\cdot}I_2$ powder with Bi_2O_3 and Fe_2O_3 do not exhibit rapid ignition and steady combustion, while its mixtures with CuO readily ignite and burn rapidly and steadily, similarly to Al/CuO mixtures.

5 Acknowledgment

This research was supported by the U.S. Department of Defense (Grants No. W911NF-12-1-0056 and No. W911NF-14-1-0034; Grant Officer's Representative: Dr. Ralph A. Anthenien of the Army Research Office; Co-GOR: Dr. Clifford D. Bedford of the Office of Naval Research).

References

[1] R. Russell, S. Bless, M. Pantoya, J. Energy Mater. 29 (2011) 175–192.
[2] K.T. Sullivan, C. Wu, N.W. Piekiel, K. Gaskell, M.R. Zachariah, Combust. Flame 160 (2013) 438–446.
[3] C.E. Johnson, K.T. Higa, T.T. Tran, W.R. Albro, MRS Online Proc. Libr., 2013, 1405.
[4] S. Zhang, M. Schoenitz, E.L. Dreizin, J. Phys. Chem. C 114 (2010) 19653–19659.
[5] S. Zhang, C. Badiola, M. Schoenitz, E.L. Dreizin, Combust. Flame 159 (2012) 1980–1986.
[6] S. Zhang, M. Schoenitz, E.L. Dreizin, J. Phys. Chem. Solids 71 (2010) 1213–1220.
[7] M.A. Machado, D.A. Rodriguez, Y. Aly, M. Schoenitz, E.L. Dreizin, E. Shafirovich, Combust. Flame 161 (2014) 2708-2716.
[8] D.A. Rodriguez, E.L. Dreizin, E. Shafirovich, Combust. Flame 62 (2015) 1498–1506.

Limitations of Classic Local Approach Kachanov-Rabotnov Creep Damage Model

Mohammad Shafinul Haque and Calvin M. Stewart

Department of Mechanical Engineering, University of Texas at El Paso
500 W. University Ave., El Paso, TX 79968

Abstract:
The classic Kachanov-Rabotnov (KR) creep damage model has some critical limitations in spite of its high accuracy in creep strain-deformation trajectory prediction. The damage rates of KR model become excessively high at about 90% of lifetime, and the critical damage at failure is not and cannot be unity. KR damage model exhibits stress sensitivity (when damage approaches to unity) that contributes to damage localization (not distributed around crack propagation path), and mesh shape, distribution and size dependency in FEM analysis. In this study analytical explanation and numerical analysis of the KR model limitations are demonstrated in detail. Experimental data collected from literature are used in this study. Finite element analysis of circular notched specimen containing initial crack of 304 Stainless-Steel (SS) is performed. Finally, a new approach is proposed to mitigate these issues significantly.

1 Introduction:

Accurate creep damage evolution can be predicted by accounting microstructural damage in the modeling. Development of local continuum approach considering microstructural change of material before fracture leads to accurate prediction [1]. Constitutive creep damage evolution model proposed by Kachanov-Rabotnov are usually written as follows

$$\dot{\varepsilon}_{cr} = \frac{d\varepsilon_{cr}}{dt} = A \cdot \left(\frac{\sigma}{1-\omega}\right)^{n}, \qquad \dot{\omega} = \frac{d\omega}{dt} = \frac{M \cdot \sigma^{x}}{(1-\omega)^{\phi}} \tag{1}$$

Where A and n are the Norton power law constants, σ is equivalent stress, $\omega(0 \le \omega \le 1)$ and M, χ and ϕ are tertiary creep damage constants. Rearranging strain rate equation (1) we get

$$\omega\left(\dot{\varepsilon}_{cr}\right) = \frac{\left(\frac{\dot{\varepsilon}_{cr}}{A}\right)^{1/n} - \sigma}{\left(\frac{\dot{\varepsilon}_{cr}}{A}\right)^{1/n}} \tag{2}$$

When $\dot{\varepsilon}_{cr} = \dot{\varepsilon}_{cr_{\min}}$ the denominator of equation (1) takes the form of Norton Power law, and is equal to equivalent stress σ. The ratio of equation (1) becomes unity and the damage becomes zero. As soon as $\dot{\varepsilon}_{cr} > \dot{\varepsilon}_{cr_{\min}}$,the term $\left(\dot{\varepsilon}_{cr} / A\right)^{1/n}$ represents instantaneous effective stress, higher than equivalent stress (σ), and irreversible damage starts to grow. Thus, in KR model damage builds up only in tertiary creep stage, no damage accumulates in primary and secondary creep stages. For damage to be unity at failure, instantaneous strain ($\dot{\varepsilon}_{cr}$) has to be infinitely large. But creep strain rate becomes large just before failure and remains finite throughout the lifetime. Thus, KR model damage remains very low up to 90% of lifetime. Moreover, $\dot{\varepsilon}_{cr}$ is never infinitely large thus damage cannot be unity and varies from 0.2-0.8 for most metals [2]. This can also be realized from damage rate equation (2). When damage approaches to unity, damage rate becomes infinitely large suggesting that the function attempts to encapsulate both the continuous damage of creep and discontinuous plastic damage that occurs at the instant of fracture [2]. In this study rigorous analytical explanation and numerical proof are demonstrated in detail of KR creep damage model limitations.

2 Limitations of KR model

Integrating damage evolution equation (1) and assuming initial time t_0 and initial damage ω_0 is equal to zero giving

$$\omega(t) = 1 - [1 - (\phi + 1) \cdot M \cdot \sigma^{x} \cdot t]^{\frac{1}{(\phi+1)}} \tag{3}$$

At time $t=t_r$,damage $\omega = \omega_r$, rearranging equation (3) becomes

$$M = (1 - (1 - \omega_r)^{(\phi+1)}) / ((\phi + 1)\sigma^{\chi} t_r) \tag{4}$$

Introducing equation (4) into equation (3) gives the following

$$\omega(t) = 1 - \left[\frac{t}{t_r} \cdot [(1 - \omega_r)^{\phi+1} - 1] + 1 \right]^{\frac{1}{\phi+1}} \tag{5}$$

If it is assumed that at failure $\omega_r = 1$, damage equation (5) reduces to

$$\omega(t) = 1 - \left(1 - \frac{t}{t_r} \right)^{\frac{1}{\phi+1}}, (\phi > 1) \tag{6}$$

In this form KR damage only depends on ϕ value. Figure 1 (a) shows that theoretically critical damage at failure can be unity in this form [equation (6)] and exhibits stress sensitivity as discussed in introduction section. While implementing on experimental data, critical damage have to be determined from equation (2), which cannot be unity $(\omega(\dot{\varepsilon}_r) \neq 1)$. Thus the KR model damage trajectory governing equation does not reduces to equation (6) and unable to reach unity at failure and violets the presumption of unity critical damage at rupture.

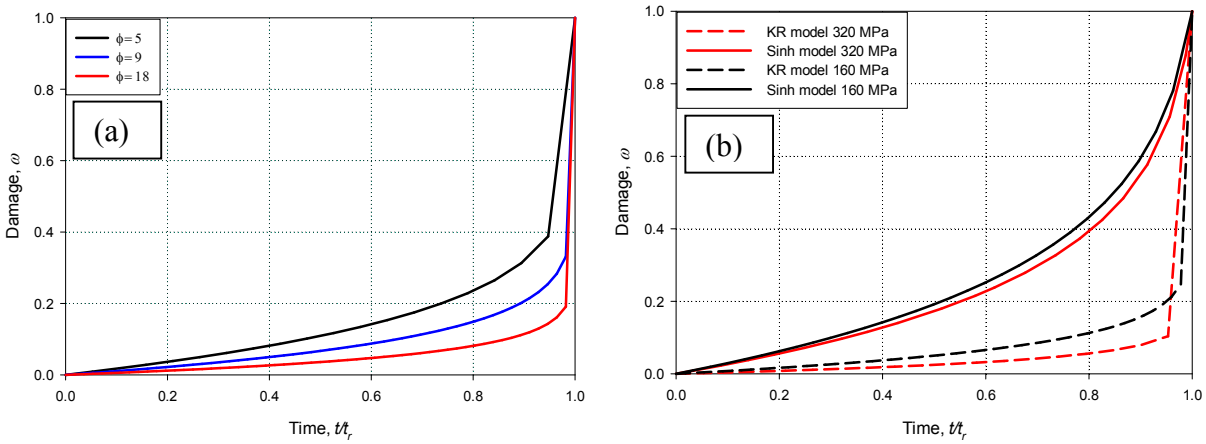

Figure 1. (a) Normalized time vs Damage. Typical KR damage evolution at different ϕ , (b) Comparison of typical KR and Sinh model

3 Stress Sensitivity

Taking variation of damage $\partial\omega(t)$ with an infinitesimal variation of stress $\partial\sigma(t)$ and replacing the portion, $M \cdot \sigma(t)^{\chi} \cdot t$, by rearranging [Equation (3)] giving

$$\partial\omega(t) = \chi \cdot \frac{1 - (1 - \omega)^{\phi+1}}{(1 - \omega)^{\phi}} \cdot \frac{\partial\sigma(t)}{\sigma(t)} \tag{7}$$

when damage is critical $(\omega_{cr} \to 1)$, the damage variation $\partial\omega(t)$ is near infinite as the denominator becomes zero and ϕ is greater than unity. Figure 1 shows typical KR creep damage curve for different

values of ϕ. From Figure 1 it is evident that damage remains very low throughout most part of the lifetime, and suddenly jumps to unity just before failure. As the value of ϕ increases this stress sensitivity becomes more dominant. Consequently localized damage can be observed.

4 Damage Localization:

Localized damage prediction suggests that damage has occurred only on the cracked surface while the surrounding area of the component is still unaffected, which is unrealistic. This type of faulty prediction takes place if any damage variable of the prediction model presumes very localized homogeneity for damage distribution. The prediction model becomes unable to maintain the required elliptical nature, may lead to premature, perfectly brittle damage evolution response [1]. Liu & Murakami [3] has observed damage localization problem in homogeneous stress field even at very small (10^{-8}) stress gradient numerical error. Damage localization may be observed at very fine meshing. FEM analysis of KR model on thin circular notched (1.5 mm dia.) specimen with initial crack exhibits damage localization [Figure 2]. It is observed that damage ranged (0.22-.99) is locally distributed within 0.1 mm distance from the crack path (mesh size 0.05 mm). Upon further mesh refinement critically localized damage may be observed.

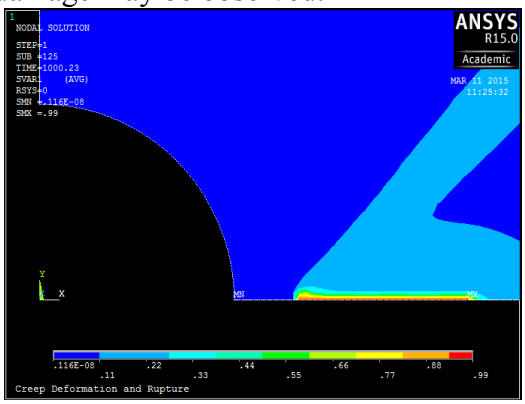

Figure 2. Comparison of typical KR and Sinh model

5 Mesh Dependency and Stress Singularity:

All materials include some form of defects or voids. FEM analysis of notched specimen with initial crack are very popular and can emulate these phenomena. But sharp edge at initial crack tip can lead stress singularity. Refining mesh size will develop very high unrealistic stress values. Stress singularity can also be observed if the governing equation is stress sensitive as discussed in the stress sensitivity section. Peerling et al. has explained this phenomena, as mesh is super-refined the fracture energy becomes zero and crack growth becomes infinite originates mesh dependency [3].

6 Future work:

The novel sinh model [1] overcomes the low damage problem of KR model [Figure 1(b)]. Exhibits more realistic elliptical trajectory and gradually grows to unity. FEM simulation of Sinh model and KR model at different mesh size can be performed to check mesh dependency of Sinh model. Sinh model can be a better replacement of KR model if upon mesh refinement crack growth rate increment remains comparatively low and damage is more distributed.

7 Reference:

[1] R. H. J. Peerlings, R. de Borst, *Localization issues in local and nonlocal continuum approaches to fracture*, *European J. of Mechanics*, Vol.21, pp 175-189, 2002.

[2] M. S. Haque, C. M. Stewart, *Comparison of a new Sinh-hhyperbolic creep damage constitutive model with the classic Kachanov-Rabotnov model using theoretical and numerical analysis*, TMS, 144th Annual Meeting and Exhibition, Florida, USA, March 15-19, 2015.

[3] Y. Liu, S. Murakami, *Damage localization of conventional creep damage models and proposition of a new model for creep damage analysis*, JSME Int. Journal, Vol. 41, 1, 1998.

TENSILE PROPERTIES OF POLYLACTIC ACID (PLA) ADDITIVE MANUFACTURED PARTS

J. Cardenas[1], C. M. Stewart[1]*
[1] Department of Mechanical Engineering, University of Texas at El Paso, El Paso, TX 79968, USA;
* Calvin M. Stewart (cmstewart@utep.edu)

Keywords*: Additive Manufacturing, PLA, honeycomb structures, tensile mechanical properties.*

ABSTRACT

In the advancement of Additive Manufacturing (AM) technologies, 3D desktop printers have become an accessible solution to address the current limited manufacturing practices. This study explores the effect build parameters have on the tensile properties of AM parts by comparing the Young's Modulus and tensile strength of polylactic acid (PLA) in the elastic region before and after the AM process. This work presents the tensile mechanical properties for specimens built using low infill rate, low layer resolution, and standard build speed and extrusion temperature to recreate the worst possible part quality attainable using MakerBot 3D Desktop printers. Using these build parameters results in a part with a hollow honeycomb interior structure, and due to its heterogeneous cross-sectional area, experimental stress-strain curves do not accurately represent its physical response to tensile loading. Therefore, an experimental-numerical study is performed, using the load-displacement experimental data acquired from tensile tests to calibrate the ANSYS Structural Mechanics simulations. The goal is to optimize the material properties in our simulation such that the displacement magnitude and vectors match the experiments. Tensile tests are performed synched with a Correlated Solutions 3D Digital Image Correlation (DIC) system to obtain surface contours of deformation using specimen speckle patterns, which are then compared to the displacement fields in the finite element analysis (FEA) simulation. When compared to the pre-manufacturing properties, post-processed PLA stiffness was reduced after printed. The failure location based on the influence interior geometry has on failure showed that specimens failed by brittle fracture across the hex pattern.

1 Introduction

Much research has focused on quantifying and improving the tensile mechanical properties of AM parts via modifying build parameters by experimental methods [1]. However, the results are only quantifiable by using the exact same set of parameters and cannot be used to envelope a broader spectrum of varying build parameters. An issue this approach represents is that of assuming the manufactured part has a completely uniform interior cross-section when subjecting it to mechanical testing. As created in a layer-by-layer manner the 3D printed part interior's periodic structure is compromised and exhibits an internal honeycomb structure, decreasing the part's strength and leading to unrepresentative results. The focus of another yet smaller field of research is to use cellular materials (such as honeycombs) to replace bulk materials as to use it only where is structurally needed [2]. These techniques have been used to improve CAD element quality and physics representation, showing part decomposition into element types according to the manufacturing process employed to obtain more accurate computer simulations. But as the design and engineering environment complexity increases so does the need to validate results

obtained from the FEM and solving software. Checking the results tends to be simpler in the elastic region of the material due to the linear relationships that can be drawn from stress, strain, and deformations. However due to our non-homogeneous cross-section, an approach combining both disciplines is employed herein using experimental test results to confirm the validity of our numerical simulations to present a method for predicting the tensile mechanical properties of PLA in the elastic region for 3D printed specimens based on our set manufacturing process.

2 Materials and Methods

2.1 Specimen Construction

Specimens are created using MakerBot Replicator 3D printers and PLA filament as the build material. PLA is the primary choice in MakerBots as it is a low-melting point polymer that exhibits a high elastic modulus, high tensile strength, and low deformability overall [3]. Pre-manufactured PLA has a tensile strength of 50-70 MPa, tensile elastic modulus of 3000-4000 MPa, elongation at break of 2-10%, and melting point of about 180 °C [3]. This project employs Type I ASTM D638-10 Standards [4] rectangular tensile specimens depicted in Fig. 1, built at the same time, in the same orientation, and using the build parameter set defined in Table 1 to study repeatability and to reduce fabrication time and induced error.

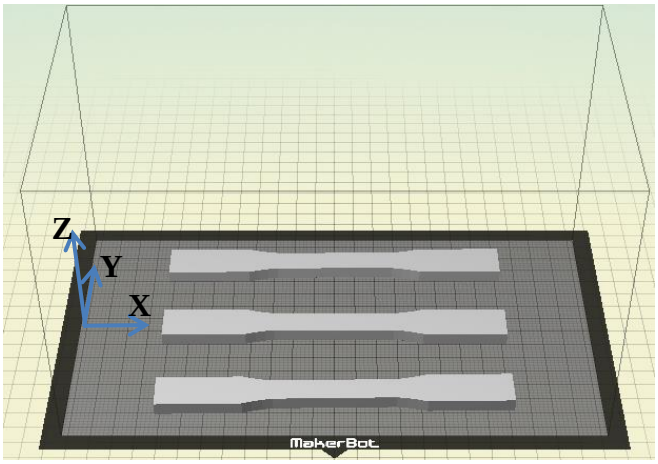

Fig. 1. XYZ build orientation used for the fabrication of ASTM D638 Type I specimens.

Table 1. MakerBot Replicator Building Parameters

Specimen	Extrusion Temperature, T_E (°C)	Infill%	Build Speed, v_b (mm/s)	Resolution
1	220	10%	50	Low

2.2 Mechanical Testing

Specimens built per specifications above were subjected to tensile testing on both an Instron 5866 and an ADMET 5603 Universal Test Machines (UTM) synched with a DIC system to obtain the tensile properties of printed PLA. The load-displacement data was extracted by the equipment's built-in software, Bluehill 2 and MTESTQuattro, respectively. Before mechanical testing, all specimens were conditioned for 40 hours at 23 ºC and 50% relative humidity, according to ASTM standard D618 [5]. The specimens are prepared with a speckle pattern for DIC measurements using standard off-the-shelf flat white and black spray paint to avoid reflection and create the needed contrast for data collection. The specimens are first covered

with a thin layer of white paint on one side covering the area of interest, in this case the gage length. The speckle pattern is then randomly sprayed on the white surface until a fine heterogeneous speckle pattern of black spots is achieved, as seen in Fig. 2. Also in Fig. 2 is the post-processed DIC data from preliminary results in the ADMET UTM, showing the strain contour in the X-direction around the fracture surface.

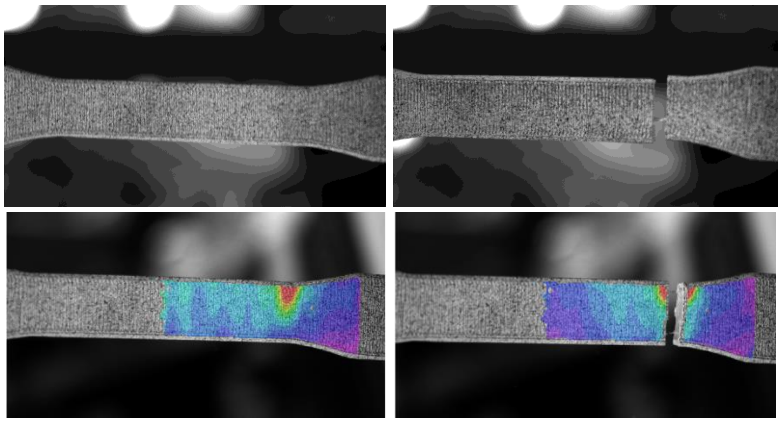

Fig. 2. Specimen speckle pattern and strain contour in the x-direction around fracture surface by DIC.

2.3 Computational Simulations

Simulations are performed using ANSYS Structural Mechanics Workbench Software R15.0 Academic. Fig. 3 depicts the CAD design utilized for these simulations which shows the test specimen with the interior honeycomb periodic structure representative of the lowest quality build parameters. The simulation module used is Static Structural Analysis, setup to represent the machine's extension control mode at a ramp rate of 5 mm/min with one fixed end.

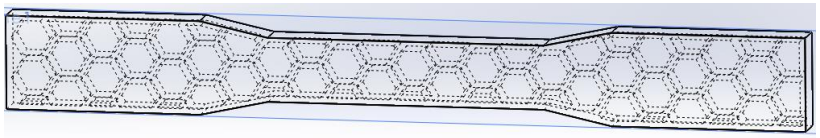

Fig. 3. CAD of test specimen with honeycomb interior structure.

3 Future Work

Future work for this project involves the constrained response surface optimization of the Young's Modulus of printed PLA in the ANSYS simulations. This will be accomplished by comparing the minimum and maximum magnitudes of the displacement vector in the numerical analysis to the tensile test, optimizing the Young's Modulus until experimental displacement is reached using load-displacement data.

References

[1] Hossain, M. S., Ramos, J., Espalin, D., Perez, M., and Wicker, R., 2013, "Improving tensile mechanical properties of FDM-Manufactured specimens via modifying build parameters," pp. 380-390.

[2] Rosen, David W. "Computer-aided design for additive manufacturing of cellular structures." *Computer-Aided Design and Applications* 4.5 (2007): 585-594.

[3] Auras, R. A., Lim, L. T., Selke, S. E. M., and Tsuji, H. "*Poly(lactic acid): Synthesis, structures, properties, processing, and applications."*1st Edition, John Wiley & Sons, Inc., Hoboken, New Jersey. 2010.

[4] ASTM International, 2014, "Designation D638-10, Standard test method for tensile properties of plastics," pp. 1-16.

[5] ASTM International, 2008, "Designation: D618-08, Standard practices for conditioning plastics for testing."

NEAR SURFACE LAYER MICROSTRUCTURAL INVESTIGATION OF A HIGHLY SCC SUSCEPTIBLE GRADE A STEEL VINTAGE GAS TRANSISSION PIPELINE

M. Torres[1]*, S. Stafford[1], J. Lopez[1],
[1] Department of Metallurgical & Materials Engineering, UTEP, El Paso, TX 79968, USA;
* Corresponding author (matorres9@miners.utep.edu)

Keywords*: Stress corrosion cracking, carbon steel pipelines.*

ABSTRACT

The emergence of natural gas as a global commodity underlies the importance of its processing, transmission, and distribution [1,2]; particularly, as the demand of this energy efficient fossil fuel is expected to markedly increase in the near future [3-4] as natural gas can provide a sustainable energy source without an adverse impact to the environment [2]. The current pipeline network infrastructure in the United States compromises miles of outdated, fragile, and vulnerable gas pipelines [5] which are exposed to aggressive operating conditions and therefore subject to in-service degradation such as stress-corrosion cracking (SCC) [1], which due to its multivariate and unpredictable nature continues to be one of the most comprising forms of external corrosion. Therefore, the aim of this investigation is to gain insight into the main microstructural features of highly SCC susceptible pipeline materials, in the region near the surface layer where crack nucleation must take place. In this manner our goal is to expand our knowledge on what makes these materials more prone to SCC and ultimately be able to develop steels resistant to SCC.

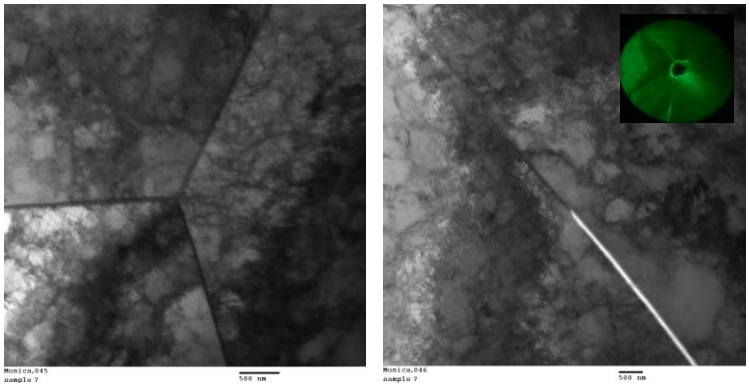

Fig 1. Bright TEM micrographs near the surface layer, showing polygonal ferrite, dislocation structures, and an intergranular crack segment near a particle at a triple point grain boundary.

1 Introduction

The natural gas business is a key sector in the energy industry and therefore to the economies of a number of countries [6]. In fact, natural gas consumption and trade have been growing progressively over the past two decades [2] and it is expected to markedly increase in the near future [3-4] as it is one of the most energy efficient fossil fuels [2] capable of satisfying the

future energy demand without an adverse impact to the environment [2]. Nevertheless, the emergence of natural gas as a global commodity underlies the importance of its processing, transmission, and distribution [1,2]. The increasing demand will require higher operating pressures and the expansion of current transmission and distribution pipeline networks to increase the capacity of the existing systems, [3,7] which includes miles of outdated, fragile, and vulnerable gas pipelines [5]. Furthermore, buried pipelines are exposed to aggressive operating conditions and therefore subject to in-service degradation as in the case of stress-corrosion cracking [1], which continues to be one of the most unpredictable forms of external corrosion. In the absence of structural integrity planning, SCC can provide catastrophic consequences due to the time dependent nature of this sub-critical cracking mechanism [8]. The aim of this investigation is to gain insight into the microstructural features of highly SCC susceptible pipeline materials and therefore expand our knowledge into what makes these API5L pipe steels more vulnerable to SCC and thus delimit the boundaries of this ubiquitous form of corrosion [9]. Conceivably, steels more resistant to SCC to guarantee the integrity of the pipeline system [10] could be developed.

2 Experimental Procedure

2.2 Materials

Sections from a vintage gas transmission pipeline removed from service in 1991 because significant cracks were found in different sections of the pipeline were used for this investigation. The maximum crack length measured 43 mm (1.7 inches) and the maximum crack depth was thru-wall. This single submerged arc welded pipe was built from Grade A steel, to API Spec 5L requirements with a 220 mm (8 5/8 inches) OD, a nominal wall thickness of 4.5 mm (0.180 inches), and a specified minimum yield strength (SMYS) of 208 MPa (30,000 psi). The pipe was coated with coal-tar enamel, and impressed-current cathodic protection (CP) had been applied. Analysis of the soil in this region revealed a pH of 9. For purposes of this research this pipeline was identified as Pipeline WS. Optical emission spectroscopy (OES) was used to identify the pipe's chemistry with testing performed in a region away from the surface cracks. The surface was prepared with an angle grinder grit 36. All of the received sections from the pipeline were tested. A minimum of three tests were performed per sample and an average calculated from the results.

2.2 Microstructural Characterization

Microstructural characterization was performed through optical and transmission electron microscopy (TEM). Optical microscopy was used to observe the material's general microstructure—microconstituents, inclusions, grain size, and crack morphology. Samples were prepared following standard metallographic techniques and subsequently etched with 2% Nital reagent (98 ml methanol and 2 ml nitric acid). The grain size was measured by the linear intercept method and the corresponding ASTM grain size was calculated per ASTM E112. On the other hand, TEM was used to observe microstructural features in the region near the outside diameter (OD); to a depth of approximately 200 μm from the surface layer where crack nucleation had taken place. In order to observe the dislocation structures, main microconstituents, and precipitates; thin foils were prepared from a section away from the cracks and close to the OD. Samples were ground to 0.2 mm in thickness from the inside diameter, keeping the OD surface essentially intact. Samples were then electropolished to perforation using a solution of 670 ml methanol and 330 ml nitric acid, at a voltage of 13.5V and a temperature of -15.5 ºC. Pipeline TEM samples were prepared parallel to the OD surface.

3 Results and Discussion

Conventional lower strength steel pipelines such as Grade A steel were primarily used around 1950 or before [3,11] and compromise about 35% of the current gas transmission infrastructure [12]. However Grade A steel has reported to be highly susceptible to SCC and no longer qualifies for use as the replacement pipe grade [13]. Grade A steel pipelines are characterized by a very low carbon content, in this case the carbon content was determined to be approximately 0.05 wt%. Additionally, the OES results also revealed a low Mn and Si content. These results demonstrate that this pipeline was made to a semi-killed or rimmed steel practice a product of partial deoxidation [14]. Partially deoxidized steels have been reported to be more susceptible to strain aging [15] and despite the fact that the detrimental impact of strain aging on SCC fracture initiation remains unclear, it continues to be a major concern for gas transmission pipelines [3].

The crack pattern observed in WS pipeline was classified as "non-classical; as the cracks were oriented in both directions—longitudinally and circumferentially. Metallographic inspection of a transverse cross-sections containing SCC cracks revealed that the crack propagation mode followed a predominantly intergranular path with extensive branching, typical characteristics of high-pH SCC (IGSCC). The main microstructural features observed were primarily slow to intermediate cooling rate microconstituents, consisting of large amounts of polygonal ferrite, isolated cementite films at ferritic grain boundaries, and a small number of pearlite colonies. These are the result of the combined action between a slow cooling rate and the low carbon content of Grade A steel. The average grain size for the investigated pipeline was about 20 μm (ASTM Grain Size No.8) and exhibited a bimodal configuration. The mixture of very small and large grains is an indication of grain growth, this effect was more noticeable towards the ID. The effect of grain size on the corrosion resistance of an alloy appears to be strongly correlated to the environment-material combination [16].

TEM analysis performed in the near-surface layer revealed the predominance of polygonal ferrite which is characterized by straight, smooth, and continuous boundaries [17-18] and normally by a low dislocation density as it occurs at high transformation temperatures, which promote the ease of dislocation rearrangement and annihilation [19]. Polygonal ferrite has not only been reported to be advantageous to the occurrence of IGSCC [20], but some authors have also concluded that it is more vulnerable to hydrogen attack and cracking as compared to acicular ferrite [21]. After hydrogen charging, the grain boundaries of polygonal ferrite developed microcracks but not those of acicular ferrite [20]. Furthermore, the region near the OD exhibited evidence of high dislocation densities and well developed dislocation cells (Fig. 1). This could be the result of a number of factors such as rolling in the non-recrystallized region [22]; differences in cooling rates between rim to core [83]; and to some extent on service conditions. Nevertheless, dislocations have been reported to contribute to SCC. Lastly, the TEM study also revealed a number of triple point junctions and a grain boundary crack near a large particle located in a triple point junction (Fig.1).

4 Conclusions

This study revealed the metallurgical features in the region near the surface layer—where crack nucleation must take place—from a vintage gas transmission pipeline removed from service after 40 years due the presence of multiple SCC cracks. In this manner this investigation provided insights into the primary microstructural features of a highly SCC susceptible material.

5 References

[1] Bott, I., De Souza, L. F. G., Teixeira, J. C. G., 2005, "High-strength steel development for pipelines: A brazilian perspective" *Metallurgical and Materials Transactions A,* 36App. 443-454.

[2] Mokhatab, S., and Poe, W.A., 2012, "*Handbook of natural gas*". Gulf Professional Publishing, USA, pp. 765.
[3] Cheng, Y.F., 2013, "Stress corrosion cracking of pipelines". Wiley, New Jersey, pp. 255.
[4] Sturm, F.J., 1997, "*Trading natural gas*". PennWell Publishing Company, Oklahoma, pp. 199.
[5] Crary, D., 2014, "Explosion reminds of NYC's aging infrastructure". Http://abcnews.Go.com/US/wireStory/explosion-Reminder-Nycs-Aging-Infrastructure-22902709, 2014(03/18)
[6] Simonoff, J. S., Restrepo, C. E., and Zimmerman, R., 2010, "Risk management of cost consequences in natural gas transmission and distribution infrastructures". *Journal of Loss Prevention in the Process Industries*, 23(2) pp. 269-279.
[7] Shanmugam, S., Ramisetti, N. K., Misra, R. D. K., 2008, "Microstructure and high strength-toughness combination of a new 700MPa Nb-microalloyed pipeline steel. *Materials Science and Engineering A*, 478pp. 26-37.
[8] Metcalfe, J., 2014, "How Gas Leaks Disasters Happen". Http://news.Msn.com/us/how-Gas-Leak-Disasters-Happen, 2014(03/18).
[9] Ru, X., and Staehle, R. W., 2013, "Historical experience providing bases for predicting corrosion and stress corrosion in emerging supercritical water nuclear technology: Part 3—review". *Corrosion*, 69(5) pp. 423-447.
[10] Van Boven, G., Chen, W., and Rogge, R., 2007, "The Role of Residual Stress in Neutral pH Stress Corrosion Cracking of Pipeline Steels. Part I: Pitting and Cracking Occurrence". *Acta Materialia*, 55pp. 29-42.
[11] Zhou, M., Du, L., Zhao, Y., 2012, "Microstructure characteristics and mechanical properties of X-80 pipeline steel". *Journal of Wuham University of Technology-Mater Sci Ed*, 27(2)
[12] US Department of Transportation, 2009, "The state of the national pipeline infrastructure". US Department of Transportation, USA.
[13] Schumura, E., Paster, M., and Bruber, J., 2005, "Existing natural gas pipeline materials and associated operational characteristics". *DOE Hydrogen Program*, FY 2005, USA.
[14] Leslie, W.C., 1981, "*The physical metallurgy of steels*". Mc Graw Hill, United States, pp. 396.
[15] Clark, E.B., and Leis, B.N., 2005, "Integrity characteristics of vintage pipelines report". *INGAA Foundation Inc*, F-2002-50435, Columbus, OH.
[16] Ralston, K. D., and Birbilis, N., 2010, "Effect of processing on grain size and corrosion of AA2024-T3". *Corrosion*, 66(7) pp. 075005-1
[17] Krauss, G., 2005, "*Steels: Processing, structure, and performance*". ASM International, Ohio, pp. 101-118, Chap. 7.
[86] El-Danaf, E., Baig, M., Almajid, A., 2013, "Mechanical, microstructure and texture characterization of API X65 steel". *Materials & Design*, 47(0) pp. 529-538.
[19] Collins, L. E., Gooden, M. J., and Boyd, J. D., 1983, "Microstructures of Linepipe Steels". *Canadian Metallurgy Quarterly*, 22(2) pp. 169-179.
[20] Zhu, M., Du, C., Li, X., 2014, "Effect of strength and microstructure on the stress corrosion cracking behavior and mechanisms of X-80 pipeline steel in high pH carbonate-bicarbonate solution". *Journal of Materials Engineering and Performance.*
[21] Dong, C. F., Li, X. G., Liu, Z. Y., 2009, "Hydrogen-induced cracking and healing behavior of X70 steel". *Journal of Alloys and Compounds*, 484(1–2) pp. 966-972
[22] Ghosh, S. K., Haldar, A., and Chattopadhyay, P. P., 2009, "The influence of copper addition on microstructure and mechanical properties of thermomechanically processed microalloyed steels". *J. Mater. Sci*, 44pp. 580-590.
[23] Haq, A. J., Muzaka, K., Dunne, D. P., 2013, "Effect of microstructure and composition on hydrogen permeation in X70 pipeline steels". *International Journal of Hydrogen Energy*, 38(5) pp. 2544-2556

THEORY OF UNIFIED VISCOPLASTIC MODELS

Luis A. Varela J. and Calvin M. Stewart

Department of Mechanical Engineering, The University of Texas at El Paso, 500 W. University Ave., El Paso, TX 79968, USA

Keywords: *Constitutive Equations, Viscoplastic Model, Inelastic.*

ABSTRACT

The broad use of metallic materials in structural applications that involve plastic deformation and expose the materials to extreme environments of high loads and elevated temperature creates the necessity of understand the materials response to these extreme environments. The good understanding of the material behavior leads to less conservative designs; therefore, reducing design and manufacturing costs of components because the material is used more effectively. The introduction of unified viscoplastic models had contributed to meet this necessity, by offering a unified solution to determine the inelastic behavior of metallic materials under multiple loading conditions. The basic structure of unified viscoplastic constitutive models is described in the present work.

1. Introduction

The interest in the prediction and/or description of the inelastic behavior of metallic materials has increased since these materials are widely used in environments where inelastic or non-elastic deformation cannot be avoided. Examples of these applications are nuclear reactor pressure vessels, energy generation and aircraft industries, where for better system's efficiencies equipment operates at high temperature and/or complex loading conditions; thus, exposing the material to complex service histories [1, [2]. In order to satisfy the interest of predicting the inelastic material behavior, numerous unified viscoplastic models have been proposed in literature [3]. The objective of the present work is to explain the theory, basic structure of unified viscoplastic models equations.

2. Theory

A unified viscoplastic models is a mathematical material model capable of describing and or predict a material's behavior under complex loading conditions at elevated temperatures. It is called a unified model because contrary to classical theories of inelastic deformation, it is unifying the creep and plastic strain into one unique inelastic strain term; the unification of this term allows the modeling of multiple loading conditions (creep, monotonic tension or cyclic loading) by using the same set of constitutive equations for any loading condition. These types of models are based in the theory of time-dependent deformation [4[5]. However, the total mechanical strain rate $\dot{\varepsilon}_{mech}$ of the material is represented by the summation of the elastic strain rate $\dot{\varepsilon}^e$ and the inelastic strain rate $\dot{\varepsilon}^i$ equation(1); where the elastic strain rate is calculated using Hook's law and the inelastic strain rate is calculated using the unified viscoplastic model.

$$\dot{\varepsilon}_{mech} = \dot{\varepsilon}^e + \dot{\varepsilon}^i \tag{1}$$

Although proposed unified viscoplastic models differ in number of conforming material constants, mathematical function used or effectiveness most models share several format details and basic structure. According to Chaboche [6] the basic structure of unified viscoplastic models should contain a flow law and hardening law equations to describe the

evolution of the inelastic strain rate and the state variables. A basic skeleton of the constitutive equations of this type of models is presented in equations (2-4) [8]. Usually these equations are stiff non-linear differential equations, meaning that a minimum change in one constant or term can considerably affect the solution of equations; thus, these equations are usually difficult to solve and complicated integration methods are used to resolve them. The flow law, equation (2) describes the inelastic strain rate as a function of the applied stress σ and the state variables that describe the hardening state of the material. Usually the strain rate equation contains a power law function or a hyperbolic sine function within its structure; besides the signum (sgn) function is added to account for reverse stress flow in case of opposite direction loading. The hardening law refers to the use of state variables to determine the strain state within the material due to the applied stress and the environment conditions, such as temperature. This hardening law is divided into kinematic and isotropic hardening [9]. Kinematic hardening R refers to the back or rest stress, which describes the global effects of repulsive forces among dislocations in pileups against obstacles; if a yield criterion is consider kinematic hardening accounts for the translation of the yield surface in the stress space, this accommodates the Bauschinger effect. Equation (3) describes the kinematic hardening with respect to time. Isotropic hardening D refers to the drag stress, which describes the drag forces that resist dislocation motion; if yield criterion is consider, then isotropic hardening accounts for the change in size of the yield surface in the stress space. Isotropic hardening with respect to time is represented by equation (4) [7].

$$\dot{\varepsilon}^i = K\left(\frac{\sigma - R}{D}\right) \tag{2}$$

$$\dot{R} = X_1\dot{\varepsilon}^i - X_2 R\left|\dot{\varepsilon}^i\right| - X_3\left|R\right| \tag{3}$$

$$\dot{D} = Z_1\dot{\varepsilon}^i - Z_2 D\left|\dot{\varepsilon}^i\right| - Z_3\left|D\right| \tag{4}$$

Usually hardening equations follow the hardening-recovery format. Terms X_1 and Z_1 represent the hardening terms of the model, these terms are function of the inelastic strain rate, meaning that they are activated only in the presence of inelastic strain rate. The presence of hardening is mainly due to the block of dislocation motion. Terms X_2 and Z_2 represent the dynamic recovery capability of the model. The dynamic recovery is active due to the presence of an inelastic strain rate which allows primary, the climbing and cross-slip of dislocations which allows dislocation motion therefore recovering some hardening. Terms X_3 and Z_3 represent the effects of static thermal recovery; these terms are not function of the inelastic strain rate, they are activated by temperature. Once certain activation temperature is reached then the recovery term is activated and some hardening is recovered, the activation temperature is depended of the material and the recovery phenomena [8]. The K, X and Z terms in the constitutive equations represent material constants; these material constants are characteristic of each material, and depending on the model they might be characteristic of each temperature level. The total number of material constants vary with each model, normally the accuracy of the model is related to the number of material constants; a model with numerous constants is expected to have a high accuracy. The material constants values are determined from creep and fatigue experimental data. Each model has a different method to calculate material constants, for example some models require the use of external

equations to calculate, other require the plotting of experimental data in a certain way or some other is just trial and error. The material constants finding process is not always an easy process, especially if the model consists of many material constants since this increase the calculation time. Even though unified viscoplastic models have been a promising solution to predict metallic material response during many years and numerous models have been proposed in literature, according to Chang and Thompson [10] there are still some shortcomings present in unified viscoplastic models. Some of them are (a) the proposed models have not been fully tested under rigorous conditions, therefore its full functionality have not been ensured (b) The material constants calculation methods are unclear since they are not well documented in all cases (c) As mentioned before the constitutive equations present a stiff regime, therefore its solution is not easy for time-dependent analysis. In order to take full advantage of these models and its capabilities, the aforementioned shortcomings must be overcome. So Even though unified viscoplastic models are not a new concept, there are still some empty spaces that need to be filled.

3. Conclusion

The importance and use of unified viscoplastic models have been presented, along with the structure of the constitutive equations. The basic hardening terms of the models were explained in microstructural level and also explained for yield criterion. Besides, areas of improvement and future work were suggested.

4. Future work

Based on the reviewed theory the authors suggest the following future work: development of a hybrid unified viscoplastic model combining two existing models to create an optimized viscoplastic model, develop a general technique to determine material constants for any unified model, incorporate existing viscoplastic models into finite element software to exercise and test the limitations and capabilities of unified viscoplastic models.

5. References

[1] A. K. Miller, “Modelling of cyclic plasticity with unified constitutive equations: improvements in simulating normal and anomalous Bauschinger effects”. *Journal of Engineering Materials and Technology*, Vol. 102, pp. 215-222, 1980.

[2] D. Slavik and T.S. Cook, “A unified constitutive model for superalloys”. *International Journal of Plasticity*, Vol. 6, pp. 651-664, 1990.

[3] Lindholm, U. S., Chan, K. S., Bodner, S. R., Weber, R. M., Walker, K. P. and Cassenti, B. N., “Constitutive modeling for isotropic materials,” *NASA Report 174718*, 1984,

[4] L. A. Dombrovsky, “Incremental constitutive equations for Miller and Bodner-Partom viscoplastic models”. *Journal of Computers and Structures*, Vol. 44, pp. 1065-1072, 1992.

[5] H. Alberg, “Material modelling for simulation of heat treatments”. *Licentiate Thesis, Department of Applied Physics and Mechanical Engineering Division of Computer Aided Design*, 2003.

[6] J. L. Chaboche, “A review of some plasticity and viscoplasticity constitutive theories”, *International Journal of Plasticity*, Vol. 24, pp. 1642-1693, 2008.

[7] M. C. Araujo, “Non-linear kinematic hardening model for multiaxial cyclic plasticity”, *Thesis submitted in The Department of Civil and Environmental Engineering at the Louisiana State University*, 2002.

[8] K. P. Walker “Research and development program for nonlinear structural modeling with advanced time-temperature dependent constitutive relationships”. *NASA report*, CR-165533, 1981.

[9] R. D. Krieg, “Numerical integration of some new unified plasticity-creep formulations”, *Proc. Of 4th International Conference on Structural Mechanics in Reactor Technology*, San Francisco, M6/b, 1977.

[10] T.Y. Chang and R.L. Thompson, “A computer program for predicting nonlinear uniaxial material responses using viscoplastic models”. *NASA report*, TM-83675, 1984.

FLOW CHARACTERIZATION OF LIQUID FUELED HIGH VELOCITY OXY-FUEL THERMAL SPRAYS

Diaaeldin Mohamed[1], Luisa Cabrera[1], Ana Rios[1], Norman Love[1] and Ahsan Choudhuri[1*]
[1] Department of Mechanical Engineering, University of Texas at El Paso, El Paso, Texas 79968, USA
* Corresponding author (ahsan@utep.edu)

ABSTRACT

High-velocity oxy–fuel (HVOF) thermal spraying system is a highly promising technique for applying durable coatings on structural materials for corrosive and high temperature environments in advanced ultra-supercritical coal-fired (AUSC) boilers, steam turbines, and gas turbines. Liquid-fueled high-velocity oxy-fuel (HVOF) thermal spraying systems are capable of generating more momentum output to powder particles in comparison with gas-fueled systems. The use of low-cost fuel such as kerosene makes this technology particular attractive. The combustion of kerosene is very complicated due to the variation of fuel composition and subsequently makes it extremely challenging for process control. A computational fluid dynamics (CFD) model has been developed to predict gas dynamic behavior in a liquid fueled HVOF thermal spray gun in which non-premixed oxygen and kerosene are burnt in a combustion chamber linked to a parallel-sided converging-diverging nozzle. The CFD analysis is applied to investigate axisymmetric, steady-state, turbulent, compressible, chemically reacting, subsonic and supersonic flow inside and outside the gun. The gas axial velocity and axial temperature are presented for various locations inside and outside the gun. The calculated results show that the most sensitive parameters affecting the process are the equivalence ratio and total gas flow rate. Gas dynamic behavior along the centerline of the gun depends on both total gas flow rate and equivalence ratio. The numerical simulations show that the gas axial velocity and axial temperature distribution depend on both flow rate and equivalence ratio. The maximum velocity and temperature are achieved at the highest flow rate and/or richest equivalence ratio.

1. Methodology

In this study, flow in the dual fueled HVOF thermal spray gun presented in a previous study by the same authors[1] is computationally modeled using liquid fuel (kerosene). A detailed schematic of the gun is illustrated in Fig. 1-a. The gun consists of five main components: injector, combustion chamber, converging-diverging nozzle, barrel, and cooling jacket. Non-premixed kerosene and oxygen streams are injected axially into the combustion chamber and energy generated by the combustion process is transformed into a hot high-pressure gas. This gas is accelerated down through the convergent–divergent nozzle and the long barrel. An advanced ethylene glycol formula called ‘Dynalene (HC-10)’ is utilized to avoid over-heating of the gun. Powder particles are injected into the middle section of the barrel through a tapered angle by a carrier gas; this design can effectively reduces the overheating of powder particles. The current study is focused on the combustion process and subsequent gas flow pattern, while particle dynamics and gas–particle interactions are not included. The computational domain used in the present simulation is shown in Fig. 1-b. Since the gun geometry is symmetrical about its axis, a two-dimensional (2-D) axisymmetric grid is used to simulate the gas phase flow behavior.

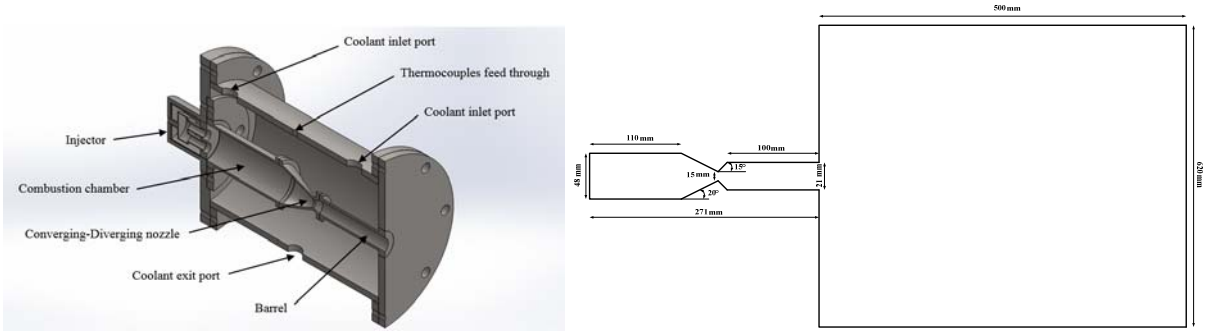

(a) (b)

Figure 1. a) 3-D cross-sectional schematic of the current HVOF thermal spray gun; b) Schematic of gun geometry and computational domain with dimensions shown

A commercial CFD code, ANSYS Fluent 13.0 is used to perform numerical simulations of the fluid flow in HVOF thermal spray system by solving the conservation equations of mass, momentum, energy and species. A two-equation, realizable k −ε turbulence model is employed for the turbulent flow field. In comparison with the standard k –ε model, the realizable k −ε model contains a new formulation of the turbulent viscosity where the dynamic viscosity coefficient is no longer constant.

1.1 Modeling Parameters

Table 1 presents a summary of working conditions for the investigated cases in this study. Three different oxygen mass flow rates were considered, namely: A (20 g/s), B (25 g/s), and C (30 g/s). At each of these flows three different equivalence ratios were investigated: 0.9 (lean fuel mixture), 1.0 (stoichiometric fuel mixture), and 1.1 (rich fuel mixture). Equivalence ratio for this study is defined as the fuel to oxygen ratio divided by its stoichiometric value. The inlet temperatures of oxygen and kerosene are considered to be uniform at 300 K. Axisymmetric boundary conditions are applied along the central axis of the combustion chamber. The interior surfaces of the gun are protected by the coolant from outside and defined as non-slip wall from inside with a constant temperature of 350 K. The gas exhausts from the gun to air, where external pressure boundary is applied to the ambient temperature of 300 K and ambient pressure of 1.013×10^5 Pa.

Table 1. Summary of working conditions

Case	Oxygen mass flow rate, g/s	Kerosene mass flow rate, g/s		
		Φ = 0.9 (Lean, L)	Φ = 1.0 (Stoichiometric, S)	Φ = 1.1 (Rich, R)
A	20	5.2	5.8	6.4
B	25	6.5	7.2	7.9
C	30	7.7	8.6	9.5

2. Results & Discussion

Figure 2-a shows the gas axial velocity along the centerline. Case C-L has velocity of 2300 m/s at nozzle exit while case C-R has a velocity of 2650 m/s at same location. Therefore, the maximum axial gas velocity is achieved at a rich equivalence ratio with constant flow rate. Case

A-R has a velocity of 1850 m/s at nozzle exit while case C-R has a velocity of 2650 m/s at same location, Fig 2-a. Hence, the maximum axial velocity is achieved at the highest total flow rate at constant equivalence ratio. Consequently, increasing the total gas flow rate and/or equivalence ratio results in increasing the axial velocity at nozzle exit as well as the barrel section exit. It is clear that gas velocity decay in the free jet due to entrainment of air.

Figure 2-b shows the variation of centerline gas axial temperature with axial distance. The gas temperature starts at an atmospheric value near the injector face followed by a significant increase in the combustion chamber. Temperature continues increasing inside the convergent-divergent nozzle and reaches its maximum value at nozzle throat. Case C-L has a temperature of 3200 K at nozzle throat while case C-R has a temperature of 3300 K at same location. Hence, maximum gas temperature is achieved at the richest equivalence ratio with constant flow rate. Cases A-R, B-R and C-R have temperatures of 3075 K, 3150 K, and 3300 K respectively at nozzle throat, Fig. 2-b. Maximum gas temperature is achieved at the highest total flow rate at constant equivalence ratio. Consequently, increasing the flow rate and/or equivalence ratio results in increasing the gas temperature in the barrel section. It is clear that gas temperature decay in the free jet due to the entrainment of air.

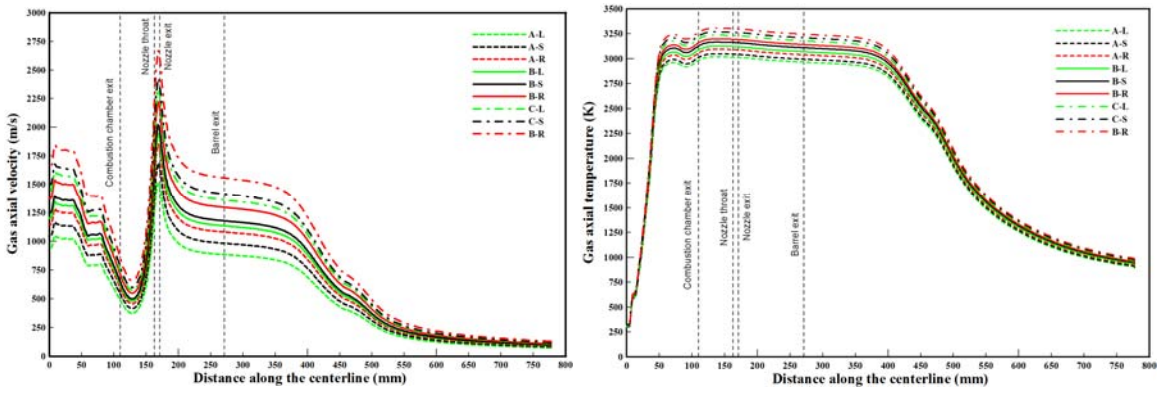

(a) (b)

Figure 2. a) Variation of gas axial velocity with distance along the centerline of the computational domain; b) Variation of gas axial temperature with distance along the centerline of the computational domain

References

[1] Mohamed, D., Cabrera, L., Love, N., Choudhuri, A., "High Velocity Oxy-Fuel Thermal Spray Gun Design" *52nd Aerospace Sciences Meeting*, 2014, National Harbor, MD, USA.

DESIGN AND WATER FLOW TESTING OF A LOX/LCH4 PINTLE INJECTOR

I. Lopez[1], A. Johnson[1], A. Patel[1], R. Ponce[1], M. Lopez[1], E.Flores[1], G.Martinez[1], Ahsan Choudhuri[1*]
[1] Mechanical Engineering, University of Texas at El Paso, El Paso, TX 79968, USA
* Director of Center for Space Exploration Technology Research (cSETR)

ABSTRACT

The present paper discusses of the development and construction of a liquid oxygen (LOX) and liquid methane (LCH_4) pintle injector for a 2000 lbf rocket engine. The focus of the project includes the design and fabrication of an injector that matches set thruster requirements as well as the construction of an experimental set up to perform preliminary water flow tests to confirm expected spray patterns from design principles and previous CFD modeling [1].

1 Introduction

In rocket propulsion science, injector design is of particular importance given its direct influence on rocket engine performance and stability [2]. Different injection methods have been developed over time for different applications, such as showerhead, impinging, or coaxial injection. The pintle injector was developed around the 1950s and demonstrated the capacity to deliver stable high combustion efficiency (96-99%) and throttleability for an extensive range of thrust levels (5 lbf – 650 klbf) in bipropellant engines [3]. This particular injector stands apart due to its exclusive geometrical features and propellant injection. In general, this type of injector comprises of the impingement between an axial and a radial propellant jet. The radial jet is usually delivered from a central channel with a contoured end (or pintle head) that distributes the flow outwardly. The axial jet is formed by injecting propellant from an annular orifice formed between the central channel and the body of the injector. The collision between both creates a conical spray towards the combustion chamber, as shown in Fig 1 [3].

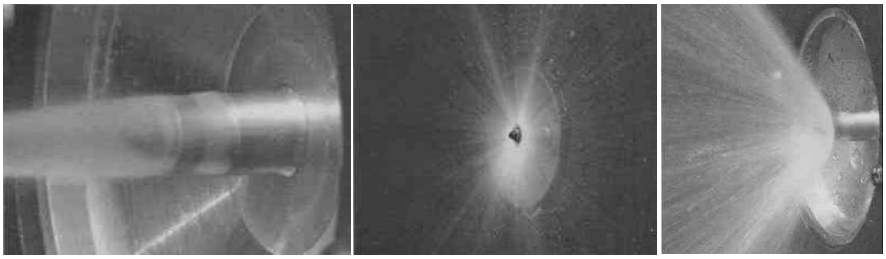

Fig. 1. Injection characteristics of a pintle injector (axial, radial, and combined flow)

2 Project Requirements

Given its advantages, the pintle injector was selected to be studied for use in a 2000 lbf LOX/LCH_4 rocket engine. Table 1 summarizes some of the requirements for this engine.

Parameter	Description
Max Thrust	2000 lbf
Specific Impulse (I_{sp})	216 s
Chamber Pressure	213 psia (200 psig)
Mixture Ratio (MR)	2.7

Table 1. Design requirements for the pintle injector

Maximum thrust, specific impulse, chamber pressure, and MR were taken from defined parameters necessary for the flight of a suborbital vehicle [1]. Propellant weight flow rates were then defined from the thrust, specific impulse, and mixture ratio. They are 6.76 lbf/s and 2.50 lbf/s for LOX and LCH_4, respectively.

3 Injector Design

With the requirements established, it was possible to create preliminary geometries to design and fabricate a pintle injector for those parameters. The major areas of interest in the injector design were the pressure drop across the injector, area of injection, and the total momentum ratio.

3.1 Pressure Drop and Area of Injection

Adequate propellant pressure drop (ΔP) across the injector is of significant importance because it imparts the increase in injection velocity necessary for propellant atomization and prevents the onset of low frequency instabilities [2]. From literature, a reasonable ΔP should be no less than 20 percent of chamber pressure [1][2]. Since the chamber working pressure was to be 200 psig, a 20 psi ΔP was chosen. In order to create the pressure drop, it is necessary to size the area of injection that will deliver that ΔP. To do so, Eq. 1 was employed [2].

$$A = W\sqrt{\frac{2.238K}{\rho\Delta P}} \tag{1}$$

Here A is the area of injection, W is the propellant weight flow rate, K is the minor loss coefficient, ρ is the propellant density, and ΔP is the pressure drop. Employing this formula, it was determined that the area of injection for both LOX and LCH_4 should be 0.247 in^2 and 0.126 in^2, respectively. Utilizing the injection areas and the flow rates allow one to calculate the injection velocities of 55.3 ft/s for LOX and 108.3 ft/s for LCH_4.

3.2 Total Momentum Ratio

An important design factor in pintle injectors is the total momentum ratio (TMR). The TMR is defined as the ratio between the momentum of the radial jet and the momentum of the axial jet, as shown in Eq. 2 [4].

$$TMR = \frac{(mv)_r}{(mv)_a} \tag{2}$$

Here m is the mass flow rate, v is the jet velocity, and subscripts r and a stand for radial and axial, respectively. In this design, the oxidizer (LOX) was selected to be the radial propellant to keep the fuel closer to the wall and provide cooling (called oxidizer-centered). Consequently, the TMR = 1.380. As mentioned before, collision between propellant jets creates a conical spray;

thus, the resulting spray cone half angle depends on the TMR. To estimate the spray half angle, θ, a direct sum of the momentum vectors of both the radial and axial jets was conducted to find the resulting vector and the corresponding half angle. This results in the following relationship (Eq. 3) [1].

$$\theta = tan^{-1}(TMR) \tag{3}$$

In a previous study, CFD analysis was conducted to test the validity of Eq. 3 and the results were acceptable [1]. Using Eq. 3, the half angle was estimated to be around 54 degrees. In oxidizer-centered designs, impact of the oxidizer on the chamber walls can cause damage or affect combustion efficiency [1][4]. To assess this matter, future tests with varying TMR values will be conducted to observe its effect on the injection characteristics and spray angle.

4 Water Testing

In order to verify the design principles and performance of the injector, water flow tests will be conducted. The main objectives for these tests are to measure the ΔP vs. flow rate to measure flow resistance and validate the design pressure drop, to visually characterize the spray pattern and angle, and to vary the mixture ratio and TMR to observe its effect on the spray angle (and compare to preceding CFD models [1]).

From the defined geometrical characteristics and dimensions an injector was designed and fabricated for water flow testing. The injector was sized so as to keep water flow rates equal to the actual LOX and LCH_4 flows. The design and fabricated injector can be seen in Fig 2.

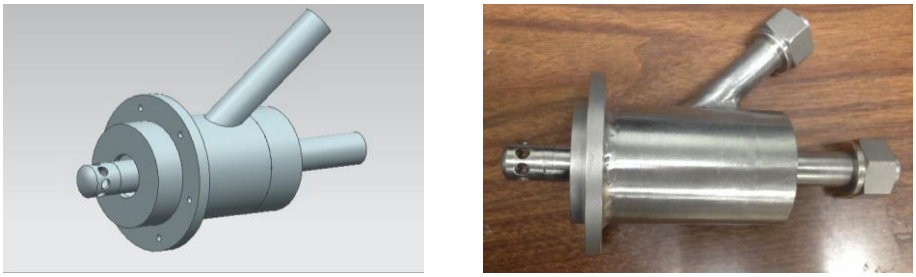

Fig. 2. Pintle CAD model and actual fabricated pintle injector

Moreover, a water test setup was constructed to test the current and future injectors. This setup is shown in Fig. 3.

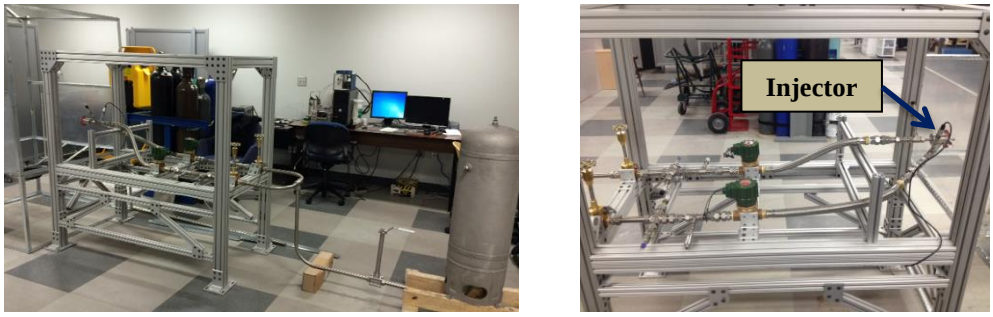

Fig. 3. Test setup for injector water flow testing

5 Conclusions and Future Work

A pintle injector was selected to operate for a 2000 lbf LOX/LCH_4 engine. Based on a set of operating conditions, the critical components of the injector were defined to design and construct a first generation injector. Water tests will follow to test the performance of the injector. To do so, a water test setup was constructed, which will also be employed to water test future injectors. Once initial tests are conducted and the necessary data acquired, a new and improved injector will be designed for cold flow (cryogenic) testing.

7 References

[1] G. Martinez, I. Lopez, J.L. Mena, and A. Choudhuri, "CFD analysis of a LOX/methane pintle injector rocket engine". 4th Southwest Energy Science and Engineering Symposium, El Paso, TX, 2014.

[2] D. K. Huzel, D. H. Huang, "*Mondern egineering for design of liquid-propellant rocket engines"*, Rev Sub ed., American Institute of Aeronautics and Astronautics, 1992.

[3] G. A. Dressler, J. M. Bauer, "TRW pintle engine heritage and performance characteristics," *AIAA 2000-3871*, pp. 1-22, 2000.

[4] V. Yang, M. Habiballah, J. Hulka, M. Popp, "*Liquid rocket thrust chambers aspects of modeling, analysis, and design"*, Rev Sub ed. American Institute of Aeronautics and Astronautics, 2004.

THE DESIGN OF A LOX/LCH4 REACTION CONTROL SYSTEM THRUSTER

A. Johnson[1], I. Lopez[1], A. Patel[1], R. Ponce[1], M. Lopez[1], E.Flores[1], Ahsan Choudhuri[1*]
[1] Mechanical Engineering, University of Texas at El Paso, El Paso, TX 79968, USA
* Director of Center for Space Exploration Technology Research (cSETR)

ABSTRACT

The research done within this report consists of the development of a LOX/LCH4 reaction control system (RCS) thruster. This project is a continuation of past work between the University of Texas at El Paso (UTEP) and NASA JSC. The focus was to design a small thrust range RCS thruster which operated at a high efficiency while still meeting project requirements. The development of the thruster is outlined within this report which breaks down numerous components and theory used to design.

1 Introduction

Green propellant combinations such as LOX/LCH4 have been of recent study due to the many advantages that they present. Oxygen and methane have the potential for in-situ resource utilization (ISRU) on the surface of Mars which is a goal of NASA's to travel to in the near future [1]. The research done within this project analyzes a reaction control system (RCS) thruster that uses LOX/LCH4 as its propellant. RCS thrusters in practice are generally used to rotate and/or stabilize a vehicle in space about three axes [2]. The background for this project was research that had been conducted on a previous RCS thruster that NASA JSC provided to UTEP. More specifically, this project looks into the design of the thruster and the proper sizing to ensure high efficiency, reliable ignition, and thrust repeatability. The following sections outline the design requirements and the theory behind the design of various components for the thruster.

2 Design Requirements

Table 1 below highlights the design requirements used for the RCS thruster

Parameter :	Description:
Propellant Combination	LOX/LCH4
Theoretical Specific Impulse	220-seconds (sea level)
Thrust	8 lbf Steady State
Chamber Pressure	100 psia
Minimum Impulse Bit	> 21 lbf-s (3 sec burns)
Ignition Method	Spark ignition for liquid-liquid firings

Table 1. Design requirements for RCS thruster

Project goals were also established for future testing with major areas of concern being specific impulse (I_{sp}) values, ignition reliability, and repeatable impulse bits. For this design the Isp requirement was to be greater than 85% theoretical max I_{sp}; and, ignition reliability was to be greater than 90% of total test firings.

3 RCS Thruster Design

For this specific design, the thruster could be broken up into 4 multiple parts which include the nozzle, the chamber, ignition source, and the LOX/LCH4 manifolds. Much of the thermodynamic analysis for LOX/LCH4 combustion was analyzed through software named Rocket Propulsion Analysis (RPA) which contains databases of propellant combination

properties [3]. Using RPA and the design requirements mentioned in the previous section a direct correlation between thruster efficiency and propellant mixture ratio could then be analyzed to obtain optimal performance. From this correlation an I_{sp} of 220-seconds at a mixture ratio of 2.7 was then found to be optimal. Using these two parameters propellant inlet conditions could then be found which would then size injection and chamber components.

3.1 Nozzle Design

The nozzle was designed to be conical with an area expansion ratio of ~ 10. This parameter was selected primarily based off of past research which stated that for sea level thrusters an area ratio of 10 was common [4]. Using the characteristic velocity, C*, that was obtained from the combustion properties of LOX/LCH4 the throat of the chamber could then be sized. The formula below relates area of the throat to C* [4]

$$C^* = \frac{P_c A_t g_c}{w_p} \tag{1}$$

Since the chamber pressure, P_c, and weight flow of propellant, w_p, were also known, the area of the throat was found to be $A_t = 0.0695$ in.^{2} which gave a throat diameter of $D_t = 0.3$ in.

3.2 Chamber Design

Chamber design was iterative in that three major parameters needed to be known: delta P across the LCH4 injection orifices, residence time, and sauter mean diameter (SMD) of a LCH4 droplet. The injection type for this thruster was shear coaxial in which the sprays from both LCH4 and LOX would impinge upon each other. Since chamber volume is dependent on residence time, LCH4 injection was the primary driver for the sizing of the thruster chamber volume. In order to calculate the injection area necessary to produce the required pressure drop across the injector, the following relationship was used, which employs a simplified form of the Bernoulli's equation including minor head losses [2].

$$A = \dot{W}\sqrt{\frac{2.238K}{\gamma \Delta P}} \tag{2}$$

Where A is the injection area, W is the propellant flow rate, ΔP is the pressure drop across the injector, ɣ is the propellant specific weight, and K is the sum of the minor loss coefficients across the injection orifices. For this analysis a liquid methane flow rate of 0.1 lb/s and a pressure drop of 40 psi were employed, with an assumed K = 1.7. Once this relationship was established a specific orifice diameter could then be determined for a given number of orifices. Knowing this orifice diameter for the injector the SMD of a droplet could then be calculated based off of the following relationships [5]

$$SMD = A\left[\frac{\sigma^{0.5}\mu_L}{\rho_A^{0.5}\Delta p_L}\right]^{0.5}[t\cos(\theta)]^{0.25} + B\left[\frac{\sigma\rho_L}{\rho_A\Delta p_L}\right]^{0.25}[t\cos(\theta)]^{0.75} \tag{3}$$

$$A = 2.11[\cos 2(\theta - 30)]^{2.25}\left(\frac{3.4\times10^{-4}}{d_0}\right)^{0.4} \qquad B = 0.635[\cos 2(\theta - 30)]^{2.25}\left(\frac{3.4\times10^{-4}}{d_0}\right)^{0.2}$$

Where σ is the liquid surface tension, μ_L is the liquid viscosity, ρ_A is the density of the environment (Assumed to be the density of the combustion products at 100psi), ρ_L is the liquid density, ΔP_L is the injection pressure differential across the nozzle, θ is the half spray angle, d_o is the discharge orifice diameter, and t is the film thickness, given by [5]

$$t = 2.7\left(\frac{d_0 FN\mu_L}{\sqrt{\Delta p_L \rho_L}}\right)^{0.4} \qquad FN = \frac{\dot{m}_L}{\sqrt{\Delta p_L \rho_L}} \tag{4}$$

All properties were known and found at a fuel inlet pressure of 140 psi. Therefore, the only unknown was the orifice diameter, d_o, which depended on delta P across the injector as mentioned in equation 2. After these relationships were known the residence time could then be found based off of a relationship between drop lifetime and drop diameter. Drop lifetime is given as [6]

$$t_e = \frac{\rho_F {D_o}^2}{8(\frac{k}{c_p})_g \ln(1+B)} \qquad B = \frac{c_{pg}(T_f - T_b)}{L} \tag{5}$$

The values for each are found based off of the combustion properites of LOX/LCH4 using RPA software. The definition of each value is as follows: T_f is the flame temperature, T_b is the boiling point of fuel, L is the latent heat of vaporization, c_{pg} is the mean specific heat of gas, ρ_F is the density of fuel, k is the thermal conductivity of gas, and D_o is the initial drop diameter. Once SMD was found in equation 3 this value could be used to interpret the residence time in equation 5. Knowing the residence time the chamber volume could then be calculated based off the following relationship [2]

$$V_c = \dot{W} v t_s \tag{6}$$

Where V_c is the total chamber volume, W is the propellant flow rate, v is the combustion product specific volume, and t_s is the residence time. Using a contraction ratio of 3:1 the area of the chamber could be readily determined based off the area of the nozzle. This gave a diameter of the chamber to be 0.5 in. With 4 LCH4 injection orifices at 0.014 in. in diameter, the length of the chamber from the injection orifices to the convergent section of the nozzle was then found to be 2.02 in. For LOX injection 4 sets of impinging orifices were designed based off of a 20 psi pressure drop (line injection pressure was at 140 psi) using equation 2; the value of each orifice was found to be 0.015 in.

3.3 Ignition Source

The ignition for the thruster would be spark ignited through an extended electrode tip from a spark plug. 25 kV would be used for the spark in which an arc would take place between the electrode tip and the chamber wall. Figure 1 below shows the configuration of the spark plug in the chamber

Fig.1. Spark plug configuration within thruster chamber

3.4 LOX/LCH4 Propellant Manifolds

For both LOX and LCH4 injections the manifolds were made such that a pressurized ring of fluid would form. This is because of the injection type which is shear co-axial for both the oxidizer and the fuel. A key note is the LCH4 manifold which extends a great length of the chamber with a pocket to allow for cooling of the nozzle and the chamber. Cooling of the nozzle and the chamber is done by a separate line which contains LCH4 as well. This allows for varied percentages of cooling to take place which could then be evaluated once testing begins commencement. Figure 2 below shows a cross sectional view of the RCS thruster with each component specified and figure 3 shows an external view of the thruster

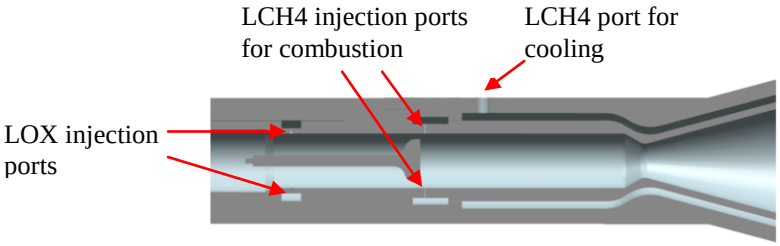

Fig.2. Cross sectional view of RCS thruster assembly

Fig.3. Exterior view of RCS thruster assembly

4 Conclusions and Future Work

Overall, the research done provides a reaction control system thruster which was sized based off of optimal thruster performance. This thruster is designed as a first iteration for cooling such that it is not in flight ready. Cooling of the thruster is a primary research topic moving forward since it has a substantial amount to do with system I_{sp}. Therefore, hot fire tests will be conducted in the future to obtain proper cooling percentages which will still enable project goals. From there, a second iteration of the thruster will be designed to include LCH4 for combustion and cooling in one line instead of two separate lines.

5 References

[1] "NASA's Journey to Mars". (n.d.). Retrieved January 1, 2015, from http://www.nasa.gov/content/nasas-journey-to-mars/#.VQDUFvnF_3Q.

[2] D. K. Huzel and D. H. Huang "*Modern engineering for design of liquid-propellant rocket engines*". Washington, DC, AIAA, 1992.

[3] A. Ponomarenko "*RPA: Tool for Liquid Propellant Rocket Engine Analysis C++ Implementation*". 2010.

[4] C. D. Brown "*Spacecraft Propulsion*". Washington, DC, AIAA, 1996.

[5] X. F. Wang and A. H. Lefebvre "*Atomization and Spray Technology*". Vol. 3, pp 209, 1987.

[6] A. Lefebvre "*Atomization and Sprays*". West Lefayette, Taylor and Francis, 1989.

A DESIGN STAGE OPTIMIZATION METHOD OF WIND FARM PLACEMENT LAYOUT ON NON-FLAT TERRAINS

Carlos A. Garcia Rosales[1], Tzu-Liang (Bill) Tseng[1]*
[1] Department of Industrial, Manufacturing and System Engineering
The University of Texas at El Paso
500W, University Ave.
El Paso, TX 79968, USA;
* Corresponding author (btseng@utep.edu)

Keywords: *wind turbine; cluster identification algorithm (CIA); multi-objective genetic algorithm (MOGA); optimization of wind farm layout; wind energy*

1 Introduction

Currently, wind energy is receiving considerable attention as an emission-free, low cost alternative to traditional energy sources. For large grid-connected arrays of turbines, they are becoming an increasingly important source of wind power-produced commercial electricity. In this paper, a method entitled Cluster Identification Algorithm (CIA) and an optimization approach called a Multi-Objective Genetic Algorithm (MOGA) [1] are integrated and developed to solve the problem of determining the optimal wind farm layout [2]
on non-flat terrain and at the same time it maximize wind power, the efficiency of wind power affected by the aerodynamic losses and minimizes cost due to the size and quantity of wind turbines installed in the wind farms.

2 Methodology

Based on the findings from literature review and our current research objectives, the Cluster Identification Algorithm (CIA) and an optimization approach called a Multi-Objective Genetic Algorithm (MOGA) are proposed. Figure 1 depicts detailed steps in applying the algorithms.

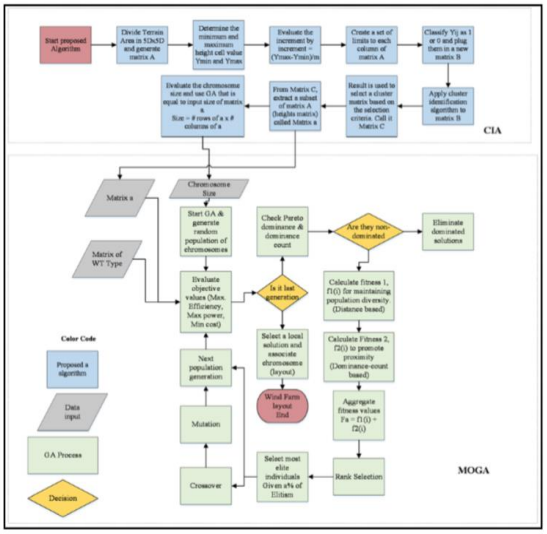

Figure 1. Detailed steps in applying the algorithms

2.2 Objective functions

The main objective of this paper is to determine the optimal positioning of wind turbines [3-5] that will maximize wind power generation, maximize wind power efficiency and minimize the cost by using the genetic algorithm in a non-flat terrain application. It can be summarized in the next optimization statement:

Efficiency

$$\text{Max}\ \{\sum_{j=1}\sum_{i=1} 1/2(\rho A U^{3}_{(ij)} X_{ij}\text{Area}_{ij})\}/\{\sum_{j=1}\sum_{i=1} P_{avg}(\frac{Y_{aij}+L_K}{H_o})^{(3*\alpha)}\ X_{ij}\text{Area}_{ij}\} \quad (1)$$

Power

$$\text{Max}\ \{\sum_{j=1}\sum_{i=1} 1/2\rho A U^{3} X_{ij}\text{Area}_{ij}\} \quad (2)$$

Cost

$$\text{Min}\ \sum_{j=1}\sum_{i=1} X_{ij}(\text{Unit cost})\ \ \forall\ i = 1,2,3 \ldots . n, j = 1,2, \ldots m \quad (3)$$

Where:

Pavg= the average power in the wind at a height H0 in W/m2, Yij = is the height of the terrain at an specific (i, j) position in meters, where (i=1, 2….m) (j=1, 2….n), LK= Hub Height in meters, H0= wind data normally 10 m and α = is the friction coefficient.

3 Case study results

A mountain terrain has been selected as the test site for this study. The CIA and MOGA algorithms are applied for this location in order to provide a validation for the proposed approach. A specific data set is available as the quantity of turbines by the types and characteristics. Terrain height information and wind speed data are also available (random generated). The height range of the mountainous terrain is from 10 km by 12.5 km. Figure 2 represents the selected and a matrix of height average. Figure 3 present the CIA matrix results and figure 4 the MOGA results (pareto front) after the 200th generation.

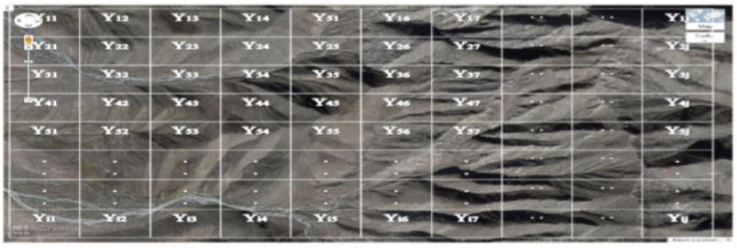

Figure 2. represents the selected and a matrix of height average

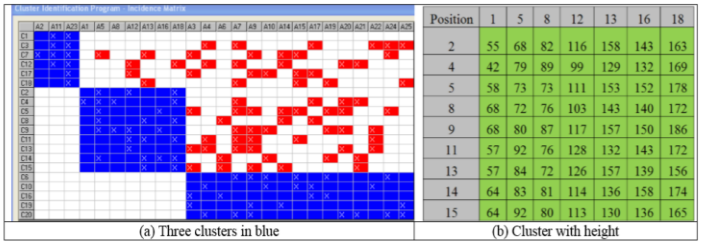

Position	1	5	8	12	13	16	18
2	55	68	82	116	158	143	163
4	42	79	89	99	129	132	169
5	58	73	73	111	153	152	178
8	68	72	76	103	143	140	172
9	68	80	87	117	157	150	186
11	57	92	76	128	132	143	172
13	57	84	72	126	157	139	156
14	64	83	81	114	136	158	174
15	64	92	80	113	130	136	165

(a) Three clusters in blue (b) Cluster with height

Figure 3. CIA matrix result

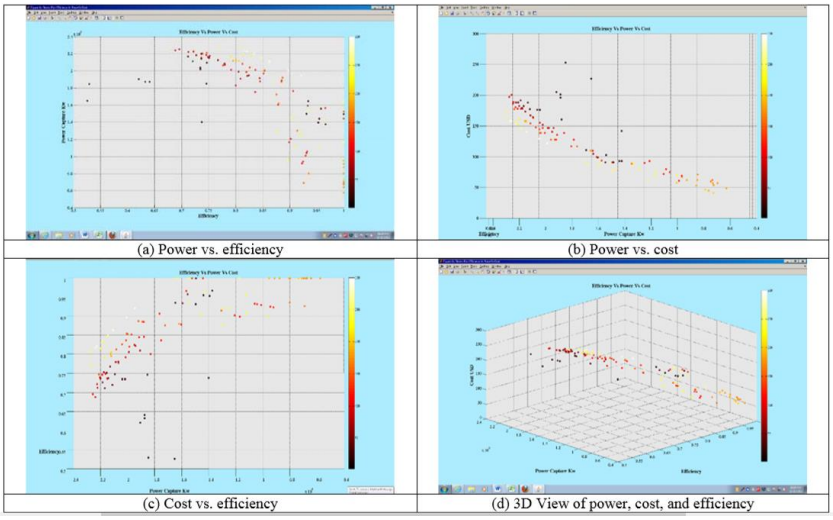

Figure 4. Pareto front 2D and 3D views

4 Conclusions

Most real-world wind farm design layout and real terrain cases are not exactly as two-dimensional. Many wind farm layout problems demand a simultaneous optimization of multi-objectives. The present work addresses such problems by integrating the CIA and MOGA algorithms to find the optimal positions of wind turbines on non-flat terrain areas. Optimal positions represent a specific location within the area under evaluation, which maximizes the wind power and the efficiency, while minimizing the cost. The function of CIA is to determine a cluster (subset) of suitable possible positions from a large-scale mountainous region that follows a path of heights from lower to higher in accordance with the wind directions. The outcome is to generate a subset of suitable cells, which serves as an input to the MOGA algorithm. The MOGA algorithm develops a set of non-dominated solutions for wind turbine positions that optimize the power, efficiency and cost.

References

[1] Taboada, H., Espiritu, J. & Coit, D., 2008. "MOMS-GA: A Multi-Objective Genetic Algorithm for System Reliability Optimization
Design Problems", IEEE Transactions on Reliability 57, 188-189.
[2] Stefan Lundberg, 2008, "Evaluation of wind farm layouts". Department of Electric Power Engineering Chalmers University of
Technology, S-412, 96.
[3] Hui Li, Zhe Chen, Henk Polinder., 2009, "Optimization of Multibrid Permanent-Magnet Wind Generator Systems", IEEE
TRANSACTIONS ON ENERGY CONVERSION 24, NO. 1
[4] Carlos M. Ituarte-Villarreal and Jose F. Espiritu, 2011, "Optimization of wind turbine placement using a viral based optimization
algorithm", Procedia Computer Science 6, 469–474.
[5] Grigorios Marmidis, Stavros Lazarou, Eleftheria Pyrgioti., 2008, "Optimal placement of wind turbines in a wind park using Monte
Carlo simulation". Renewable energy 33, 1455-1460.

DATA-DRIVEN FORECASTING ON BUILDING ENERGY CONSUMPTION

C. Cui[1]*, T. Wu[1]
[1] School of Computing, Informatics, and Decision Systems Engineering,
Arizona State University, Tempe, AZ, USA;
J. Weir[2]
Department of Operational Sciences
Air Force Institute of Technology, Dayton 45433, USA
J. Wen[3]
Department of Architectural and Environmental Engineering
Drexel University, Philadelphia 19104, USA
K. Lewis[4]
Department of Mechanical and Aerospace Engineering
University at Buffalo, Buffalo 14260, USA
H. Kim[5], B. Tseng[5]
Department of Industrial, Manufacturing and Systems Engineering
University of Texas at El Paso , El Paso, 79968, USA
* Corresponding author (ccan1@asu.edu)

ABSTRACT

This paper evaluates various data-driven approaches for forecasting on short-term (daily) building energy consumption. Specifically, 6 meta-modeling algorithms are tested on 8 different types of commercial reference buildings developed by Department of Energy. It is concluded that the overall data-driven modeling performance is satisfactory. Kriging generally outperforms others in terms of prediction accuracy and robustness, and Artificial Neural Network and Multivariate Adaptive Regression Spline also perform well in some cases.

1 Background

In energy industry, data-driven modeling has emerged as an alternative to physics-based modeling for real-time system modeling and forecasting. Various data-driven models have been proposed, including statistical and machine learning models. Researchers have taken a trial-and-error approach, that is, a number of different data-driven models are studied and evaluated and among which the best performer (evaluated against metrics, e.g., accuracy) is chosen. In this research, we are interested in evaluating various data-driven models for energy consumption forecasting in the context of buildings. Specifically, we carefully choose six methods due to their demonstrated applicability in this industry. The six methods are Kriging [1], Support Vector Regression (SVR) [2], Radial Basis Function (RBF) [3], Multivariate Adaptive Regression Splines (MARS) [4], Artificial Neural Network (ANN) [5] and Polynomial Regression (PR) [6]. Eight different types of simulated buildings with the climate zone set as Phoenix, Arizona (DoE Reference buildings) [7] are tested. Their performance is compared in terms of prediction accuracy and robustness.

2 Experimental Setup

2.1 Training and Validation Data Generation

Similar to [8], both specification data and lagged data are included in the training data set for model development. Let *c* be the periodicity of the seasonality, *n* be the number of lags, *m* be the specification lag, *t* be the current time data index, the specification data indices are *t* - *c*, *t* - 2*c*,…, *t* - *mc*, while the lagged data indices are *t* -1, *t* -2,…, *t* - *n*. Let the test data *t* be F_0, and the unit of lag being one day, we have *n* being 6 (days), *c* being 7 (days). As a result, the training data consist of six days of lagged data and three days of specification data given test day being F_0. Note each day has 48 data points as the data is collected in a half-hour basis.
It is worth noting that it may not be appropriate to directly apply traditional cross-validation on time series data, because theoretical problems with respect to temporal evolutionary effects and data dependencies are encountered, where the fundamental assumptions of cross-validation might be invalidated. Racine [9] proposes "hv-block" cross-validation which is consistent for general stationary observations in the sense that the probability of selecting the model with the best predictive ability converges to 1 as the total number of observations approaches infinity. For illustration purpose, a graph depicting the designed cross-validation split on the training data set is given in Fig. 1 with the test data set F_0 being a Friday.

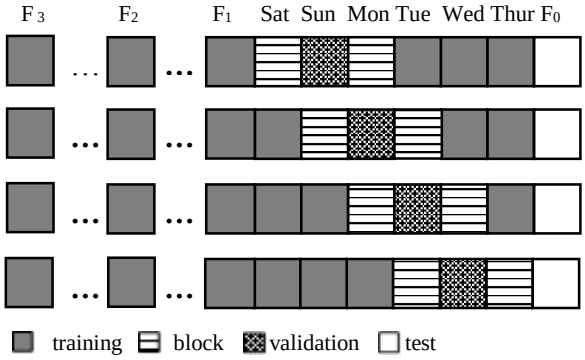

Fig.1. Cross-validation of training data split

2.2 Performance Evaluation Criteria

Normalized Root Mean Square Error (NRMSE) is used as the accuracy metric:

$$NRMSE = \sqrt{\frac{\sum_{t=1}^{n}(y_t - \hat{y}_t)^2}{n}} / (y_{max} - y_{min}), \quad (1)$$

where $\hat{y}_t$ is the model prediction for time *t*, y_t is the true output at time *t*, y_{max} is the maximum of y_t, y_{min} is the minimum of y_t, *n* is the number of time points, in this study y is the energy consumption (in kilowatt).

3 Experimental Result and Analysis

Table 1 summarizes the statistics of NRMSE of the six meta-models on 8 building scenarios with the best performers highlighted.

Table 1 NRMSE of 6 models on 8 buildings

Building Type	Kriging	SVR	RBF	MARS	ANN	PR
Large Office	0.043	0.177	0.055	0.026	**0.024**	0.066
Medium Office	**0.019**	0.101	0.063	0.038	0.029	0.035
Small Office	0.041	0.144	0.105	**0.030**	0.041	0.072
Supermarket	**0.020**	0.095	0.066	0.034	0.051	0.045
Full Service Restaurant	**0.017**	0.070	0.049	0.020	**0.017**	0.033
Hospital	**0.014**	0.113	0.149	0.023	0.025	0.030
Large Hotel	**0.031**	0.127	0.090	0.108	0.045	0.066
Midrise Apartment	0.026	0.120	0.099	**0.023**	0.033	0.044

It is observed that the overall performance of the six meta-models in terms of prediction accuracy is satisfactory with the average NRMSE being 0.058 (accuracy of 0.942). Among the six methods, Kriging generally outperforms others, and ANN and MARS perform well on one or two building scenarios as well. Table 2 summarizes the mean and standard deviation of the 6 models across 8 buildings. The standard deviation measures how consistent the corresponding model performs on different building cases, which could be interpreted as robustness. As seen in Table 2, the top robust models (measured by the standard deviation) are Kriging and ANN, while the least robust models are SVR and RBF.

Table 2 Mean and standard deviation of NRMSE on 6 models

Statistics	Kriging	SVR	RBF	MARS	ANN	PR
Mean	**0.026**	0.119	0.085	0.038	0.033	0.049
Std dev	**0.011**	0.033	0.033	0.029	**0.011**	0.017

The performance of the models is comprehensively evaluated using accuracy and robustness. It is concluded that Kriging is overall the best model among others. It is also observed that ANN and MARS perform well in some cases. The research findings provide practical guidelines for choosing forecasting models on building energy consumptions.

References

[1] G. Matheron, "note geostatistique N 28.pdf." p. 11, 1960.

[2] H. Drucker, Chris, B. L. Kaufman, A. Smola, and V. Vapnik, "Support vector regression machines," in *Advances in Neural Information Processing Systems 9*, 1997, vol. 9, pp. 155–161.

[3] N. Dyn, D. Levin, and S. Rippa, "Numerical Procedures for Surface Fitting of Scattered Data by Radial Functions," *SIAM Journal on Scientific and Statistical Computing*, vol. 7. pp. 639–659, 1986.

[4] J. H. Friedman, "Multivariate Adaptive Regression Splines," *The Annals of Statistics*, vol. 19. pp. 1–67, 1991.

[5] W. S. McCulloch and W. H. Pitts, "A logical calculus of ideas imminent in nervous activity," *Bull. Math. Biophys.*, vol. 5, pp. 115–133, 1943.

[6] J. D. Gergonne, "The application of the method of least squares to the interpolation of sequences," *Hist. Math.*, vol. 1, no. 4, pp. 439–447, Nov. 1974.

[7] M. Deru, K. Field, D. Studer, K. Benne, B. Griffith, P. Torcellini, B. Liu, M. Halverson, D. Winiarski, and M. Rosenberg, "U.S. Department of Energy Commercial Reference Building Models of the National Building Stock," 2011.

[8] J. Crespo Cuaresma, J. Hlouskova, S. Kossmeier, and M. Obersteiner, "Forecasting electricity spot-prices using linear univariate time-series models," *Appl. Energy*, vol. 77, no. 1, pp. 87–106, Jan. 2004.

[9] J. Racine, "Consistent cross-validatory model-selection for dependent data : hv -block cross-validation," *J. Econom.*, vol. 99, pp. 39–61, 2000.

STRESS TRUSS OPTIMIZATION BY GENETIC ALGORITHM & FEA

Mohammad Tauhiduzzaman, Dr. Pavana Prabhakar*
Department of Computational Science,
University of Texas at El Paso, El Paso, TX 79968, USA;
* Corresponding author (pprabhakar@utep.edu)

Keywords*:* 1. Genetic Algorithm; 2. Truss; 3. Crossover; 4. Mutation; 5. Fitness function

ABSTRACT

Genetic algorithm is an evolutionary algorithm which is population based metaheuristics and it also uses stochastic method. Initially the parameters selected for phenotype and this phenotype is converted to genotype. Every parameter has the boundary condition and possible generation is initialized by satisfying all condition. Convergence and divergence operator will operate on the population and give the offspring. So the best possible will go through a fixed number of iterative process and finally optimal solution set is produced. Since the main objective is to obtain the minimum weight for the structure and there is certain stopping criteria for the solution, so there is chance to select best possible solution set. Genetic algorithm is so ubiquitous that it can play a great role in the arena of structural optimization.

1. Introduction

Truss is a system of straight bars which are joined together at their end and also they have friction free joints. The trusses give us idea about two important parts which are members and the nodes. Traditionally, analyses of truss include stresses in the members and deflection at nodes. When load are applied to the truss nodes, it will subjected to tensile and compressive forces. Structural optimization has taken much attraction in recent times. During an optimization process, the optimal solution is achieved iteratively, with several repeated analysis for intermediate design "[1]".

2. Truss Optimization

Truss optimization based on three categories: 1) Sizing 2) Configuration 3) Topology Optimization. Sizing optimization takes cross- sectional area as a design variable. Configuration optimization takes nodal co- ordinates as design variables. Topology optimization use number of nodes and connectivity between nodes as design variables. Genetic algorithm is very efficient in doing multi- objective optimization. In this paper we are dealing with the following structure

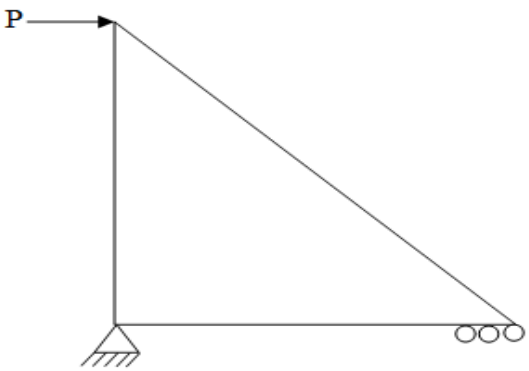

Fig.1. Truss structure

3. Genetic Algorithm

Holland first proposed the idea of genetic algorithm which is based on Darwin theory: if a population is of animal and plants lives in a some ecosystem, a better chance to survive and to leave the descendants have the individuals more adapted to the environment "[2]". Similar to nature, a set of possible solutions is created and they will compete with each other for propagation. Genetic algorithm gives us the possible solution of our objective function. Here are some important components of Genetic Algorithm:

3.1 Chromosomes

Chromosomes are the fixed length of binary strings of genetic algorithm. Every bit will carry certain characteristics. There will be certain parameters which are called phenotype and are converted to binary strings to represent genotype. By following the evolutionary operators best offspring are created.

3.2 Selection

Selection of individuals is based on fitness function. There are different kinds of selection process such as roulette wheel selection and tournament selection. Roulette wheel selection is based on fitness function and random values.

3.3 Crossover

Crossover is one the most important convergence operator. Initially two parent chromosomes are selected based on random values and then random position is created between these two mating chromosomes and they swap their bits and consequently new offspring are available.

Parent 1 : **A B C D E F G H** Offspring 1: **A B C D e f g h**

Parent 2 : **a b c d e f g h** Offspring 2 : **a b c d E F G H**

3.4 Mutation

Mutation is the divergence operator which change the bit based on random numbers. So, there is always a chance of every bit in the string to change from its initial condition. Since binary string is composed of 0 and 1 so the change of bit is limited to changing from 0 to 1 and vice versa.

Previous Offspring : **A B C D e f g h**
New Offspring: **A B C *D* e f g h**

4. Methodology

The stress truss optimization is based on the objective function:

$$W = l * \rho * A \quad (1)$$

The number of bits in each chromosome is depends on the number of gene. Here the only gene is area and the range of area gives us the idea of the length of binary string. Finally, it will give us the optimum set of solutions. It is clear that weight is decreasing for a certain number of iteration and then the optimum weight is available for the structure.

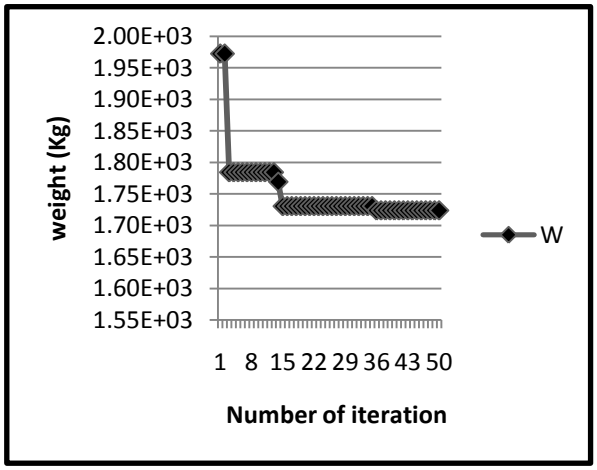

Fig.2. Weight vs number of iteration

5. Conclusion

In this paper, the main objective function is to get the minimum weight of the truss structure and genetic algorithm creates the possible solution set. MATLAB is used to perform the coding. More work regarding with FEA is required to perform by ABAQUS and the exchange of data between MATLAB and ABAQUS will give us the best optimum solution.

6. References

[1] Xu, T., Zuo, W., Xu, T., Song, G. & Li, R."*An adaptive reanalysis method for genetic algorithm with application to fast truss optimizaiton*".
[2]Sesok, D.& Belevicius, R." *Use of genetic algorithms in topology optimization of truss structures*".

MEASURED VERSUS GENERATED TEMPERATURE AND RAINFALL DATA IN A PAVEMENT SECTION IN NEW MEXICO

M.R Islam[1]*, M.A Hasan[1], R.A Tarefder[1]
[1] Department of Civil Engineering, University of New Mexico, Albuquerque, NM 87131, USA;
* Corresponding author (mdislam@unm.edu)

Keywords: *asphalt concrete, temperature, rainfall, AASHTOWare, measurement*

ABSTRACT

This study investigates the difference between the measured and the AASHTOware Pavement Mechanistic-Empirical (ME) Design software predicted temperature and rainfall data. These data are the basic input for designing Asphalt Concrete (AC) pavement. As a first step, temperatures at four different depths of AC have been measured from January 2013 to December 2013 in an instrumented pavement section in New Mexico. Then, the temperature profile of AC has been generated using the AASHTOWare Pavement ME Design software. Similar to the temperature, the rainfall data for the site has been measured from January 2013 to November 2013; this data was then compared with the predicted data using the AASHTOWare Design software. Results show that the AASHTOWare generated temperature is less than the measured temperature in summer; however, it is higher in winter. In addition, the AASHTOWare generated rainfall is always higher (up to 8 times) than the measured data.

Fig. 1. Installation of temperature probes and weather station.

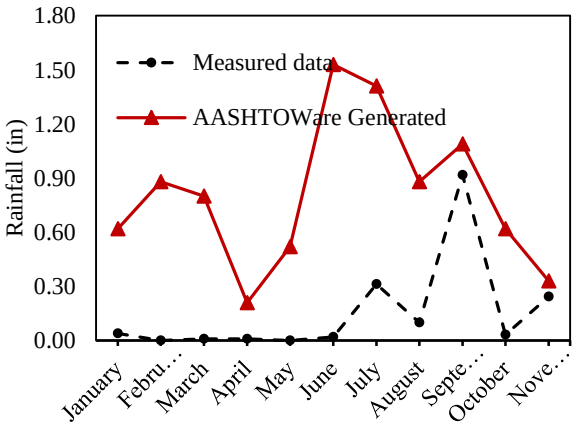

Fig. 2. Measured vs. predicted rainfall.

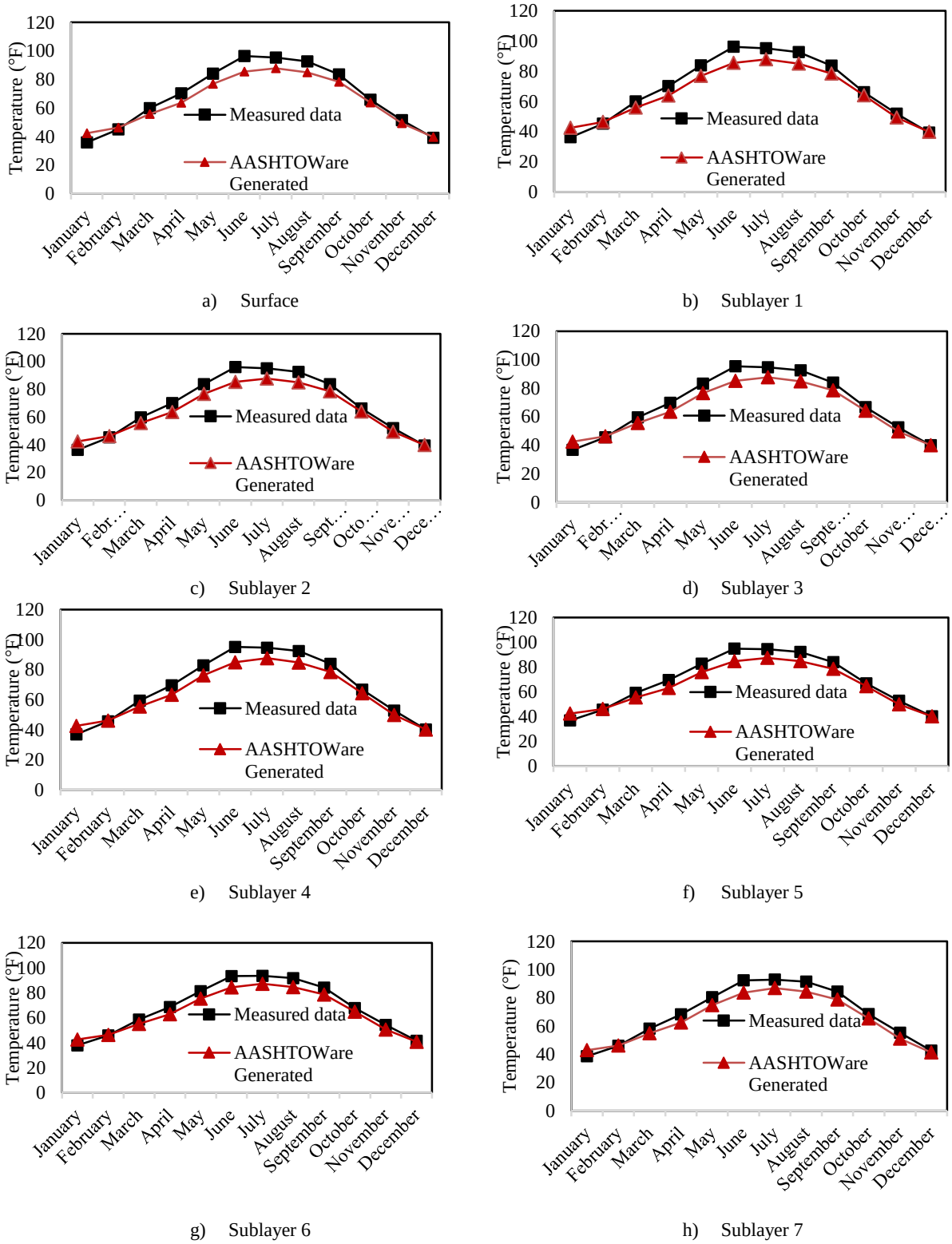

Fig. 3. Measured and AASHTOWare generated temperature in AC.

1 Introduction

The recently developed AASHTOWare Pavement Mechanistic-Empirical (ME) Design software correlates material properties with the climate data [1]. After correlating, it determines the probable damage in pavement. The climate data is obtained from the weather station close to the site. However, if there no weather station is available, it generates the climate data by interpolation using few weather stations' data located nearby. This study examines the generated temperature and rainfall data by comparing with the measured data for a pavement site in New Mexico.

2 Installing Temperature Probes

Four temperature probes were installed in the AC. The total depth of AC of the pavement was 10.5 in. The probes were bundled together such that after installing these remained at the surface level, at 2, 4 and 10.5 inches of depths of the AC. The bundled probes are shown in Fig.1. It also shows the installed weather station which measures the continuous rainfall data.

3 Analysis and Results

Fig. 2 shows the measured and the AASHTOWare generated rainfall data. It can be seen that the predicted rainfall data is always higher than the measured data. For example, the average measured rainfall at the test site was 0.01 in; however, the AASHTOWare generates this value to be 0.8 in. This over prediction is true for other months as well. The temperatures at four different depths of AC have been measured; the temperature at any other depth of AC has been calculated using interpolation. The interpolation is needed as the AASHTOWare divides the AC layer into different sublayers. Then, it determines the temperature at these sublayers. Fig. 3 presents the results obtained from the measurement and the AASHTOWare generated data. From Fig. 3(a), the predicted surface temperature is 18% greater than the measured temperature in January; however, it is 11% smaller than the measured temperature in June. These variations are almost same for any sublayer.

4 Conclusions

This study compares the AASHTOWare generated and the measured climate data for a pavement site in New Mexico. Based on the study on a single site, the following conclusions can be made:

(a) The AASHTOWare generated temperature data is less than the measured data in summer; however, it is good in winter.
(b) The AASHTOWare generated rainfall is always higher (up to 8 times) than the measured data.

Acknowledgements

The authors would like to appreciate the research funding provided by the New Mexico Department of Transportation (NMDOT).

References

1. AASHTO. *Mechanistic-Empirical Pavement Design Guide.* A Manual of Practice, July 2008, Interim Edition, American Association of State Highway and Transportation Officials, Washington D. C., 2008.

DESIGN AND NUMERICAL ANALYSIS OF HELICAL SHAPED TUBULAR SOLAR RECEIVER FOR CONCENTRATED SOLAR POWER PLANT

N. Hossain[1], S. Afrin[1], V. Kumar[1]*
[1] Computational Science, Mechanical Engineering, El Paso, TX 79968, USA;
* Nazmul Hossain (nhossain@miners.utep.edu)

Keywords: *Helical Receiver; Heat Transfer Fluid (HTF); Solar Power Tower; Residence time*

ABSTRACT

In the field of conventional cleaner power generation technology, concentrated solar power plants have introduced remarkable opportunity. In solar power tower, solar energy concentrated by the heliostats at one point produces very high temperature. Falling solid particle or heat transfer fluid passing through that high temperature region absorbs heat to generate electricity. Increasing the residence time of falling particle will result in more heat gain and increase efficiency. A novel design of solid particle receiver is approached in this paper which can increase residence time of falling particle resulting higher temperature gain. The helical shaped tubular solar receiver, placed at the focused sunlight region meets the higher outlet temperature and efficiency according to DOE's SunShot goal. Receiver material, Quartz-glass provides transparency and high temperature durability for greater performance. Helical shaped tubular solar receiver is modeled and analyzed with granular particle and air in multiphase flow to observe the temperature rise in one cyclic operation. Eulerian granular multiphase model is used with simulation software Ansys Fluent to analyze the flow.

1. Introduction

With rising demand of energy, scientists and engineers are looking for efficient ways of power generation from cleaner energy source to ensure a sustainable future. Unlike Concentrated Photovoltaic (CPV), CSP plant with thermal storage system can generate power when the sun is not available. In CSP plants, focused sunlight from heliostats provides a very high temperature at a small region. Heat gain by the heat transfer fluid at that region determines the efficiency.

Recent central solar receiver technologies can reach up to 600^{o}C using either steam or molten nitrate salt as the heat transfer fluid (HTF) [1]. Above 600^{o}C molten nitrate salt becomes unstable and shortcoming of steam as HTF is of its low heat capacity [2; 3]. In order to achieve cost effective power generation, we need to develop novel high temperature HTF and efficient high temperature solar receiver. National Renewable Energy Laboratory has proposed a near black body falling particle receiver with 85% efficiency and Sandia National Laboratories is developing a prototype of a curtain shape falling particle receiver with their facility [4; 5]. As the residence time of HTF is very small, it is important to maximize the residence time, so that sufficient heat absorption will occur at the concentrated beam region and required HTF temperature can be achieved in one cyclic operation. This may lead to generating electricity with conventional source in more cost competitive way.

In concentrated solar power tower, sunlight from a large area is accumulated by using heliostats to concentrate at one point. HTF is passed through that critical region to absorb heat energy and stored in absorber tank. It can be used to generate steam with heat exchanger. This steam is then passed through turbine to generate electricity. A schematic of solar power tower is as follows.

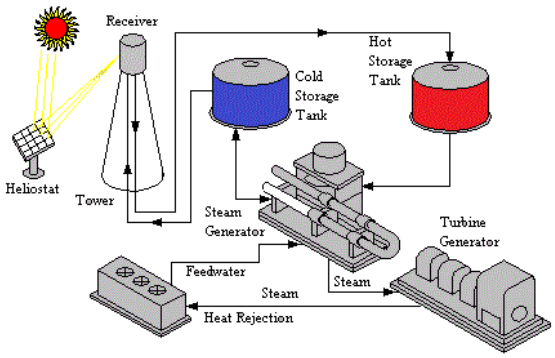

Fig: Schematic Diagram of Solar Power Tower Plant

2. Problem Statement

2.1. General Description

Our purpose is to increase residence time of falling particle. So, instead of vertical free falling, helical shaped tubular solar receiver is placed at the concentrated beam region. Dropping particle through helical receiver enables solid particles to gain more heat energy by increasing residence time.

For designing, Solidworks2013 software is used and for simulation, commercial software FLUENT 15.0 is used. In FLUENT, Eulerian granular multiphase model is considered. Air is used as primary phase and Alumina solid particle as secondary phase.

Receiver is designed as helical shaped hollow tube. The receiver is designed with height 1 m, width 0.4 m, tube thickness 3 mm, clockwise rotation with variable pitch 0.24 m and tube diameter. Quartz glass is considered as material of receiver for transparency and high temperature durability. The design dimensions are given in the following table.

Table 1: Dimension of Receivers

Receiver	tube inner dia (mm)	Pitch (mm)	Rotation	Arc Length (mm)
R1	44	250	4	5122.556
R2	54	250	4	5122.556
R3	64	250	4	5122.556
R4	44	200	5	6359.119
R5	54	200	5	6359.119
R6	64	200	5	6359.119

2.2. Computational Modeling

Multiphase flows where two phases exist but not chemically related are very common and several types of models are found relative to this system. Mixture model with homogeneous flow and Eulerian granular model are recommended in Ansys Fluent user guide. Mixture model has some limitations. So, Eulerian granular model for multiphase flow is considered for simulation.

Systems of mass, momentum and energy equation are solved for each phase. Two phases are coupled. Considering plug flow, laminar model is used for dispersed flow of solid particle in air. Air is used as primary

phase. Alumina [7] solid particles are used as secondary phase. Gravitational acceleration 9.81 m/s is applied at negative y-direction. Phase coupled simple scheme is used.

Alumina (AL2O3) is used as falling particle of diameter 0.5 mm, spherical shaped. Receiver wall outer surface temperature is considered 1000^{o}C and Inlet temperature 27^{o}C for both phases. Inlet velocity 1 m/s is used for air and 0.05 m/s for solid particle with 0.2 volume fraction. Alumina particle of 0.5 mm diameter with maximum packing limit 75% is considered.

3. Result

For solid particle through the helical receiver, following temperature change has been observed using the Ansys Fluent software. Velocity and temperature are plotted for six receivers with average values at 13 sections throughout y-axis.

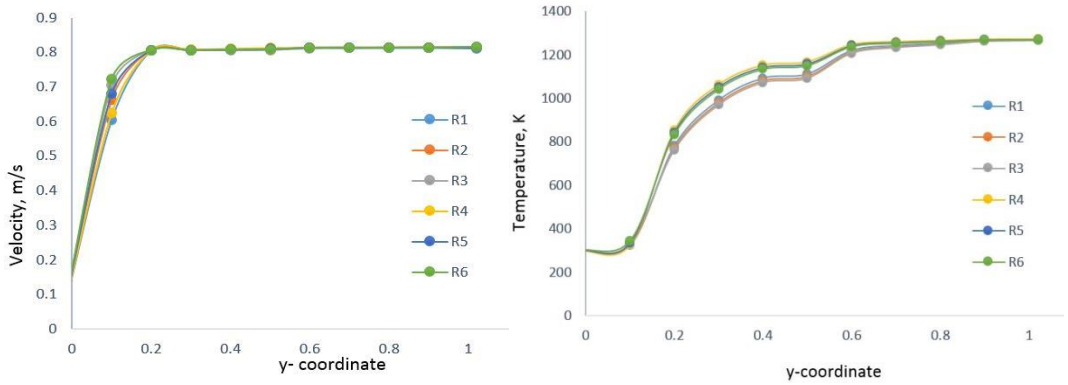

Figure 6: y-coordinate vs average velocity and average Temperature of alumina particle

4. Acknowledgements

The authors would like to acknowledge the Computational Science Program, Department of Mechanical Engineering, the Student Employment Program, UTEP, and the Department of Energy for their support.

5. References

[1] www.sandia.gov/????
[2] H.E. Patel, S.K.Das,T. Sundararagan, A.S. Nair, B. Geoge, T. Pradeep, Thermal conductivities of naked and monolayer protected metal nanoparticle based nanufluids: manifestation of anomalous enhancement and chemical effects, Applied Physics Letter, 2003, vol. 83, pp. 2931-2933
[3] D. Shin, D. Banarjee, International Journal of Heat and Mass Transfer, 2011, vol. 54, pp. 1064-1070
[4] Coastal Chemical Co. L.L.C Brenntag Company, HITEC Heat Transfer Salt. http://www.coastalchem.com.
[5] FLUENT 6.1 Documentation. http://www.cfd-online.com
[6] http://www.technicalglass.com/technical_properties.html
[7] http://en.wikipedia.org/wiki/Aluminium_oxide

A Polynomial Chaos Approach to Ensemble Kalman Filter SLAM for Autonomous Robot Motion

P. Delgado[1*], V. Kumar[2],
[1] Computational Science, El Paso, TX 79968, USA;
[2] Mechanical Engineering, El Paso, TX 79968, USA;
* Corresponding author (pmdelgado2@utep.edu)

Keywords: Robotics, Automation, SLAM, Polynomial Chaos,

ABSTRACT

One of the greatest challenges in the automation of robot motion is the problem of Simultaneous Localization and Mapping (SLAM). Current approaches rely heavily on linearization of sensor and motion models which can lead to unstable, non-convergent posterior probability estimates. In this paper, we develop an approach to solve the SLAM problem directly without linearization by utilizing a polynomial chaos-based Ensemble Kaman Filter (EnKF).

1 Introduction

One of the greatest challenges in the development of Self-Driving Cars, such as the Google Car, is equivalent to the Simultaneous Localization and Mapping problem in Robotics. A fully autonomous vehicle/robot needs to generate a map of its local environment dynamically while at the same time also identifying its position within the generated map. Feature based methods, such as Extended Kalman Filter SLAM and GraphSLAM, have been developed to approximate a solution with varying degrees of success. One common disadvantage in previously these algorithms is the need to linearize the motion/sensor model, which can lead to instability and lack of convergence in some cases. In this paper, we develop an alternative method to solve the SLAM problem utilizing the Ensemble Kalman Filter with Polynomial Chaos Expansions. As we shall demonstrate, this alternative approach eliminates the need to linearize the motion/sensor models and treats the non-linearity directly. The use of polynomial chaos expansions enables the propagation of uncertainty dynamically through stochastic galerkin projections.

2 SLAM

2.1 Models

Kinematic motion of a robot can be characterized [3] in 2D by linear (v) and angular (w) velocity controls and their effects on the robot's pose (x,y,θ) over a given time Δt. The equations of motion with stochastic noise v_t, w_t, γ_t are given by

$$
\begin{aligned}
x_{t+1} &= x_t - \frac{v_t}{w_t}\sin\theta + \frac{v_t}{w_t}\sin(\theta + w_t\Delta t) \\
y_{t+1} &= y_t \frac{v_t}{w_t}\cos\theta - \frac{v_t}{w_t}\cos(\theta + w_t\Delta t) \\
\theta_{t+1} &= \theta_t + w_t\Delta t + \gamma\Delta t
\end{aligned}
\tag{1}
$$

Sensor measurements to a landmark i with coordinates ($m_{i,x}$,$m_{i,y}$) at timestep t from a given robot pose (x,y,θ) are described by a measurement model [3] in terms of polar coordinates with respect to the current robot pose. The measurement model is given by

$$
z_t^i = \begin{bmatrix} \sqrt{(m_{j,x}-x)^2 + (m_{j,y}-y)^2} \\ a\tan 2(m_{j,y}-y, m_{j,x}-x) - \theta \\ m_{j,s} \end{bmatrix} + N\left(0, \begin{bmatrix} \sigma_r & 0 & 0 \\ 0 & \sigma_\theta & 0 \\ 0 & 0 & \sigma_s \end{bmatrix}\right). \tag{2}
$$

2.2 Ensemble Kalman Filter

The models (1) and (2) above can also be described in terms of the continuous system

$$
\begin{aligned}
\dot{\vec{x}} &= g(\vec{x}) + \varepsilon(t) \\
z' &= h(\vec{x}) + \delta(t)
\end{aligned}
\tag{3}
$$

with nonlinear vector functions g,h, and zero-mean Gaussian noise ε,δ. The Ensemble Kalman Filter is a monte-carlo approximation [4] to the linear Kalman Filter for discrete systems such as (3). In this approach, an ensemble of N initial states s1,…,sN are propagated through the model at each time step and are used to estimate the mean and variance associated with the pose (x,y,θ) and landmark coordinates ($m_{i,x}$,$m_{i,y}$). As with most monte-carlo approximations, a large ensemble size N is required to obtain adequate adequate accuracy in the approximation. To avoid the large computational expense associated with propagation of a large ensemble, we exploit the fact that the noise terms ε, δ can be characterized in terms of the statistical moments of the input variable u and characterize the noise as a polynomial function of random variables [4].

2 Polynomial Chaos Approach

We are primarily interested in the expectation and variance of the solution distribution, which are characterized by integrals

$$
\begin{aligned}
E[u] &= \int u\rho \\
Var[u] &= E[(u - E[u])]
\end{aligned}
\tag{4}
$$

at each timestep t, with ρ is the probability density function associated with the Gaussian distribution. We can characterize the components of the solution u_i in terms of a polynomial chaos expansion

$$u_i = \sum_{j=0}^{P} u_{ij}(t)\phi_{ij} \tag{5}$$

where φ_{ij} is the jth Hermite polynomial of the ith vector component[5]. We can apply a similar expansion for the measurement vector z. Substituting (5) into the ith equation of the continuous system, multiplying by a test function φ_{ij} and taking the expectation of the resulting equation, we obtain

$$\begin{aligned} \sum \int u_{ij}'(t)\phi_{ij}\phi_{kl}\rho &= \int g\left(\sum u_{ij}(t)\phi_{ij}\right)\phi_{kl}\rho \\ \sum \int z_{ij}\phi_{ij}\phi_{kl}\rho &= \int h\left(\sum u_{ij}(t)\phi_{ij}\right)\rho \end{aligned} \tag{6}$$

In doing so, we obtain a galerkin projection of the solution onto a space of orthogonal polynomials of the random variables in a similar fashion to the finite element method. The resulting system of non-linear equations (6) is expressed in terms of coefficients $u_{ij}(t)$ which, by themselves, have no physical meaning. However, by the orthogonality of the polynomials, the statistical moments are trivially obtained with equation (4) as

$$\begin{aligned} Exp[u_i(t)] &= u_{i0}(t) \\ Var[u_i(t)] &= \sum {u_{ij}}^2 Exp[{\phi_{ij}}^2] \end{aligned} \tag{7}$$

2 Discussion & Future Work

We have derived a polynomial chaos expansion approach to solve the robot SLAM problem with the Ensemble Kalman Filter. We obtained a non-linear system of equations similar to the galerkin finite element method and obtained the statistical moments of the robot pose and positions of landmarks (7) at low computational costs. Though the error of the expansion decays exponentially with polynomial order, the cost of our method also grows exponentially with polynomial order. For maps with a large number of landmarks, an efficient numerical solver is required to solve the non-linear system. In our future work, we will explore the effectiveness of different solvers for this problem.

References

[1] Bailey, T., Nieto, J., Guivant, J., Stevens, M., & Nebot, E. (2006, October). Consistency of the EKF-SLAM algorithm. In Intelligent Robots and Systems, 2006 IEEE/RSJ International Conference on (pp. 3562-3568). IEEE.

[2] Thrun, S., & Montemerlo, M. (2006). The graph SLAM algorithm with applications to large-scale mapping of urban structures. The International Journal of Robotics Research, 25(5-6), 403-429.

[3] S. Thrun, W. Burgard, D. Fox "*Probabilistic Robotics"*. 2st edition, MIT Press, 2005.

[4] Li, J., & Xiu, D. (2009). A generalized polynomial chaos based ensemble Kalman filter with high accuracy. Journal of computational physics, 228(15), 5454-5469.
[5] D. Xiu, & Karniadakis, G. E. (2002). The Wiener--Askey polynomial chaos for stochastic differential equations. SIAM Journal on Scientific Computing, 24(2), 619-644.

COMPUTATIONAL MODELING OF ISENTROPIC FLOW THROUGH A CONICAL NOZZLE

O. Vidaña[1], M. Chaidez[1], and N. Love[1]*
[1] Department of Mechanical Engineering, University of Texas at El Paso, El Paso, TX 79968, USA;
* Norman D. Love (ndlove@utep.edu)

Keywords: *Computational, Isentropic, Flow, Conical, Nozzle*

ABSTRACT

The de Laval nozzle is widely used in rocket and turbofan engines alike due to their ability to accelerate gases to supersonic velocities. A standard 15 degree half angle conical nozzle design with a throat diameter of 15 mm and a length of 88.23 mm was modeled in the FLUENT program. To validate the FLUENT model, it was assumed that full combustion of methane and oxygen occurred yielding only carbon dioxide as its product. The isentropic flow equations were utilized to determine the exit temperature, velocity, and pressure of the de Laval nozzle. To complete the analysis, it was assumed that the de Laval nozzle had an initial pressure of 241.32 kPa and an initial temperature of 3500 K. In the FLUENT model, the same initial condition as that of the isentropic flow equations were utilized. The theoretical calculated values using the isentropic flow equations were very similar to the results from the simulation. It can be concluded that FLUENT is a reliable validation source to isentropic flow type of problems as the error margin proved to be negligible.

1. Introduction

The de Laval nozzle, also known as converging-diverging nozzle, was first invented by Gustaf de Laval in 1888 for a small steam turbine [3]. The de Laval nozzle design contains a converging section were subsonic, isentropic gases are compressed until they reach Mach 1 at the throat. Following the throat, the difference in pressures between the chamber and throat accelerate the gases to supersonic speeds. Due to the de Laval nozzle's ability to reach supersonic speeds, it has been widely used in rocket, as well as in turbofan engines. Therefore, extensive computational research has been conducted to understand the gas flow as it travels through the converging-diverging section of the nozzle.

The de Laval nozzle can contain a conical or bell contour for the diverging exit section. The conical nozzle was widely utilized due to its ease in manufacturability and its ability to adapt easily to various expansion ratio. As the de Laval nozzle was adapted to be used in rocket engines, the design changed due to the demand for shorter and more lightweight nozzles. Hence, the bell nozzle was designed. The bell nozzle design is commonly used in rocket engine due to its shorter length and higher performance than the traditional conical nozzle. The bell nozzle contains a gradual parabolic shape that allows the gases to expand slowly, hence preventing oblique shocks from occurring. The design of the bell nozzle can be completed using a standard 15 degree half angle conical nozzle as a guide. The length of the bell nozzle is obtained by using 80% of the total length of the conical nozzle and its optimum parabolic contour of the bell nozzle is obtained by implanting Rao's parabolic approximation.

The design of a conical diverging converging nozzle for a MHD generator that uses methane and oxygen as the fuel and oxidizer is being developed. This paper will focus in the validation of theoretical values obtained for the gases of the nozzle using a FLUENT computational model.

2. Theoretical Analysis of Gases

A standard 15 degree half angle conical nozzle design with a throat diameter of 15 mm and a length of 88.23 mm was used to be simulated in the FLUENT program. The throat section contains a circular arc with a radius 1.5 of the diameter of the throat to prevent local overheating. In order to determine the missing dimensions of the nozzle, the area ratio of the nozzle was calculated. The area ratio would provide the required exit diameter of the nozzle so that the desired exit parameters were met.

$$\varepsilon = \frac{A_e}{A*} = \frac{1}{M_e}\sqrt{\left[\frac{2+M_e{}^2(\gamma-1)}{\gamma+1}\right]^{\gamma+1/\gamma-1}} \tag{1}$$

To complete the analysis, it was assumed that the methane and oxygen injected inside the combustor were fully combusted to produce carbon dioxide as its product. The de Laval nozzle was expected to have an exit velocity of 1200 m/s or Mach number of 4, at a measured chamber pressure and temperature of 241.3 kPa and 3500 K respectively. To facilitate the analysis, the gases were assumed to be isentropic. With the known parameters the temperature, velocity, and pressure at the exit of the de Laval nozzle could be calculated using the following isentropic relations:

$$T_t = T\left[1 + \frac{M^2(\gamma-1)}{2}\right] \tag{2}$$

$$V = M\sqrt{\gamma RT} \tag{3}$$

$$P_t = P\left[1 + \frac{\gamma-1}{2}M^2\right]^{\gamma/\gamma-1} \tag{4}$$

A FLUENT model of the de Laval nozzle using the parameters described above was also constructed. The theoretical values were then utilized to validate the computational results.

3. Results

The isentropic flow equations were used to calculate the velocity, temperature and pressure across the converging/diverging sections of the nozzle up to Mach 4. The computed values are displayed in Table 1.

Mach #	Velocity (m/s)	Temperature (K)	Pressure (Pa)
0.5	453.46	3377.97	205989.76
1	862.92	3058.10	132174.72
1.5	1202.93	2641.26	68753.70
2	1469.78	2218.00	31549.22
2.5	1672.95	1839.08	13680.59
3	1825.94	1521.41	5871.98
3.5	1941.31	1263.48	2564.18
4	2029.04	1056.76	1155.78

Table 1

The same constraints were entered in the Boundary Conditions section of FLUENT, which yielded the following results.

As expected from theory, the Mach number contours revealed subsonic velocities in the converging section, sonic at the throat, and supersonic in the diverging section. At the the end of the nozzle the simulation revealed precisely Mach 4 velocities as it was designed for. When the velocities were transalted to meters per second the acceleration across the system was seen more in detail. The lowest speeds were located around the inlet at 453m/s, and the highest on the outlet at 2028m/s.

The pressure contours revealed a pressure drop that varied from 241.32 kPa to 1.12 kPa. This decline was predicted as well, as the Bernoulli equation states that if the velocity of a fluid increases the pressure decreases.

Similarly, the temperature went down. This makes sense according to the ideal gas equation, which indicates that if the pressure of a gas decreases, then the temperature decreases proportionally. The contours displayed an inlet temperature of 3500 K as specified, while the outlet temperature was 1051 K.

4. Conclusion

The theoretical calculated values using the isentropic flow equations were very similar to the results from ANSYS FLUENT. Table 2 compares the exit values for both methods and the percent error between them. The biggest error margin was associated with the pressure with a minimal 3.34%.

	Theoretical Exit Value	**FLUENT Exit Value**	**Percent Error**
Velocity (m/s)	2029.04	2027.67	0.07
Temperature (K)	1056.76	1050.88	0.56
Pressure (Pa)	1155.78	1117.15	3.34

Table 2

It can be concluded that FLUENT is a reliable validation source to isentropic flow type of problems as the error margin proved to be negligible. However, this specific model is not recommended for nozzle design as only one flowing fluid can be specified on the initial conditions. In real life applications combustion does not only yield CO_2 but also H_2O and many other residuals, ignoring all these other substances could return inaccurate data. The model analyzed in this paper served as the basis for the design of the nozzle section of the MHD system, but as the design began to evolve the isentropic flow simulation was replaced by a non-premixed combustion model.

References

[1] Çengel, Yunus A., and John M. Cimbala. *Fluid Mechanics: Fundamentals and Applications*. Boston, Mass.: McGraw-Hill, 2010. Print.

[2] Huzel, Dieter K., David H. Huang, and Harry Arbit. *Modern Engineering for Design of Liquid-propellant Rocket Engines*. Washington, D.C.: American Institute of Aeronautics and Astronautics, 1992. Print.

[3] Ward, Thomas A. *Aerospace Propulsion Systems*. Singapore: John Wiley & Sons, 2010. Print.

Department of Mechanical Engineering | Engineering Annex/ Suite 126
The University of Texas at El Paso | 500 W. University Avenue | El Paso, TX. 79968.0521
Ph (915) 747 5450 I Fax (915) 747 5019 | Http:// me.utep.edu/
tellME@utep.edu |

Department of Mechanical Engineering | Engineering Annex, Suite 126
The University Of Texas At El Paso | 500 W. University Avenue | El Paso, Tx. 79968-0521
Ph (915) 747 5450 | Fax (915) 747 5019 | Http://me.utep.edu/
Mechanical@utep.edu | Meug@utep.edu | Megrad@utep.edu